

AFAPL-TR-77-13

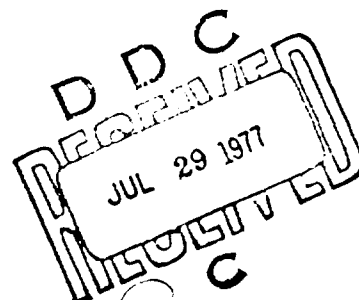
AD A 042233

## CLOSED-CYCLE RARE-GAS ELECTRICAL-DISCHARGE LASER

RESEARCH APPLICATIONS DIVISION  
SYSTEMS RESEARCH LABORATORIES, INC.  
2800 INDIAN RIPPLE ROAD  
DAYTON, OHIO 45440

APRIL, 1977

TECHNICAL REPORT AFAPL TR 77 13  
FINAL REPORT FOR PERIOD 1 JUNE 1973 - 30 SEPTEMBER 1976



Approved for public release; distribution unlimited

AD No. \_\_\_\_\_  
DDC FILE COPY


AIR FORCE AERO PROPULSION LABORATORY  
AIR FORCE WRIGHT AERONAUTICAL LABORATORIES  
AIR FORCE SYSTEMS COMMAND  
WRIGHT-PATTERSON AIR FORCE BASE, OHIO 45433

NOTICE

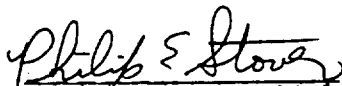
When Government drawings, specifications, or other data are used for any purpose other than in connection with a definitely related Government procurement operation, the United States Government thereby incurs no responsibility nor any obligation whatsoever; and the fact that the government may have formulated, furnished, or in any way supplied the said drawings, specifications, or other data, is not to be regarded by implication or otherwise as in any manner licensing the holder or any other person or corporation, or conveying any rights or permission to manufacture, use, or sell any patented invention that may in any way be related thereto.

This report has been reviewed by the Information Office (OIP) and is releasable to the National Technical Information Service (NTIS). At NTIS, it will be available to the general public, including foreign nations.


This technical report has been reviewed and is approved for publication.

  
PETER BLETZINGER  
Project Engineer

FOR THE COMMANDER

  
PHILIP E. STOVER, Chief  
High Power Branch

ACCESSION FOR	White Series <input checked="" type="checkbox"/>	Blue Series <input type="checkbox"/>
NTIS		
DOC		
UNANNOUNCED		
JUSTIFICATION		
BY		
DIST. CODE	DISTRIBUTION/AVAILABILITY CODES	
	AVAIL. CODE	SPECIAL



Copies of this report should not be returned unless return is required by security considerations, contractual obligations, or notice on a specific document.

UNCLASSIFIED

SECURITY CLASSIFICATION OF THIS PAGE (When Data Entered)

REPORT DOCUMENTATION PAGE		READ INSTRUCTIONS BEFORE COMPLETING FORM
1. REPORT NUMBER AFAPL-TR-77-13	2. GOVT ACCESSION NO.	3. RECIPIENT'S CATALOG NUMBER
4. TITLE (and Subtitle) Closed-Cycle Rare-Gas Electrical-Discharge Laser.		5. TYPE OF REPORT & PERIOD COVERED Final rept. 1 June 1973 - 30 Sept 1976
7. AUTHOR(s) Robert A. Olson Dennis F. Grosjean		6. PERFORMING ORG. REPORT NUMBER 14 SRL-6792-Final
9. PERFORMING ORGANIZATION NAME AND ADDRESS Systems Research Laboratories, Inc. 2800 Indian Ripple Road Dayton, Ohio 45440		8. CONTRACT OR GRANT NUMBER(s) F33615-73-C-4130
11. CONTROLLING OFFICE NAME AND ADDRESS		10. PROGRAM ELEMENT, PROJECT, TASK AREA & WORK UNIT NUMBERS Project 2301 Task S2 Work Unit 75
14. MONITORING AGENCY NAME & ADDRESS (if different from Controlling Office) Air Force Aero Propulsion Laboratory AFAPL/POP Wright-Patterson Air Force Base Ohio 45433		12. REPORT DATE Apr 1977
16. DISTRIBUTION STATEMENT (of this Report) Approved for public release; distribution unlimited.		13. NUMBER OF PAGES 17 (12) 179p.
17. DISTRIBUTION STATEMENT (of the abstract entered in Block 20, if different from Report)		15. SECURITY CLASS. (of this Report) Unclassified
18. SUPPLEMENTARY NOTES		15a. DECLASSIFICATION DOWNGRADING SCHEDULE
19. KEY WORDS (Continue on reverse side if necessary and identify by block number)		
laser seed compounds photoabsorption afterglow closed cycle axial fan pulsed transverse energy-transfer fast flow ferrofluidic seal excitation pumping ultrahigh vacuum preionization laser gain dissociative rare-gas lasers xenon laser-output power recombination molecular lasers buffer gas high-repetition rate photoionization		
20. ABSTRACT (Continue on reverse side if necessary and identify by block number) The recently developed technology of high-pressure molecular lasers has been combined with ultrahigh-vacuum technology to develop a fast-flow high-pressure laser system capable of long-duration closed-cycle operation with rare gases. The system has been used to investigate laser media excited by short, fast-rising high-voltage pulses under conditions of high pressure, fast flow, and low-background impurity level. Experimental results of parametric investigations of high-repetition-rate laser performance for Ar-Xe and He-Xe mixtures are given.		

DD FORM 1 JAN 73 1473

EDITION OF 1 NOV 65 IS OBSOLETE

UNCLASSIFIED

SECURITY CLASSIFICATION OF THIS PAGE (When Data Entered)

340400

UNCLASSIFIED

SECURITY CLASSIFICATION OF THIS PAGE(When Data Entered)

Ultraviolet photoionization characteristics of molecular lasers are presented. The photoabsorption cross sections and photoionization yields of N,N-dimethylaniline, triethylamine, trimethylamine, and tri-n-propylamine are given and their use as laser seed compounds discussed; nitric oxide is also considered. UV emission spectra of spark sources applicable to CO and CO<sub>2</sub> preionized lasers are presented.

UNCLASSIFIED

SECURITY CLASSIFICATION OF THIS PAGE(When Data Entered)

## PREFACE

This final report was prepared by the Research Applications Division of Systems Research Laboratories, Inc., under Contract No. F33615-73-C-4130, Project 2301, Task S2, Work Unit 75, with Dr. Peter Bletzinger as Government Project Monitor. The research was conducted by Mr. Robert A. Olson and Mr. Dennis F. Grosjean.

This research was funded jointly by the Air Force Aero Propulsion Laboratory, the Air Force Avionics Laboratory, and the Air Force Weapons Laboratory.

# TABLE OF CONTENTS

SECTION	PAGE
I INTRODUCTION	1
II CLOSED-CYCLE RARE-GAS ELECTRICAL-DISCHARGE LASER	3
2.1 Background	3
2.2 System Design and Construction	18
2.2.1 Vacuum and Recirculating-Flow System	18
2.2.2 Laser Discharge and Optical Cavity	30
3.3.4 High-Repetition-Rate Pulser	37
2.3 Experimental Results	46
2.3.1 Performance of the 12-cm-Gain-Length Laser with Xe-Buffer-Gas Mixtures	46
2.3.2 Performance of 25-cm-Gain-Length Laser with Xe-Buffer-Gas Mixtures	82
2.4 Discussion of Results	114
III UV PHOTOIONIZATION	124
3.1 Introduction	124
3.2 Experimental Results	125
IV CONCLUSIONS	156
REFERENCES	158

PRECEDING PAGE BLANK NOT FILMED

# LIST OF ILLUSTRATIONS

FIGURE		PAGE
1	CO <sub>2</sub> -Laser Energy Levels	5
2	Normalized Saturation Intensity as a Function of Flow Transit Time	5
3	Laser Discharge and Cavity Geometries	7
4	Atmospheric Transmission from 1.7 to 5.5 $\mu$ and cw Xenon Laser Lines	19
5	Isometric Drawing of Closed-Cycle Rare-Gas Electrical-Discharge Laser	20
6	Fan and System Flow Characteristics	23
7	Schematic Diagram of Externally Driven Axial Fan Assembly	24
8	Photographs of Externally Driven Axial Fan Assembly	25
9	CCRGEDL System Pressure as a Function of Time for Fan Operating under Vacuum Conditions	27
10	Photograph of 1-kW Heat Exchanger	28
11	Photograph of Pitot-Static Probe Assembly	29
12	Pitot-Static Probe Data for 12-cm-Gain-Length Configuration	31
13	Schematic Diagram of Laser Discharge and Flow Transition Section of Gas Recirculation Loop	32
14	Photograph of Internal-Mirror Mounting Configuration	34
15	Schematic Diagram of 25-cm-Gain-Length Laser Configuration	35
16	Photograph of 25-cm-Gain-Length Laser Configuration	36
17	Pitot-Static Probe Data for 25-cm-Gain-Length Configuration	38
18	Schematic Diagram of 1-kW High-Repetition-Rate Pulser	39
19	Schematic Diagram of Optoelectronic Receiver for 1-kW Pulser	40
20	Schematic Diagram of Oscillator and Pulse-Train Network	41

# LIST OF ILLUSTRATIONS (cont'd)

FIGURE		PAGE
21	Oscillograms of Discharge Current and Voltage Pulses With (a) and Without (b) Secondary Capacitor	43
22	Schematic Diagram of 15-kW High-Repetition-Rate Pulser	44
23	Schematic Diagram of Optoelectronic Receiver for 15-kW Pulser	45
24	Block Diagram of Power Distribution for CCRGEDL	47
25	Schematic Diagram of Experimental Setup for Gain Measurements	48
26	Oscillogram of Pulsed Gain at 2.03 $\mu$ in 12-cm-Gain-Length Laser	49
27	Oscillograms of Pulsed Gain at 4 $\mu$ in 12-cm-Gain-Length Laser	51
28	Gain at 4 $\mu$ as a Function of Pressure in 12-cm-Gain-Length Laser	52
29	Oscillograms of Laser Pulses from 12-cm-Gain-Length Laser at a Pressure of 700 Torr He-Xe (1400:1)	54
30	Dependence of Average Laser Output Power upon PRF for 12-cm-Gain-Length Laser at a Pressure of 700 Torr He-Xe (1400:1)	55
31	Dependence of Average Laser Output Power upon Continuous Operating Time for 12-cm-Gain-Length Laser at a Pressure of 700 Torr He-Xe (1400:1)	57
32	Pressure Dependence of Average Laser Output Power for Ar-Xe Mixtures in 12-cm-Gain-Length Laser	60
33	Dependence of Average Laser Output Power upon (a) PRF and (b) Charging Voltage for Ar-Xe Mixtures in 12-cm-Gain-Length Laser	62
34	Dependence of Average Laser Output Power upon (a) PRF and (b) Charging Voltage for Ar-Ne-Xe Mixture in 12-cm-Gain-Length Laser	63
35	Oscillograms of Laser Pulses Obtained at a Pressure of 300 Torr He-Xe (200:1) in 12-cm-Gain-Length Laser	66



# LIST OF ILLUSTRATIONS (cont'd)

FIGURE		PAGE
36	Pressure Dependence of Peak Output of Laser Pulses from He-Xe (100:1) in 12-cm-Gain-Length Laser	67
37	Pressure Dependence of Peak Output of Laser Pulses from He-Xe (200:1) in 12-cm-Gain-Length Laser	68
38	Pressure Dependence of Peak Output of Laser Pulses from He-Xe (300:1) in 12-cm-Gain-Length Laser	69
39	Pressure Dependence of Peak Output of Laser Pulses from He-Xe (400:1) in 12-cm-Gain-Length Laser	70
40	Pressure Dependence of Peak Output of Laser Pulses from He-Xe (1000:1) in 12-cm-Gain-Length Laser	71
41	Pressure Dependence of Peak Output of Laser Pulses from He-Xe (2000:1) in 12-cm-Gain-Length Laser	72
42	Pressure Dependence of Peak Output of Laser Pulses from He-Xe (5000:1) in 12-cm-Gain-Length Laser	73
43	Pressure Dependence of Peak Output of Laser Pulses from He-Xe (10,000:1) in 12-cm-Gain-Length Laser	74
44	Pressure Dependence of Peak Output of 4.02- $\mu$ Laser Pulse from He-Xe Mixtures in 12-cm-Gain-Length Laser	75
45	Pressure Dependence of Average Output Power from He-Xe Mixtures in 12-cm-Gain-Length Laser	76
46	(a) Voltage Dependence of Peak Discharge Current for He-Xe Mixtures in 12-cm-Gain-Length Laser; (b) Voltage Dependence of Peak Output of 4.02- $\mu$ Laser Pulse for He-Xe Mixtures in 12-cm-Gain-Length Laser	78
47	Dependence of Average Laser Output Power upon Charging Voltage for Ar-Ne-Xe Mixture in 12-cm-Gain-Length Laser	79
48	Dependence of Average Laser Output Power upon PRF for Ar-Ne-Xe Mixture in 12-cm-Gain-Length Laser	80
49	Dependence of Average Laser Output Power upon Continuous Operating Time for Ar-Ne-Xe Mixture in 12-cm-Gain-Length Laser	81
50	Photograph of CCRGEDL with 25-cm-Gain-Length Configuration	83

# LIST OF ILLUSTRATIONS (cont'd)

FIGURE		PAGE
51	Discharge Current, Voltage, and Power Pulse Shapes for He-Xe and Ar-Xe Mixtures in 25-cm-Gain-Length Laser	85
52	Dependence of Discharge Breakdown Voltage upon Charging Voltage for He-Xe and Ar-Xe Mixtures in 25-cm-Gain-Length Laser	86
53	Dependence of Peak Discharge Current upon Charging Voltage for He-Xe and Ar-Xe Mixtures in 25-cm-Gain-Length Laser	87
54	Oscillograms of Laser Pulses Obtained at a Pressure of 200 Torr Ar-Xe (200:1) in 25-cm-Gain-Length Laser	90
55	Oscillograms of Laser Pulses Obtained at a Pressure of 200 Torr He-Xe (200:1) in 25-cm-Gain-Length Laser	91
56	Pressure Dependence of Peak Output of Laser Pulses from He-Xe (50:1) in 25-cm-Gain-Length Laser	93
57	Pressure Dependence of Peak Output of Laser Pulses from He-Xe (100:1) in 25-cm-Gain-Length Laser	94
58	Pressure Dependence of Peak Output of Laser Pulses from He-Xe (200:1) in 25-cm-Gain-Length Laser	95
59	Pressure Dependence of Peak Output of Laser Pulses from He-Xe (500:1) in 25-cm-Gain-Length Laser	96
60	Pressure Dependence of Peak Output of Laser Pulses from He-Xe (1000:1) in 25-cm-Gain-Length Laser	97
61	Pressure Dependence of Peak Output of Laser Pulses from He-Xe (2000:1) in 25-cm-Gain-Length Laser	98
62	Pressure Dependence of Peak Output of Laser Pulses from He-Xe (5000:1) in 25-cm-Gain-Length Laser	99
63	Pressure Dependence of Peak Output of Laser Pulses from Ar-Xe (100:1) in 25-cm-Gain-Length Laser	100
64	Pressure Dependence of Peak Output of Laser Pulses from Ar-Xe (200:1) in 25-cm-Gain-Length Laser	101
65	Pressure Dependence of Peak Output of Laser Pulses From Ar-Xe (500:1) in 25-cm-Gain-Length Laser	102

# LIST OF ILLUSTRATIONS (cont'd)

FIGURE		PAGE
66	Dependence of Average Laser Output Power upon PRF for He-Xe and Ar-Xe Mixtures in 25-cm-Gain-Length Laser	103
67	Pressure Dependence of Average Laser Output Power for He-Xe Mixtures in 25-cm-Gain-Length Laser	104
68	Pressure Dependence of Average Laser Output Power for Ar-Xe Mixtures in 25-cm-Gain-Length Laser	105
69	Pressure Dependence of Average Laser Output Power for He-Xe (200:1) at Various Charging Voltages in 25-cm-Gain-Length Laser	106
70	Pressure Dependence of Average Laser Output Power for Ar-Xe (200:1) at Various Charging Voltages in 25-cm-Gain-Length Laser	107
71	Dependence of Average Laser Output Power upon Charging Voltage for He-Xe Mixtures in 25-cm-Gain-Length Laser	108
72	Dependence of Average Laser Output Power upon Charging Voltage for Ar-Xe Mixtures in 25-cm-Gain-Length Laser	109
73	Dependence of Average Laser Output Power upon Charging Voltage for He-Xe (200:1) at Various Pressures in 25-cm-Gain-Length Laser	111
74	Dependence of Average Laser Output Power upon Charging Voltage for Ar-Xe (200:1) at Various Pressures in 25-cm-Gain-Length Laser	112
75	Dependence of Peak Laser Output at Various Wavelengths upon Charging Voltage for Ar-Xe Mixtures in 25-cm-Gain-Length Laser	113
76	Xe Energy-Level Diagram	118
77	Percentage of Discharge Energy into Formation of Ionic and Excited Species in He-Xe (200:1) as a Function of E/N	120
78	Percentage of Discharge Energy into Formation of Ionic and Excited Species in Ar-Xe (160:1) as a Function of E/N	121
79	Pumping Mechanisms in Ar-Xe and He-Xe	122

LIST OF ILLUSTRATIONS (cont'd)

FIGURE		PAGE
80	Experimental Apparatus for Absorption Measurements Using Continuum Illumination	126
81	Absorption Coefficients of CO <sub>2</sub> for the Ranges (a) 125 to 160 nm and (b) 160 to 185 nm	127
82	Measured Absorption Coefficient of CO Between 125 and 160 nm, Taken With Pressures of (a) 20 Torr and (b) 100 Torr	128
83	Measured Transmission of a 5-mm-thick Sample of Calcium Fluoride from 125 to 185 nm	130
84	Measured Transmission of a 2-mm-thick Sample of Magnesium Fluoride from 115 to 130 nm After Use	131
85	Schematic Diagram of Experimental Arrangement for Measurement of Photoionization Efficiencies and Photoabsorption Cross Sections	132
86	Typical Spectral Output of Monochromator for Photoionization Measurements	133
87	Photoabsorption Cross Sections (a) and Photoionization Yields (b) of N,N-Dimethylaniline	135
88	Photoabsorption Cross Sections (a) and Photoionization Yields (b) of Triethylamine	136
89	Photoabsorption Cross Sections (a) and Photoionization Yields (b) of Trimethylamine	137
90	Photoabsorption Cross Sections (a) and Photoionization Yields (b) of Tri-n-propylamine	138
91	Comparison of Measured Photoionization Efficiency of NO with Published Data	140
92	Ion-Production-Rate Curves with Pressure Optimized for Radiation at (a) 121.6 and 165 nm for Dimethylaniline, (b) 121.6 and 165 nm for Triethylamine, (c) 121.6 and 154 nm for Trimethylamine, and (d) 121.6 and 165 nm for Tripropylamine	142
93	Ion-Production-Rate Curves for Nitric Oxide at Two Different Pressures, Calculated from Data of Watanabe, et al. <sup>104</sup>	143

# LIST OF ILLUSTRATIONS (cont'd)

FIGURE		PAGE
94	Comparative Spectral Emission (Qualitative) of Pin Spark in Several Molecular Gases	145
95	Schematic Diagram of the Experimental Arrangement for Calibration of UV Monochromator Response	147
96	Normalized Quantum Yield of Sodium-Salicylate Detector	149
97	Comparative Spectral Emission of Pin Spark in CO Mixtures	150
98	Spectral Emission of Pin Spark in 100-Torr Ar + 1-Torr Kr	152
99	Comparative Spectral Emission of Surface Spark in CO Mixtures	153
100	Spectral Emission of Surface Spark in a CO + N <sub>2</sub> Mixture	155

# LIST OF TABLES

TABLE		PAGE
1	Molecular-Gas Discharge Lasers with Recirculating Flow	4
2	Pulsed High-Pressure Rare-Gas Lasers <sup>6</sup>	14
3	Pressure Drop in Loop Components	22
4	Xe-I Laser Lines Observed in He-Xe Discharge (12-cm Gain Length)	64
5	Xe-I Laser Lines Observed in He-Xe Discharge (25-cm Gain Length)	88
6	Xe-I Laser Lines Observed in Ar-Xe Discharge (25-cm Gain Length)	89
7	Xenon Gas Discharge Lasers with Recirculating Flow	115
8	Xe-I Laser Lines Obtained from CCRGEDL	116

## SECTION I INTRODUCTION

The rapid development of high-power, high-pressure molecular lasers during the last decade was made possible by the innovative application of techniques for the uniform excitation of gases at high pressure. Convective cooling, preionization, and pulsed transverse-excitation techniques have been vital to the achievement of uniform discharges in molecular gases at pressures up to and above atmospheric. This work has been discussed in several review articles<sup>1-4</sup> which provide a comprehensive listing of the published literature in this area.

Application of the above technology to atomic gas lasers is still in an early stage.<sup>5-8</sup> This report describes the result of such an application--a fast-flow, high-pressure laser system capable of long-duration closed-cycle operation with atomic gases. The nucleus of this closed-cycle rare-gas electrical-discharge laser (CCRGEDL) is a gas-recirculation loop, constructed from ultrahigh-vacuum components, through which gas is circulated by an axial fan. Pulsed transverse excitation is employed, using Rogowski electrodes and preionization wires in the Lamberton-Pearson configuration.<sup>9</sup> The ultrahigh-vacuum properties of the CCRGEDL system result in a very low contamination rate of the laser medium, which is of critical importance in the case of rare gases.

In the development of the CCRGEDL system, the main problem encountered was that of contamination of the laser medium by the gas-recirculation fan. In initial attempts to use a fan situated entirely within the gas-flow loop, the rate of outgassing from fan motor and bearing lubricant was unacceptably high. This problem was solved by locating the fan motor outside the gas-flow loop and driving the fan propeller through a high-speed rotary vacuum seal.

A brief discussion of fast-flow lasers in Section 2.1 provides the background for the development of the CCRGEDL. The design and performance of the vacuum/gas-recirculation system is given in Section 2.2.1. The laser discharge and optical cavity for 12-cm- and 25-cm-gain-length configurations are described in Section 2.2.2. The 1-kW and 15-kW high-repetition-rate

pulsers used to drive the laser discharge are described in Section 2.2.3. The results of parametric evaluations of laser performance for Xe-buffer gas mixtures in the 12- and 25-cm-gain-length configurations are given in Sections 2.3.1 and 2.3.2, respectively. A discussion of results in Section 2.4 compares the performance of the CCRGEDL with previously published results and suggests the laser pumping mechanisms for Ar-Xe and He-Xe mixtures. The photoabsorption and photoionization characteristics of gases suitable for UV preionized gas discharges are presented in Section 3. Conclusions are given in Section 4.



## SECTION 11

### CLOSED-CYCLE RARE-GAS ELECTRICAL-DISCHARGE LASER

#### 2.1 Background

The first proposals for the application of gas-dynamic techniques to lasers appear to have been made in 1963 by Hertzberg and Hurle<sup>10</sup> and by Basov and Oraevskii.<sup>11</sup> Since that time gas flows have been used with great success for convective mixing and cooling of laser media and for the production of population inversions during rapid gas expansion (see Ref. 1-4).

The first report of a CO<sub>2</sub> gas-discharge laser with recirculating flow was made by Tiffany, *et al.*,<sup>12</sup> in 1969. Since then most of the work in this area has been concentrated on the CO<sub>2</sub> laser. This is pointed up in Table 1 where most of the recirculating-flow lasers described in the open literature up to the present time are listed. It is instructive to investigate the reasons why CO<sub>2</sub> is particularly well-suited to flowing-gas operation.

One of the most important benefits of gas flow in a CO<sub>2</sub> laser is the removal of heat generated in the discharge volume. The pertinent energy levels for the 10.6-μ CO<sub>2</sub> laser are shown schematically in Figure 1. The lower laser level 10<sup>0</sup>0 decays to the 00<sup>0</sup>0 level via the 01<sup>1</sup>0 level which is about 1000°K above ground state. In order to avoid thermal population of 01<sup>1</sup>0--which tends to reduce the depopulation rate of 10<sup>0</sup>0 and, therefore, the population inversion--it is essential to maintain a low gas temperature.

In the case of static or slow-flow lasers, depopulation of the 01<sup>1</sup>0 level is dependent upon diffusion of this species to the tube walls. In the multi-Torr pressure region, convective cooling is much more effective than diffusion cooling. The ratio of laser output power in the convection and diffusion cases is<sup>24,3</sup>

$$\frac{P_{\text{conv}}}{P_{\text{diff}}} \propto \frac{dV_F}{\lambda V_T}, \quad (1)$$

where  $d$  = width of laser interaction region,  $\lambda$  = mean free path,  $V_F$  = flow velocity, and  $V_T$  = thermal velocity. Under the conditions pressure = 20 Torr, room temperature,  $d$  = 1 cm, and  $V_F$  = 30 m/sec, the ratio  $P_{\text{conv}}/P_{\text{diff}} \propto 500$ .

TABLE 1  
MOLECULAR-GAS DISCHARGE LASERS WITH RECIRCULATING FLOW

Gas	Reference	$\lambda$ ( $\mu$ )	PRF (kHz)	Pulse Energy (J)	Average Output Power	Efficiency (%)	Pressure (Torr)	Flow	Discharge Dimensions (HWL) (cm)
CO <sub>2</sub>	Tiffany, <u>et al.</u> <sup>12,13</sup> (1969)	10.6	cw	-	1 kW	6	20	30 m/sec 0.15 lb/sec	100 (L)
	Beaulieu <sup>14</sup> (1971)	10.6	1.2	0.5	600 W		1 atm		150 (L)
	Hill <sup>15</sup> (1971)	10.6	cw	-	15 kW (150-200 W input) 17 pass amp	10-20	50	28,000 CFM 0.6 lb/sec	5.6×76×100
	Rabe* (1976)								
	Turgeon <sup>16</sup> (1971)	10.6	1	0.065	65 W			1.6 m/sec	2.5×2×100
	Dumanchin, <u>et al.</u> <sup>17</sup> (1972)	10.6	0.1	20	2 kW		1 atm	50 m/sec	10×10×100
	Seguin & Sedgwick <sup>18</sup> (1972)	10.6	cw	-	200 W	5	11	40 m/sec 0.015 lb/sec	3.8×?×36
	Brown & Davis <sup>19</sup> (1972)	10.6	cw	-	27.2 kW (150 W input) 11 pass amp	17.2	30	1 lb/sec	6.3×53×244
	Glanford, <u>et al.</u> <sup>20</sup> (1973)	10.6	1	0.32	320 W	4.5	1 atm	50 m/sec	1×1×50
	Dzakowic & Wutzke <sup>21</sup> (1973)	10.6	0.6	0.33	200 W	6	510	41.5 m/sec	1.1×1.5×33
N <sub>2</sub>	Tulip, <u>et al.</u> <sup>22</sup> (1976)	10.6	2	0.75	1.5 kW?	5?	1 atm	100 m/sec	2.5×2.5×60
	Targ <sup>23</sup> (1972)	0.337	1.2	0.001	1.5 W [300 kW (peak)]	0.014	35	30 m/sec	4×?×76

\* Private communication

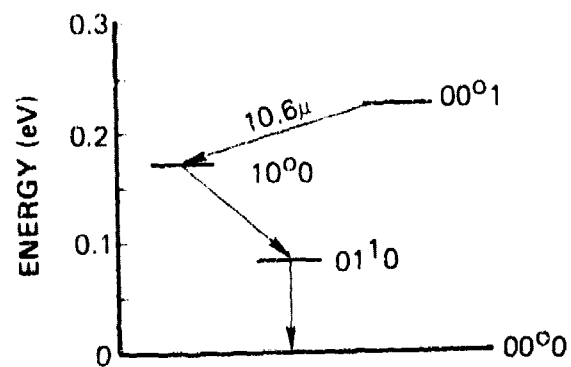


Figure 1. CO<sub>2</sub>-Laser Energy Levels

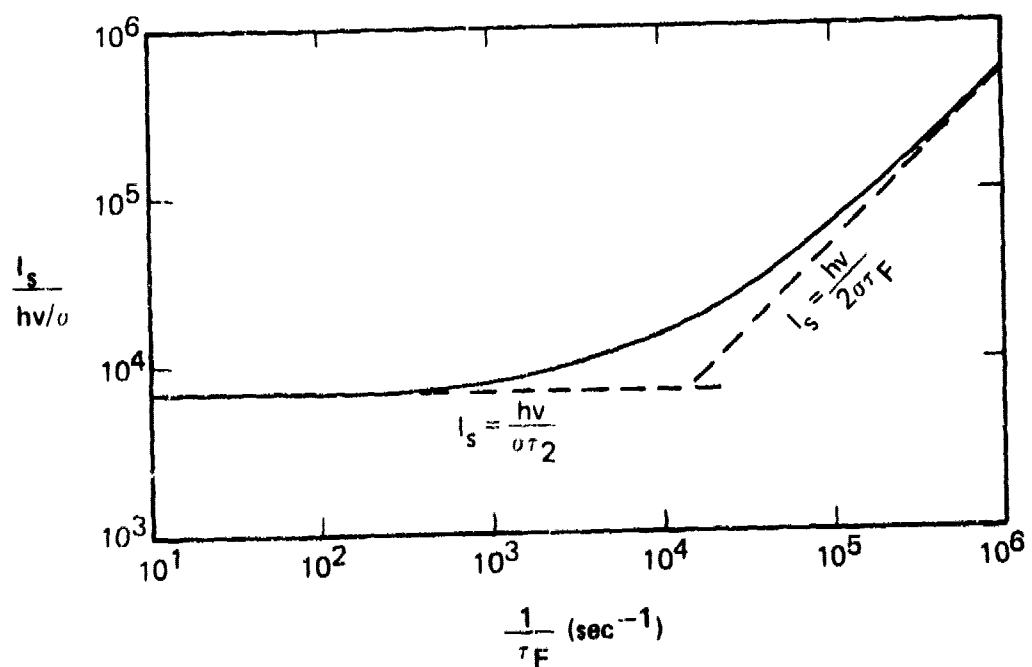


Figure 2. Normalized Saturation Intensity as a Function of Flow Transit Time

Another important benefit of flow in the CO<sub>2</sub> laser is the enhancement of the saturation intensity. Demaria<sup>3</sup> has discussed this effect based upon the results given in Ref. 25 and 26. For an idealized two-level system,

$$I_s = \frac{h\nu}{\sigma} \left[ \frac{\tau_2 \tau_F}{\tau_2 + \tau_F} + \frac{\tau_1 \tau_F}{\tau_1 + \tau_F} \right]^{-1}, \quad (2)$$

where  $I_s$  = saturation intensity,  $h\nu$  = photon energy,  $\sigma$  = stimulated-emission cross section,  $\tau_2$  = collisional lifetime of upper laser level,  $\tau_1$  = collisional lifetime of lower laser level, and  $\tau_F$  = flowing-gas transit time across the discharge region. Demaria<sup>3</sup> gives decay rates (at 300°K) for 00<sup>0</sup>1 to 00<sup>0</sup>0 of  $\approx 385 \text{ Torr}^{-1} \text{ sec}^{-1}$  and for 10<sup>0</sup>0 to 01<sup>1</sup>0 of  $\approx 3850 \text{ Torr}^{-1} \text{ sec}^{-1}$ . Therefore, at 20 Torr,  $\tau_2 \approx 1.3 \times 10^{-4} \text{ sec}$  and  $\tau_1 \approx 1.3 \times 10^{-5} \text{ sec}$ .

For these lifetimes the variation of the normalized saturation intensity  $I_s / \frac{h\nu}{\sigma}$  as a function of the inverse of the flowing-gas transit time is shown in Figure 2. Since the increase in saturation intensity at high flow rates is not accompanied by a decrease in small signal gain, the maximum power obtainable from the laser increases. From Figure 2 it can be seen that for a 1-cm-wide discharge region and a 100-m/sec flow, a factor-of-two increase in saturation intensity is possible.

Various laser-discharge and cavity geometries which have been used in convectively cooled lasers are discussed in the review articles by Foster,<sup>2</sup> Demaria,<sup>3</sup> and Karniushin and Soloukhin.<sup>1</sup> The various geometries discussed by Demaria are shown in Figure 3, where rectangular coordinates are used to specify directions of flow (v), current (I), optical axis (O), and magnetic field (B). Advantages and disadvantages of each configuration are listed below:

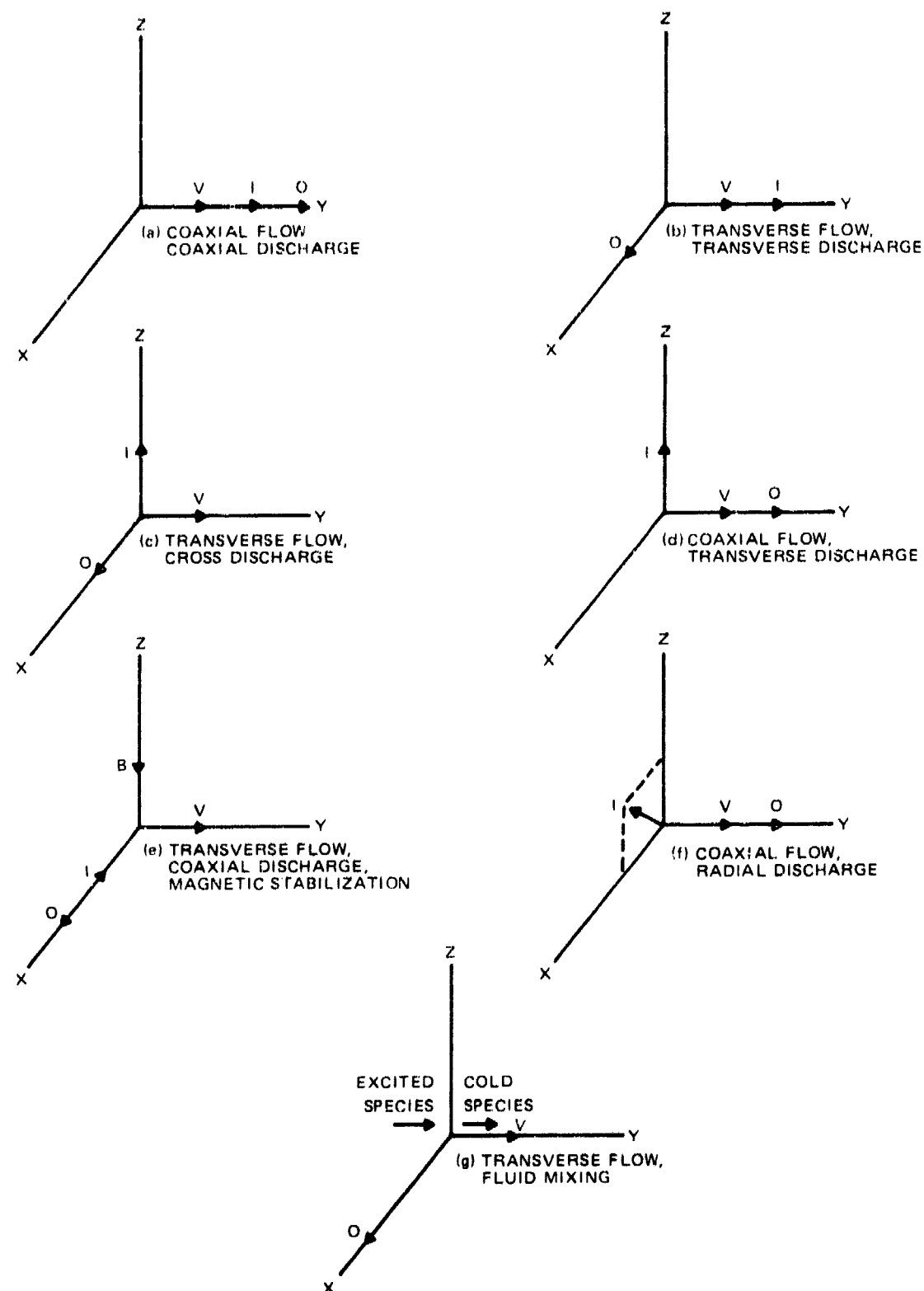


Figure 3. Laser Discharge and Cavity Geometries

Figure 3(a)<sup>27-30</sup>

Advantages (A):

- A1 Cylindrical-discharge configuration matches cylindrical configuration of Gaussian-mode resonators; amenable to single-mode operation.
- A2 Favorable geometry for closed-cycle operation; relatively well-behaved discharge.

Disadvantages (D):

- D1 Longitudinal flow requires high flow speed to minimize transit time. High flow speed results in high pressure drop which increases power required for gas pumping.
- D2 Large electrode spacing requires high voltage to maintain required E/N.

Figure 3(b)<sup>15,19,31-33</sup>

Advantages:

- A3 Close-spaced electrodes yield high electric fields (necessary at high pressure) at moderate voltages.
- A4 Transverse flow results in efficient convective cooling at moderate flow speeds.
- A5 Well suited for scaling to high power levels by increasing the discharge volume.
- A6 Well suited for auxiliary ionization.

Disadvantages:

- D3 Rectangular laser cross section is poor geometrical match with conventional Gaussian cavities; more suitable as power amplifier than oscillator.

Figure 3(c) 8, 12-14, 16-18, 34-36

Advantages:

A3, A4, A5, and A6 given above.

Disadvantages:

D3 given above.

D4 Bowing of discharge downstream of flow; for cw operation, maximum-gain region is downstream of discharge axis.

D5 Large discharge widths are possible only with auxiliary ionization. Large discharge widths result when discharge volumes are increased for high-power operation.

Figure 3(d)

Advantages:

A3, A5, and A6 given above.

Disadvantages:

D1, D3, and D5 given above.

Figure 3(e) 37-38

Advantages:

A1 and A4 given above.

A7 Downstream bowing of discharge by gas flow is prevented by magnetic field.

Disadvantages:

D1 given above.

Figure 3(f)

Advantages:

A3 and A6 given above.

Disadvantages:

D1 given above.

Figure 3(g) <sup>39-41</sup>

Advantages:

A4 and A5 given above.

A8 No direct excitation of lower laser levels.

A9 Optimal discharge conditions for excited species.

A10 Molecular gas for quenching lower laser level is not dissociated by collisions with discharge electrons.

Disadvantages:

D3 given above.

D6 Closed-cycle operation impossible.

D7 Complex construction.

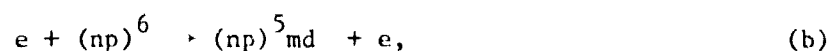
In addition to the advantages and disadvantages of particular geometries, closed-cycle operation introduces the advantages of economy and compactness since the gas is reused and, therefore, a relatively small supply of gas is required. Disadvantages of closed-cycle operation are (1) changes in composition of the laser medium due to molecular dissociation or chemical reaction of active species and (2) discharge instabilities (arcing) and/or upper-laser-level quenching due to contaminants initially present or generated by the discharge.

Aside from the multimode limitation, the geometries of Figure 3(b) and (c) are the most suitable for fast-flow, high-pressure operation. The 3(b) geometry is best suited for a multi-pass power amplifier; the 3(c) geometry is best suited for a power oscillator with either cw or pulsed operation.



Short-width discharges have been investigated by Targ<sup>23</sup> and Ben-Yosef, et al.<sup>36</sup> Large-width discharges with auxiliary ionization (double discharge,<sup>42-45</sup> photoionization,<sup>46-48</sup> and electron beams<sup>49</sup>) have been studied by many investigators. Promising results have been obtained with relatively wide electrodes (with no auxiliary ionization) fabricated from a resistive-composition material.<sup>50,51</sup> This material provides a series ballast which opposes arc formation.

The general characteristics of pure-rare-gas lasers have been discussed by Bennett.<sup>52</sup> The ground states in Ne, Ar, Kr, and Xe are closed-shell  $(np)^6$  configurations with  $n = 2, 3, 4$ , and  $5$ , respectively. Atomic excitation occurs mainly through the reactions



where  $m = n+1, n+2$ , etc. States in the  $(np)^5_{mp}$  configuration satisfy the requirements for lower laser levels, i.e., short lifetimes and small population rates.

At pressures sufficiently large ( $\approx 0.01$  Torr) for complete resonance trapping of transitions from  $s$  and  $d$  states to the ground state, resonance trapping has the effect of making levels in the  $(np)^5_{ms}$  configuration metastable. It is then possible for a metastable bottleneck<sup>53</sup> situation to develop, where resonance trapping of the  $mp \rightarrow ms$  transitions or the reaction



tends to reduce the population inversion.

The strongest  $s \rightarrow p$  and  $d \rightarrow p$  transitions occur in the  $1$  to  $10\text{-}\mu$  region. In the heavier rare gases, oscillation on the  $d \rightarrow p$  transitions is favored since (1)  $d$  levels become more depressed with respect to  $s$  levels in going

from Ne to Xe and require increasingly less excitation energy, (2) cross sections for reaction (b) are generally about an order of magnitude greater than those for reaction (a), and (3)  $d \rightarrow p$  transition probabilities are generally larger than those for  $s \rightarrow p$  and, therefore, should have more gain for the same population inversion.

Generally three types of electrical discharges have been used for the excitation of neutral gas lasers:<sup>54</sup> weakly ionized dc and rf discharges, pulsed afterglow discharges, and short rise-time pulsed discharges.

The positive column of a glow discharge ( $\approx 100 \text{ mA/cm}^2$  current density) is the most common cw laser medium for neutral species. The electron temperature  $T_e$  in the positive column is a function of the product of pressure and tube diameter ( $pd$ ), increasing as  $pd$  decreases. The functional dependence of  $T_e$  on  $pd$  is a result of the balancing of charged-particle production by ambipolar diffusion losses. Labuda and Gordon<sup>55</sup> have measured  $T_e$  as a function of  $pd$  for He-Ne discharges. For  $p = 1 \text{ Torr}$  and  $pd = 5 \text{ Torr mm}$ ,  $T_e \approx 70,000^\circ\text{K}$  from their results. An ambipolar diffusion time  $\tau_a \approx 2 \times 10^{-5} \text{ sec}$  can be calculated for these conditions using

$$\tau_a = \frac{1}{D_a} \left( \frac{r}{2.4} \right)^2,$$

where  $D_a$  = ambipolar diffusion constant and  $r$  = discharge radius. As the pressure increases,  $\tau_a$  increases and  $T_e$  decreases. If the charged-particle loss is determined by convective flow rather than diffusion, the decrease in  $T_e$  is alleviated. For a flow transit time equal to the above ambipolar diffusion time, a flow speed of  $\approx 250 \text{ m/sec}$  is required.

Maintaining  $T_e$  at a high value is necessary to provide a large number of energetic electrons capable of exciting either upper laser levels or buffer-gas metastables for energy-transfer pumping. Convective flow is beneficial in this respect as it is in the case of a metastable bottleneck where removal of the metastables reduces the population of the lower laser level.

Enhancement of cw rare-gas laser output by convective flow cannot be predicted because the mechanisms which limit laser output have not been determined unambiguously. For the He-Ne laser the data of Bennett<sup>53</sup> point to an output-power limitation due to a buildup of population in the lower laser state ( $2p_4$ ) caused by radiation trapping of the transition from  $2p_4$  to  $1s_2$  (metastable) in Ne. Gordon and White<sup>56</sup> maintain that the output-power limitation is caused by saturation of the upper-state formation rate due to He metastable destruction by second-kind collisions with electrons at high discharge currents. Bennett's work was on the  $1.15\text{-}\mu$  transition, while that of Gordon and White was on the  $6328\text{-}\text{\AA}$  and  $3.39\text{-}\mu$  transitions. From these results, it appears that an enhanced output power can be expected at  $1.15\text{ }\mu$  for a flowing-gas He-Ne laser.

As Gordon and White have shown, the limitation of laser output power with increasing discharge current can be the result of electron saturation of the upper state. This process occurs when the electron quenching rate is comparable to or larger than the spontaneous-emission (or collisional) loss rate. For an excited state of population  $N$ , excitation cross-section  $\sigma$ , spontaneous lifetime  $T$ , and de-excitation cross section  $\sigma^*$ , the rate equation is

$$\frac{dN}{dt} = \langle v\sigma \rangle n_e N_0 - N\left(\frac{1}{T} + \langle v\sigma^* \rangle n_e\right),$$

where  $v$  = electron velocity,  $\langle \rangle$  indicates an average over the electron velocity distribution,  $n_e$  = electron density, and  $N_0$  = density of the ground state. In the steady state,  $dN/dt = 0$  and

$$N = \frac{\langle v\sigma \rangle n_e N_0}{\frac{1}{T} + \langle v\sigma^* \rangle n_e}.$$

For small  $n_e$ ,  $(\frac{1}{T} \gg \langle v\sigma^* \rangle n_e)$  and  $N$  increases linearly with  $n_e$ ; but for large  $n_e$ ,  $(\frac{1}{T} \ll \langle v\sigma^* \rangle n_e)$  and  $N = \text{const.} = N_0 \langle v\sigma \rangle / \langle v\sigma^* \rangle$ . The electron quenching process can consist of excitation to higher states, de-excitation to lower states, and ionization. High-pressure operation increases  $N_{\text{sat}} = N_0 \frac{\langle v\sigma \rangle}{\langle v\sigma^* \rangle}$  through an increase in  $N_0$ ; however,  $\langle v\sigma \rangle$  decreases and  $\langle v\sigma^* \rangle$  increases with pressure.

TABLE 2  
PULSED HIGH-PRESSURE RARE-GAS LASERS<sup>6</sup>

Laser Species	$\lambda_{vac}$ ( $\mu$ )	Identification	Total Pressure [He + X (Torr)]	X (% total)	Output Power
He	2.0584	$2p_1^0 - 2s_1^0 S_0$ (tentative)	65		Weak
Ne	1.1525	$2s_2 - 2p_4$			Weak
	1.1994	$2s_3 - 2p_2$ (tentative)			Weak
	1.2468	$2s_4 - 2p_5$ (tentative)	30	Ne (30%)	Weak
	1.5237	$2s_2 - 2p_1$			Weak
	3.3923	$3s_2 - 3p_4$			Strong
Ar	1.2705	$3s_1 - 2p_2$	100		Weak
	1.7919	$3d_6 - 2p_7$ or $3d_5 - 2p_6$	760		Strong (0.4 kW)
	2.2083	$3d_5 - 2p_3$			Strong
	2.3973	$3d_6 - 2p_2$	100	Ar (30%)	Strong
	5.8038*				Medium
	7.2932*				Medium
Kr	2.5231	$3d_5 - 2p_6$			Strong
	3.0653	$3p_{10} - 2s_5$	760	Kr (7%)	Strong
?	1.3585*	?	150		Weak

\* Previously unreported.

The limitation of laser output by electron quenching is most serious when the upper-laser-level lifetime is long. It is interesting that this situation can result in high gain but low power output, as in the case of the 3.51- $\mu$  Xe line.<sup>57,58</sup> The electron quenching for a 1.15- $\mu$  He-Ne laser is much less severe than for Xe since the upper-level lifetime of 96 ns<sup>59</sup> is much shorter than the corresponding lifetime in Xe (1360 ns).

In contrast to the uncertainty of enhancement of cw rare-gas laser output by convective flow, the beneficial effect of flow for pulsed rare-gas lasers has been demonstrated for He-Xe<sup>8</sup> and should be realizable for a number of other rare-gas laser transitions. The main benefit to be realized from flow in a pulsed laser is the removal of heat and residual ionization products (which degrade discharge uniformity) from the discharge volume during the interpulse time. The output pulse energy may be optimized at low PRF and then fast flow used to increase the PRF and, in turn, the average output power.

Pulsed transverse excitation appears to be the most effective means of producing laser action in gases at high pressure. High-pressure operation results in high-peak-power output and large pressure-broadened linewidths. Many high-gain laser lines have been observed in low-pressure rare gases under pulsed excitation conditions.<sup>60-61</sup> High-pressure laser action has been reported<sup>6</sup> for atomic gases under conditions of pulsed transverse excitation (multiple-pin TEA configuration, 179 cm long with 1.9-cm gap). Excitation was obtained by discharging a 0.02- $\mu$ F capacitor (25 kV) through a triggered spark gap at a repetition rate of 3 pps. Laser-output pulse lengths were 0.2 to 5  $\mu$ sec. Data for the rare-gas laser lines reported in Ref. 6 are reproduced in Table 2.

Ahmed and Schmidt<sup>7</sup> have investigated high-pressure laser action in rare-gas mixtures using transverse (multiple pin and double discharge), longitudinal, and distributed longitudinal excitation. Interestingly enough, they found that maximum power was obtained with the distributed longitudinal excitation, whereas maximum optimum pressure occurred for transverse excitation. They used a 60-cm-long, 1.2-cm-diam. discharge tube. A capacitor charged to

26 kV produced 1- $\mu$ sec pulses with peak currents of 100 A (PRF up to 3 kHz). Laser pulses were 1 to 2  $\mu$ sec long. For transverse excitation, the optimum pressures were 64 Torr for Ne (3.39  $\mu$ ), 27 Torr (20:1) for He-Ne (6328  $\text{\AA}$ ), and 170 Torr (15:1) for He-Xe.

Superradiant laser action has been reported by Ryan<sup>62</sup> for the 1.79- $\mu$  line in He-Ar (16% Ar) at 300-Torr total pressure using a multiple-pin TEA configuration with a gap of 2.5 cm. Two 0.05- $\mu$ F capacitors in series (charged to 16 kV) were discharged through a spark gap to give 1  $\mu$ sec pulses with peak currents of 900 A. Laser pulse duration was  $\approx$  0.1  $\mu$ sec. The shortness of the laser pulse was attributed to the rapid buildup of the lower-laser-level population.

Pulsed laser action (longitudinal excitation) in He-Ne and He-Ar mixtures at pressures of  $\approx$  200 torr was reported in Ref. 63.

A number of publications<sup>64-73</sup> have appeared on laser action in the afterglow of a pulsed He-Ne discharge. Power enhancement of the 1.15- $\mu$  line occurs in the afterglow since the electron-thermalization time is much shorter than the 6- $\mu$ sec decay time<sup>52</sup> of He ( $2^3S$ ) metastables, thereby enhancing the population inversion. Due to the much shorter decay time ( $\approx$  0.6  $\mu$ sec)<sup>52</sup> of the He ( $2^1S$ ) metastables, oscillation at 6328  $\text{\AA}$  is not enhanced in the afterglow.

Laser emission or superradiance resulting from transitions terminating on metastable levels has been observed for all of the rare gases. These self-terminating lasers must be excited by a current pulse with a rise time shorter than the radiative lifetime of the laser transition. The Ne  $2p_1 \rightarrow 1s_4$  transition at 5401  $\text{\AA}$  has the highest limiting efficiency (9%)<sup>74</sup> among the neutral rare-gas lasers. Many publications concerning this transition have appeared in the literature.<sup>75-82</sup> A peak power of 190 kW (1.5-ns pulse) was achieved by Shipman<sup>77</sup> using Blumlein excitation (75 KV, 500 kA, 4 ns) with a lasing volume 0.3-cm high and 10-cm wide and a pressure of 30 Torr. Leonard<sup>79</sup> obtained 85 kW (10 ns pulse) of peak power at 46 kV and a pressure of 30 Torr in a multiple-transmission-line-fed discharge channel 0.3-cm high,

10-cm wide, and 100-cm long. Since laser pulse energy depends exponentially upon laser length (in Ref. 22 energy increased from  $2 \times 10^{-4}$   $\mu$ J to 0.5  $\mu$ J as the length was varied from 15 to 75 cm), it is desirable to have laser lengths of about 100 cm.

The first closed-cycle system utilizing an atomic gas was the He-Xe laser developed by Targ, *et al.*<sup>8</sup> The cw Xe laser is an inherently low-power device<sup>57-58</sup> due to the onset of thermal equilibrium at relatively low pressure and current.<sup>58</sup> The pulsed Xe laser, however, is capable of generating kW peak powers at high Xe partial pressure (5 to 50 Torr).<sup>5</sup> Targ obtained high average power (11 W) by operating a high-pressure pulsed He-Xe laser with transverse gas flow, which allowed a high PRF (kHz). The fast flow removed waste heat and residual ions from the discharge region during the interpulse time, thereby preserving discharge uniformity (no arcing).

It should be noted that two important benefits attributable to fast flow in CO<sub>2</sub> lasers are absent in the Xe laser and, for that matter, in any rare-gas laser. The cooling effect is of little consequence as far as thermal population of lower states is concerned, since these states lie at high energies. Also, the lifetimes of the laser levels are so short that prohibitively high flow rates would be required to achieve enhanced saturation intensity as shown in Figure 2 (calculated radiative lifetimes for the 3.508- $\mu$  transition of Xe are  $\tau_2 = 1365$  ns and  $\tau_1 = 45$  ns).

The requirement for a low contamination rate of the laser medium is more stringent for rare-gas than for CO<sub>2</sub> lasers since rare-gas laser media are adversely affected by slight amounts of impurities such as N<sub>2</sub>, O<sub>2</sub>, and H<sub>2</sub>O. Excited and ionized rare-gas species are rapidly destroyed by interactions with gas contaminants. For example, the reaction rate constant for He-ion charge transfer to N<sub>2</sub>,  $12.5 \times 10^{-10}$  cm<sup>3</sup> sec<sup>-1</sup>, is large compared to that for He-ion charge transfer to Xe,  $0.1 \times 10^{-10}$  cm<sup>3</sup> sec<sup>-1</sup>.<sup>83</sup> The competition of N<sub>2</sub> in de-exciting the He metastable states directly appears to be less important since the He(2<sup>3</sup>S<sub>1</sub>) transfer to Xe is very rapid.

Xe-buffer gas mixtures were chosen as the most promising rare-gas laser media for initial studies in view of:

1. demonstrated lasing at high pressure and high repetition rate.
2. possibility of simultaneous oscillation on a number of Xe lines in several atmospheric transmission windows (see Figure 4).
3. good detector (InSb) response in the atmospheric transmission windows.

## 2.2 System Design and Construction

### 2.2.1 Vacuum and Recirculating-Flow System

Figure 5 is an isometric drawing of the CCRGEDL system. The gas-recirculation loop is constructed of 15-cm-o.d. ultrahigh-vacuum components (tees, nipples, elbows, bellows) joined together by Conflat flanges. The volume of the loop is ~ 100 liters. Research-grade gases are admitted to the system from a gas manifold equipped with ultrapure-gas regulators and metal-sealing ultrahigh-vacuum valves. The gas fill pressure is measured by a bakeable capacitance manometer having a measurement range of 0.1-1000 Torr.

The system is initially evacuated through a 15-cm metal-sealing ultrahigh-vacuum valve by a 500-liters/sec vertical-axis turbomolecular pump. After system bakeout, the base pressure is of the order of  $5 \times 10^{-8}$  Torr. When the pump is valved off, the pressure increases at a rate of  $4 \times 10^{-7}$  Torr/min, which results in a ppm impurity level in 100 Torr of working gas after 4 hr. This outgassing rate is much greater than that which occurs when the system is filled with working gas at pressures of hundreds of Torr. The turbo pump is protected against power failure, overheating, and excessive pressure rise by an interlock control system which monitors foreline pressure, cooling-water temperature, and flow rate. The turbo pump is automatically shut down and the foreline valve closed if monitored parameter values range beyond preset limits. In the event of a momentary power failure, the turbo pump is not restarted automatically because the rotational speed of the pump must be less than 8000 rpm for restarting. A control panel indicates the status of all automatically controlled valves and switches as well as foreline pressure on each side of the foreline valve.





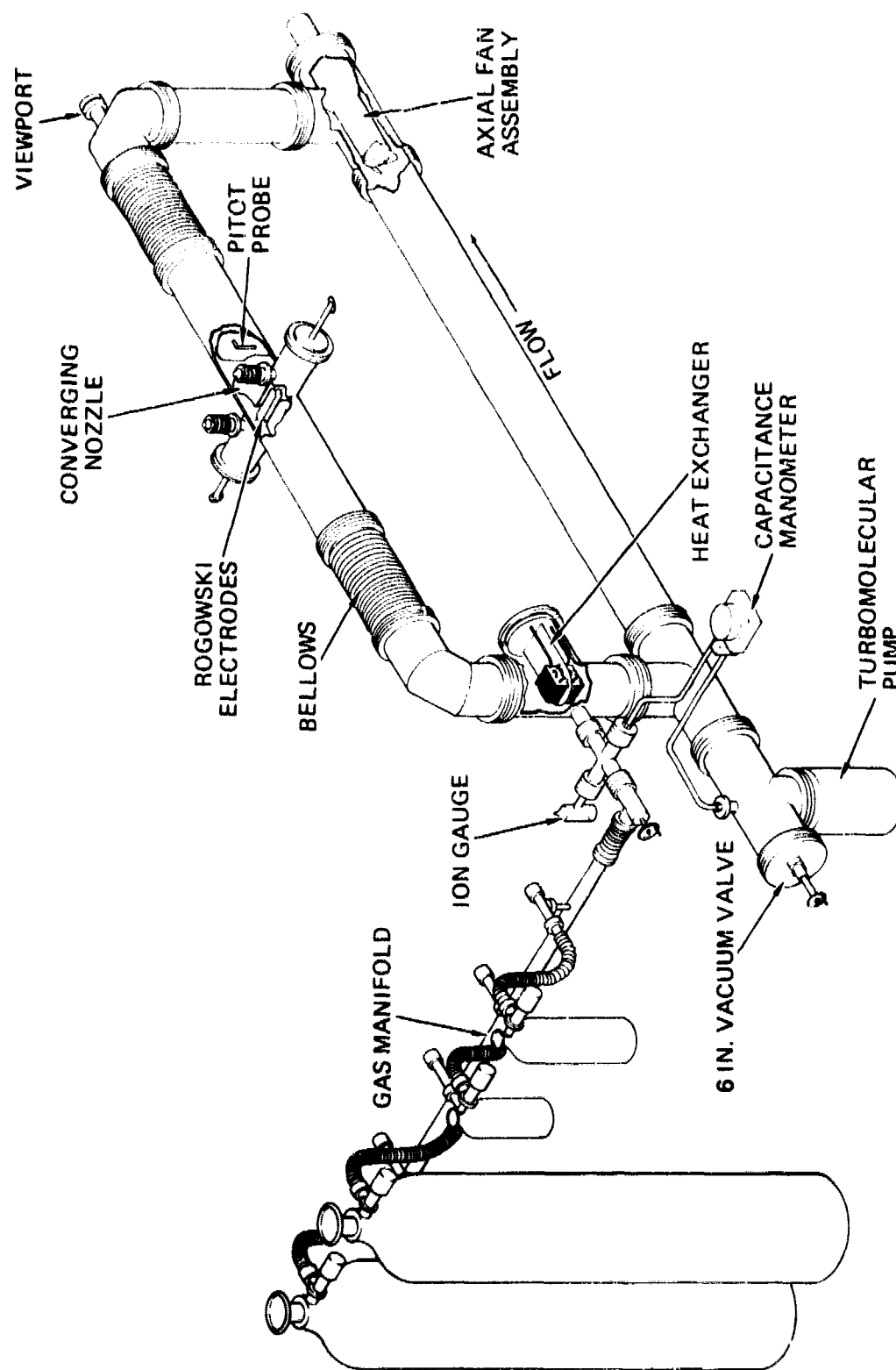


Figure 5. Isometric Drawing of Closed-Cycle Rare-Gas Electrical-Discharge Laser

The proper fan for the recirculating-flow system was chosen by matching fan performance to system requirements. Fan-performance data were obtained from the manufacturer, and the system characteristic was determined by calculating the pressure losses in the individual components of the loop.

The pressure drops were calculated for the following conditions: gas, He; pressure, 300 Torr; temperature, 59°F; and flow rate, 300 cfm. The results of the calculations are given in Table 3, where  $f$  = Darcy friction factor for smooth surfaces,  $L/D$  = length-to-diameter ratio,  $A$  = area,  $(V.P.)$  = velocity pressure =  $\rho v^2/2g$ , and  $k(\alpha)$  = a factor which varies from 0.15 for a cone angle  $\alpha$  of 10° to 1 for an abrupt expansion.

The total pressure drop in the loop (sum of the  $\Delta P$ 's of Table 3) is 0.53 in. of water. This can be converted to an equivalent atmospheric-air (at 59°F) value by multiplying by the density ratio ( $\rho_{air}/\rho_{He}$ ) which yields  $\Delta P = 9.7$  in. of water. The system-resistance curve (for atmospheric air at 59°F) can be obtained, assuming strictly turbulent flow, from  $\Delta P = C_1 Q^2$  where  $C_1 = 9.7/(300)^2 = 1.08 \times 10^{-4}$  and  $Q$  = volume flow rate. The system-resistance curve is plotted in Figure 6 along with the fan characteristic. The intersection of the system characteristic and the fan characteristic determines the operating conditions.

The matching of fan performance to system requirements is an approximate procedure. The calculated pressure loss at the electrodes, which is  $\approx 85\%$  of the total pressure drop around the loop, may be too high by as much as 50%. Also, the fan characteristic is for ideal conditions, whereas in actual use the fan discharges into a 90° bend (with considerable blockage of the flow) and a reduction in performance must be expected.

The externally driven axial-fan assembly is shown schematically in Figure 7 and pictorially in Figure 8. This configuration, with the motor and bearings located external to the gas loop, was used to avoid fan contamination. The stainless-steel fan housing is flange mounted to a 15-cm tee located at a corner of the loop. A ferrofluidic rotary vacuum seal is mounted through a hole in a vacuum bulkhead which is welded to the housing. A Viton O-ring

TABLE 3  
PRESSURE DROP IN LOOP COMPONENTS

Component	v (ft/sec)	$\Delta P$ (V.P.)	Total $\Delta P$ (in. of water)
6-in. Pipe	27	$f L/D$	0.0074
Mitered Elbow	27	1.15	0.0214
3-Section Elbow	27	0.45	0.0084
1 x 6 in. Section	120	$f L/D$	0.0156
Converging Nozzle	27 → 120	0.04	0.0072
Diffuser and Abrupt Expansion	120 → 50 → 27	$k(\alpha) (1 - A_1/A_2)^2$ $+ (1 - A_2/A_3)^2$	0.0160
Contraction	120 → 300	0.04	0.0452
Electrodes } Expansion	300 → 120	$(1 - A_1/A_2)^2$	0.4070

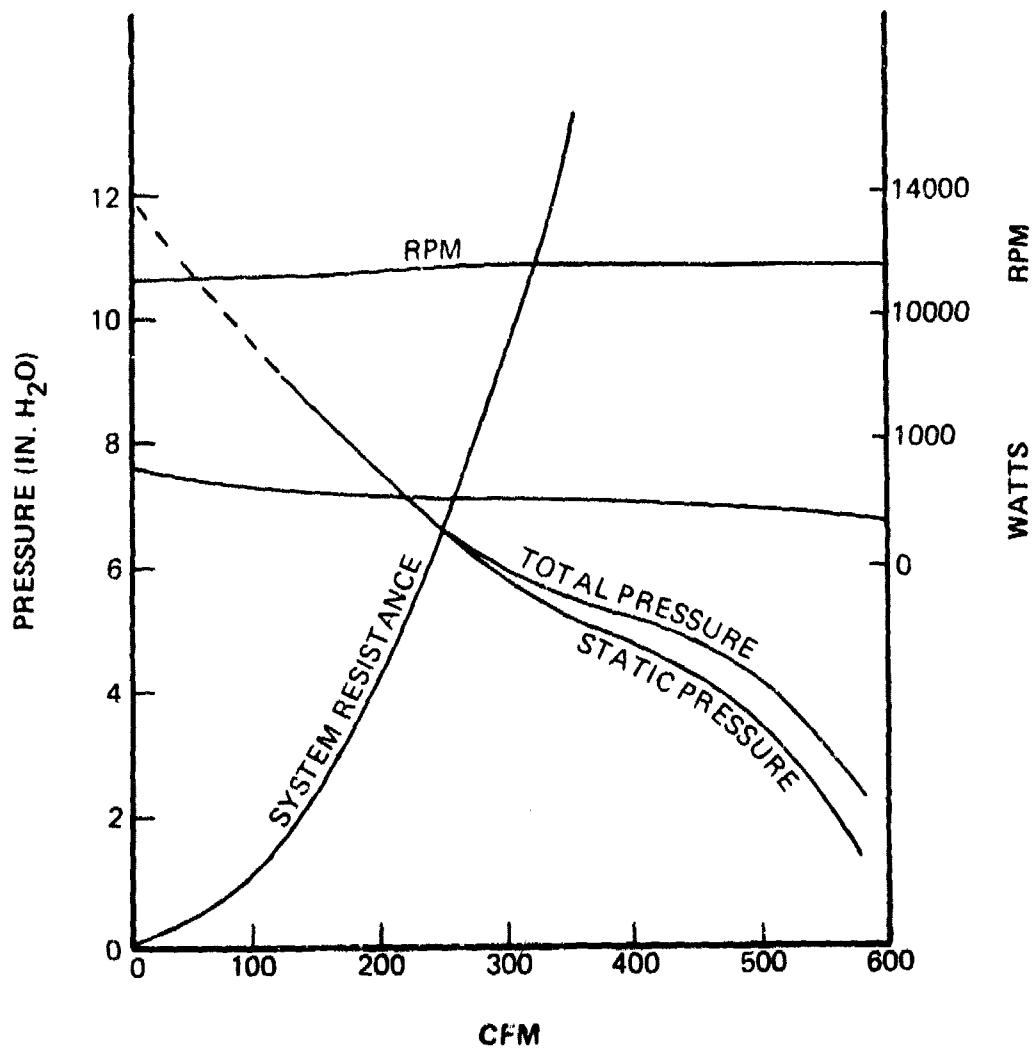


Figure 6. Fan and System Flow Characteristics

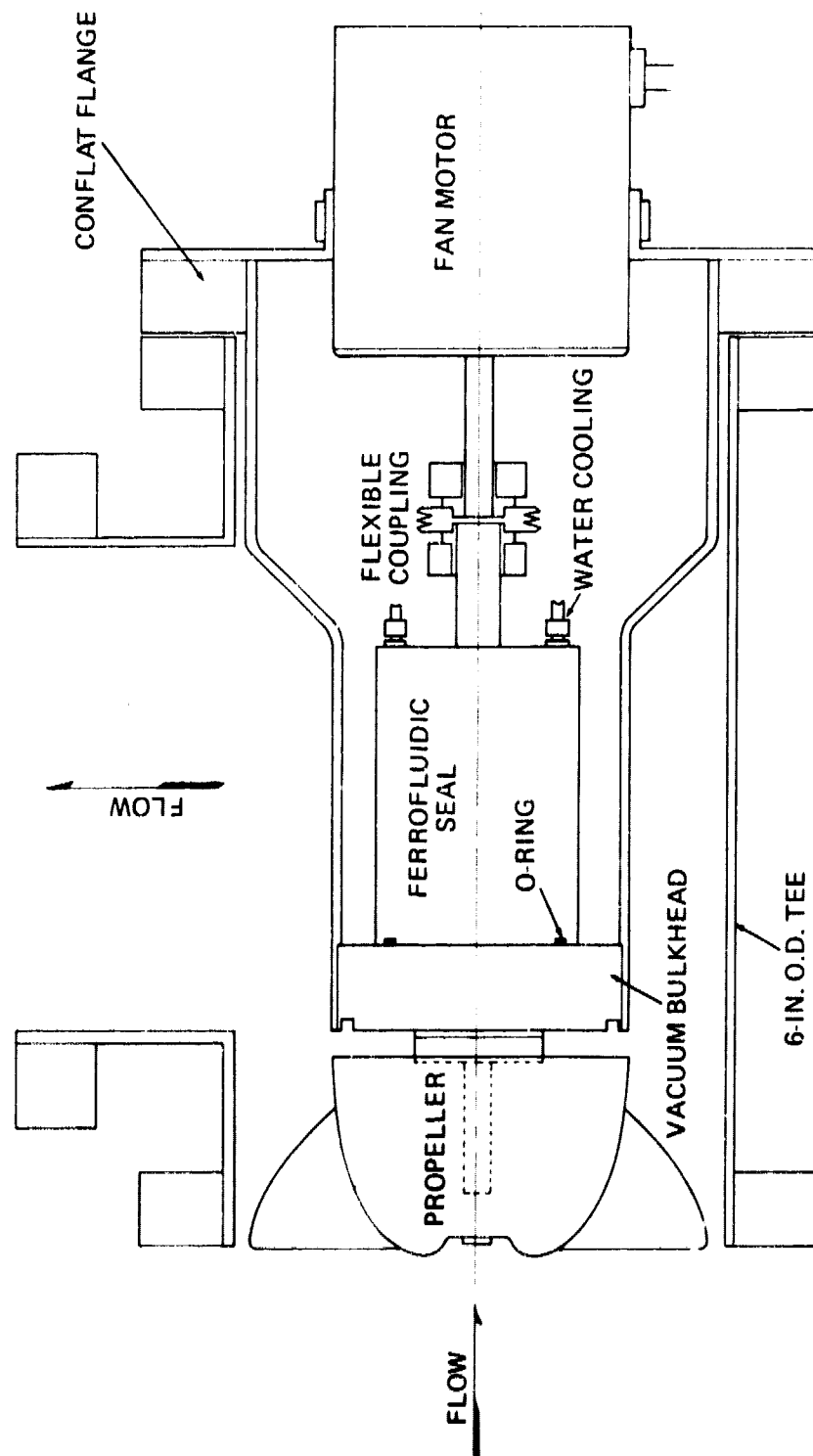


Figure 7. Schematic Diagram of Externally Driven Axial Fan Assembly

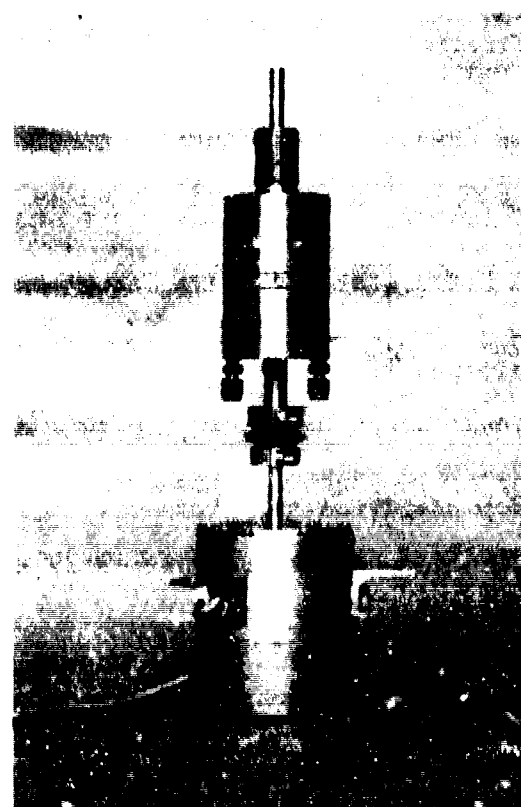
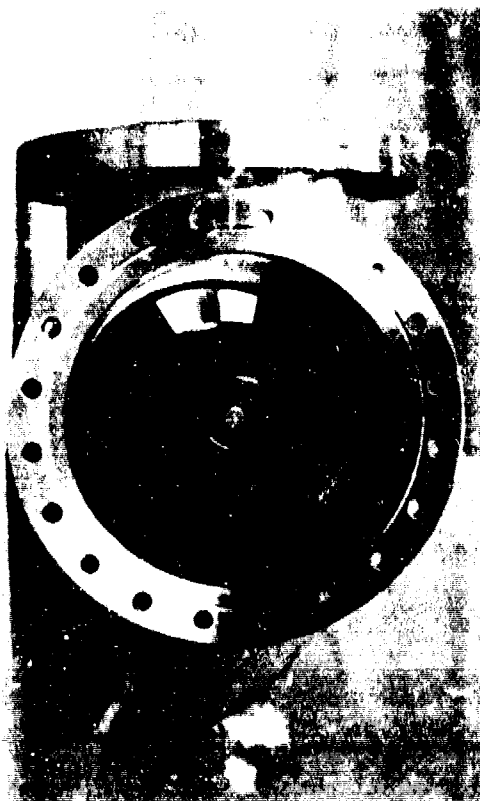


Figure 8. Photographs of Externally  
Driven Axial Fan  
Assembly

is used as a vacuum seal between the bulkhead and the body of the rotary seal, and an aluminum propeller is mounted on the rotary seal shaft extending into the gas loop. The atmospheric side of the shaft is connected to the shaft of a 400-Hz motor via a high-speed flexible coupling. The coupling permits a small amount of angular ( $\sim 2^\circ$ ) and parallel ( $< 0.1$  mm) misalignment of the shafts. The motor is fastened securely to the housing flange.

Since individual components of the fan assembly were specified as being suitable for high-speed operation, the fan was not dynamically balanced after assembly. The vibration level at the fan rotation speed of 11,500 rpm was found to be acceptable. During operation of the fan in vacuum, the system pressure increased about an order of magnitude and then decreased slowly as shown in Figure 9. Similar behavior<sup>84</sup> has been attributed to gas evolution from the regions between individual ferrofluid barriers of the rotary seal. In order to minimize contamination due to this outgassing of the rotary seal, the fan is operated under vacuum conditions until gas evolution is minimized.

Waste heat generated by the high-pressure electrical discharge is transferred from the system by a flange-mounted 1-kW heat exchanger (shown in Figure 10) constructed of OFHC copper sheet brazed to OFHC copper tubing which, in turn, is brazed to a 20-cm-o.d. Conflat flange. The heat exchanger is connected to a refrigeration unit capable of  $-40^\circ\text{C}$ .

A Pitot-static probe located upstream of the discharge region is used to measure on-axis values of velocity pressure ( $\rho v^2/2$ ) in the 15-cm pipe. The differential pressure across the Pitot-static probe is measured by a bakeable capacitance manometer having a measurement range of 0.001-10 Torr. The measured values of velocity pressure in the 15-cm pipe are used to calculate the velocity in the interelectrode region. Figure 11 is a photograph of the flange-mounted Pitot-static probe assembly. A total-temperature probe consisting of a copper-constantan thermocouple within a stainless-steel sheath is mounted on the same flange. The gas temperature is required for determining gas density.



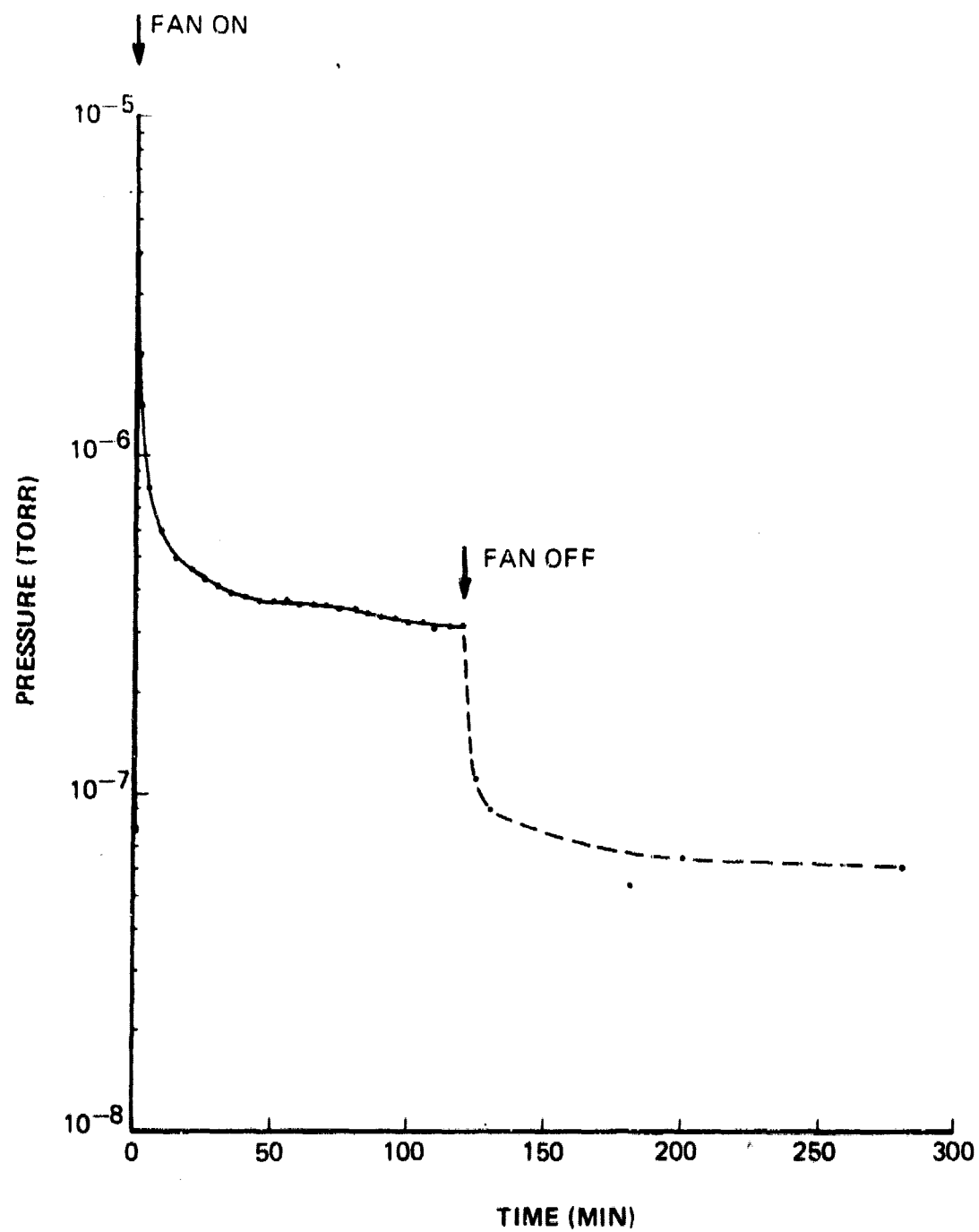


Figure 9. CCRGEDL System Pressure as a Function of Time for Fan Operating under Vacuum Conditions

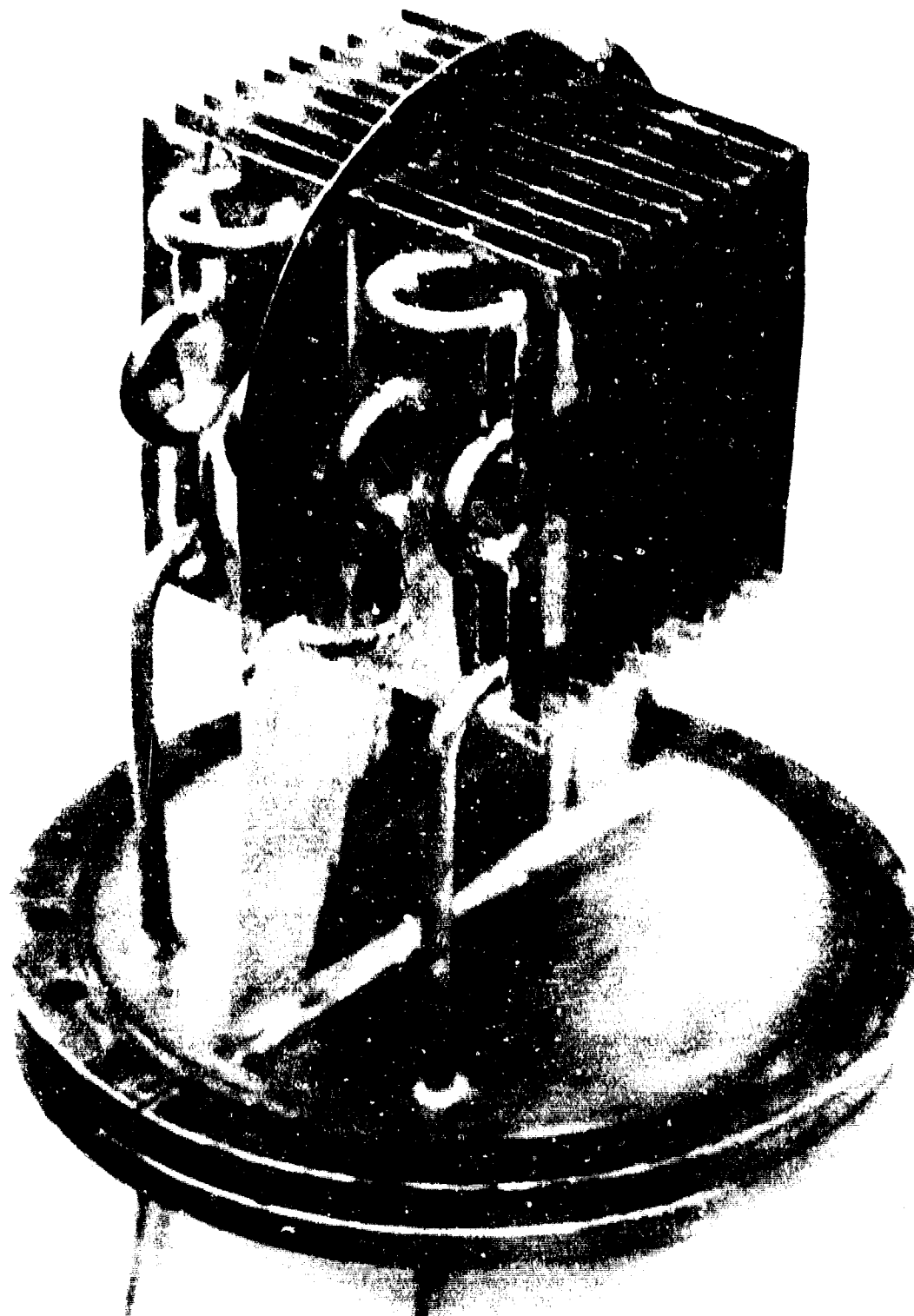


Figure 10. Photograph of 1-kW Heat Exchanger

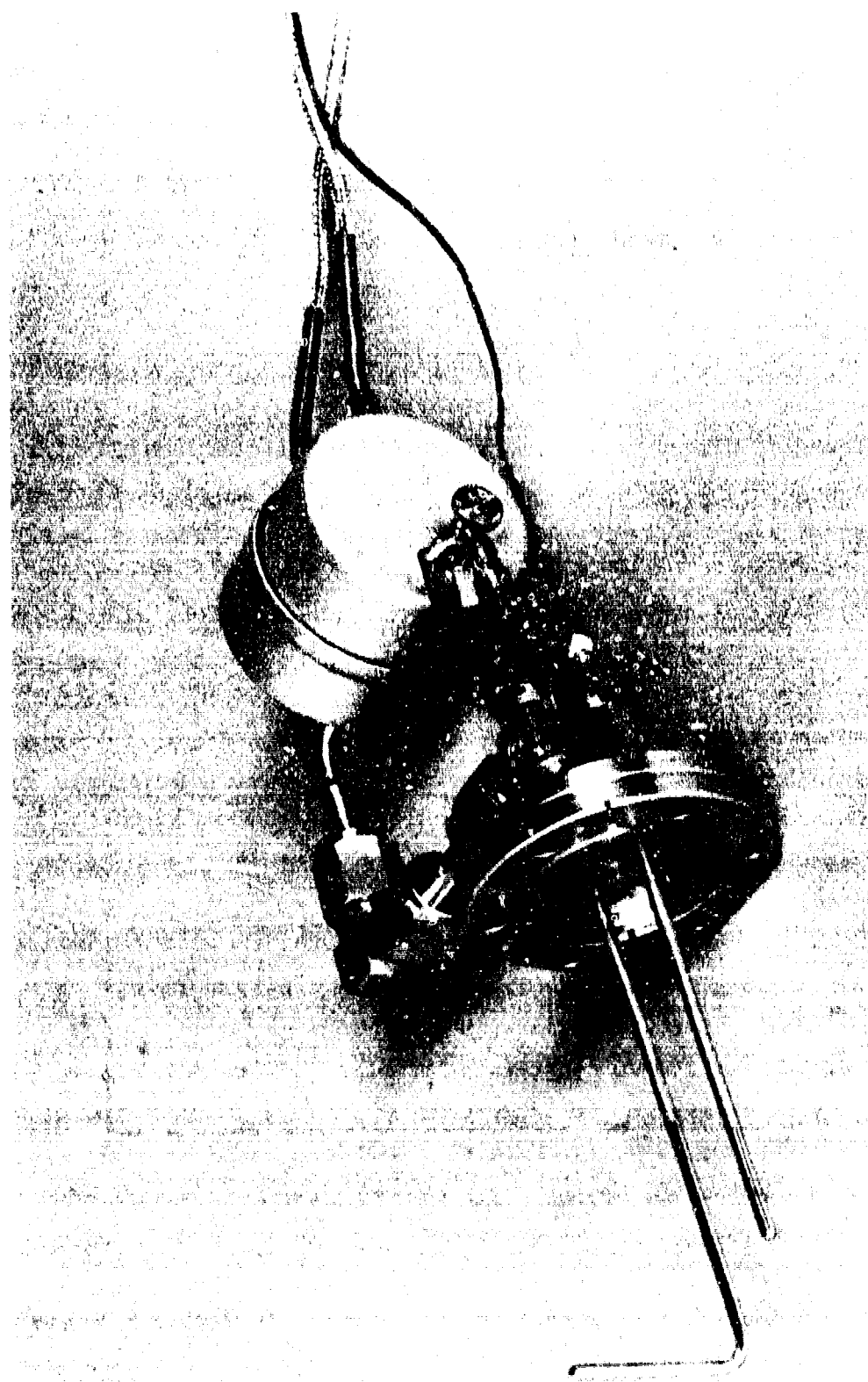


Figure 11. Photograph of Pitot-Static Probe Assembly

Typical results of Pitot-static probe measurements in He are shown in Figure 12. The differential-pressure data are used to calculate the flow speed in the 15-cm pipe from  $\Delta p = \rho v_1^2/2$ . Gas throughput is calculated from  $Q = A_1 v_1$ , and interelectrode flow speed is then calculated from  $v_2 = Q/A_2$ , where  $A_1$  and  $A_2$  are the cross-sectional areas of the 15-cm pipe and the interelectrode region, respectively.

### 2.2.2 Laser Discharge and Optical Cavity

The laser discharge region is located within the section of the gas loop between the bellows used for vibration isolation (see Figure 5). A side view of this section is shown schematically in Figure 13. The converging and diverging flow transitions, formed from stainless-steel sheet, channel the flow into and out of a region of  $2.5 \times 15$ -cm cross section defined by flat glass plates. Aluminum Rogowski-profile electrodes (4 cm wide  $\times$  14 cm long) are mounted to the plates, and the electrode spacing is set to 1 cm by means of glass spacers at the outer ends of the plates. Tungsten preionization wires (0.25 mm) positioned at the electrode midplane are strung--between posts mounted to the plates--along the length of the electrodes on the upstream and downstream sides. The plates, electrodes, and preionization wires are assembled before insertion into the gas-loop section. Electrical connections are then made to the high-voltage feedthroughs; all high-voltage leads within the gas loop are adequately insulated.

Optical coupling to the discharge is accomplished by means of  $\text{CaF}_2$  Brewster-angle windows. The windows are epoxied to 2.5-cm-o.d. stainless steel tubes--cut at the complement of Brewster's angle ( $35^\circ 21'$ )--which are welded into 11.4-cm-o.d. rotatable Conflat flanges. The Brewster windows were aligned using a low-power He-Ne laser, a polarizer, and several apertures. The  $\text{CaF}_2$  window material, having ~ 95% external transmittance from 0.4 to 6  $\mu$ , is excellent for the visible-to-middle infrared spectral region.<sup>85</sup>

The vacuum and recirculating flow system shown in Figure 5 is supported by a structure built from steel Unistrut. The section of the gas-circulation

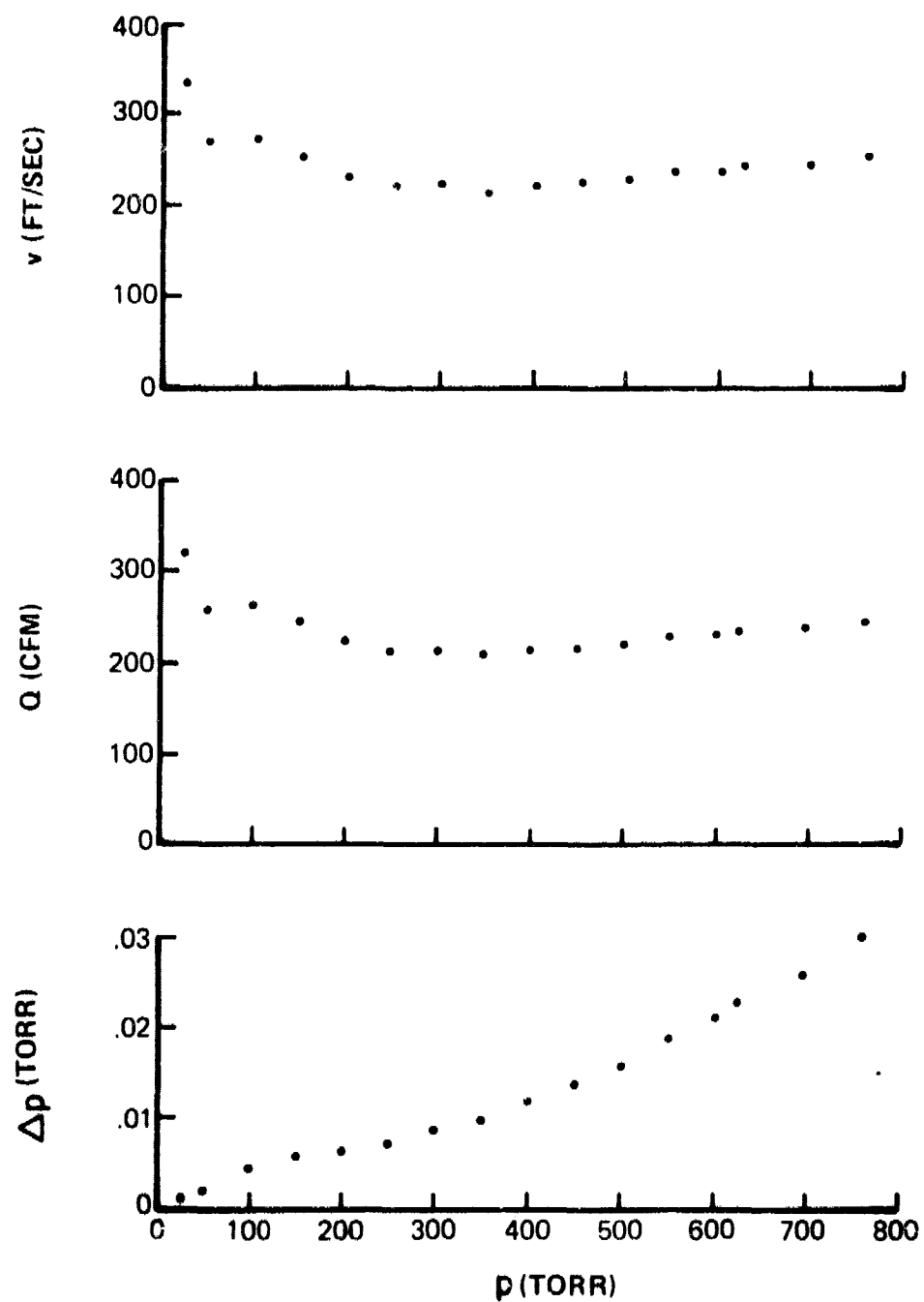


Figure 12. Pitot-Static Probe Data for 12-cm-Gain-Length Configuration

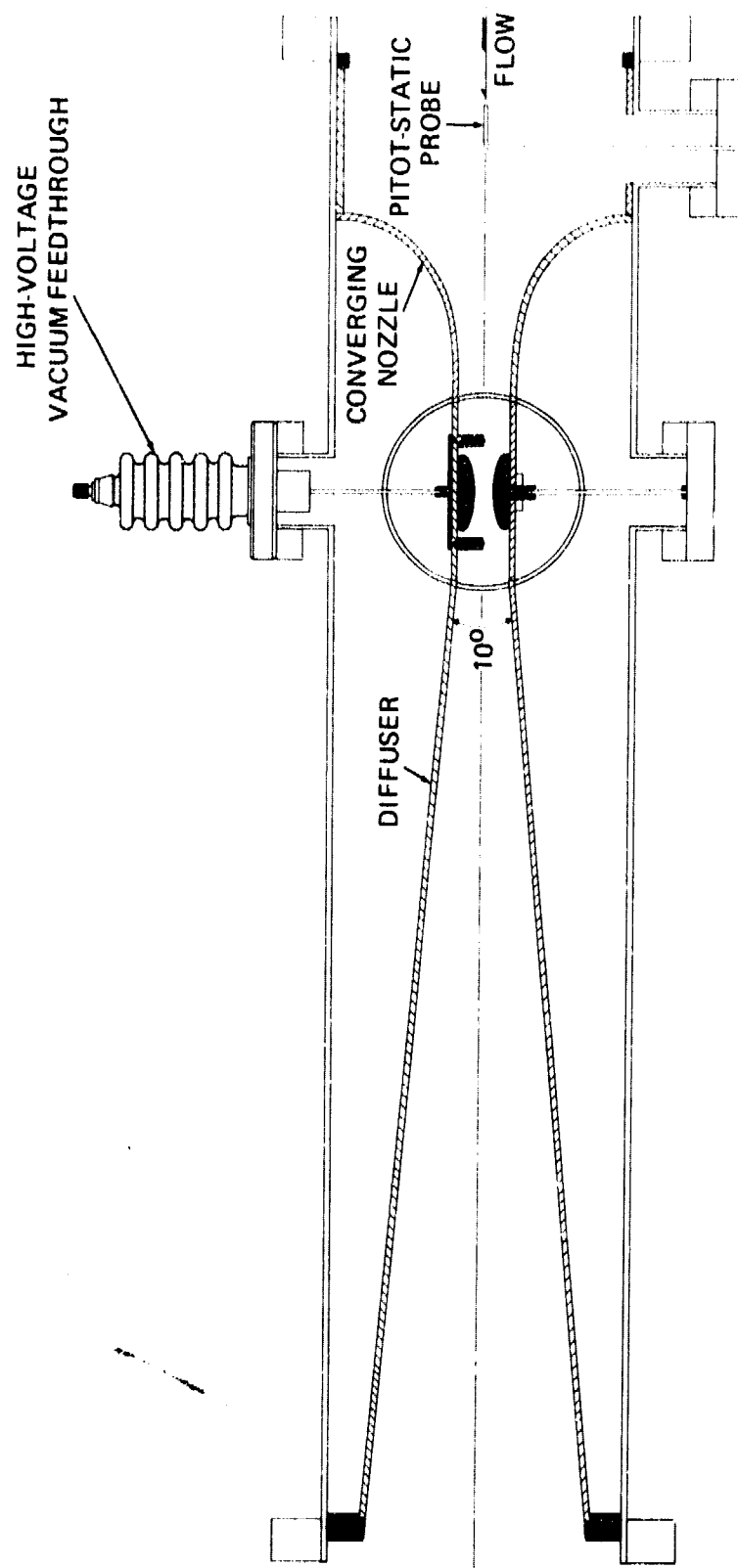


Figure 13. Schematic Diagram of Laser Discharge and Flow Transition Section of Gas Recirculation Loop

loop between the bellows is mounted to a separate Unistrut table; this table is also used to support a 2-m optical rail running parallel to and beneath the discharge electrodes. The laser cavity mirrors and associated optical components are mounted on carriers which ride on the optical rail.

The 12-cm-gain-length cavity was also operated with internal mirrors in place of the Brewster windows. Figure 14 is a photograph of the internal-mirror mounting configuration. Each mirror was affixed to a 2 3/4-in. Conflat flange which was bellows-mounted to the system. A micrometer-driven pivoting mechanism permitted rotation of the mirror about two axes through the center of the bellows. The optical cavity was formed by two mirrors ~ 53 cm apart --a 2-m total reflector mounted on the vacuum side of a blank flange and an O-ring-mounted partially transmitting flat.

Following the evaluation of the 12-cm-gain-length CCRGEDL, the gain length was increased to 25 cm. This was accomplished by replacing the section of gas recirculation loop shown in Figure 13 with a 12-in.-diam. vacuum envelope containing appropriate stainless-steel flow transitions and a Pyrex electrode-mounting structure. An end-view (along the flow axis) of this configuration is shown schematically in Figure 15 and pictorially in Figure 16.

Connections to the 28-cm-long Al Rogowski-profile electrodes were made through low-profile (low-inductance) high-voltage high-vacuum feedthroughs. Two parallel-plate capacitors (~ 25 pF each) were used to couple energy to the upstream and downstream preionization wires (0.010-in.-diam. Mo). The internal-mirror mounting configuration employed 1-in.-diam. mirrors affixed to 2 3/4-in. Conflat flanges which were bellows mounted to 8-in.-diam. flanges. The micrometer-driven pivoting mechanism (mounted to the 8-in.-diam. flange) shown in Figure 14 was used for mirror alignment. A 2-nF energy-storage capacitor and an HY-5 thyatron were coaxially mounted atop a low-inductance feedthrough. The coaxial configuration is favorable for achieving fast-rising pulses.

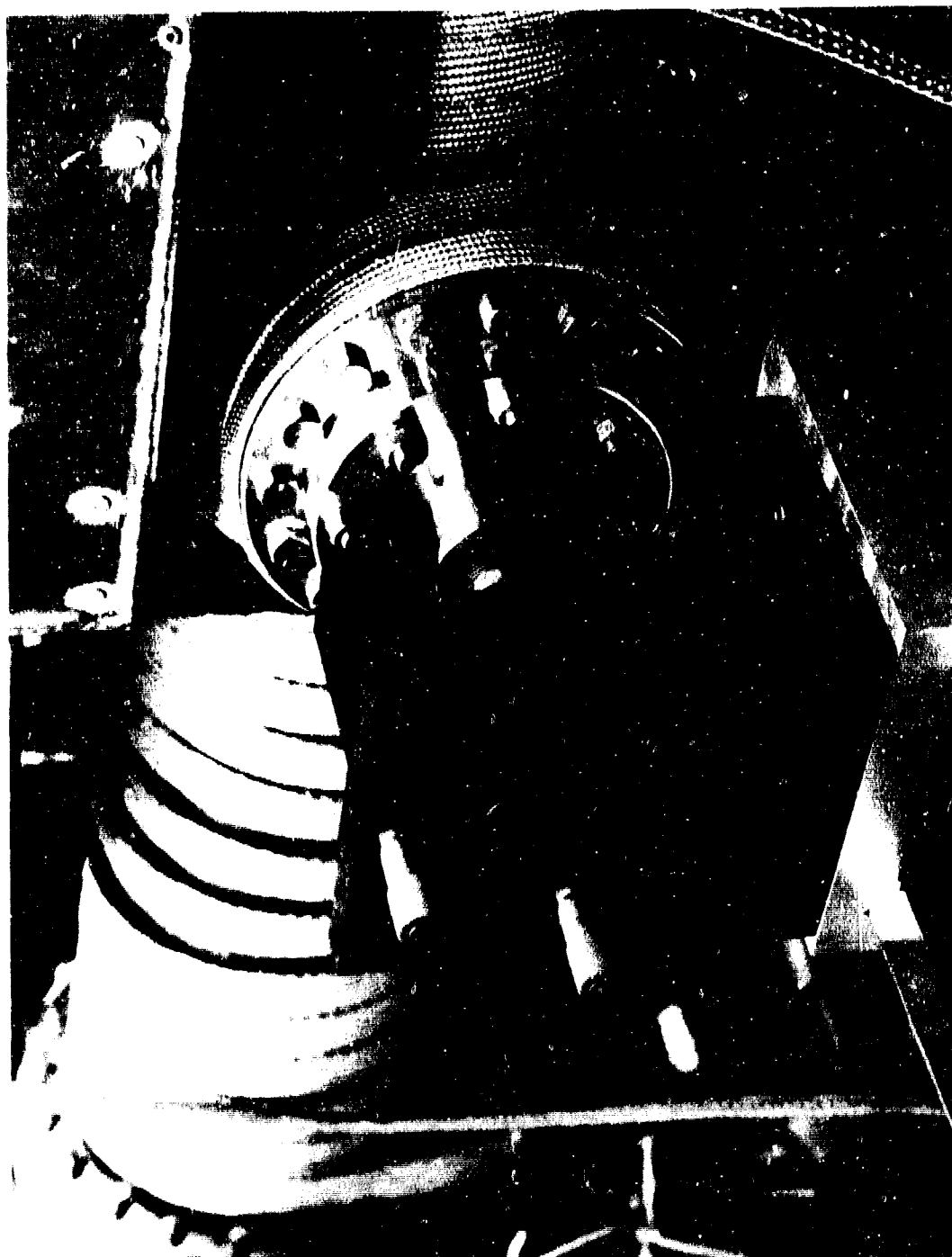


Figure 14. Photograph of Internal-Mirror Mounting Configuration



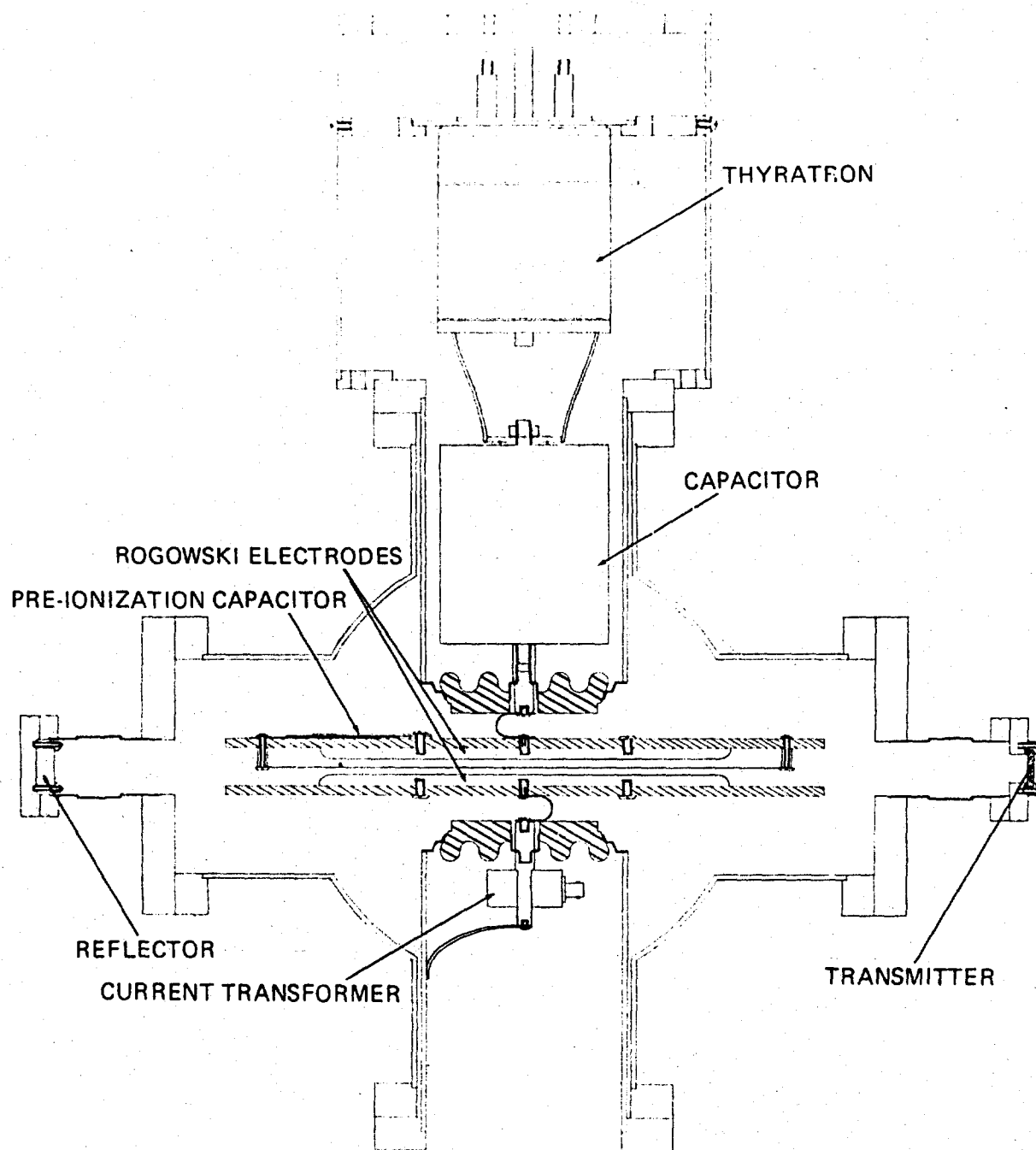


Figure 15.. Schematic Diagram of 25-cm-Gain-Length Laser Configuration



Figure 16. Photograph of 25-cm-Gain-Length Laser Configuration

In order to evaluate fan performance in the gas-flow loop after doubling of the laser gain length, Pitot-static probe measurements were made in the 6-in. pipe, at a location 6 in. upstream of the fan inlet. The results of measurements in He are shown in Figure 17. The error bars indicate the magnitude of fluctuations (probably due to whirl) in the readings. The gas throughput ( $Q$ ) and interelectrode flow speed ( $V$ ) were calculated using average values of the differential-pressure data. Compared with data obtained before doubling of the gain length,  $Q$  had almost doubled and  $V$  had decreased slightly. The decrease in  $Q$  and  $V$  with increasing pressure may be related to the increase in  $\Delta p$  fluctuations with pressure. If these fluctuations are indicative of whirl, the addition of stator vanes in the fan discharge in order to transform the kinetic energy of whirl into pressure head should reduce the tendency of  $Q$  to decrease with increasing pressure.

#### 2.2.3 High-Repetition-Rate Pulser

The high-repetition-rate pulser which drives the laser discharge utilizes a thyatron-switched, low-inductance energy-storage capacitor charged through a tetrode pulse modulator. The tetrode isolates the charging supply from the thyatron during each pulse and permits control of the charging time interval and duty cycle, thereby ensuring uniform energy storage per pulse and sufficient thyatron interpulse recovery time (necessary for achieving high-repetition rate).

A pulser having 1 kW average power capability was used with the 12-cm-gain-length system. Figure 18 is a schematic diagram of the pulser circuit. The charging circuit consists essentially of a 1-kW tetrode with its filament transformers and screen-grid bias supplies and an optoelectronic receiver (Figure 19) which provides the pulse for controlling the tetrode grid. These components are surrounded by a Faraday shield (for minimizing corona) with line voltage being supplied through a 25-kV isolation transformer and the tetrode-grid control pulse being transmitted from oscillator (Figure 20) to optoelectronic receiver through fiber optics.

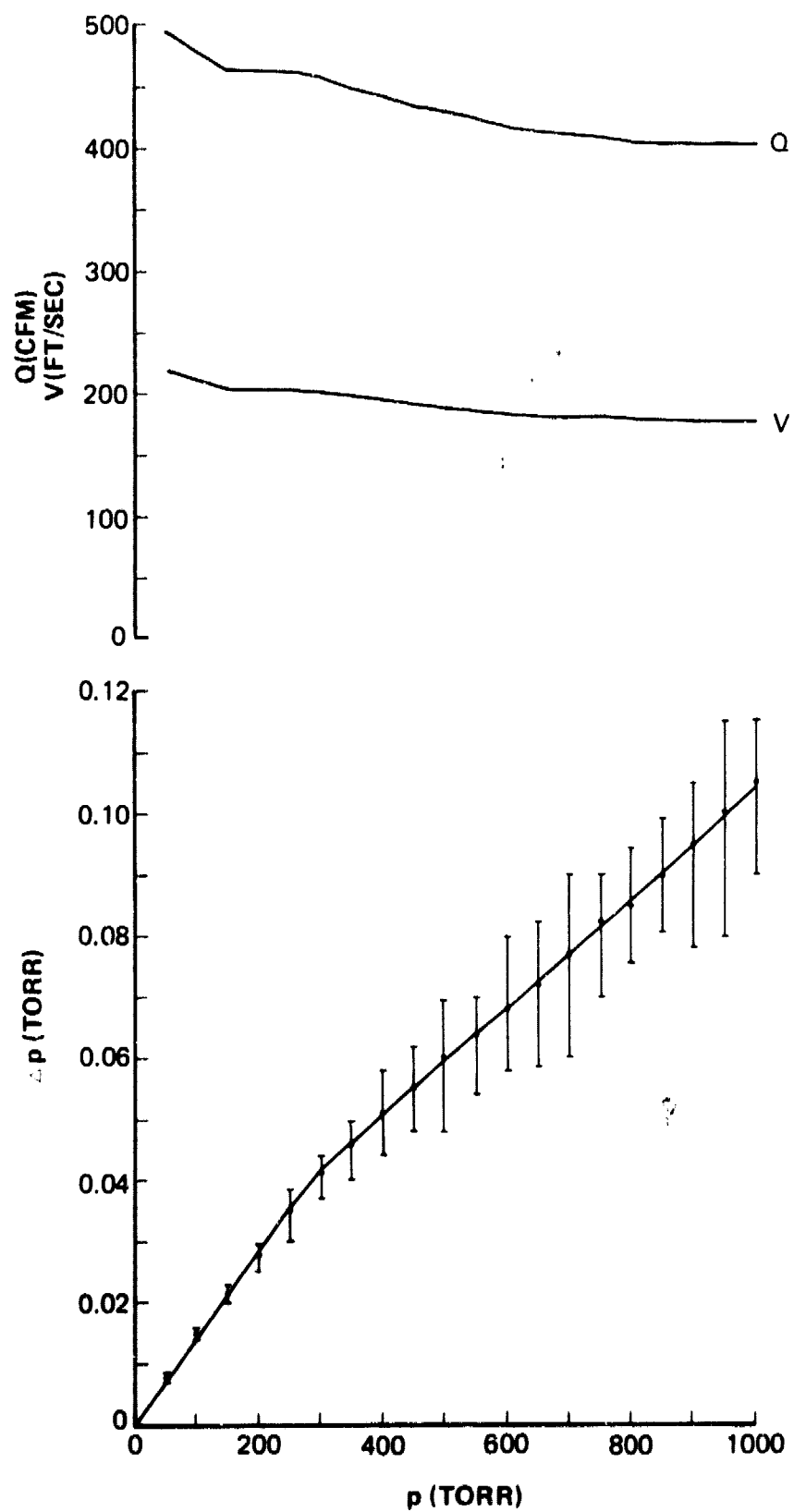


Figure 17. Pitot-Static Probe Data for 25-cm-Gain-Length Configuration

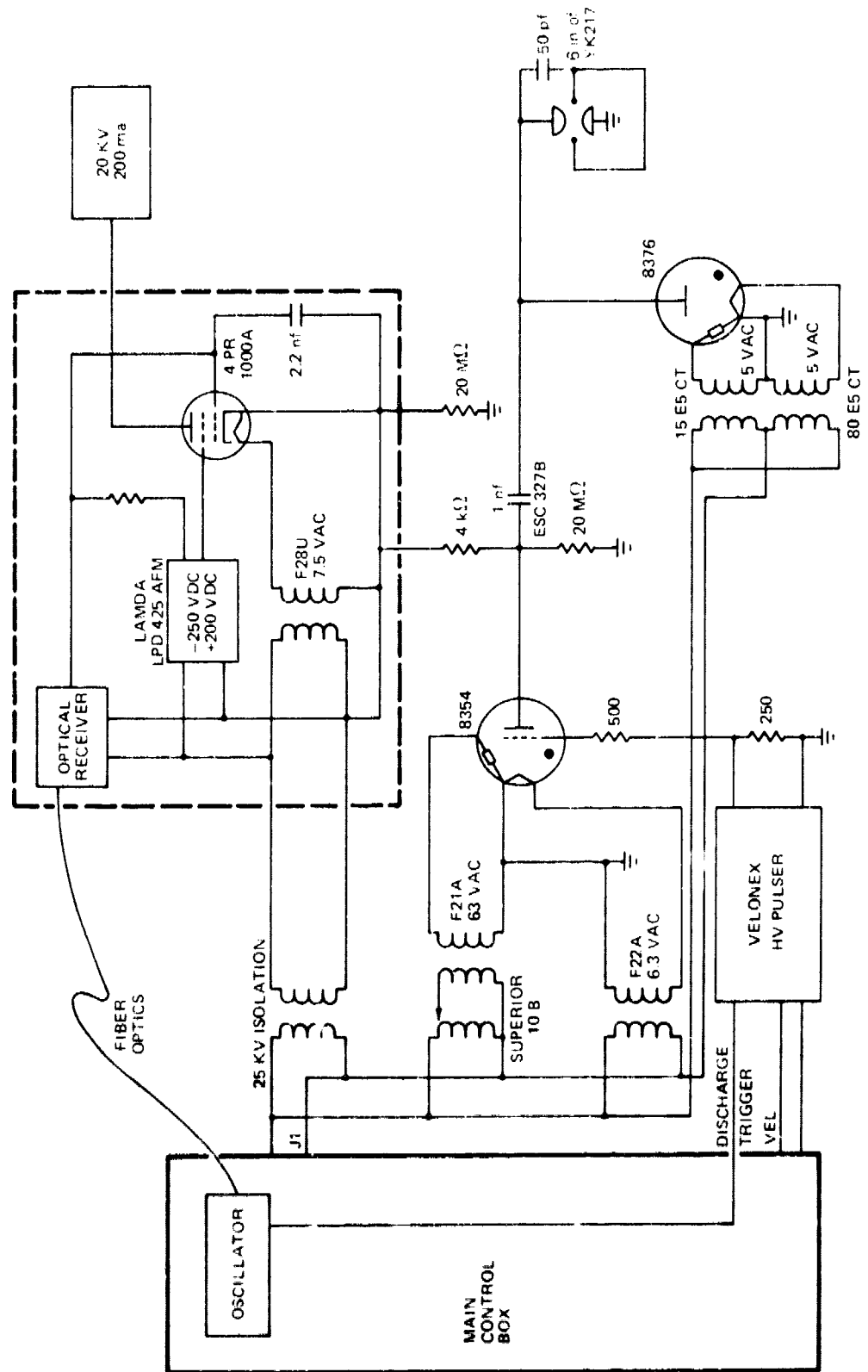


Figure 18. Schematic Diagram of 1-kW High-Repetition-Rate Pulsar



Figure 19. Schematic Diagram of Optoelectronic Receiver for 1-kW Pulsar

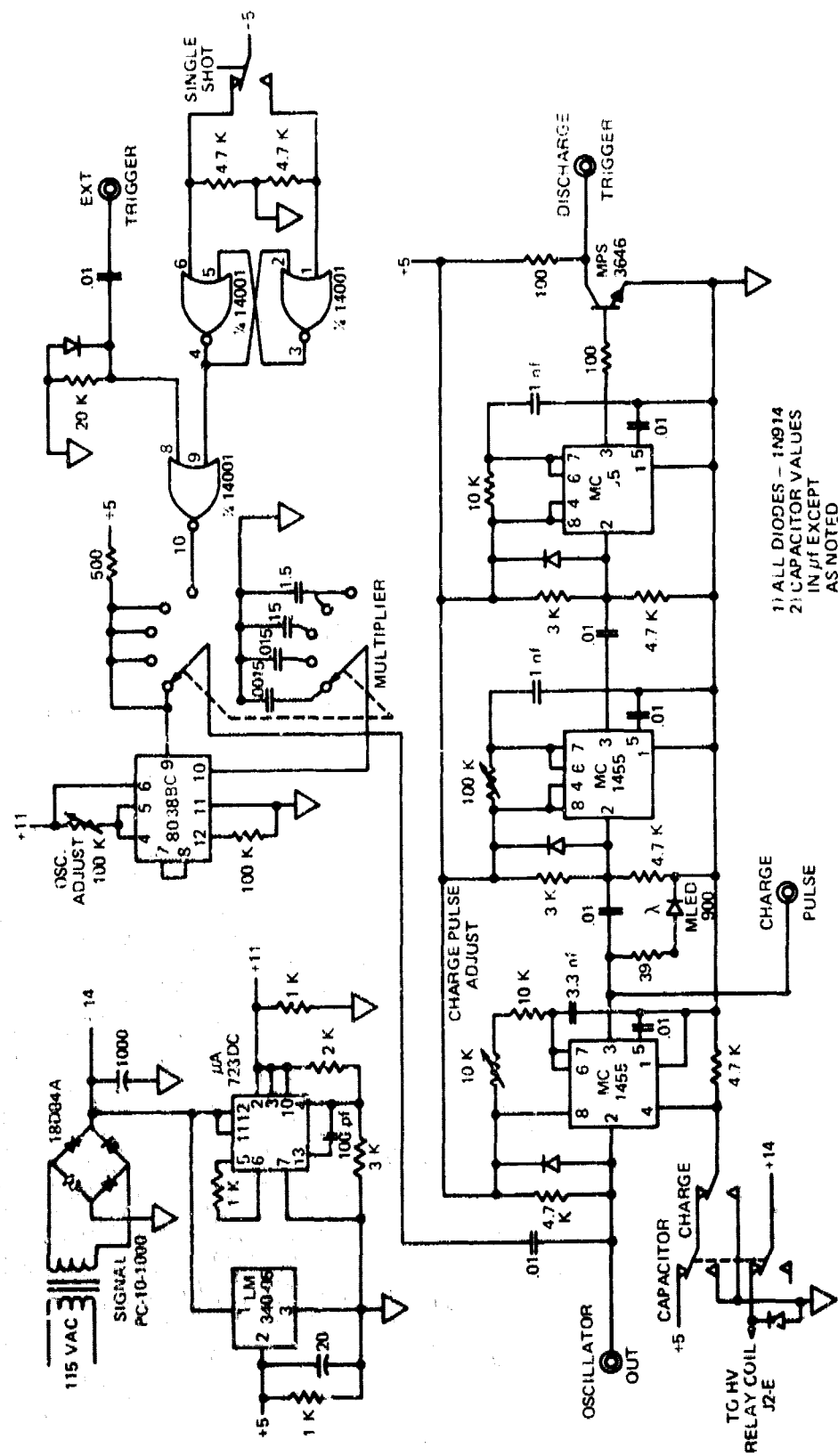


Figure 20. Schematic Diagram of Oscillator and Pulse-Train Network

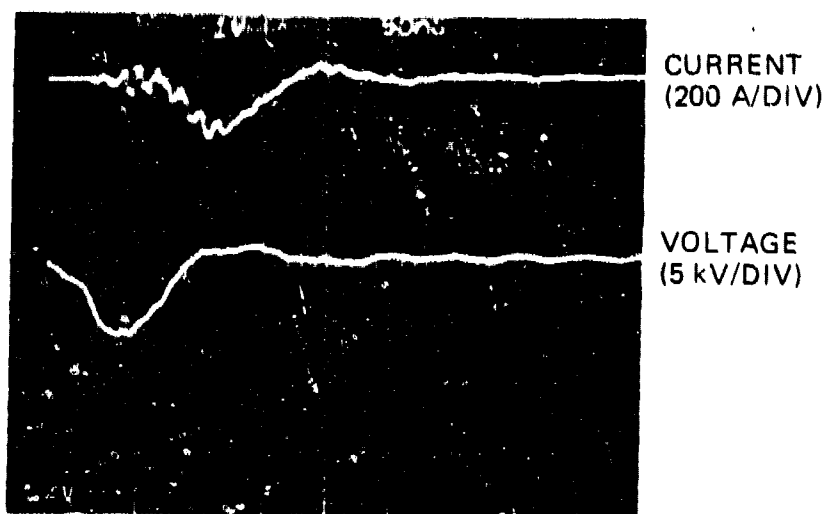
The discharge circuit consists of a 1-nF, low-inductance energy-storage capacitor (suitable for 10-kHz operation) charged through a hydrogen diode (a 1-k $\Omega$  wire-wound resistor was used initially) and switched by a 27.5-kW hydrogen thyatron triggered by a Velonex (Model 350) pulse generator. A short length of YK-217 cable is used to couple energy capacitively to the preionization wires. A wire-wound resistor is placed in series with the Velonex output to protect it from the thyatron-grid spike. A pulse from the oscillator, delayed with respect to the charging pulse, triggers the Velonex. The discharge-circuit components are laid out for minimum circuit inductance.

In order to satisfy space requirements, it was necessary to separate the charge and discharge sections of the pulser. Electrical connection is made via a 3-m length of RG-9 cable, with voltage reversal being prevented by a wire-wound resistor. Even though the charging and discharging circuits are enclosed by grounded aluminum boxes, the RFI generated by the fast-rising high-voltage pulses made it necessary to make small-signal diagnostic measurements in a shielded room.

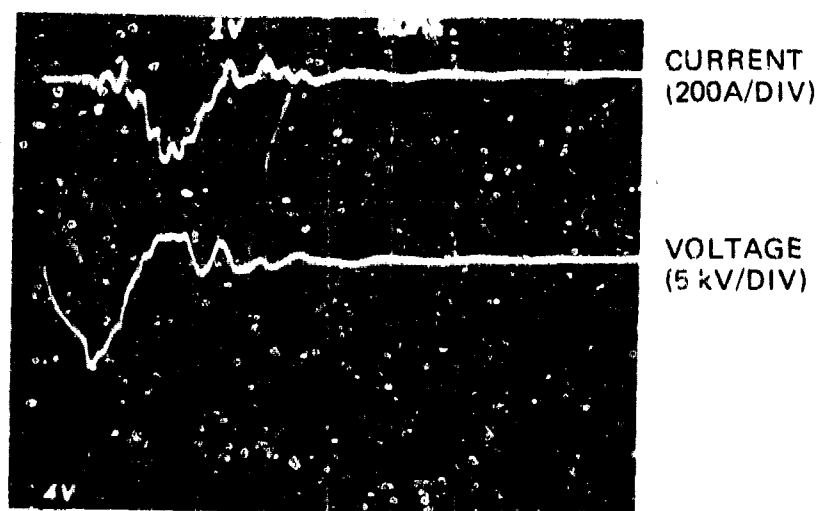
Initially, a capacitive-transfer discharge circuit was used, with a 1-nF secondary capacitor shunting the discharge electrodes. Removal of the secondary capacitor resulted in increased discharge current and voltage and a faster risetime. A comparison of the current and voltage pulses with and without the secondary capacitor is shown in Figure 21 for the following conditions: 400-Torr He-Xe (1400:1), 10-kV charging voltage, and 3-kHz PRF.

A pulser having 15-kW average power capability was used with the 25-cm-gain-length system. The pulser (Figure 22) utilized the same oscillator as the 1-kW pulser but a different optoelectronic receiver (Figure 23) and tetrode-grid control circuit, and higher-power tetrode (15 kW) and thyatron (100 MW peak). A current-feedback network was utilized to control the tetrode-grid bias voltages, permitting linear capacitor charging at current levels from 0.4 to 1.5 A. A General Electric 33.6-kW power supply (24 kV, 1.4 A) was used for the high-voltage supply.





(a) WITH SECONDARY CAPACITOR



(b) WITHOUT SECONDARY CAPACITOR

Figure 21. Oscillograms of Discharge Current and Voltage Pulses With (a) and Without (b) Secondary Capacitor

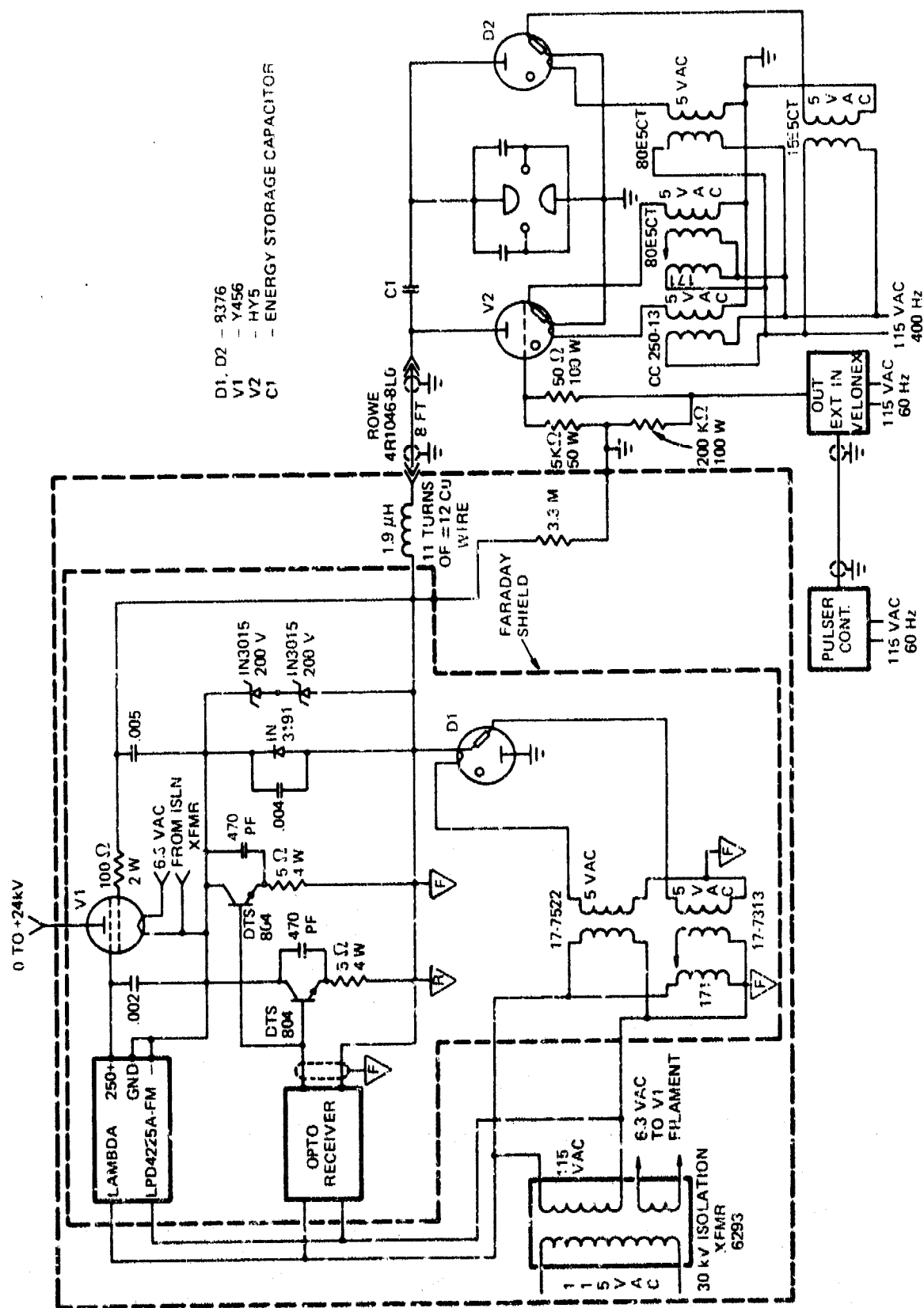
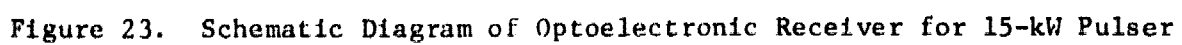


Figure 22. Schematic Diagram of 15-kW High-Repetition-Rate Pulsar



The main components of the charging circuit are located within a Faraday shield held at tetrode-grid potential (inner dashed line of Figure 22). The entire charging circuit is contained within an RF1 shielded rack (outer dashed line of Figure 22). The inverse voltage on the pulser network following the discharge is reduced by clamping diodes  $D_1$  and  $D_2$ .  $D_2$  also serves as a charging diode.

Power distribution to the various electronic components is interlocked, as shown in Figure 24. This circuit permits capacitor charging only after the thyatron has reached operating temperature (900-sec delay) and only when the tetrode cooling fan is operating with exhaust below a preset temperature limit.

### 2.3 Experimental Results

#### 2.3.1 Performance of the 12-cm-Gain-Length Laser with Xe-Buffer-Gas Mixtures

Experiments with the CCRGEDL system were made initially using He-Xe mixtures in the 12-cm-gain-length configuration with external mirrors. Airco Grade-6 (1-ppm impurities) He and Grade-4.5 (50-ppm impurities) Xe were used. Gain measurements for He-Xe mixtures excited by the pulser shown in Figure 18 in the capacitive-transfer configuration were made using the oscillator-amplifier setup shown in Figure 25.

The signal-oscillator laser used was a commercial low-pressure positive-column Xe laser obtained on loan from AFAL/WRW-3. It was necessary to use the 6-mm-diam. beam out of the laser bore to achieve sufficient intensity to yield an adequate signal-to-noise ratio. Strictly single-line cw operation (using the Littrow prism) was impossible since the  $3.51\text{-}\mu$  line could not be entirely suppressed under any conditions.

An oscillogram of the pulsed gain at  $2.03\text{ }\mu$  for a pressure of 400 Torr (100:1 He-Xe), charging voltage of 8 kV, and PRF of 800 Hz is shown in Figure 26. The maximum gain is 3.4%/cm, assuming a discharge length of

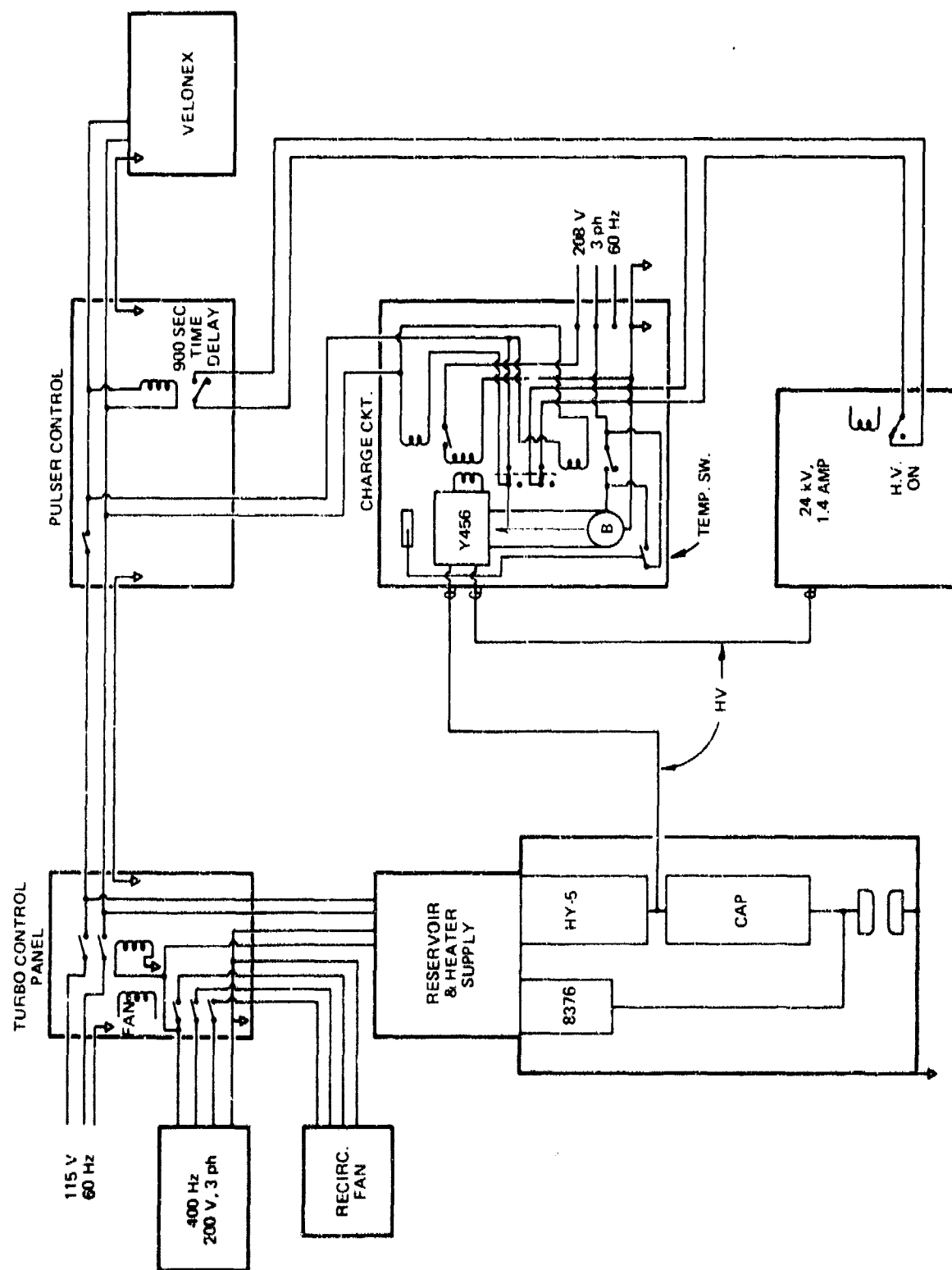


Figure 24. Block Diagram of Power Distribution for CCRGEDL

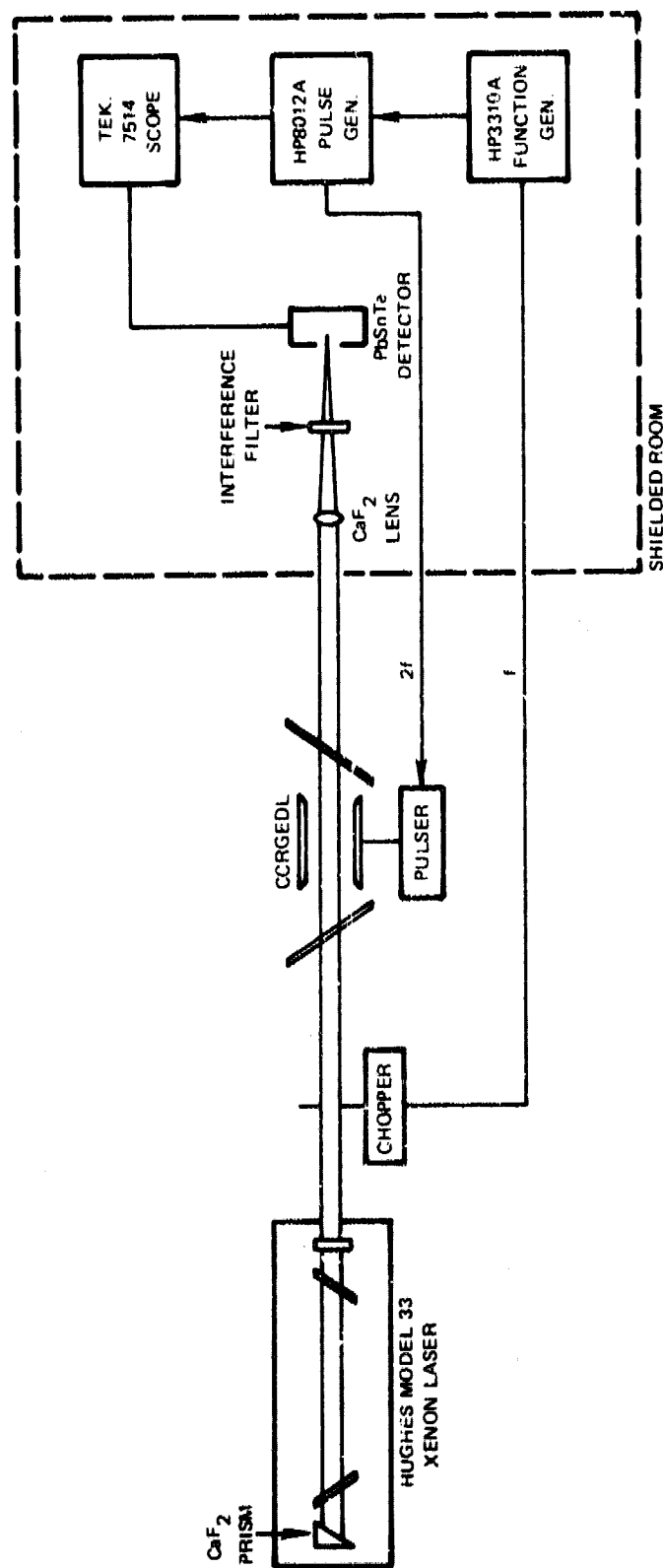


Figure 25. Schematic Diagram of Experimental Setup for Gain Measurements

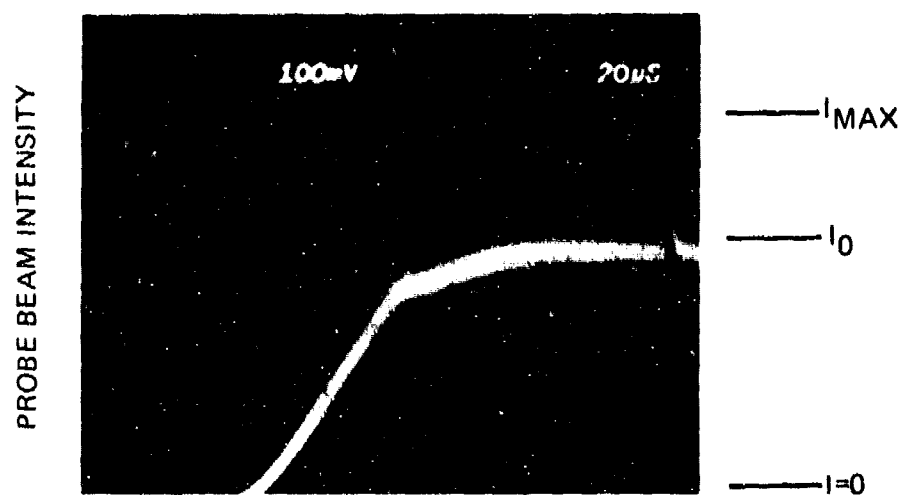


Figure 26. Oscillogram of Pulsed Gain at  $2.03 \mu$  in 12-cm-Gain-Length Laser

12 cm. Typical results of gain/absorption measurements at 4  $\mu$  are shown in Figure 27. The upper oscillogram shows absorption at 300 Torr, 15-kV charging voltage, and 1-kHz PRF; the lower one shows gain at 3 Torr, 12-kV charging voltage, and 1-kHz PRF. Gain was calculated from

$$G = \frac{I_{\max} - I_{\text{spont}}}{I_0}$$

Gain data at 4  $\mu$  are shown in Figure 28 for 50:1, 100:1, and 200:1 He-Xe mixtures in the pressure range 1-400 Torr. These data are of questionable reliability in view of the poor signal-to-noise ratio as evident in Figure 27. No evidence of gain or absorption was found at 4.6  $\mu$ . From Figure 28 it can be seen that the gain at 3 Torr is  $\sim 1.2$  (or 1.5%/cm). The mirror transmission that yields maximum output power can be calculated from<sup>86</sup>

$$T_{\text{opt}} = -L_1 + \sqrt{g_0 L_1}$$

where  $L_1$  = residual loss due to absorption, scattering, and diffraction and  $g_0 = \alpha \ell$ , where  $\alpha$  = unsaturated gain and  $\ell$  = gain length. Assumption of a residual loss of 4% yields a  $T_{\text{opt}}$  of 4.5%.

Measurement of the gain of a pressure-broadened transition in the high-pressure He-Xe discharge by means of a probe beam from a low-pressure Xe laser can yield misleading results as a consequence of the frequency shift of Xe lines resulting from the collisional interaction of He and Xe atoms. Pressure broadening of the 3.5- $\mu$  line by He-Xe collisions is given by<sup>87</sup>

$$\Delta\nu = (3.7 + 19 p) \text{ MHz}$$

where  $p$  = total pressure in Torr. This yields a  $\Delta\nu$  of  $\sim 10$  GHz at a pressure of 700 Torr. The frequency shift of several Xe laser lines at He pressures up to 4 Torr has been measured by Brochard and Vetter.<sup>88</sup> The pressure shift for the 4- $\mu$  line was found to be  $8 \times 10^{-5} \text{ cm}^{-1}/\text{Torr}$ . If this holds at 700 Torr, the resulting frequency shift is  $\sim 2$  GHz. This frequency difference between the pressure-broadened transition and the probe-laser line leads to an off-maximum measurement of gain.



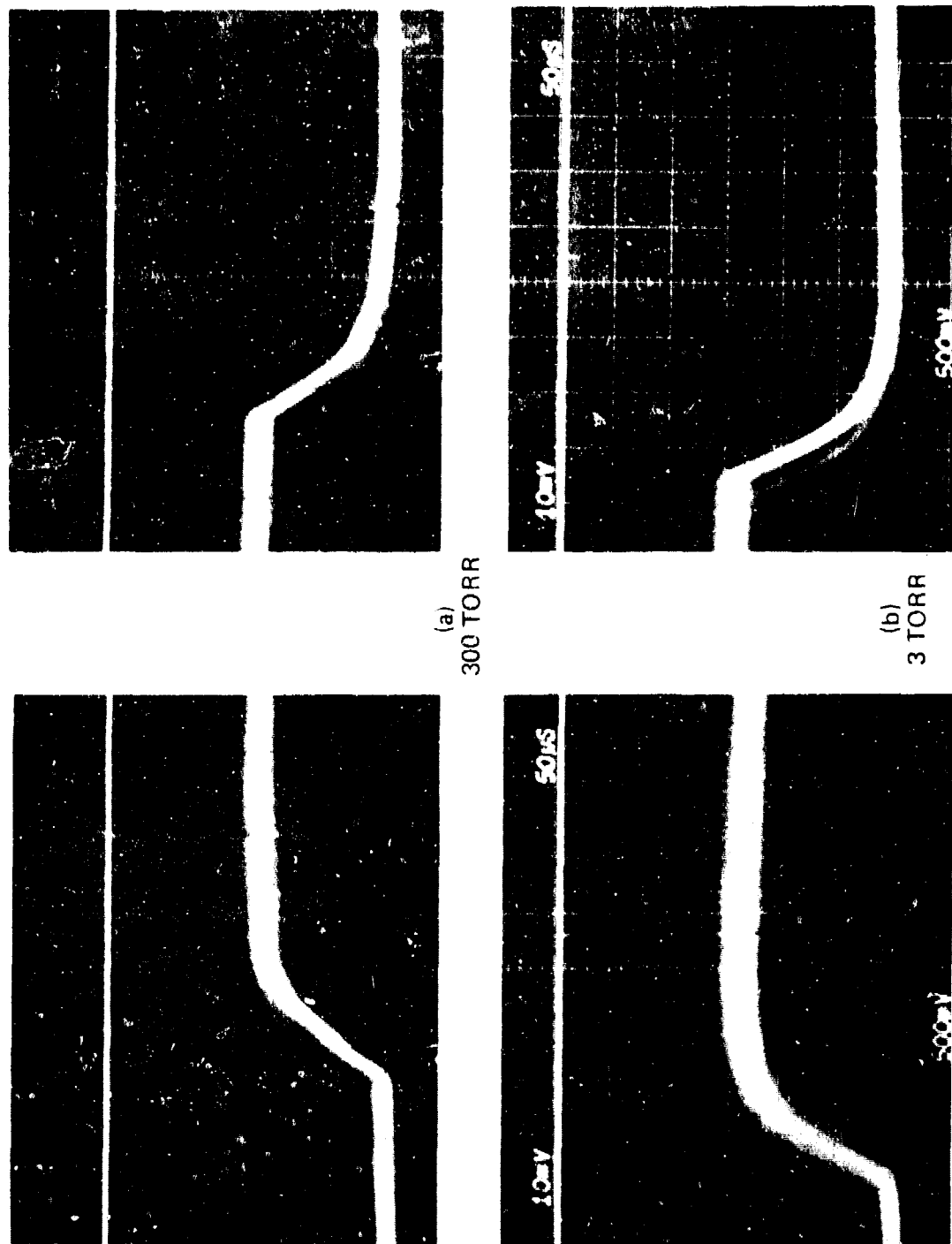


Figure 27. Oscillograms of Pulsed Gain at  $4 \mu$  in 12-cm-Gain-Length Laser

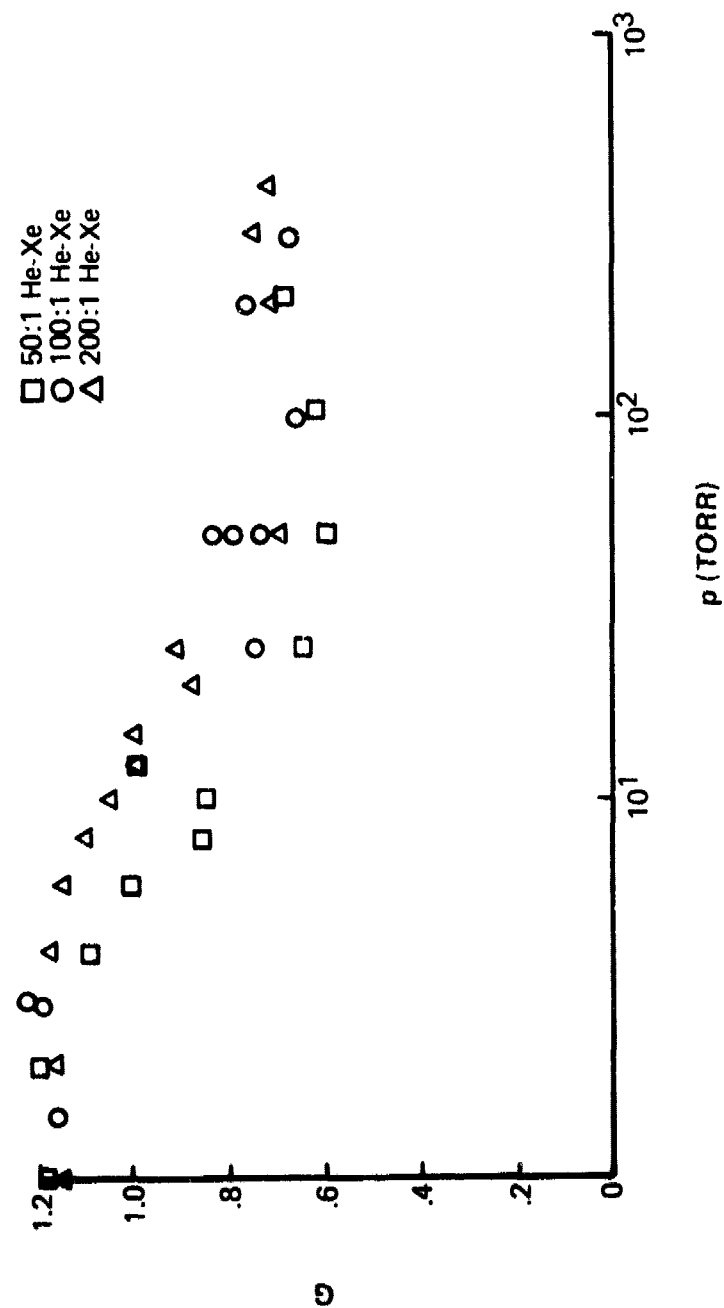


Figure 28. Gain at 4  $\mu$  as a Function of Pressure in 12-cm-Gain-Length Laser

After the gain measurements had been made, it was found that improved laser performance resulted when the secondary capacitor was removed from the pulser circuit, and subsequent measurements were made without this capacitor. Also, it was observed that higher laser output power was obtained when high-pressure dilute mixtures of Xe in He were used. For example, the laser pulses of Figure 29 were obtained at a pressure of 700-Torr He-Xe (1400:1), a charging voltage of 10 kV, and a PRF of 1 kHz. Pulse amplitudes are uncalibrated and reflect improved grating and detector response with increasing wavelength. A 1-m confocal cavity consisting of a total reflector and an output mirror having 10% transmittance was used. The laser output was focused on the entrance slit of a Jarrell-Ash Model 82-000, 0.5-m Ebert scanning spectrometer equipped with an infrared grating blazed at 5  $\mu$ . A liquid-nitrogen-cooled PbSnTe detector was used at the spectrometer exit slit. Lasing occurred predominantly in the afterglow of the 100-nsec discharge, lasting up to 5  $\mu$ sec after the current pulse. An indication of pulse-to-pulse stability of the laser output is given by the trace width of the optical pulse, which is a superposition of thousands of pulses occurring during the 5-sec exposure time.

An oscillogram of the current and voltage pulses is shown at the top of Figure 29 with an expanded time scale of 50 ns/cm. The voltage pulse was measured with a Tektronix P 6013A high-voltage probe at the cathode and the current pulse with a Pearson Model 110 current transformer which surrounded the cathode lead. A Tektronix 7904 oscilloscope was used to display the pulses. The phase shift between current and voltage is probably due to inductance in the discharge circuit, particularly in the thyatron.

Average laser power output was measured by focusing (with a 5-cm-diam. NaCl lens) the  $\sim 1 \times 3$ -cm output beam onto a Cintra disk-type calorimeter. Plots of average power as a function of PRF are shown in Figure 30. A 1-m confocal cavity with an output mirror having 15% transmission at 3.65  $\mu$  was used. Oscillation occurred at 3.65, 2.65, and 2.03  $\mu$  simultaneously. The break in the curves at 3 kHz is associated with a change in discharge conditions. As the PRF was increased up to 3 kHz, the discharge concentrated into a bright band at the downstream edge of the electrodes. As the PRF was increased

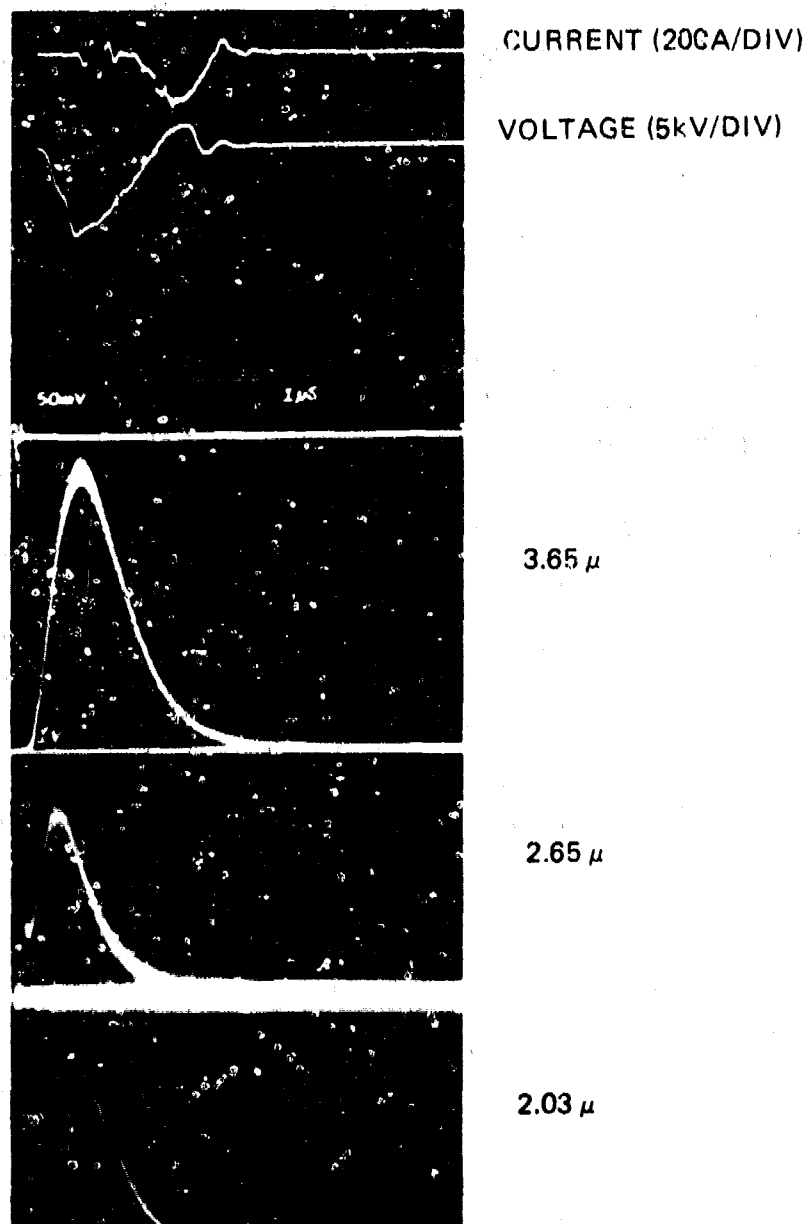


Figure 29. Oscillograms of Laser Pulses from 12-cm-Gain-Length Laser at a Pressure of 700 Torr He-Xe (1400:1)

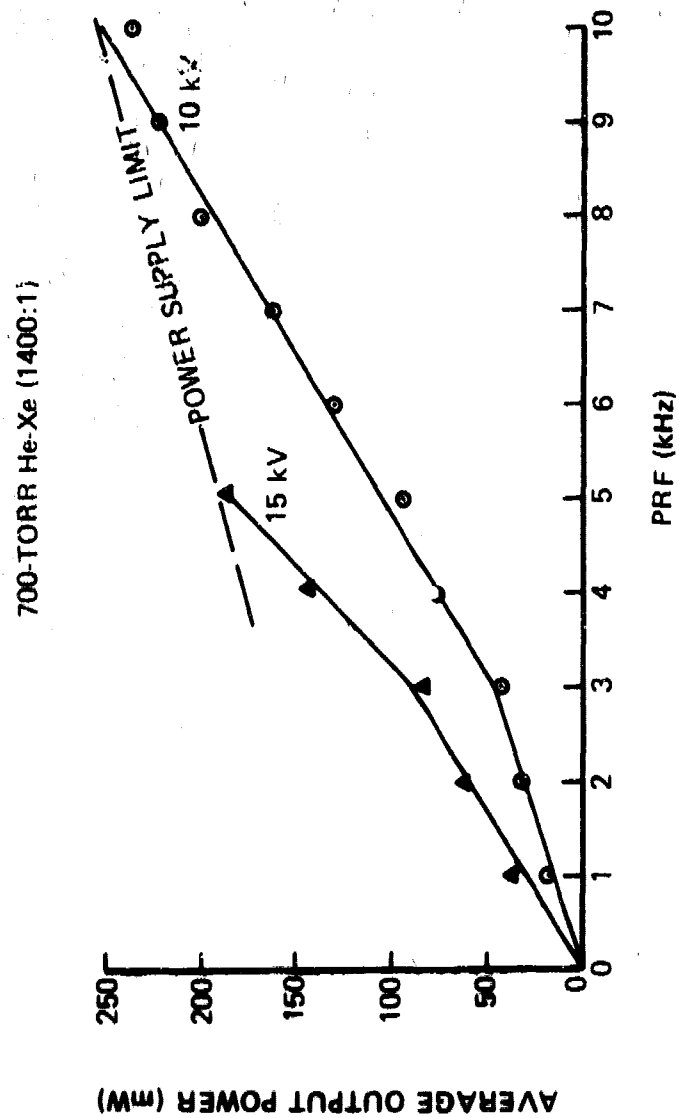


Figure 30. Dependence of Average Laser Output Power upon PRF for 12-cm-Gain-Length Laser at a Pressure of 700 Torr He-Xe (1400:1)

beyond 3 kHz, the band expanded to fill the entire interelectrode region. These observations indicate that the break in the curves may be due to a discharge-clearing effect. Dzakowic and Wutzke<sup>21</sup> define a clearing ratio as the ratio of the minimum time between arc-free pulses to the gas transit time through the interelectrode gap. For the data of Figure 30, the clearing ratio is 1 at a PRF of 2.5 kHz and 0.25 at 10 kHz. The results given in Ref. 21 for a fast-flow transverse-discharge CO<sub>2</sub> laser show a minimum clearing ratio of 2.

The upper limit to the curves of Figure 30 was dictated by the 200-mA current capability of the Spellman 4-kW (20 kV, 0.2 A) power supply. The 1-nF energy-storage capacitor was charged at this current for 100  $\mu$ sec, which limited the maximum PRF to 10 kHz. The average output power from the 1-nF capacitor at 10 kHz and 10 kV was 500 W, which for the 100-nsec discharge corresponded to a peak power of 500 kW. Much of this power was not expended in the discharge, owing to impedance mismatch. From the 10-kV data of Figure 30, the energy of the laser pulses was calculated to be 20  $\mu$ J. Based upon the electrical energy output of the 1-nF capacitor, the laser efficiency at 10 kHz and 10 kV was 0.04%.

As a result of the short gain length ( $\sim 12$  cm) of the CCRGEDL and the cavity losses due to the Brewster-angle windows, lasing was achieved in He-Xe for the strongest lines (2.03, 2.65, and 3.65  $\mu$ ) only. At high pressure the gain is limited--through its dependence on  $\Delta N/\Delta \nu$ --by pressure broadening of the linewidth  $\Delta \nu$ . The pressure broadening of Xe lines by He buffer gas has been shown to be considerable,<sup>87,88</sup> being of the order of GHz at atmospheric pressure. In contrast to the gain dependence on  $\Delta N/\Delta \nu$ , the laser pulse energy depends only upon  $\Delta N$  (the population inversion density) and therefore increases with increasing pressure for optimum E/p.

The long-time stability of the laser output is demonstrated by the data of Figure 31. The laser was operated continuously for 4 hr, with an initial output of 100 mW and a final output of 96 mW. During this time no adjustments of any kind were made. The cause of the temporal variation in output power is presently unknown. It is important to note that the data of Figure 31 were obtained 30 days after the laser had been filled with the 1400:1 He-Xe mixture.

700-TORR He-Xe (1400:1)  
PRF: 5 kHz  
CHARGING VOLTAGE: 10 kHz

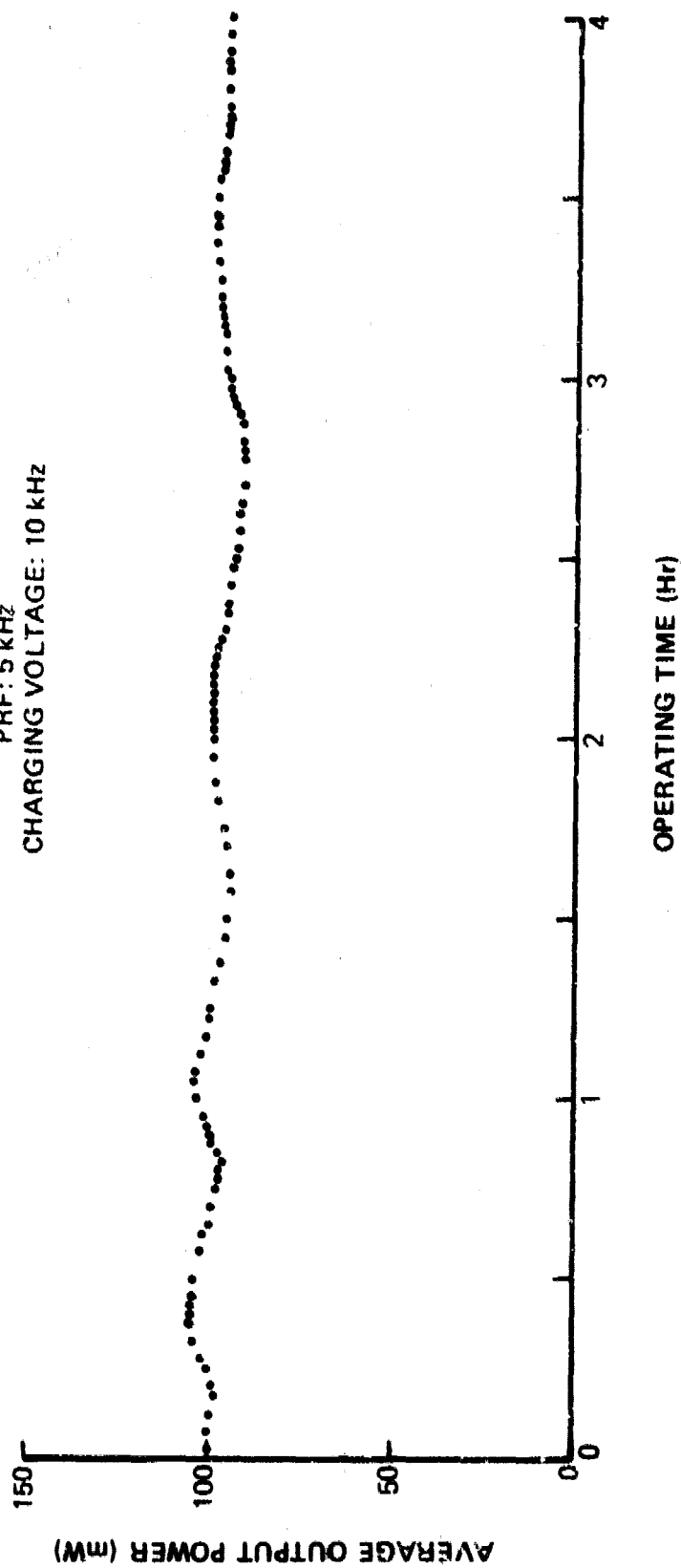


Figure 31. Dependence of Average Laser Output Power upon Continuous Operating Time for 12-cm-Gain-Length Laser at a Pressure of 700 Torr He-Xe (1400:1)

beyond 3 kHz, the band expanded to fill the entire interelectrode region. These observations indicate that the break in the curves may be due to a discharge-clearing effect. Dzakowic and Wutzke<sup>21</sup> define a clearing ratio as the ratio of the minimum time between arc-free pulses to the gas transit time through the interelectrode gap. For the data of Figure 30, the clearing ratio is 1 at a PRF of 2.5 kHz and 0.25 at 10 kHz. The results given in Ref. 21 for a fast-flow transverse-discharge CO<sub>2</sub> laser show a minimum clearing ratio of 2.

The upper limit to the curves of Figure 30 was dictated by the 200-mA current capability of the Spellman 4-kW (20 kV, 0.2 A) power supply. The 1-nF energy-storage capacitor was charged at this current for 100  $\mu$ sec, which limited the maximum PRF to 10 kHz. The average output power from the 1-nF capacitor at 10 kHz and 10 kV was 500 W, which for the 100-nsec discharge corresponded to a peak power of 500 kW. Much of this power was not expended in the discharge, owing to impedance mismatch. From the 10-kV data of Figure 30, the energy of the laser pulses was calculated to be 20  $\mu$ J. Based upon the electrical energy output of the 1-nF capacitor, the laser efficiency at 10 kHz and 10 kV was 0.04%.

As a result of the short gain length ( $\sim 12$  cm) of the CCRGEDL and the cavity losses due to the Brewster-angle windows, lasing was achieved in He-Xe for the strongest lines (2.03, 2.65, and 3.65  $\mu$ ) only. At high pressure the gain is limited--through its dependence on  $\Delta N/\Delta v$ --by pressure broadening of the linewidth  $\Delta v$ . The pressure broadening of Xe lines by He buffer gas has been shown to be considerable,<sup>87,88</sup> being of the order of GHz at atmospheric pressure. In contrast to the gain dependence on  $\Delta N/\Delta v$ , the laser pulse energy depends only upon  $\Delta N$  (the population inversion density) and therefore increases with increasing pressure for optimum E/p.

The long-time stability of the laser output is demonstrated by the data of Figure 31. The laser was operated continuously for 4 hr, with an initial output of 100 mW and a final output of 96 mW. During this time no adjustments of any kind were made. The cause of the temporal variation in output power is presently unknown. It is important to note that the data of Figure 31 were obtained 30 days after the laser had been filled with the 1400:1 He-Xe mixture.



Addition of Ar to 3 Torr of Xe (lasing at 2.03  $\mu$ ) resulted in the appearance of the following laser lines at the given Ar pressures: 17 Torr - 2.63 and 2.65  $\mu$  (at low voltage); 27 Torr - 5.57  $\mu$ ; 49 Torr - 1.73 and 3.11  $\mu$  (at low voltage); 97 Torr - 2.48  $\mu$  (at low voltage); 207 Torr - 3.37  $\mu$  (at low voltage). Oscillation on all of the above lines occurred simultaneously in the 200-500 Torr pressure region. The applied discharge voltage was varied from 5 to 7 kV.

Addition of Kr to 10 Torr of Xe (lasing at 3.11, 3.37, 3.51, and 3.89  $\mu$ ) resulted in the following changes at the given Kr pressures: 2 Torr - oscillation ceased at 3.11  $\mu$ ; 10 Torr - oscillation ceased at 3.51  $\mu$  and began at 3.68  $\mu$ ; 20 Torr - oscillation began at 2.63  $\mu$ ; 40 Torr - oscillation ceased at 3.37, 3.68, and 3.89  $\mu$  and began at 2.48  $\mu$ ; 90 Torr - oscillation began at 2.65 and 3.37  $\mu$ ; 190 Torr - oscillation ceased at 3.37  $\mu$ . Addition of Kr to 0.1 Torr of Xe resulted in the following changes at the given Kr pressures: 1-5 Torr - oscillation at 4.06  $\mu$  (Kr line); 10-50 Torr - no oscillation; and 50-100 Torr - oscillation at 2.63  $\mu$ . Achievement of an arc-free discharge in Kr-Xe mixtures was very difficult. Discharges in He-Kr were less prone to arcing. Oscillation on the 2.19- and 3.07- $\mu$  lines of Kr was achieved for 200:1 and 400:1 He-Kr mixtures at pressures of 100-200 Torr.

Addition of He to an Ar-Xe (490:3) mixture (lasing at 1.73, 2.03, 2.48, 2.63, 2.65, 3.11, 3.37, and 5.57  $\mu$ ) resulted in the following changes in the given He pressures: 11 Torr - loss of 1.73  $\mu$ ; 100 Torr - loss of 3.11  $\mu$ ; and 200 Torr - loss of 2.48, 3.37, and 5.57  $\mu$  with the appearance of 3.51  $\mu$ .

The most important aspects of the above observations are: (1) lasing was achieved in high-pressure (35-Torr) Xe; (2) high pressures of Ar are effective in inducing laser oscillation on the Xe 5d-6p transitions (simultaneous oscillation at eight wavelengths); and (3) Kr is a poor buffer gas for the Xe laser.

The effectiveness of Ar as a buffer gas was investigated further. Figure 32 shows the multiline, multimode average laser output power (as measured with a Scientech 1-in. disc calorimeter) as a function of Ar pressure for various

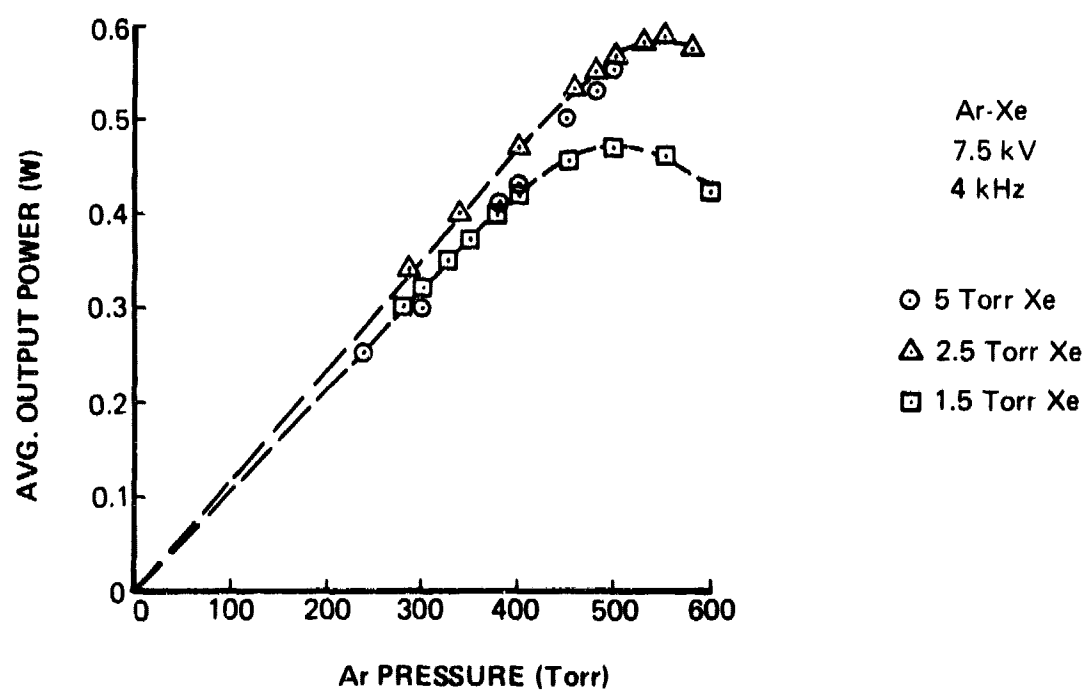


Figure 32. Pressure Dependence of Average Laser Output Power for Ar-Xe Mixtures in 12-cm-Gain-Length Laser

pressures of Xe. The voltage dependence of the output power for various total and partial pressures is shown in Figure 33(b). Figure 33(a) shows the dependence of output power on PRF for near optimum conditions of total and partial pressure. At the maximum output power of 0.9 W, the laser efficiency based on the 197-W average power output of the 1-nF energy-storage capacitor is 0.46%, which is approximately ten times that obtained for He-Xe.

The higher power and efficiency of the Ar-Xe laser, as compared to the He-Xe laser, has also been observed by Newman and DeTemple<sup>89</sup> for an e-beam-ionized high-voltage-pulse-sustained discharge. They observed significant output power from Ar-Xe at 1.73  $\mu$  (70%), 2.03  $\mu$  (weak), 2.63  $\mu$  (15%), and 2.65  $\mu$  (10%) using a Si flat as an output mirror, in contrast to the present results for which 2.03  $\mu$  is the strongest line; however, the fact that lasing is observed at 1.73  $\mu$  indicates the strength of the 1.73  $\mu$  line since the Ge output flat is nearly opaque at this wavelength.

After the data of Figures 32 and 33 were obtained, the Ge output flat with 5% transmittance at 4  $\mu$  was replaced with one having 2% transmittance at 4  $\mu$ . The data of Figure 34 were then obtained for an Ar-Ne-Xe (500:50:2.5) mixture. The addition of Ne improved the uniformity of the high-pressure Ar-Xe discharge, permitting higher discharge voltages to be applied. At the same time, however, the Ne reduced the laser output power slightly. Maximum repetition rate was limited by charging supply capabilities.

The use of an output mirror having high reflectance in the 4- $\mu$  region was motivated by a search for the 3.9966- and 4.6109- $\mu$  laser lines which have been observed under cw conditions at low pressure.<sup>54</sup> These lines have not yet been generated by the CCRGEDL; but during parametric measurements of laser output from high-pressure He-Xe mixtures using the 2% transmitter (at 4  $\mu$ ), a new Xe-neutral laser line was observed at 4.02  $\mu$ .

Simultaneous lasing at the five lines listed in Table 4 was observed under the appropriate excitation conditions. These transitions obey the selection rules of  $J_c - 1$  coupling:<sup>90</sup>  $\Delta J_c = 0$ ;  $\Delta K = 0, \pm 1$ ;  $\Delta J = 0, \pm 1$ ;  $J = 0 \leftrightarrow J = 0$ .

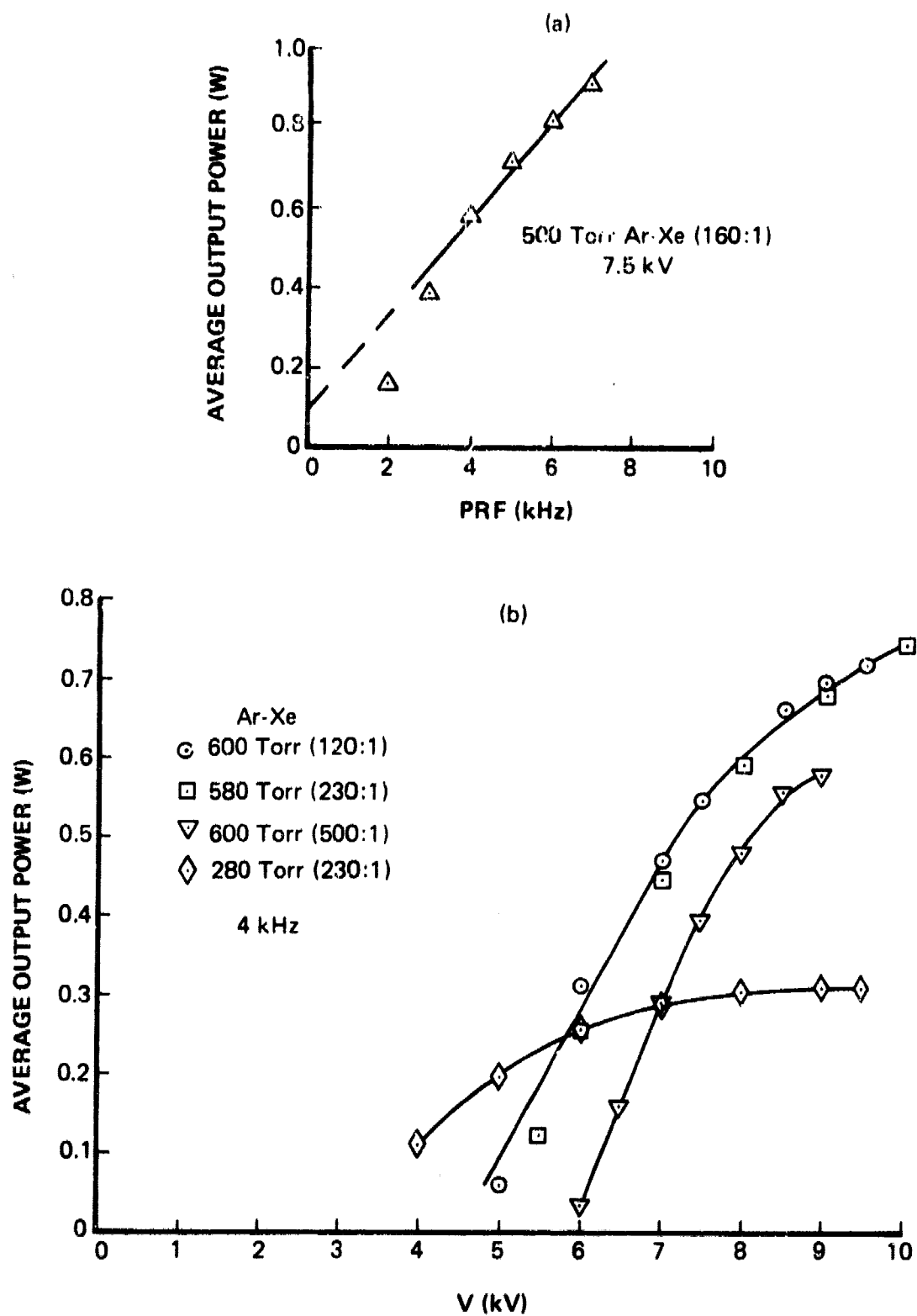


Figure 33. Dependence of Average Laser Output Power upon (a) PRF and (b) Charging Voltage for Ar-Xe Mixtures in 12-cm-Gain-Length Laser

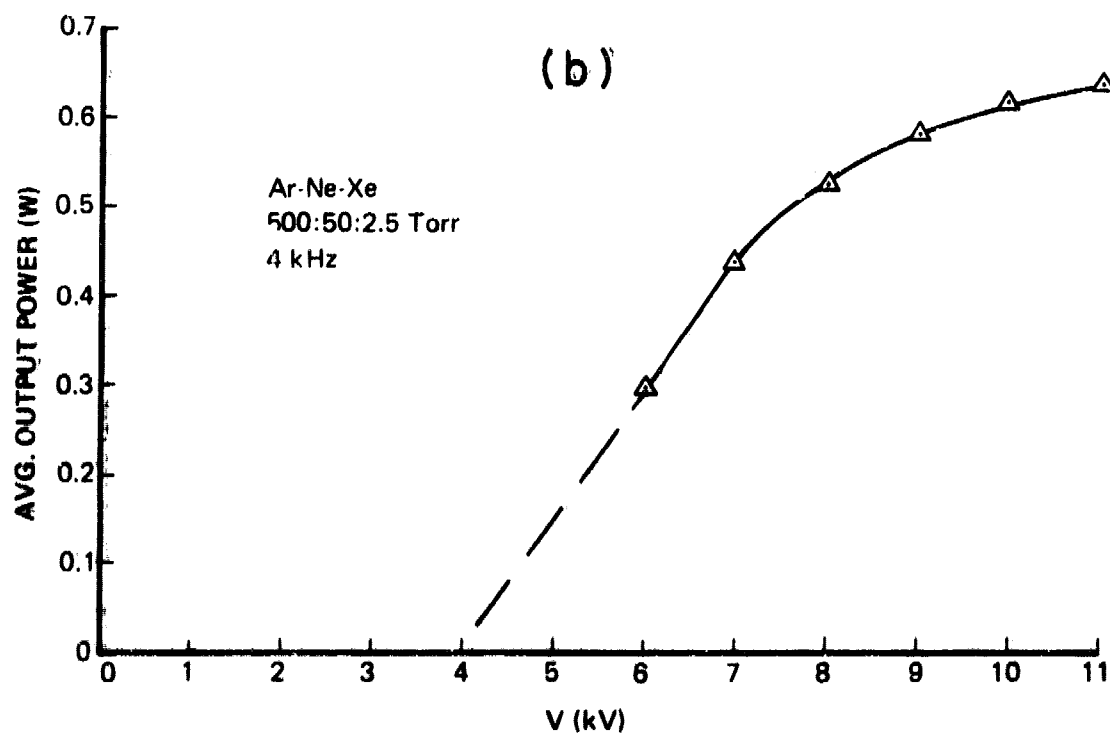
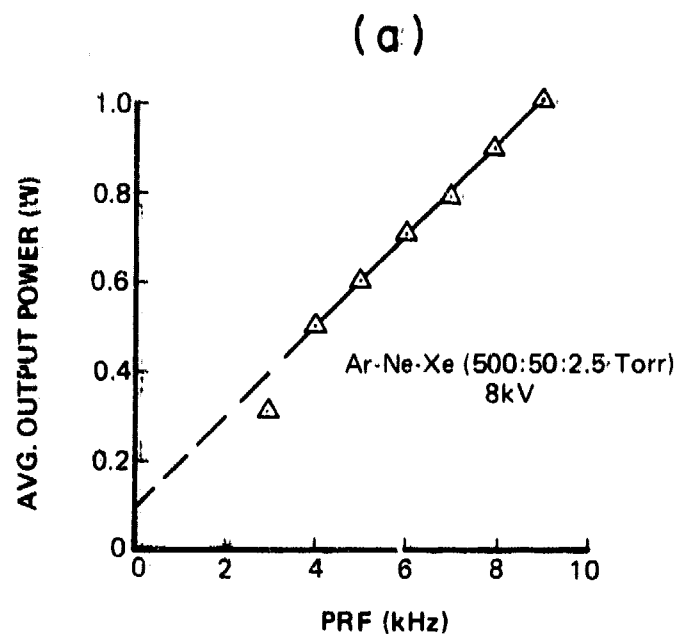


Figure 34. Dependence of Average Laser Output Power upon (a) PRF and (b) Charging Voltage for Ar-Ne-Xe Mixture in 12-cm-Gain-Length Laser

TABLE 4  
Xe-I LASER LINES OBSERVED IN He-Xe DISCHARGE  
(12-cm Gain Length)

Calculated	$\lambda_{\text{vac}}$ ( $\mu$ )	Measured	Transition (Racah Notation)
2.0268		2.0271	$5d[3/2]_1^0 - 6p[3/2]_1$
2.6518		2.6516	$5d[3/2]_1^0 - 6p[1/2]_0$
3.4344		3.4349	$7p[5/2]_2 - 7s[3/2]_1^0$
3.6518		3.6516	$7p[1/2]_1 - 7s[3/2]_2^0$
4.0207		4.0208	$7p[1/2]_1 - 7s[3/2]_1^0$ *

\* Previously unreported laser transition

Faust and McFarlane<sup>90</sup> have pointed out that transitions with  $\Delta K = \Delta J$  are comparatively strong. The first four lines of Table 4, for which  $\Delta K = \Delta J$ , exhibited high gain by lasing in a short-gain-length cavity ( $\sim 12$  cm) having an output transmittance of 40% or more. For the 4.02- $\mu$  line, however, an output transmittance of less than 5% (2% was used in the present results) was required for lasing.

The oscillograms of the laser pulses shown in Figure 35 were obtained at a pressure of 300 Torr of He-Xe (200:1), a charging voltage of 14 kV, and a PRF of 4 kHz. As before, a  $\text{CaF}_2$  lens was used to focus the laser output on the entrance slit of a Jarrell-Ash 0.5-m Ebert scanning spectrometer equipped with an infrared grating blazed at 5  $\mu$ . A liquid-nitrogen-cooled PbSnTe detector was used at the exit slit. The spectrometer was calibrated with a He-Ne laser.

As evident from Figure 35, the temporal behavior of the laser pulses varies considerably. The 2.03- and 3.43- $\mu$  pulses peak during the 100-ns discharge current pulse; the 2.65- and 4.02- $\mu$  pulses peak at  $\sim 1$  and 4  $\mu$ s, respectively, after the current pulse; and the 3.65- $\mu$  pulse peaks both during and  $\sim 1$   $\mu$ s after the current pulse.

The peak values of the directly excited and afterglow pulses at the various wavelengths are plotted in Figures 36 through 43 as a function of total pressure for He-Xe mixture ratios ranging from 100:1 to 10,000:1. Although the magnitude of the directly excited pulses decreases with decreasing Xe partial pressure, the afterglow-pulse magnitude increases with decreasing Xe partial pressure--see Figure 44 which shows the pressure dependence of the 4.02- $\mu$  pulse for various He-Xe mixture ratios. This enhancement of afterglow lasing at low Xe partial pressures is consistent with the observation by Shuker, *et al.*,<sup>91</sup> that the number of excited Xe atoms in a pulsed He-Xe discharge increased rapidly as the Xe/He concentration ratio was lowered to  $2 \times 10^{-5}$ . These investigators attributed the enhanced Xe excitation and emission to energy transfer from atomic and molecular He metastables to Xe atoms via Penning ionization.

The pressure dependence of the average laser output power (measured with the Scientech disc calorimeter) is shown in Figure 45 for various He-Xe mixture

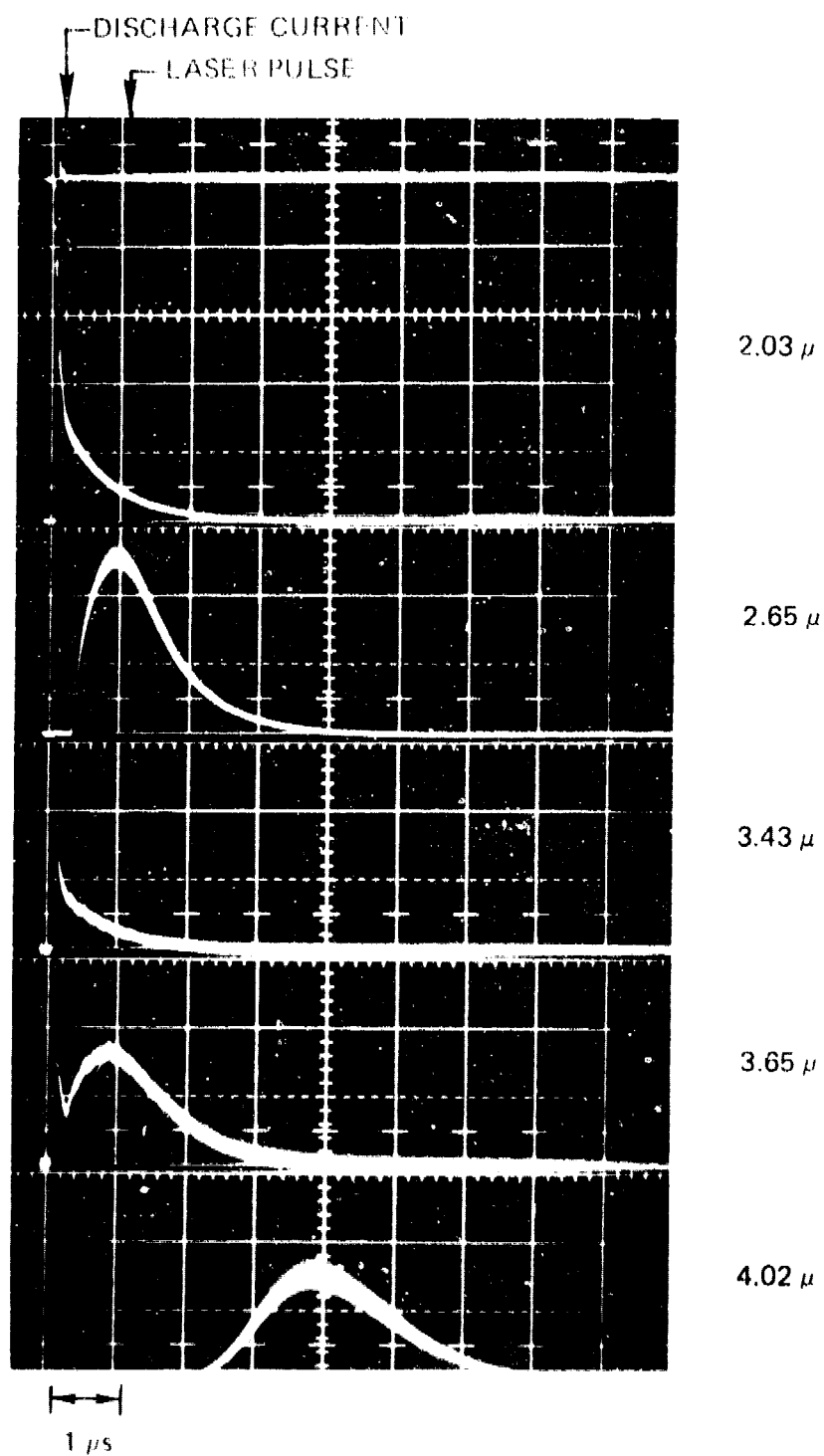


**Figure 35.** Oscillograms of Laser Pulses Obtained at a Pressure of 300 Torr He-Xe (200:1) in 12-cm-Gain-Length Laser



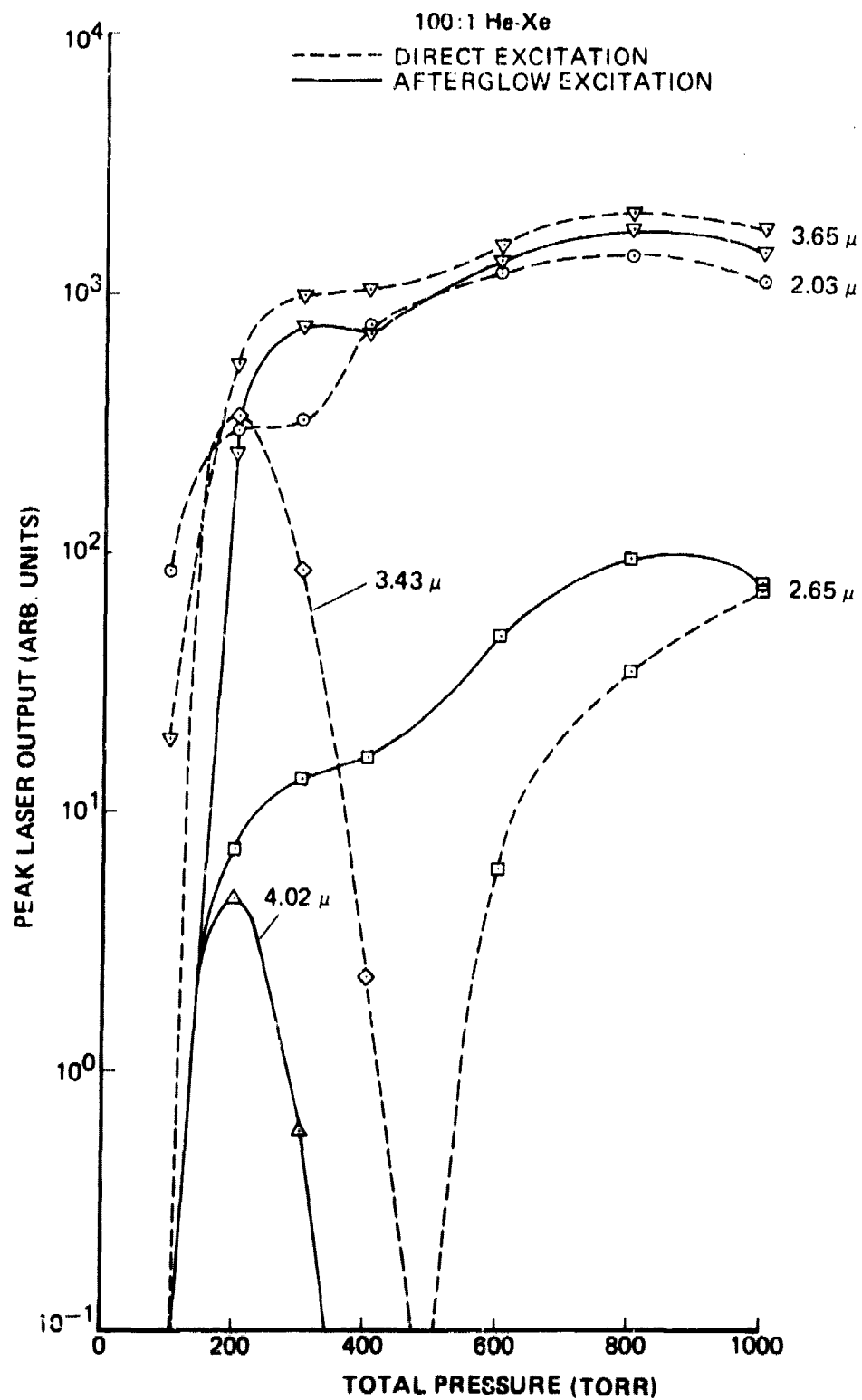


Figure 36. Pressure Dependence of Peak Output of Laser Pulses from He-Xe (100:1) in 12-cm-Gain-Length Laser

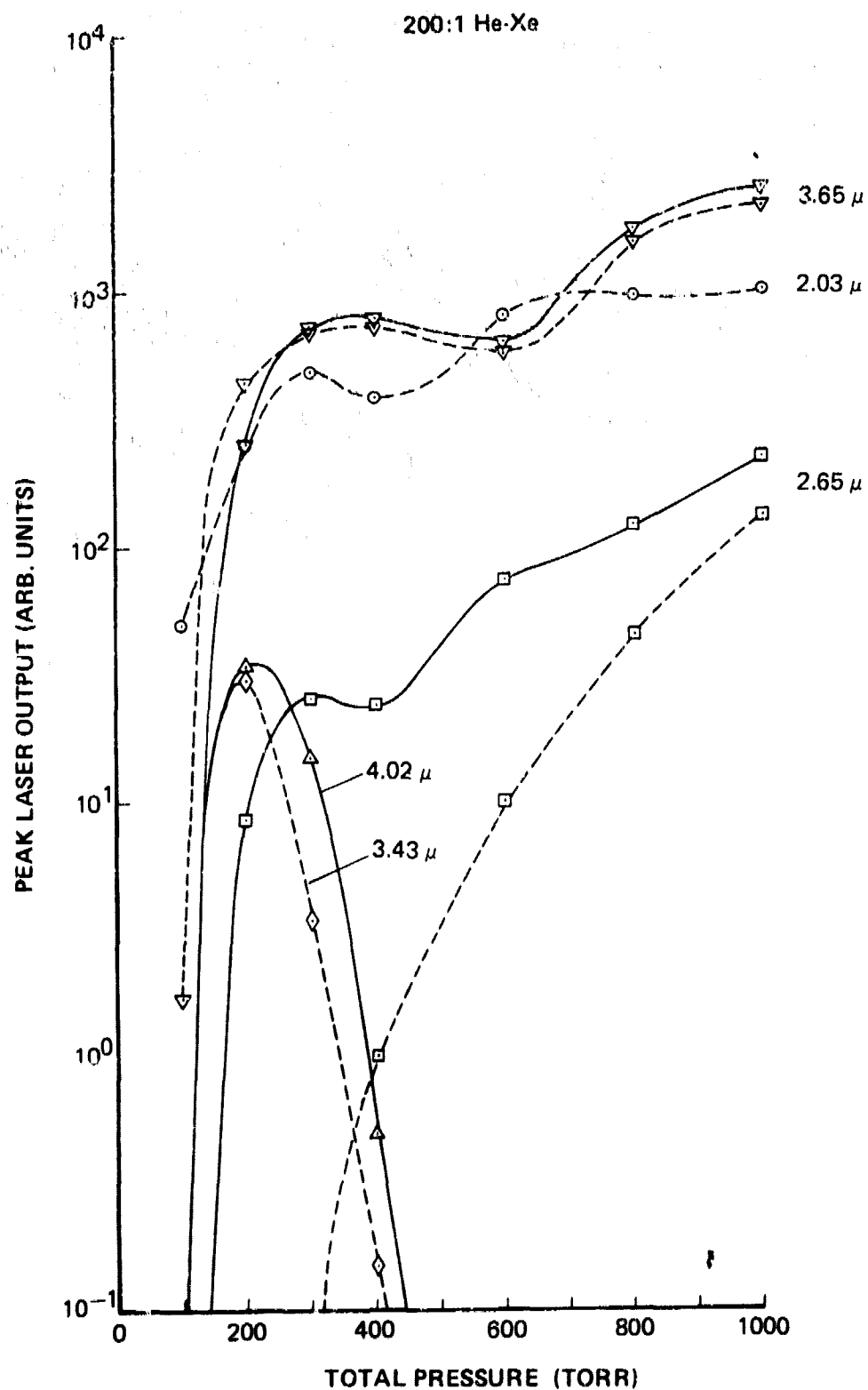


Figure 37. Pressure Dependence of Peak Output of Laser Pulses from He-Xe (200:1) in 12-cm-Gain-Length Laser

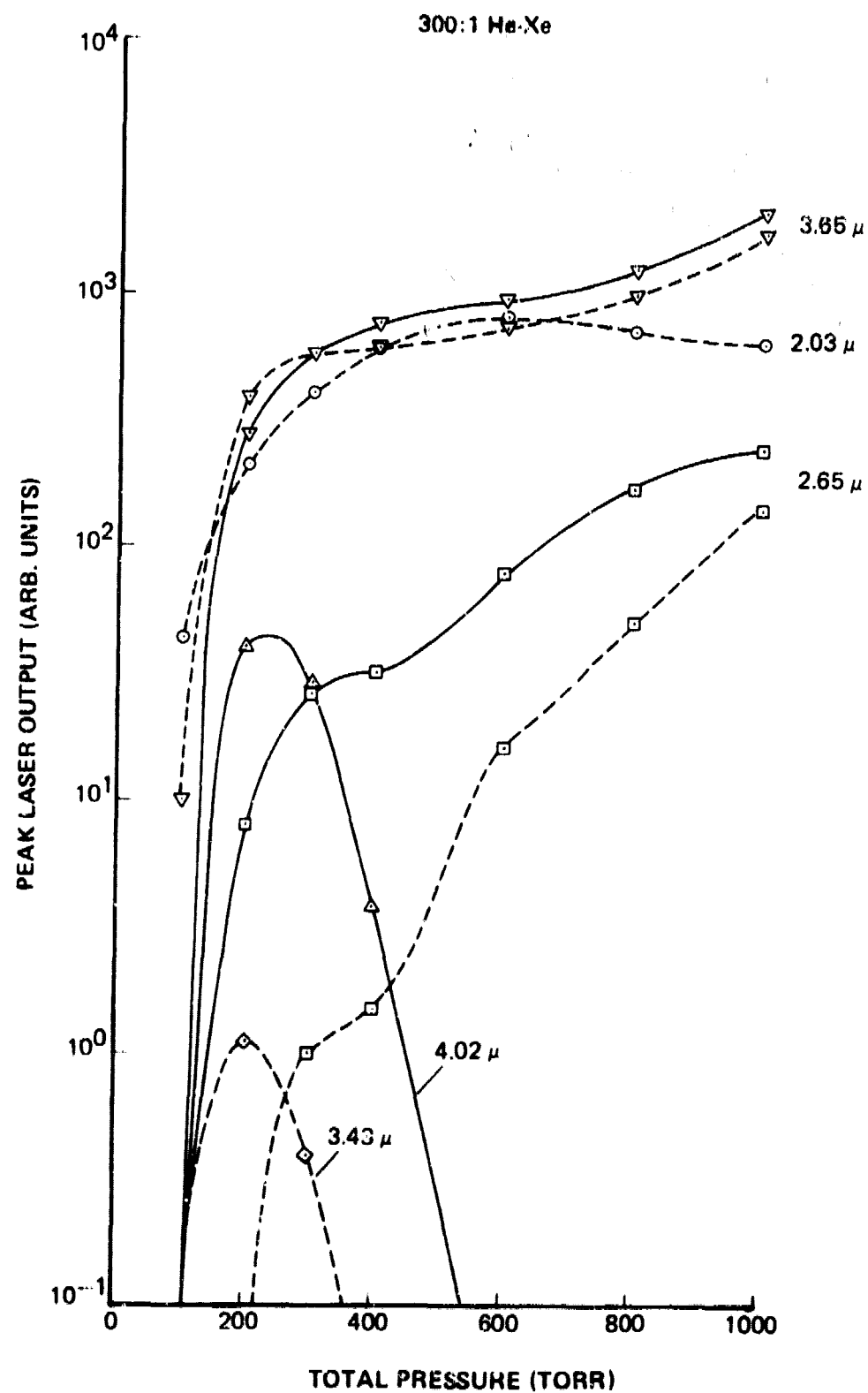


Figure 38. Pressure Dependence of Peak Output of Laser Pulses from He-Xe (300:1) in 12-cm-Gain-Length Laser

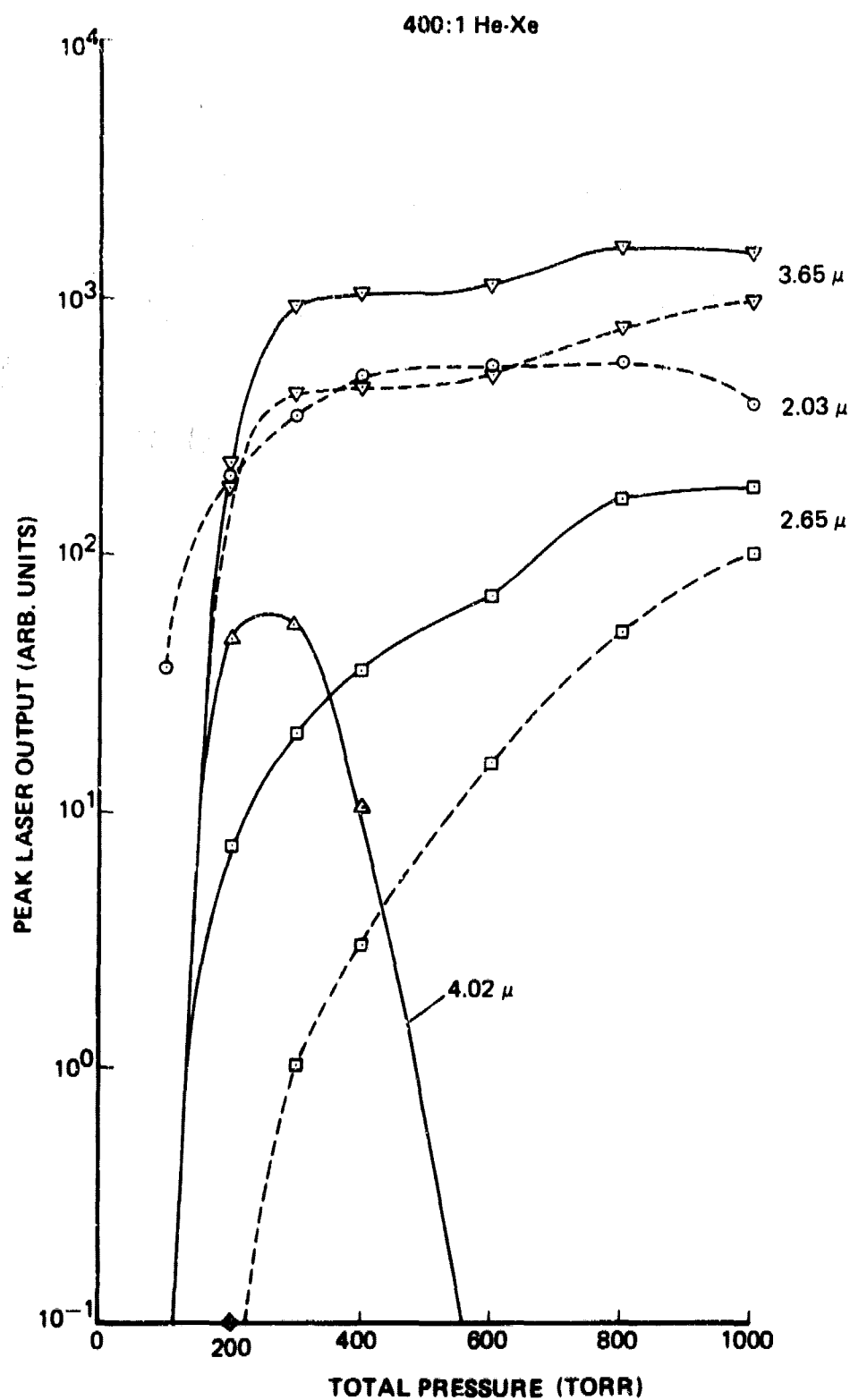


Figure 39. Pressure Dependence of Peak Output of Laser Pulses from He-Xe (400:1) in 12-cm-Gain-Length Laser

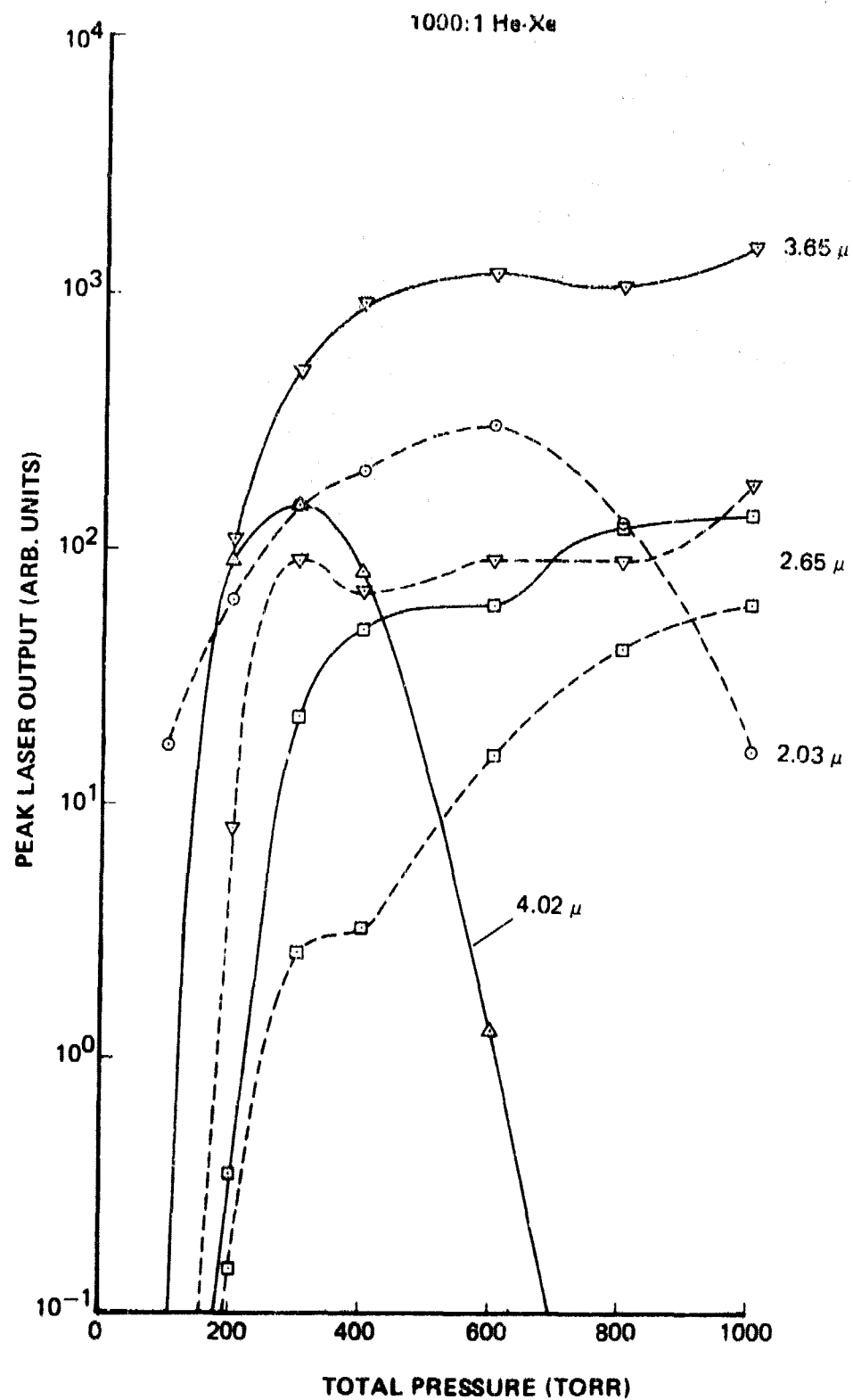


Figure 40. Pressure Dependence of Peak Output of Laser Pulses from He-Xe (1000:1) in 12-cm-Gain-Length Laser

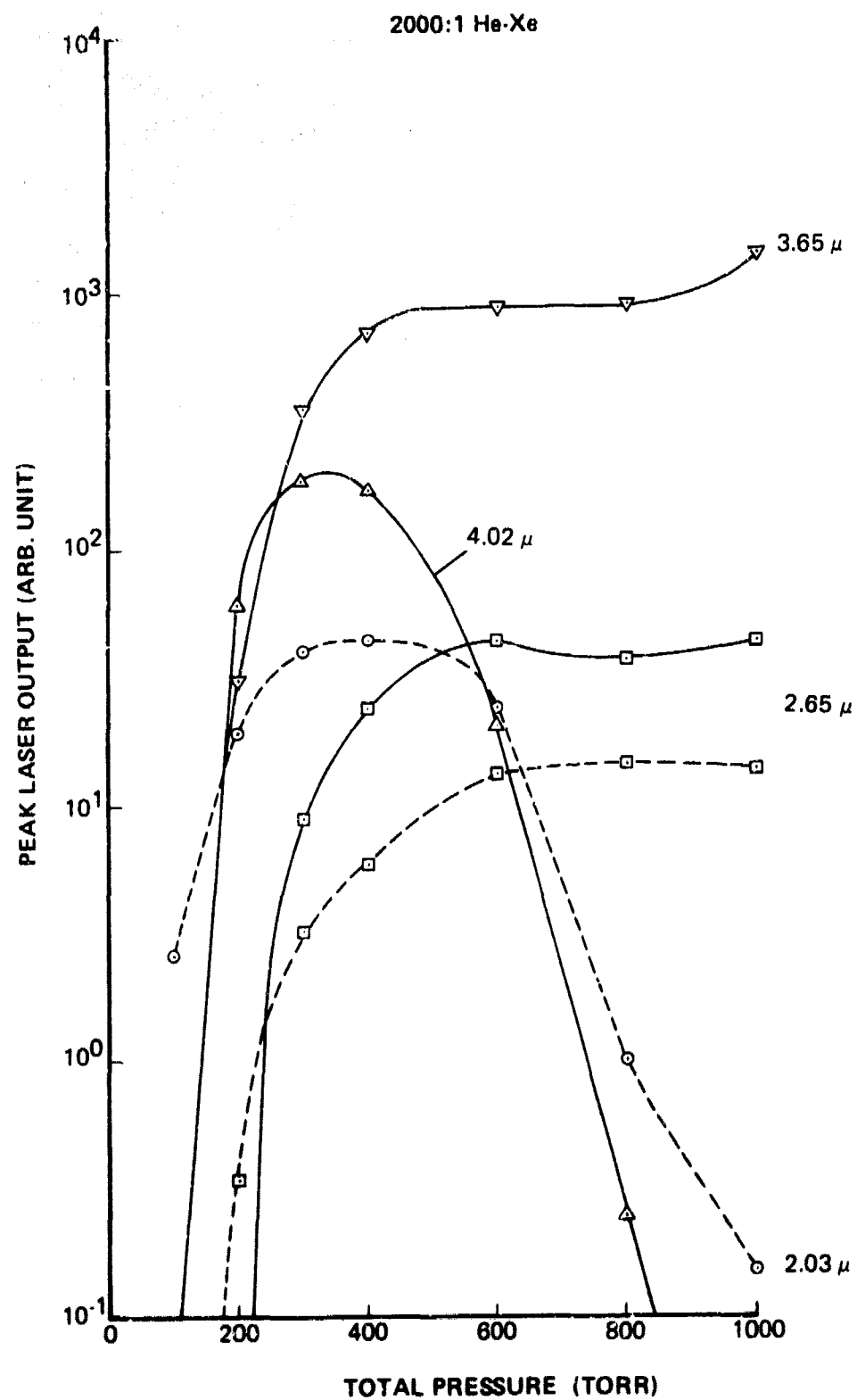


Figure 41. Pressure Dependence of Peak Output of Laser Pulses from He-Xe (2000:1) in 12-cm-Gain-Length Laser

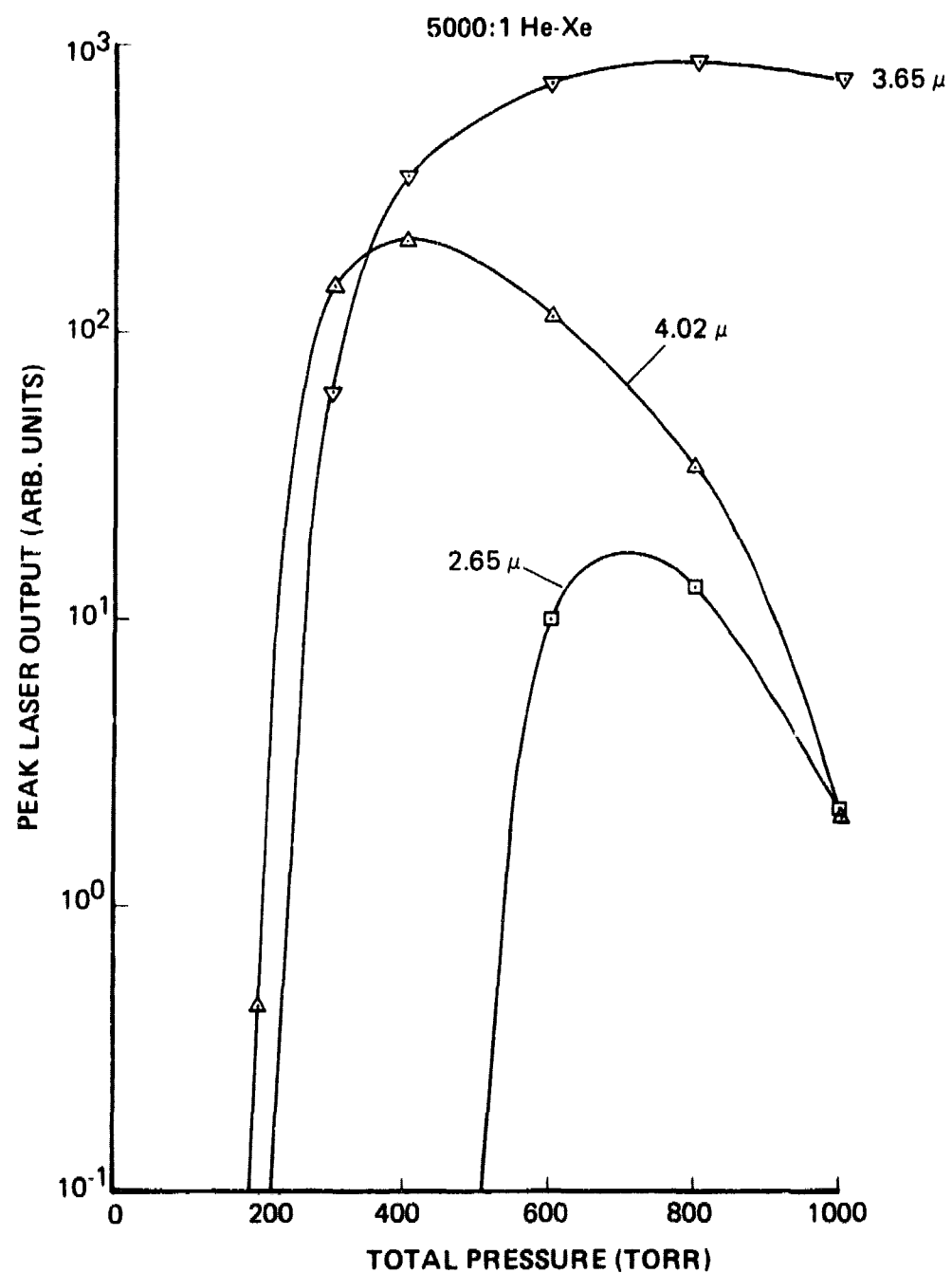


Figure 42. Pressure Dependence of Peak Output of Laser Pulses from He-Xe (5000:1) in 12-cm-Gain-Length Laser

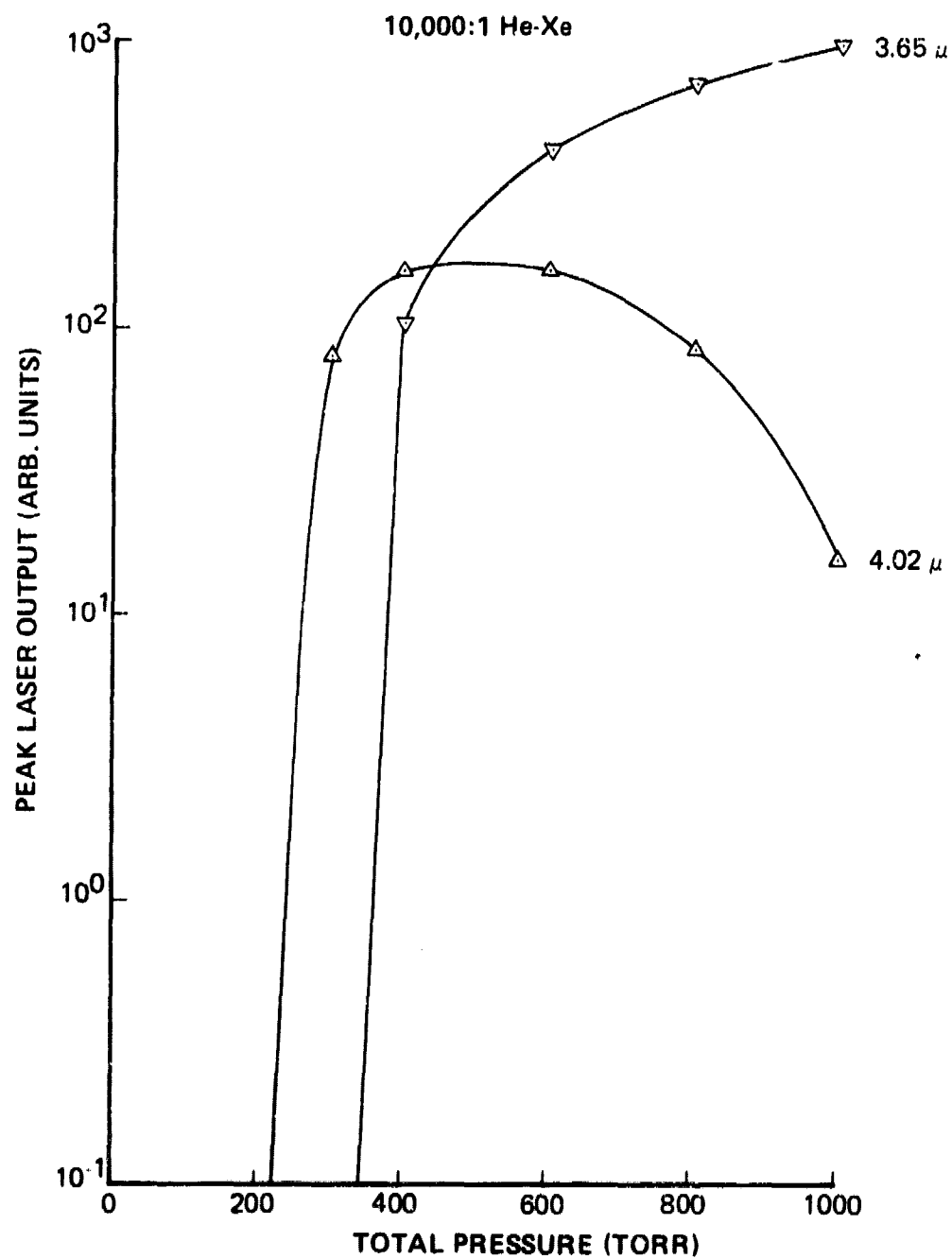


Figure 43. Pressure Dependence of Peak Output of Laser Pulses from He-Xe (10,000:1) in 12-cm-Gain-Length Laser



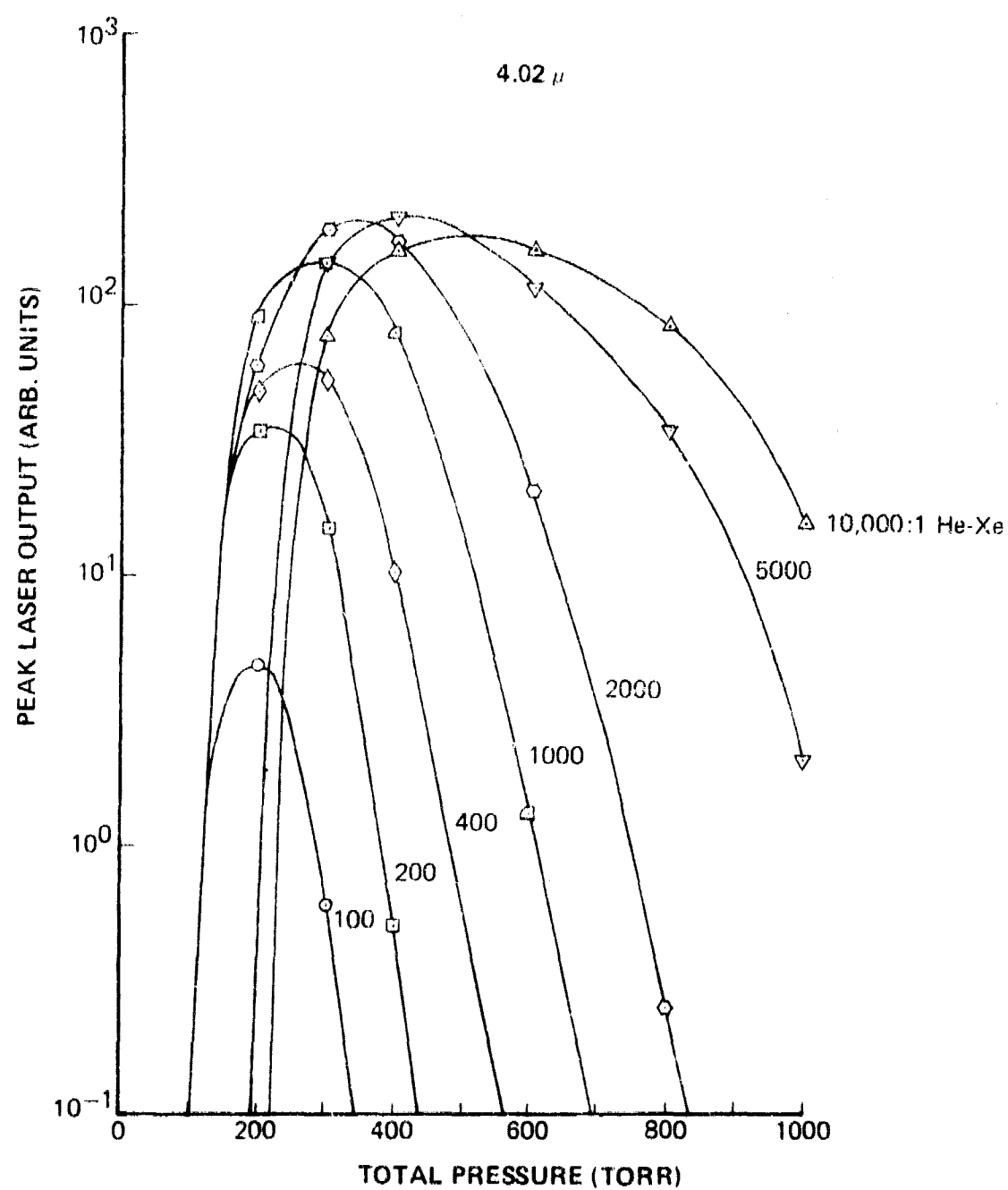


Figure 44. Pressure Dependence of Peak Output of 4.02- $\mu$  Laser Pulse from He-Xe Mixtures in 12-cm-Gain-Length Laser

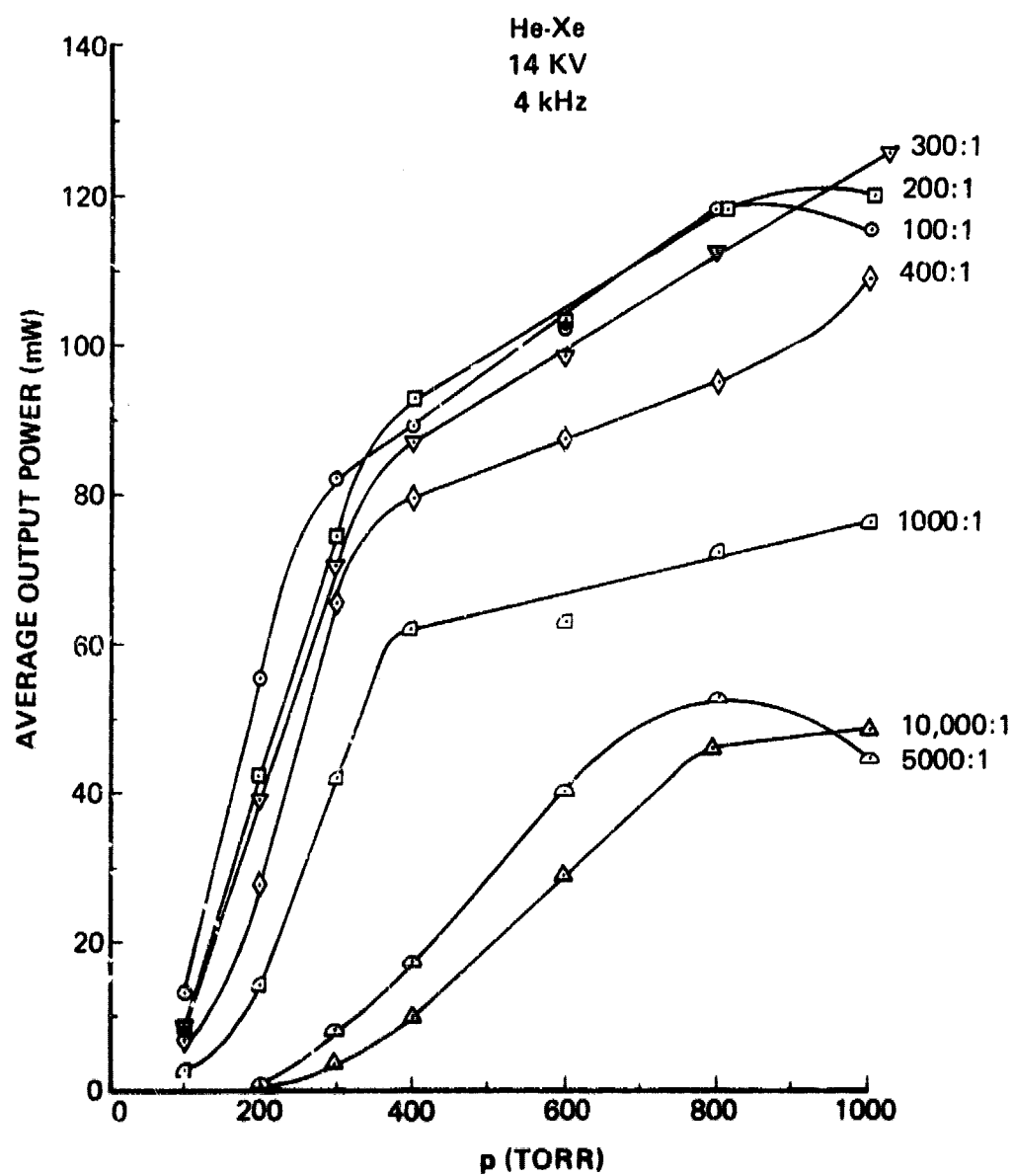


Figure 45. Pressure Dependence of Average Output Power from He-Xe Mixtures in 12-cm-Gain-Length Laser

ratios. These data were obtained concurrently with the data of Figures 35 through 44. A maximum output power of 125 mW was obtained for a 300:1 He-Xe mixture at 1000-Torr total pressure. Figure 46 (a) shows the linear dependence of peak discharge current upon charging voltage. Figure 46 (b) shows the dependence of the peak laser output at 4.02  $\mu$  upon charging voltage. The departure from linearity at the higher voltages may be due to saturation of the laser medium or charging-supply limitations.

In the Ar-Xe laser measurements employing a Ge output flat, lasing was observed at 1.73  $\mu$ , even though the Ge absorbed  $\sim 99.8\%$  of the 1.73- $\mu$  radiation. Since the short-wavelength absorption edge of Si is near 1.2  $\mu$ , as compared to  $\sim 2 \mu$  for Ge, a considerable increase in laser output at 1.73  $\mu$  should be obtainable using a Si output mirror. Measurements of the laser output, using a Si output flat having 2% transmittance at 4  $\mu$  and  $\sim 85\%$  at 1.73  $\mu$ , for a gas mixture of .97 Torr of Ar, 10 Torr of Ne, and 3 Torr of Xe are presented in Figures 47-49. Lasing occurred at 1.73, 2.03, 2.48, 2.63, 2.65, 3.1, 3.37, and 5.57  $\mu$ . At each wavelength the laser pulse was concurrent with the discharge current pulse. The 2.03-, 2.63-, and 5.57- $\mu$  pulses were of higher power than the others.

The dependence of multi-line, multi-mode average output power upon charging voltage is shown in Figure 47. The voltage dependence is the same as that obtained with the Ge output mirror, but the curve is shifted to higher power. The output-power dependence upon PRF is shown in Figure 48. Arcing occurred above 7 kHz. The laser efficiency based upon the power output of the 1-nF energy-storage capacitor is 0.7% at 7.5 kV and 0.5% at 10 kV. This approaches the 1% efficiency quoted by Newman and DeTemple.<sup>89</sup> Their higher efficiency may be due to the fact that 1.73  $\mu$  was their strongest (70%) line.

The dependence of the laser output power upon operating time is shown in Figure 49. Over a 4-hr period, the laser output decreased 32% from an initial value of 1 W to a final value of 0.685 W. During this time the charging voltage was a constant 8.2 kV; the gas temperature decreased from 78 to 73°F; and the gas pressure increased from 505 to 507 Torr. Four days after this test, the laser output was 0.52 W at 8.2 kV, 75°F, and 509 Torr. Time did

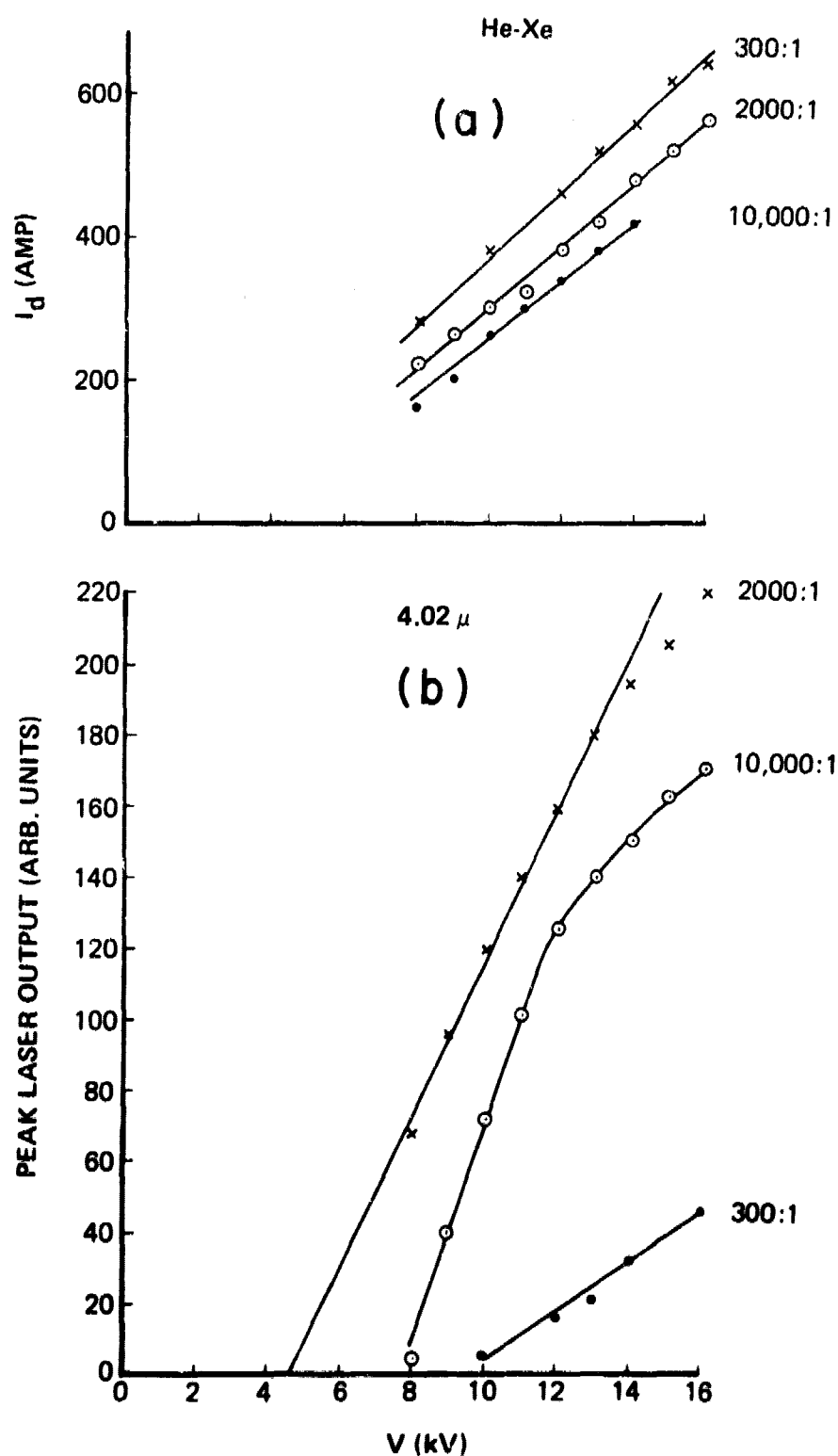


Figure 46. (a) Voltage Dependence of Peak Discharge Current for He-Xe Mixtures in 12-cm-Gain-Length Laser; (b) Voltage Dependence of Peak Output of 4.02- $\mu$  Laser Pulse for He-Xe Mixtures in 12-cm-Gain-Length Laser

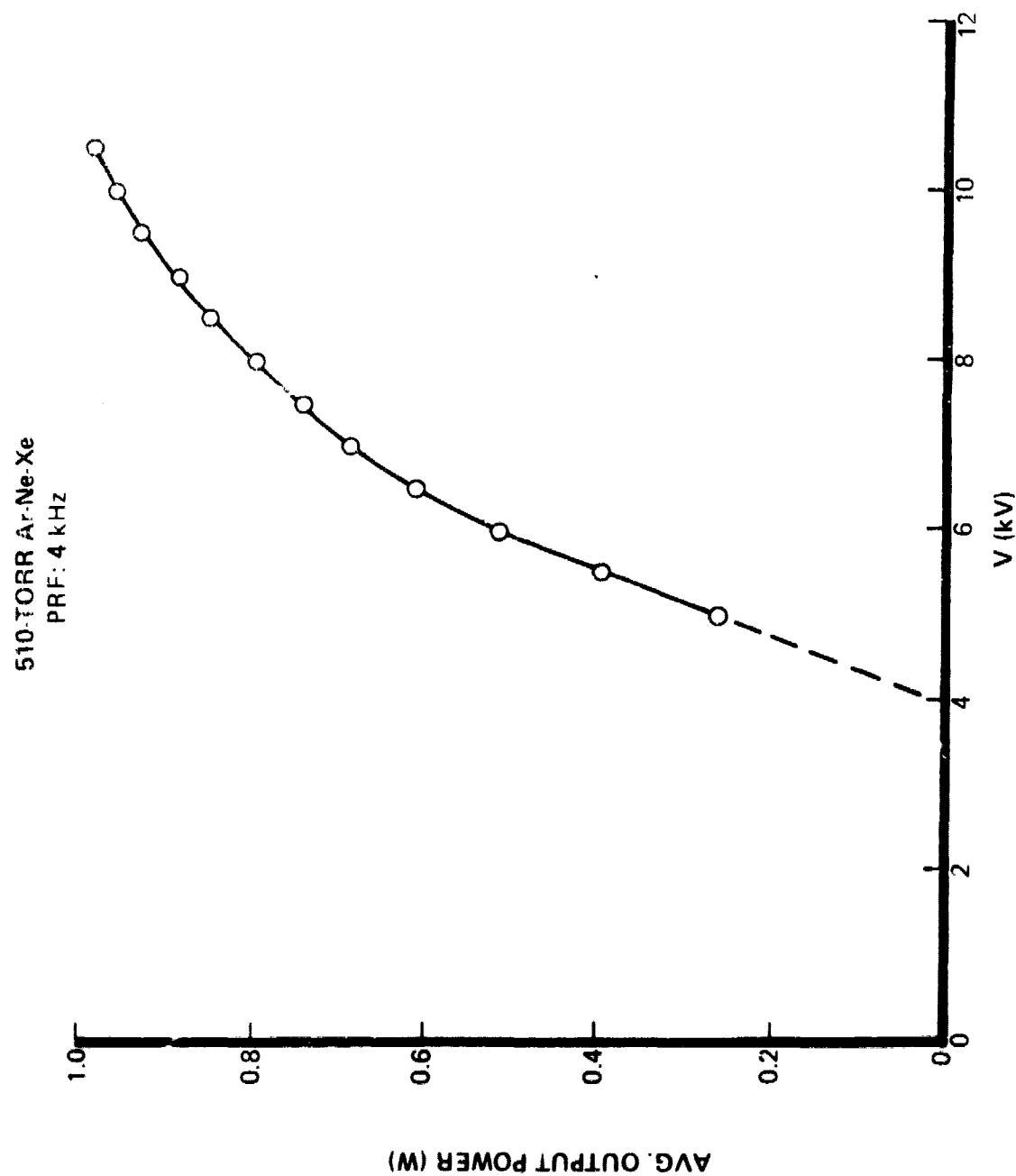


Figure 47. Dependence of Average Laser Output Power upon Charging Voltage for Ar-Ne-Xe Mixture in 12-cm-Gain-Length Laser

510-TORR Ar-Ne-Xe

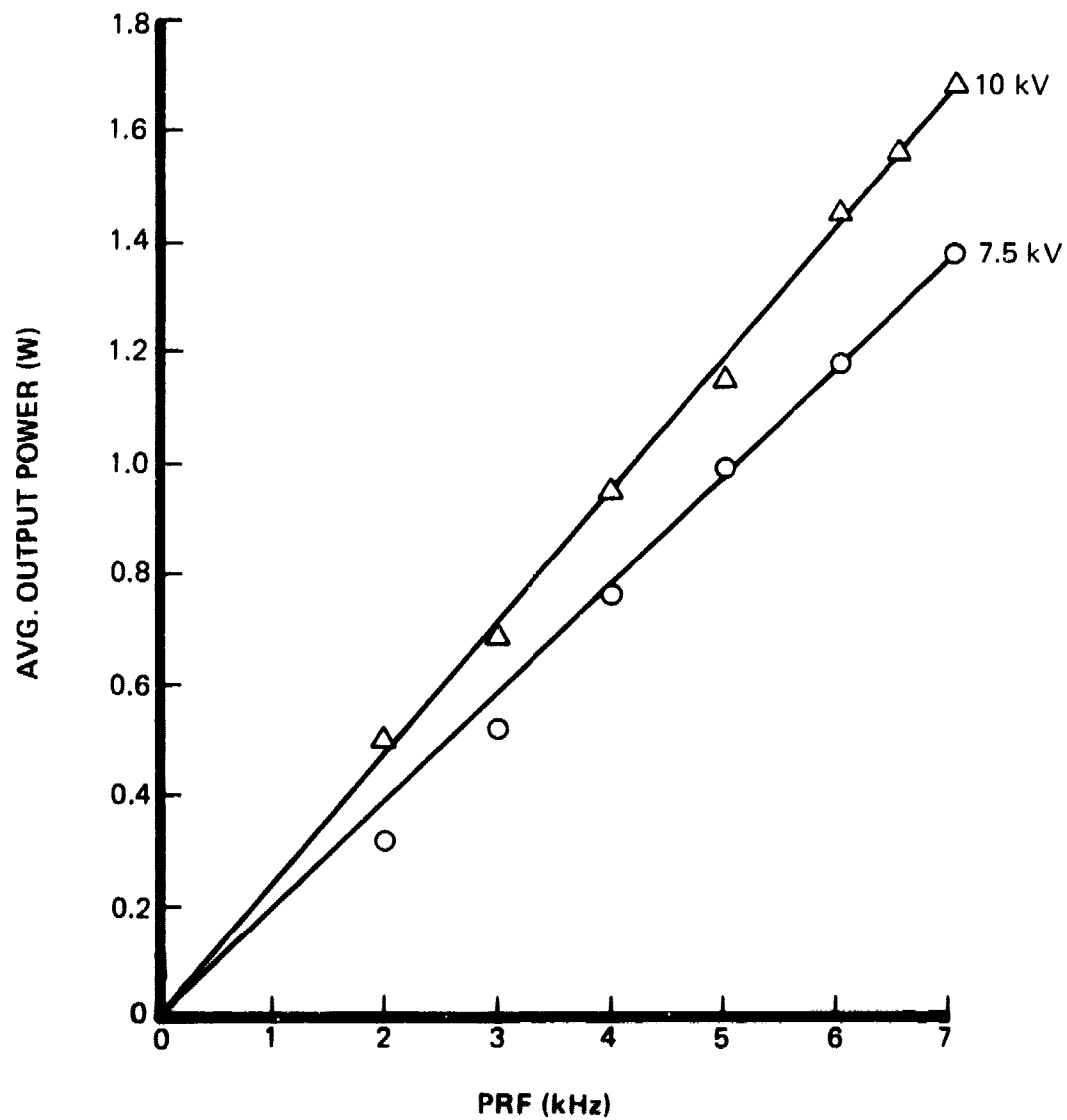


Figure 48. Dependence of Average Laser Output Power upon PRF for Ar-Ne-Xe Mixture in 12-cm-Gain-Length Laser

510-TORR Ar-Ne-Xe  
PRF: 5 kHz  
CHARGING VOLTAGE: 8.2 kV

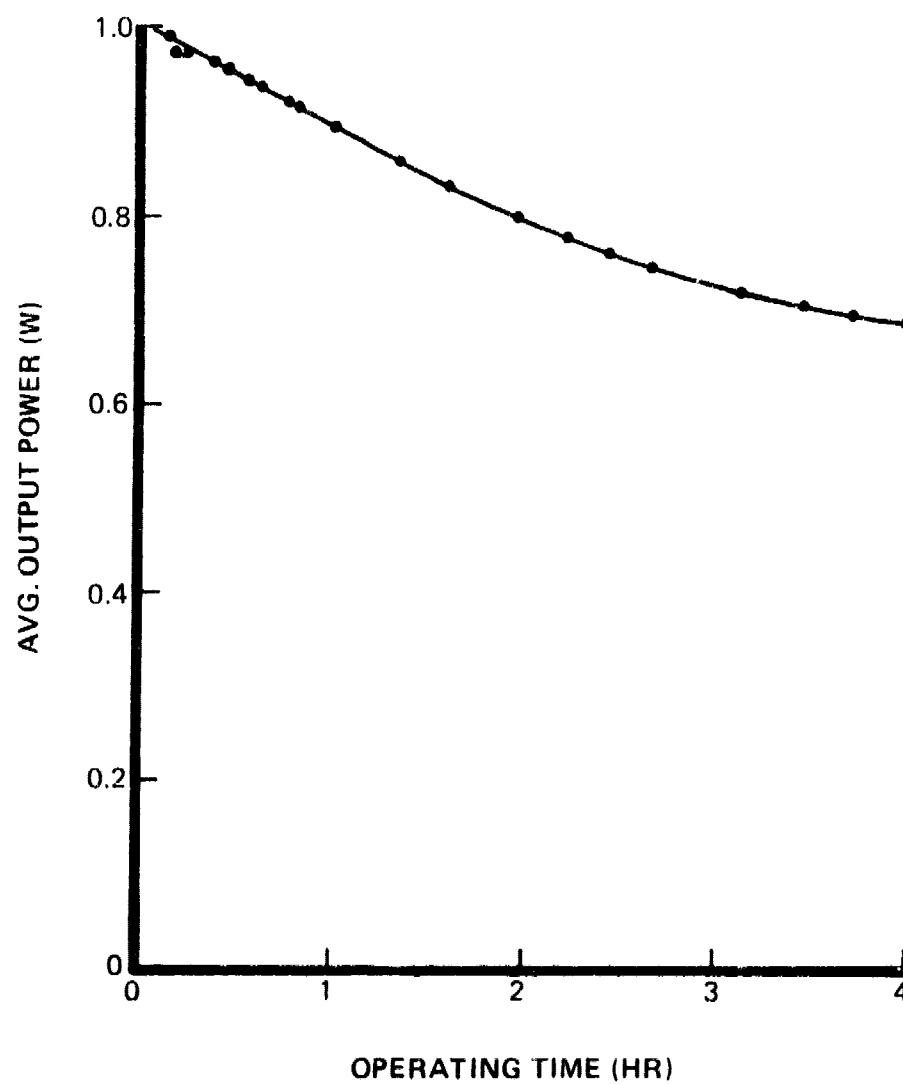


Figure 49. Dependence of Average Laser Output Power upon Continuous Operating Time for Ar-Ne-Xe Mixture in 12-cm-Gain-Length Laser

not permit an investigation of the reason for this decrease in the Ar-Xe laser output, which is in contrast to the nearly constant output from He-Xe over the same time interval. The greater sputtering rate of Ar, as compared to He, may result in the rapid evolution of impurity gases or Xe gas cleanup at the Al cathode. The former is more probable since gas pressure increased and discharge uniformity decreased with time of operation.

Lasing in the visible region of the spectrum has been reported for many ionic Xe wavelengths,<sup>92</sup> a number of which have been observed in spontaneous emission from the CCRGEDL. This provided the stimulus for a brief search for visible Xe laser lines after the evaluation of CCRGEDL performance with Xe-buffer gas mixtures had been completed. The infrared laser mirrors were replaced with a 2-m broadband reflector having 99.9% reflectance from 4500 to 6500 Å and a broadband transmitting flat having 1-5% transmission from 4500 to 6500 Å. Since internal mirrors were used, the unattenuated spontaneous emission from the discharge could not be observed. The spectrum of the emission from the optical cavity was measured with the cavity mirrors first aligned and then misaligned. For a 14-kV, 4-kHz discharge in 1000 Torr of He-Xe (1000:1), the intensity ratio of emission from the tuned cavity to that from the detuned cavity varied from 2 to 28, depending on wavelength. The apparent amplification in the tuned cavity can be attributed to cumulative transmission over many round trips of a light pulse trapped in the partially transmitting optical cavity. There was, therefore, no clear-cut indication of lasing.

#### 2.3.2 Performance of 25-cm-Gain-Length Laser with Xe-Buffer-Gas Mixtures

A parametric evaluation of the performance of the CCRGEDL in the 25-cm-gain-length configuration (as shown in Figure 50) was made for He-Xe and Ar-Xe mixtures. The 68-cm optical cavity (internal mirrors) was formed by a 2-m reflector and a Ge (for He-Xe) or Si (for Ar-Xe) output flat. A CaF<sub>2</sub> lens was used to focus the laser output on the entrance slit of the Jarrell-Ash 0.5-m Ebert scanning spectrometer equipped with an infrared grating blazed at 5 μ. A liquid-nitrogen-cooled PbSnTe detector was used at the exit slit.



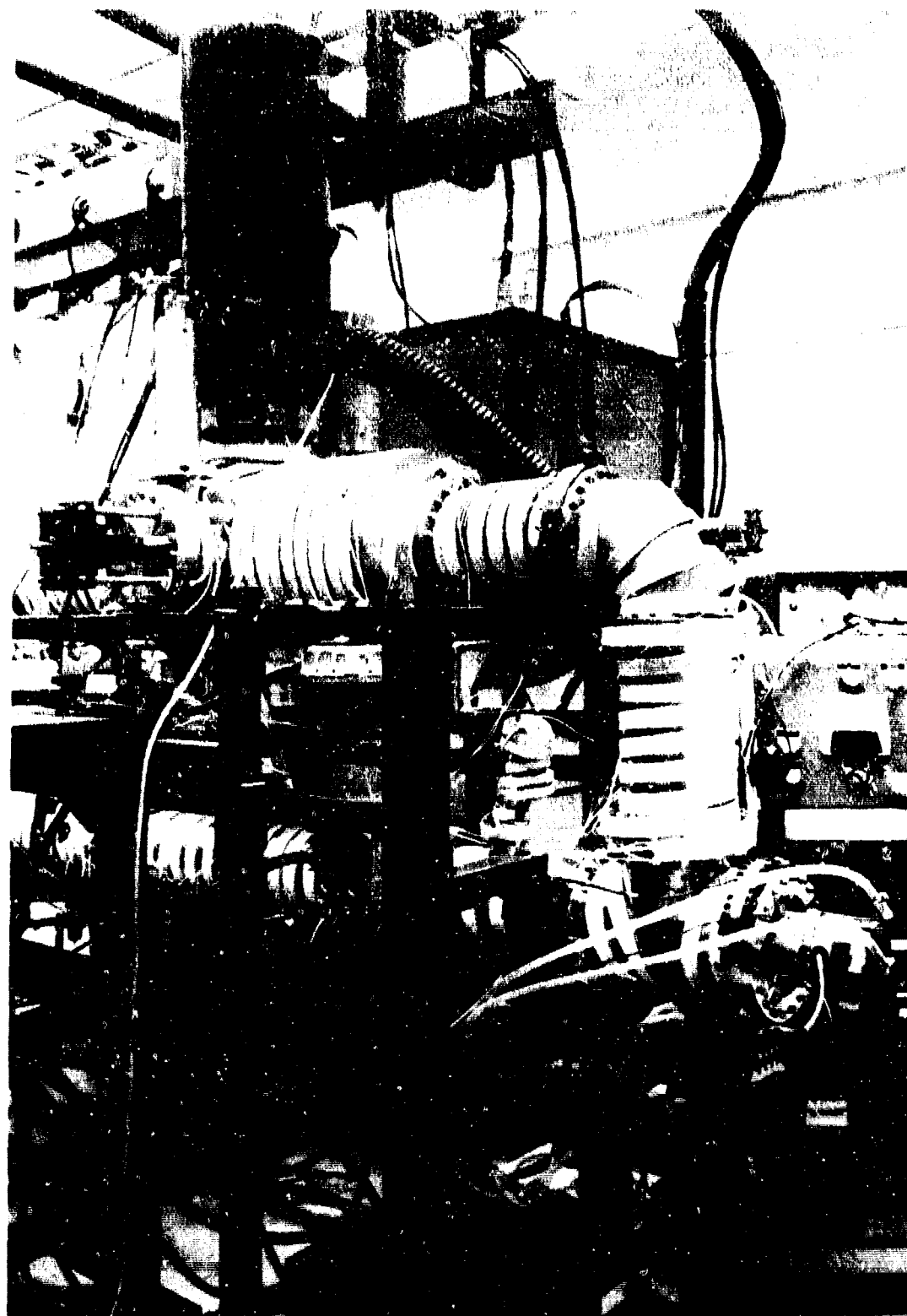


Figure 50. Photograph of CORGEDL with 25-cm-Gain-Length Configuration

Typical current and voltage pulses (redrawn from oscillograms) at 6-kV charging voltage for He-Xe and Ar-Xe mixtures are shown at the top of Figure 51 (time scale of 50 ns/cm). The instantaneous power into the discharge was calculated from these curves and is plotted below them. Integration over the positive-power peak yields 25 mJ deposited in He-Xe and 28.2 mJ deposited in Ar-Xe. The energy deposition in He-Xe is 70% and in Ar-Xe is 78% of the energy stored in the 2-nF capacitor. Since a slight error in phase between current and voltage will result in a large error in power, the apparently excellent energy transfer is questionable.

Plots of discharge-breakdown voltage and peak current as a function of charging voltage for He-Xe and Ar-Xe mixtures are shown in Figures 52 and 53, respectively. The data were obtained at a PRF of 5 kHz. A maximum charging voltage of 6 kV was achieved with Ar-Xe before arcing occurred. In the case of He-Xe, corona on the high-voltage high-vacuum feedthrough limited the charging voltage to 14 kV at pressures below ~ 400 Torr. The breakdown voltage tended to saturate with increasing charging voltage at a level which increased with increasing pressure. The peak discharge current, however, increased approximately linearly with charging voltage. Higher peak currents were obtained as the pressure was decreased, and there was an optimum Xe partial pressure at which maximum current occurred.

Under appropriate excitation conditions, simultaneous lasing was observed for the seven lines listed in Table 5 for He-Xe mixtures and for the eight lines listed in Table 6 for Ar-Xe mixtures. All of the transitions obey the selection rules of  $J_c - \ell$  coupling.

The laser-output pulses from a 200:1 mixture of Ar-Xe at a pressure of 200 Torr are shown in Figure 54. The discharge-current pulse at the upper left is ~ 100 ns wide. The seven lines lase simultaneously, and all are 5d-6p transitions. Lasing at each wavelength begins during the current pulse and lasts microseconds into the afterglow.

Laser-output pulses from a 200:1 mixture of He-Xe at a pressure of 200 Torr are shown in Figure 55. Lasing is simultaneous on these 5d-6p (2.03 and

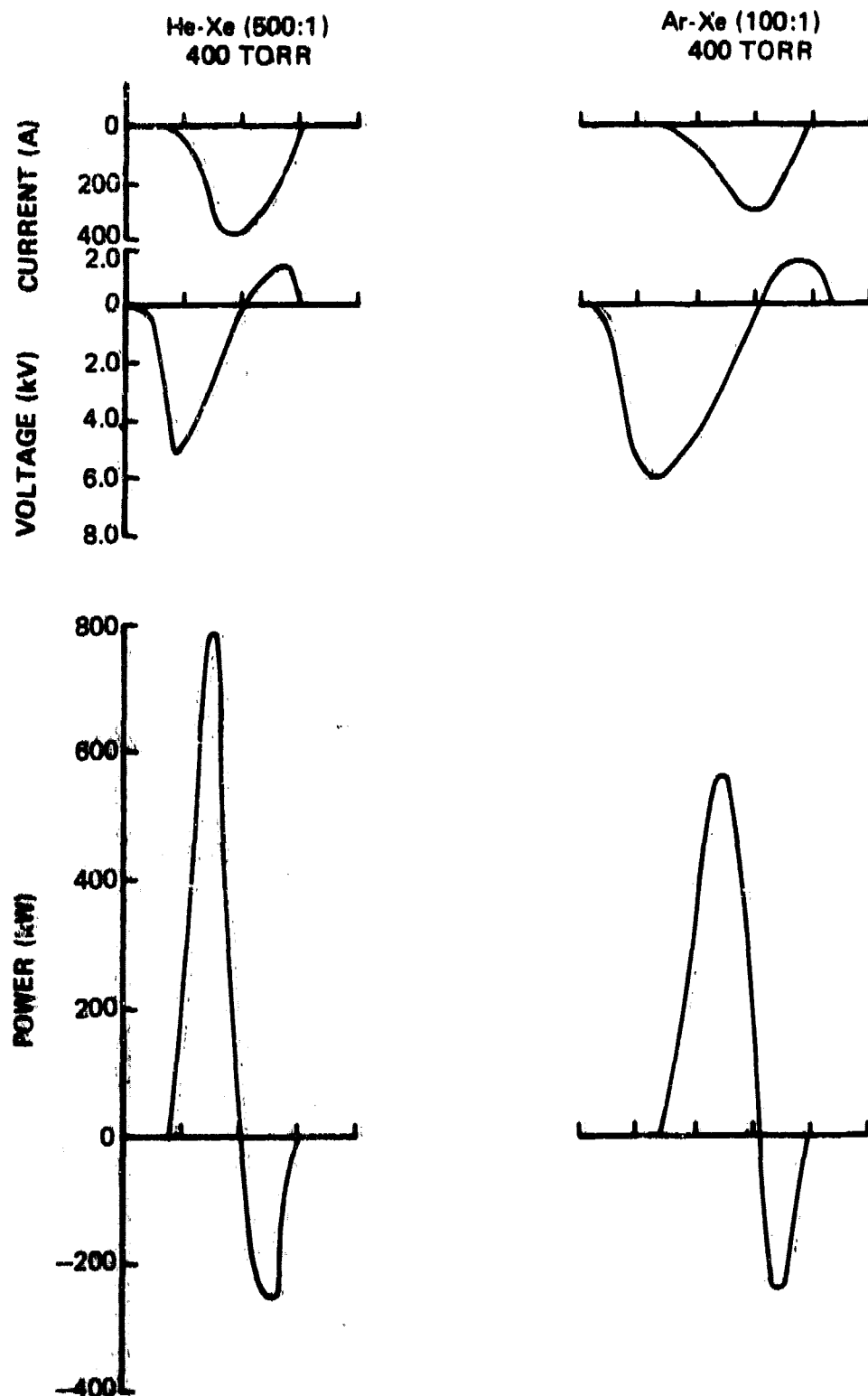


Figure 51. Discharge Current, Voltage, and Power Pulse Shapes for He-Xe and Ar-Xe Mixtures in 25-cm-Gain-Length Laser

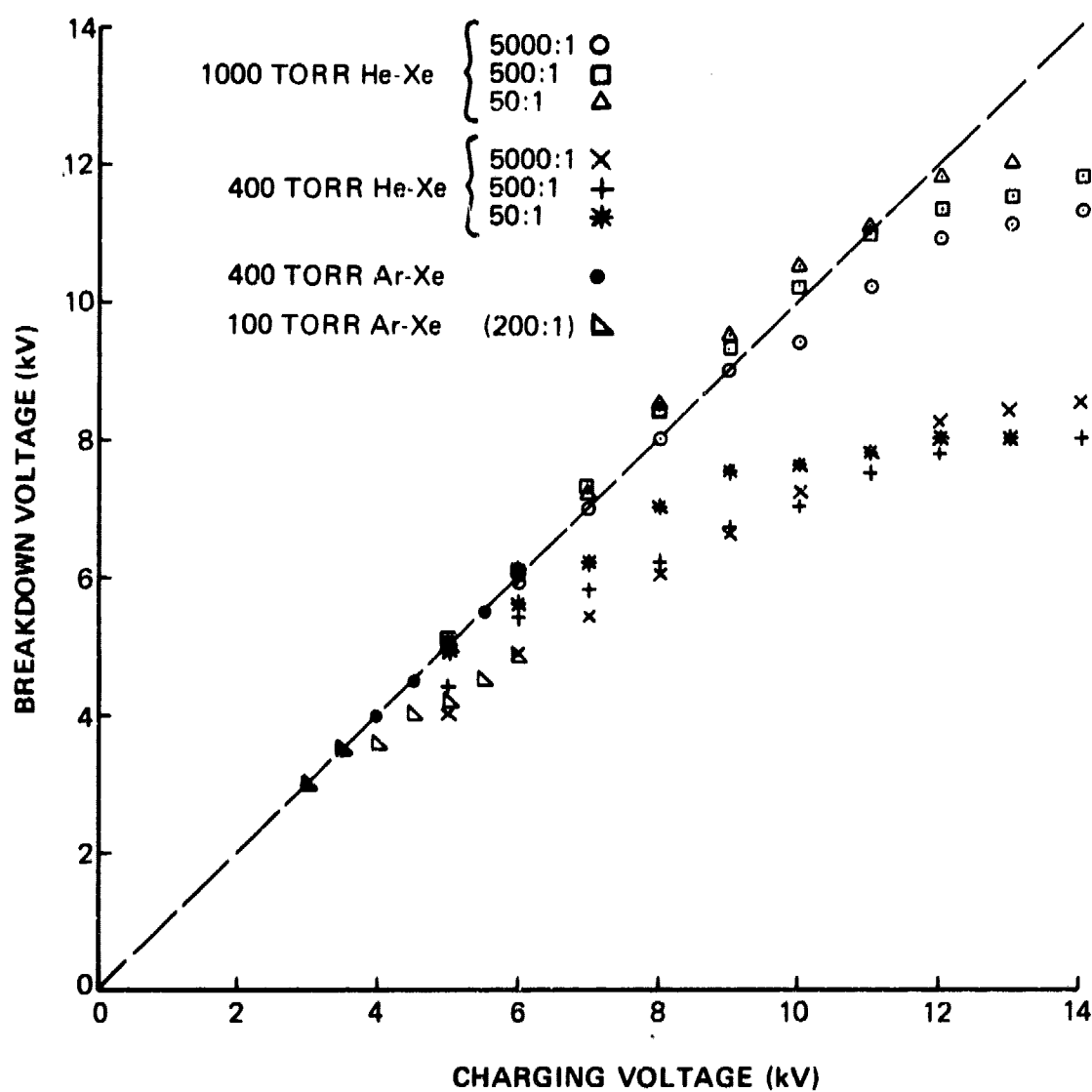


Figure 52. Dependence of Discharge Breakdown Voltage upon Charging Voltage for He-Xe and Ar-Xe Mixtures in 25-cm-Gain-Length Laser

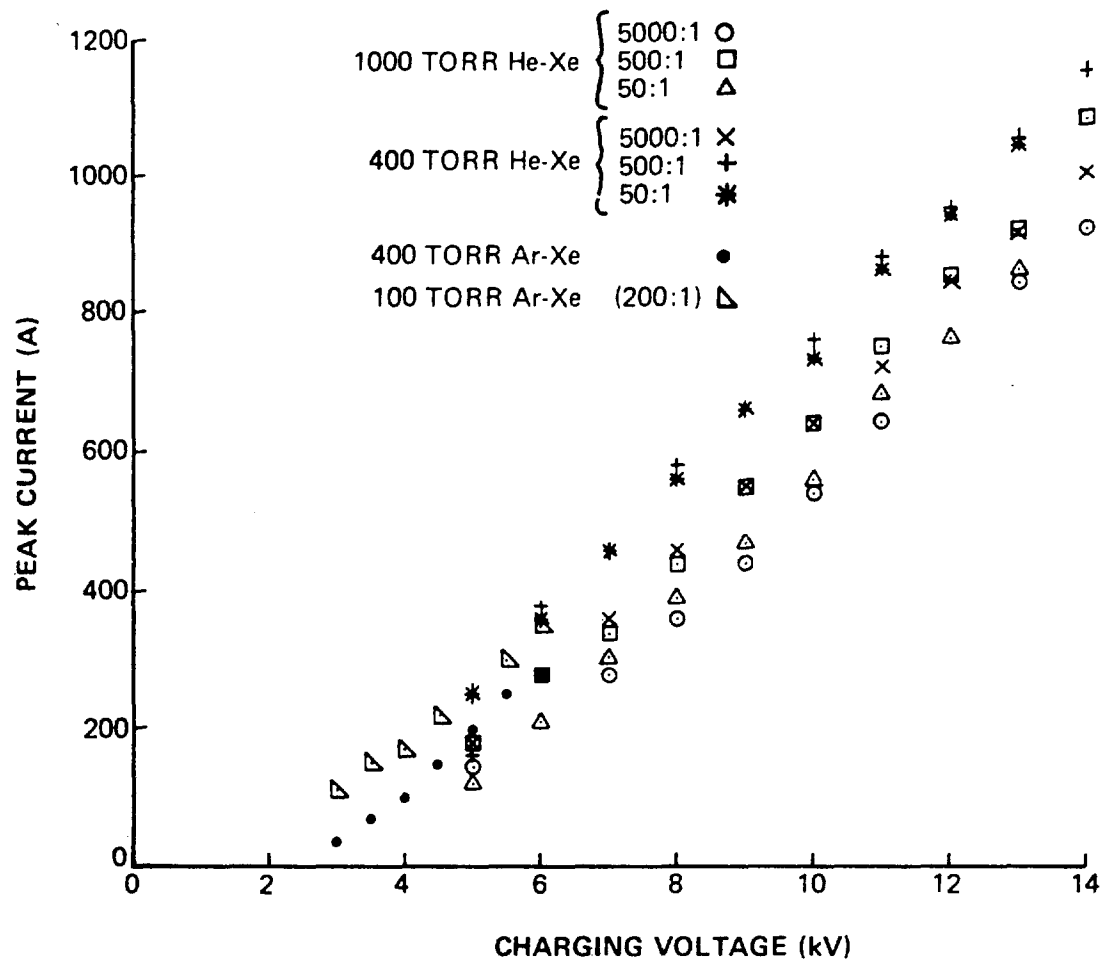


Figure 53. Dependence of Peak Discharge Current upon Charging Voltage for He-Xe and Ar-Xe Mixtures in 25-cm-Gain-Length Laser

TABLE 5  
Xe-I LASER LINES OBSERVED IN He-Xe DISCHARGE  
(25-cm Gain Length)

Calculated	$\lambda_{\text{vac}}$ ( $\mu$ )	Measured	Transition (Racah Notation)
2.0268		2.0278	$5d[3-2]_1^0 - 6p[3/2]_1$
2.6518		2.6524	$5d[3/2]_1^0 - 6p[1/2]_0$
3.0484		3.0488	$7p[5/2]_3 - 7s[3/2]_2^0 *$
3.4344		3.4352	$7p[5/2]_2 - 7s[3/2]_1^0$
3.6518		3.6522	$7p[1/2]_1 - 7s[3/2]_2^0$
3.8697		3.8700	$5d'[5/2]_3^0 - 6p'[3/2]_2$
4.0207		4.0217	$7p[1/2]_1 - 7s[3/2]_1^0 *$

\* Previously unreported laser transitions

TABLE 6

Ke-I LASER LINES OBSERVED IN Ar-Xe DISCHARGE  
(25-cm Gain Length)

Calculated	$\lambda_{\text{vac}}$ ( $\mu$ )	Measured	Transition
			(Racah Notation)
1.7330		1.7330	$5d[3/2]_1^0 - 6p[5/2]_2$
2.0268		2.0276	$5d[3/2]_1^0 - 6p[3/2]_1$
2.4831		2.4839	$5d[5/2]_3^0 - 6p[5/2]_3$
2.6276		2.6282	$5d[5/2]_2^0 - 6p[5/2]_2$
2.6518		2.6525	$5d[3/2]_1^0 - 6p[1/2]_0$
3.1078		3.1084	$5d[5/2]_3^0 - 6p[3/2]_2$
3.3676		3.3678	$5d[5/2]_2^0 - 6p[3/2]_1$
5.5754		5.5755	$5d[7/2]_4^0 - 6p[5/2]_3$

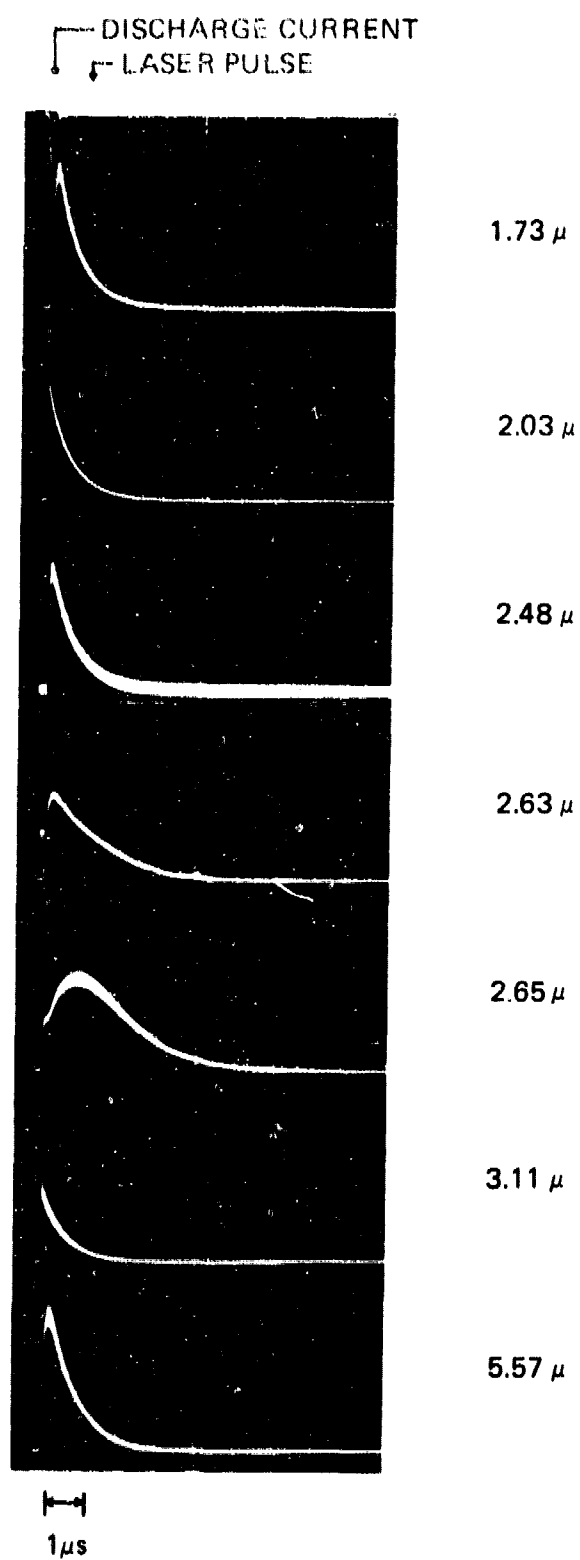


Figure 54. Oscillograms of Laser Pulses Obtained at a Pressure of 200 Torr Ar-Xe (200:1) in 25-cm-Gain-Length Laser



DISCHARGE CURRENT  
LASER PULSE

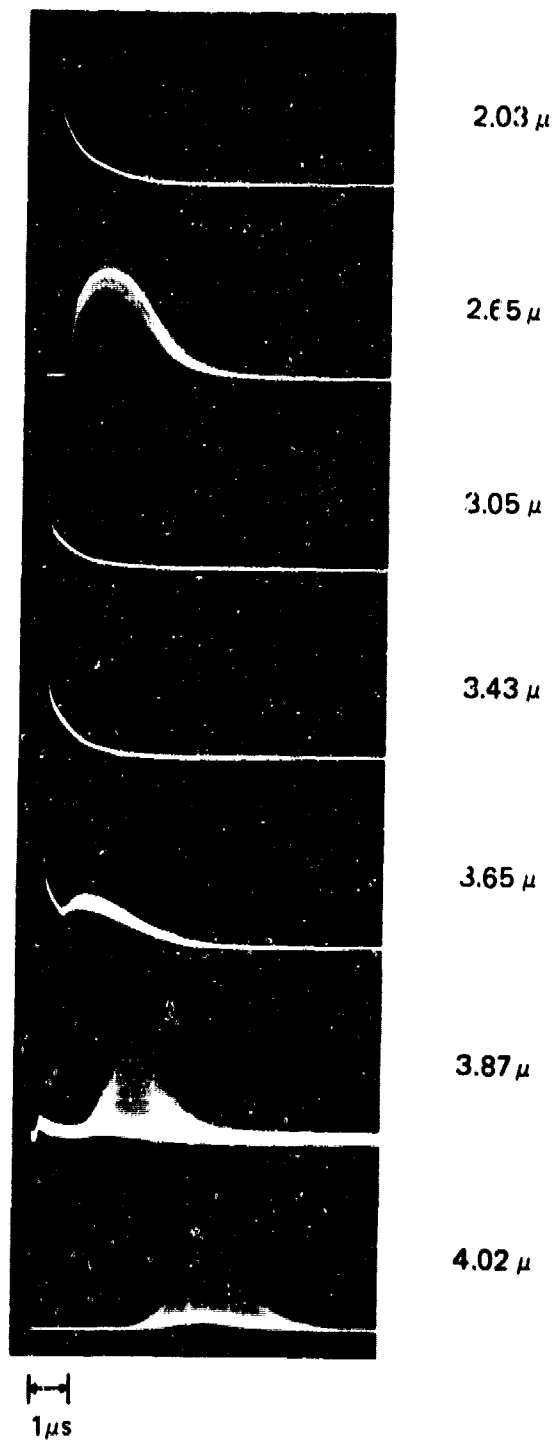


Figure 55. Oscillograms of Laser Pulses Obtained at a Pressure of 200 Torr He-Xe (200:1) in 25-cm-Gain-Length Laser

2.65  $\mu$ ), 7p-7s (3.05, 3.43, 3.65, and 4.02  $\mu$ ), and 5d'-6p' (3.87  $\mu$ ) transitions. In contrast with the Ar-Xe laser pulses, afterglow lasing is accentuated in He-Xe, particularly at 2.65, 3.65, 3.87, and 4.02  $\mu$ . Lasing at 3.05 and 4.02  $\mu$  is unique to this laser; also, this is the first observation of lasing at 3.87  $\mu$  at high pressure.

Peak values of the directly excited and afterglow pulses at the various wavelengths are plotted as a function of total pressure for He-Xe mixtures in Figures 56-62 and for Ar-Xe mixtures in Figures 63-65. These data were obtained under the following conditions: He-Xe - 12-kV charging voltage and 5-kHz repetition rate; Ar-Xe - 5-kV charging voltage and 5-kHz repetition rate. As can be seen from Figures 56-62, afterglow lasing in He-Xe is enhanced as the partial pressure of Xe is decreased.

Parametric measurements of multi-line, multi-mode average laser-output power were made concurrent with the peak-laser-output measurements. Plots of average laser-output power as a function of repetition rate for Ar-Xe and He-Xe mixtures are shown in Figure 66. The Ar-Xe laser generated greater output power (2.3 W) at higher electrical efficiency (0.86%) than the He-Xe laser (0.46 W at 0.03% efficiency). The electrical efficiency was taken to be the ratio of average laser-output power to average energy-storage-capacitor output power.

The pressure dependence of the average laser-output power is shown in Figure 67 for He-Xe mixtures and in Figure 68 for Ar-Xe mixtures. The optimum pressure for maximum output power is in the 400-600 Torr region for He-Xe. Unfortunately, 400 Torr was the highest pressure for which a uniform glow could be obtained in Ar-Xe. However, it appears that 300-500 Torr may be an optimum range of pressure for Ar-Xe.

The pressure dependence of the average laser-output power at various charging voltages is shown in Figure 69 for He-Xe (200:1) and in Figure 70 for Ar-Xe (200:1). The approximately linear dependence of output power upon charging voltage at various mixture ratios is shown in Figure 71 for 400-Torr He-Xe and in Figure 72 for 400-Torr Ar-Xe. The charging-voltage dependence of

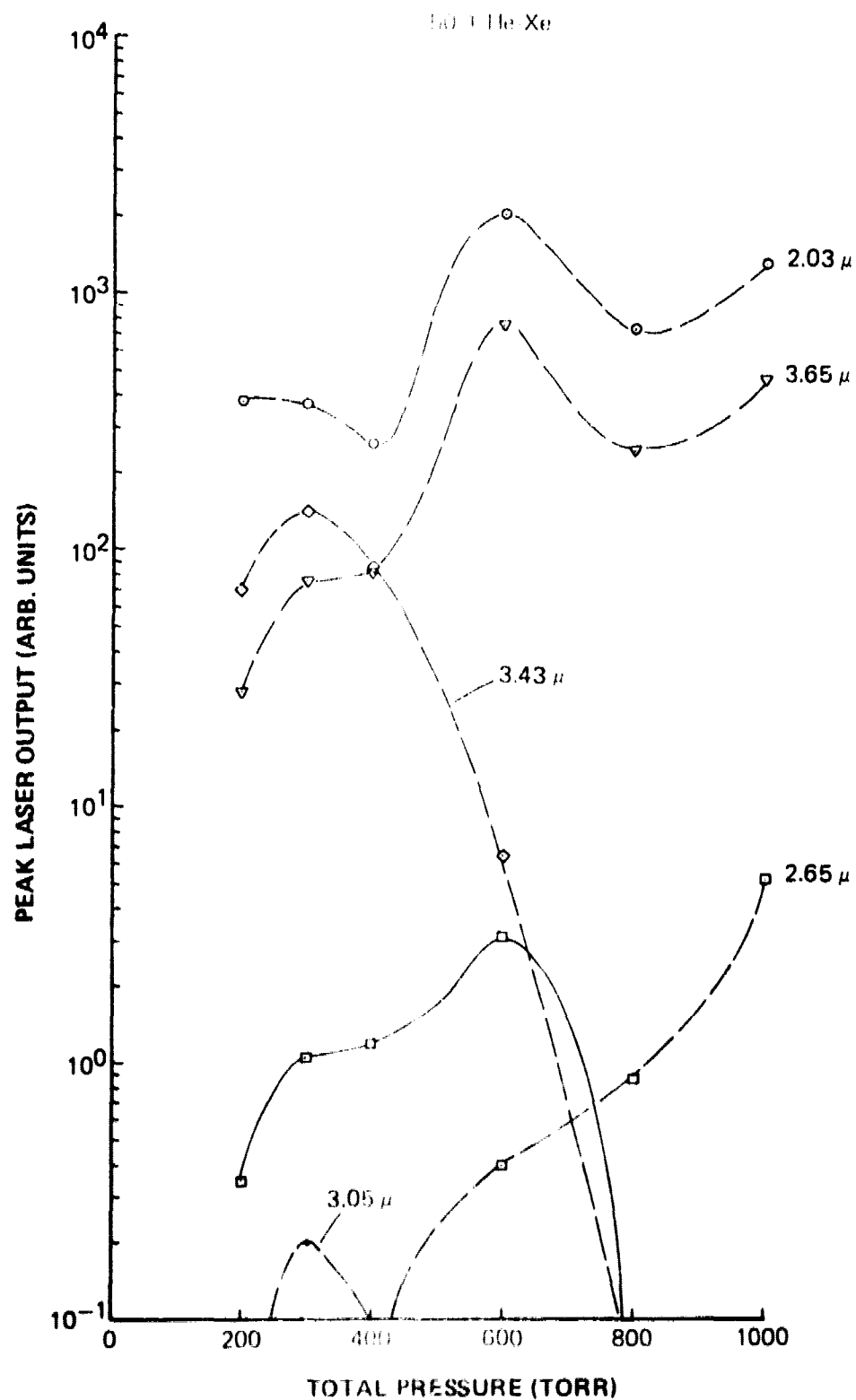


Figure 56. Pressure Dependence of Peak Output of Laser Pulses from He-Xe (50:1) 10.25-cm-gain-length Laser

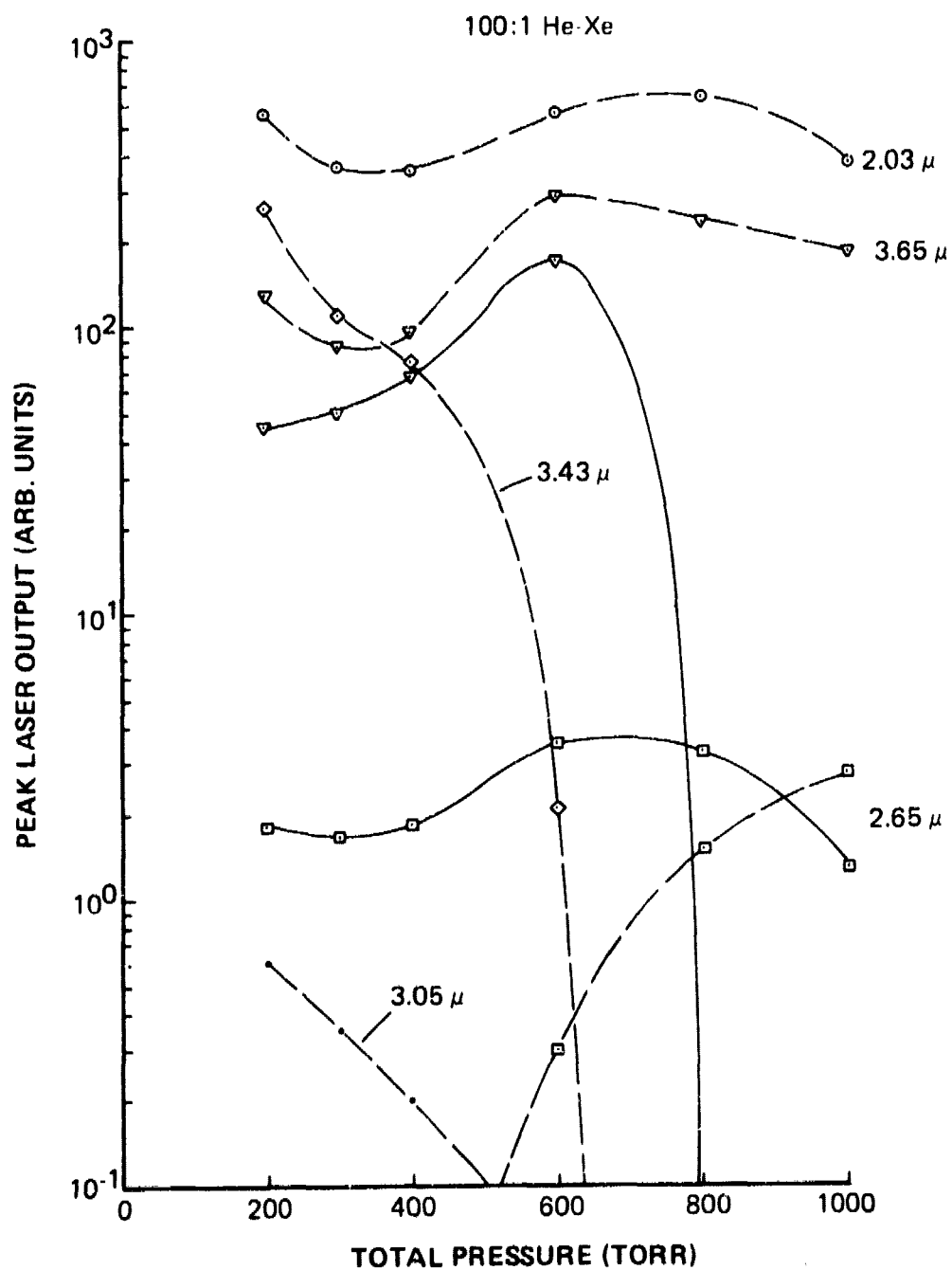


Figure 57. Pressure Dependence of Peak Output of Laser Pulses from He-Xe (100:1) in 25-cm-Gain-Length Laser

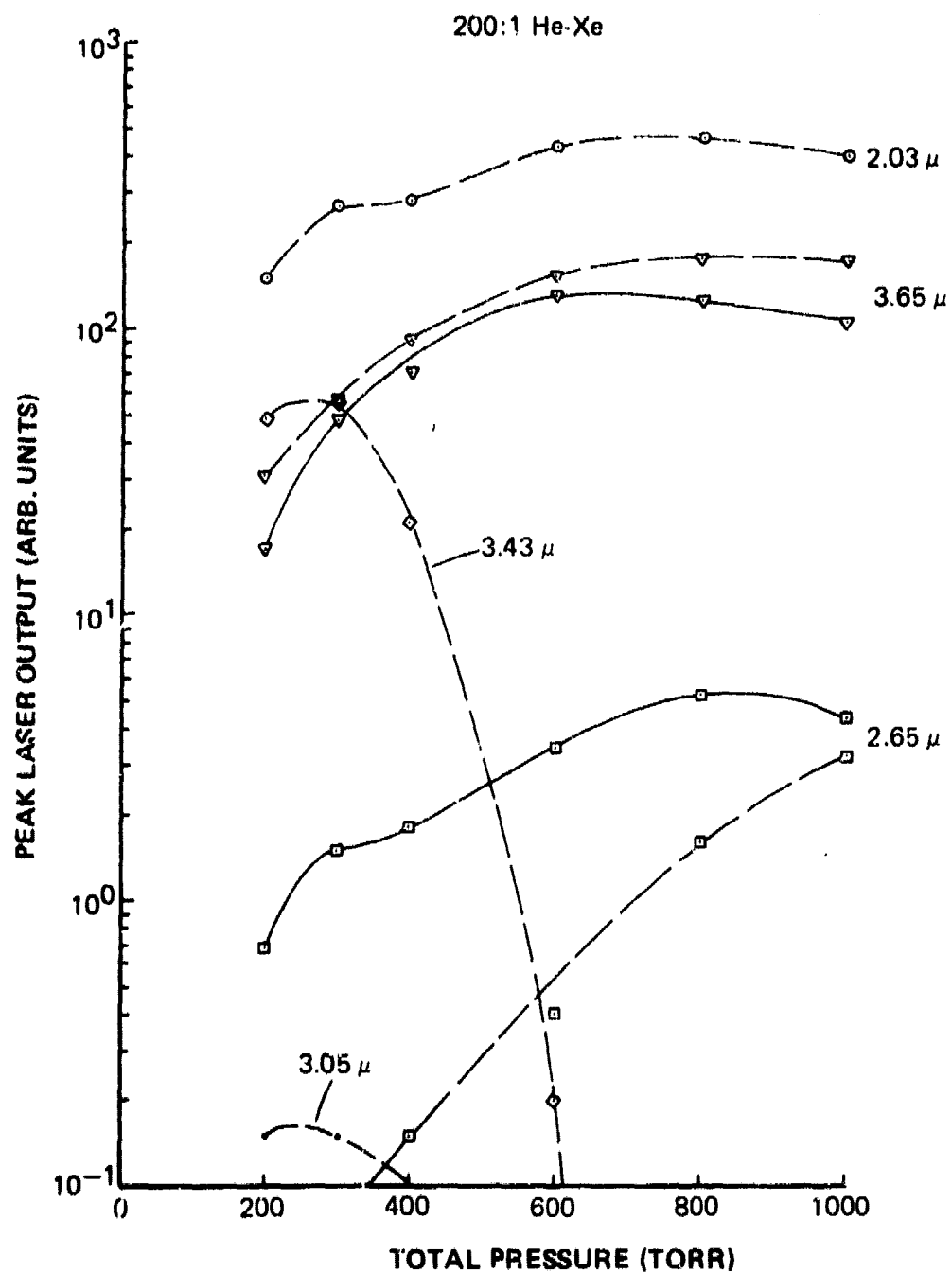


Figure 58. Pressure Dependence of Peak Output of Laser Pulses from He-Xe (200:1) in 25-cm-Gain-Length Laser

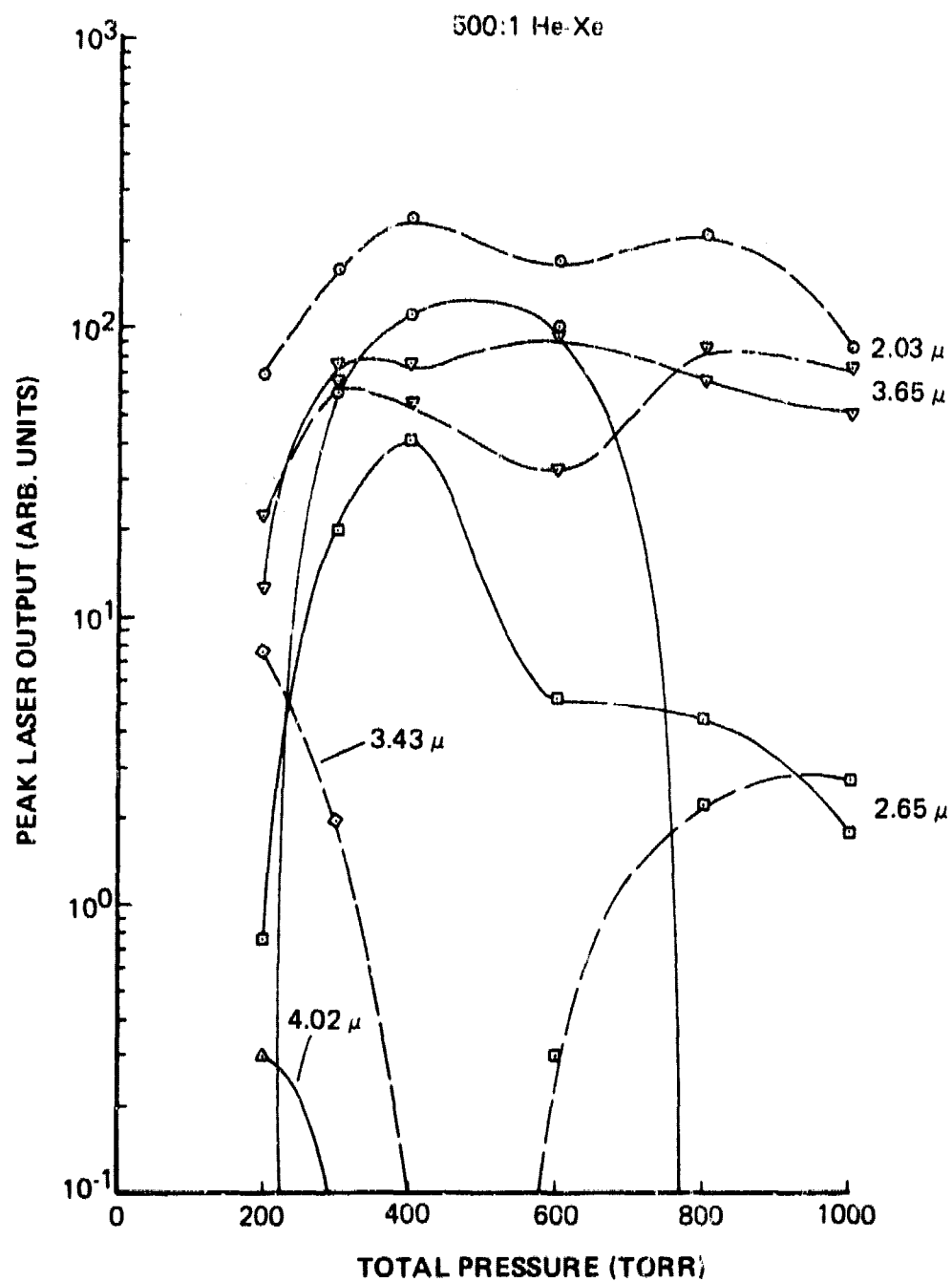


Figure 59. Pressure Dependence of Peak Output of Laser Pulses from He-Xe (500:1) in 25-cm-Gain-Length Laser

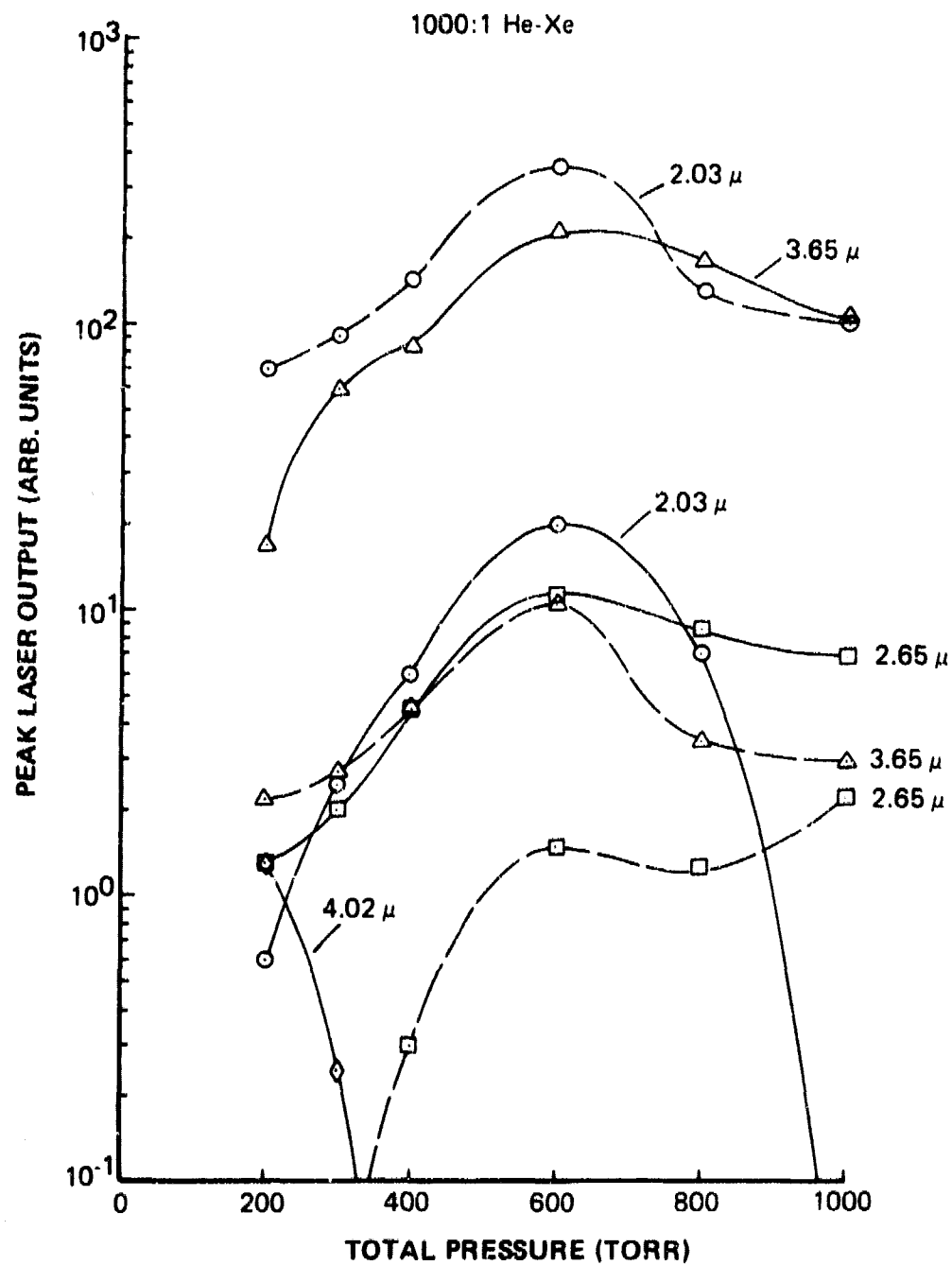


Figure 60. Pressure Dependence of Peak Output of Laser Pulses from He-Xe (1000:1) in 25-cm-Gain-Length Laser

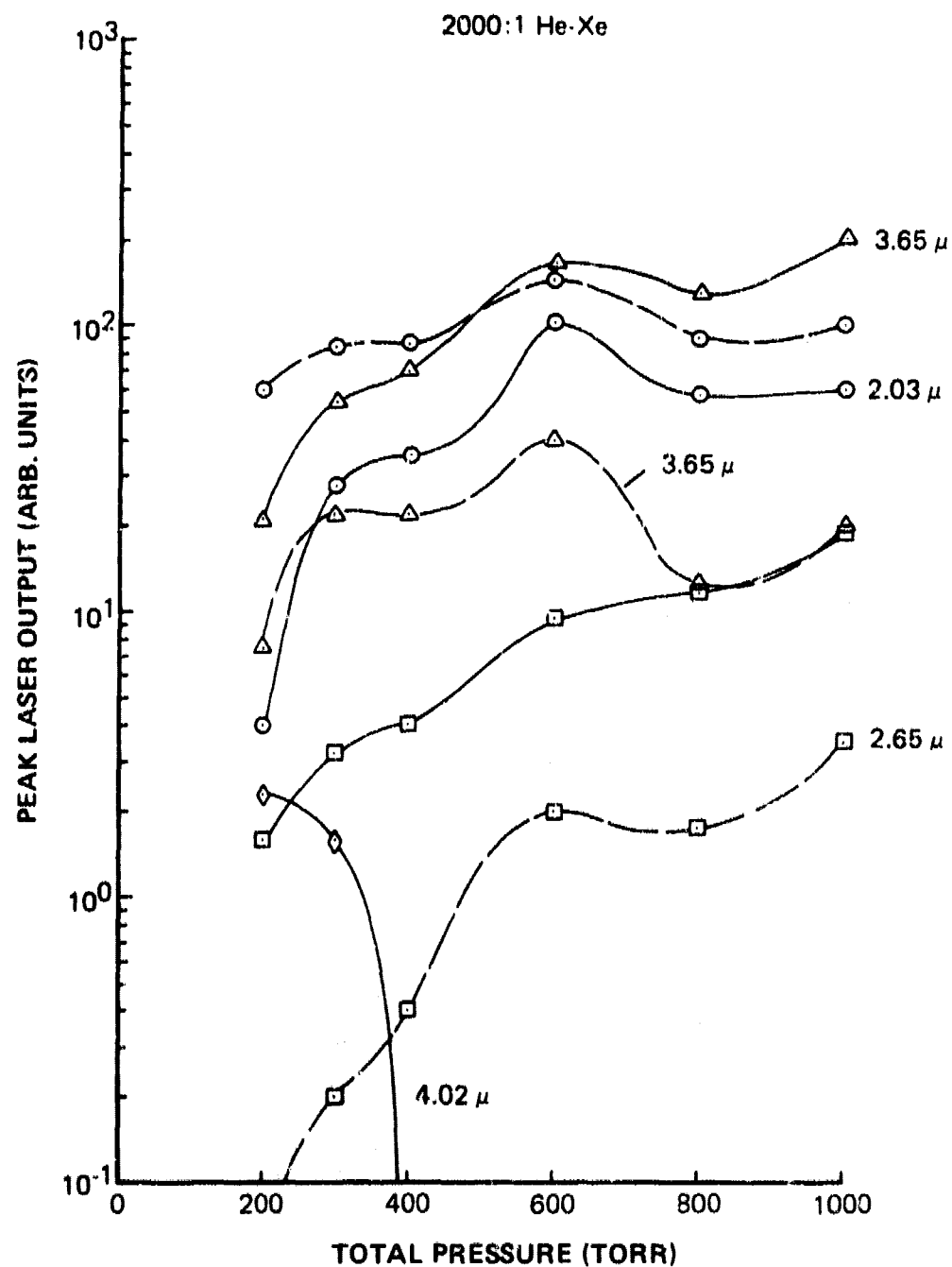


Figure 61. Pressure Dependence of Peak Output of Laser Pulses from He-Xe (2000:1) in 25-cm-Gain-Length Laser



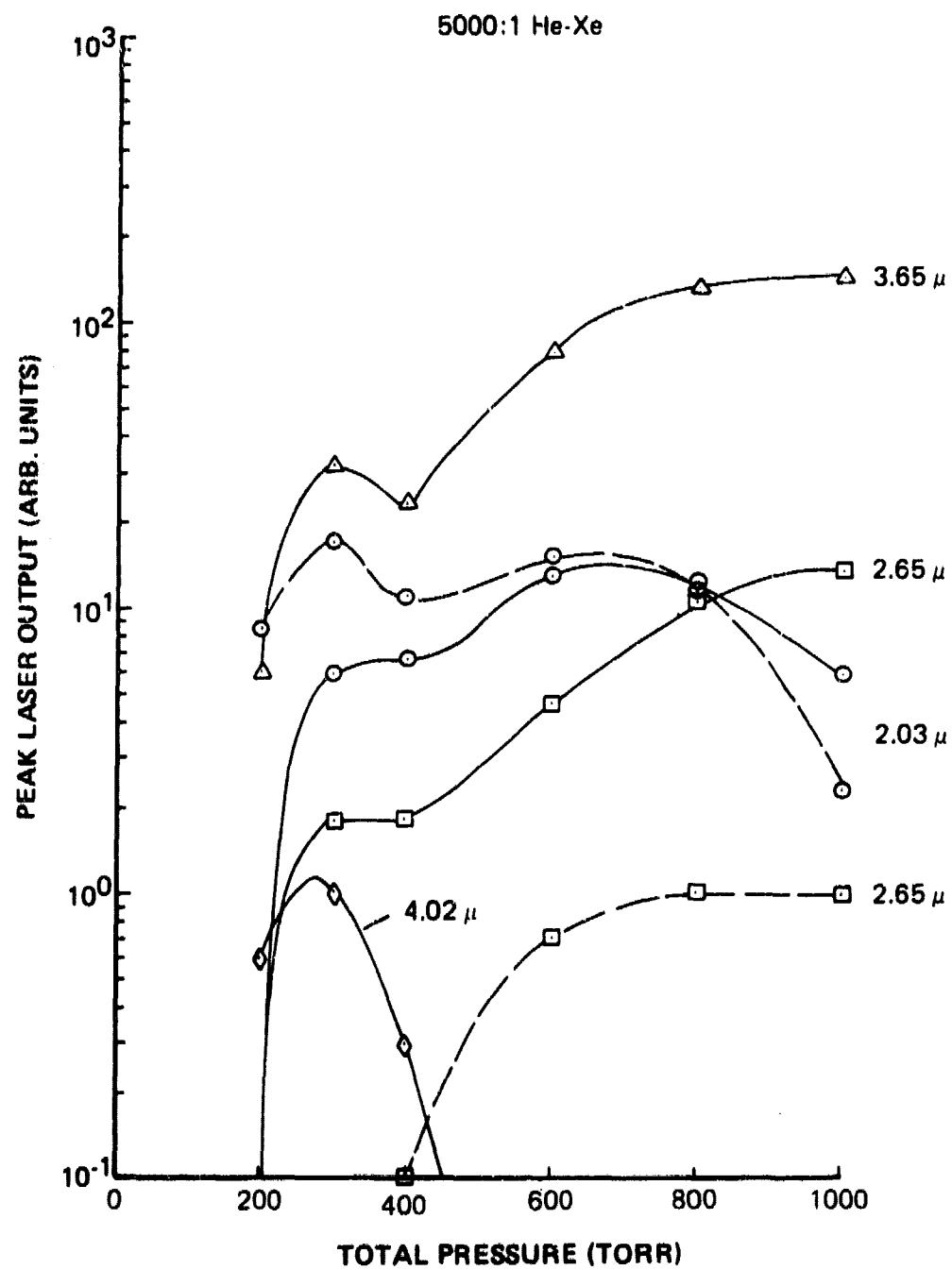


Figure 62. Pressure Dependence of Peak Output of Laser Pulses from He-Xe (5000:1) in 25-cm-Gain-Length Laser

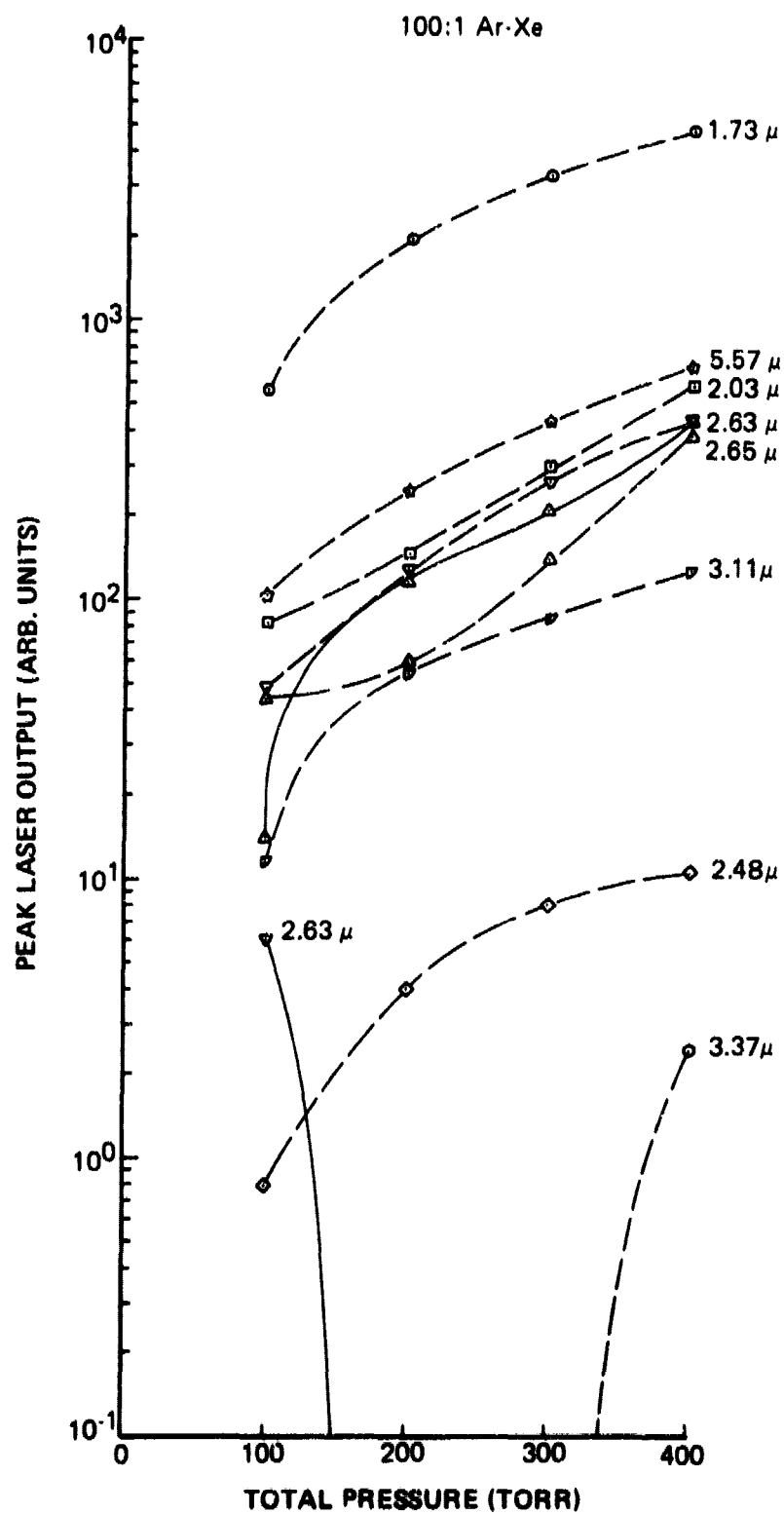


Figure 63. Pressure Dependence of Peak Output of Laser Pulses from Ar-Xe (100:1) in 25-cm-Gain-Length Laser

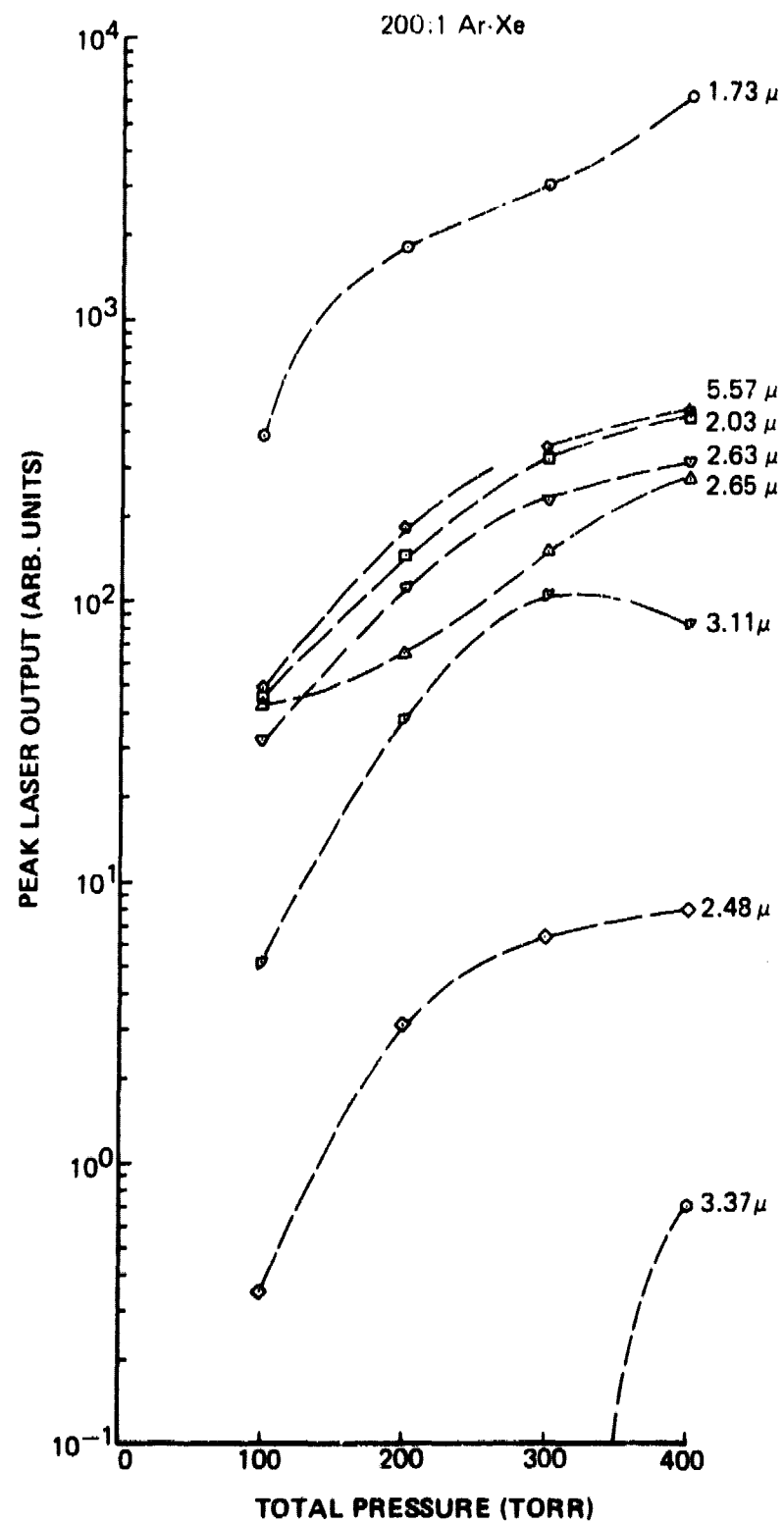


Figure 64. Pressure Dependence of Peak Output of Laser Pulses from Ar-Xe (200:1) in 25-cm-Gain-Length Laser

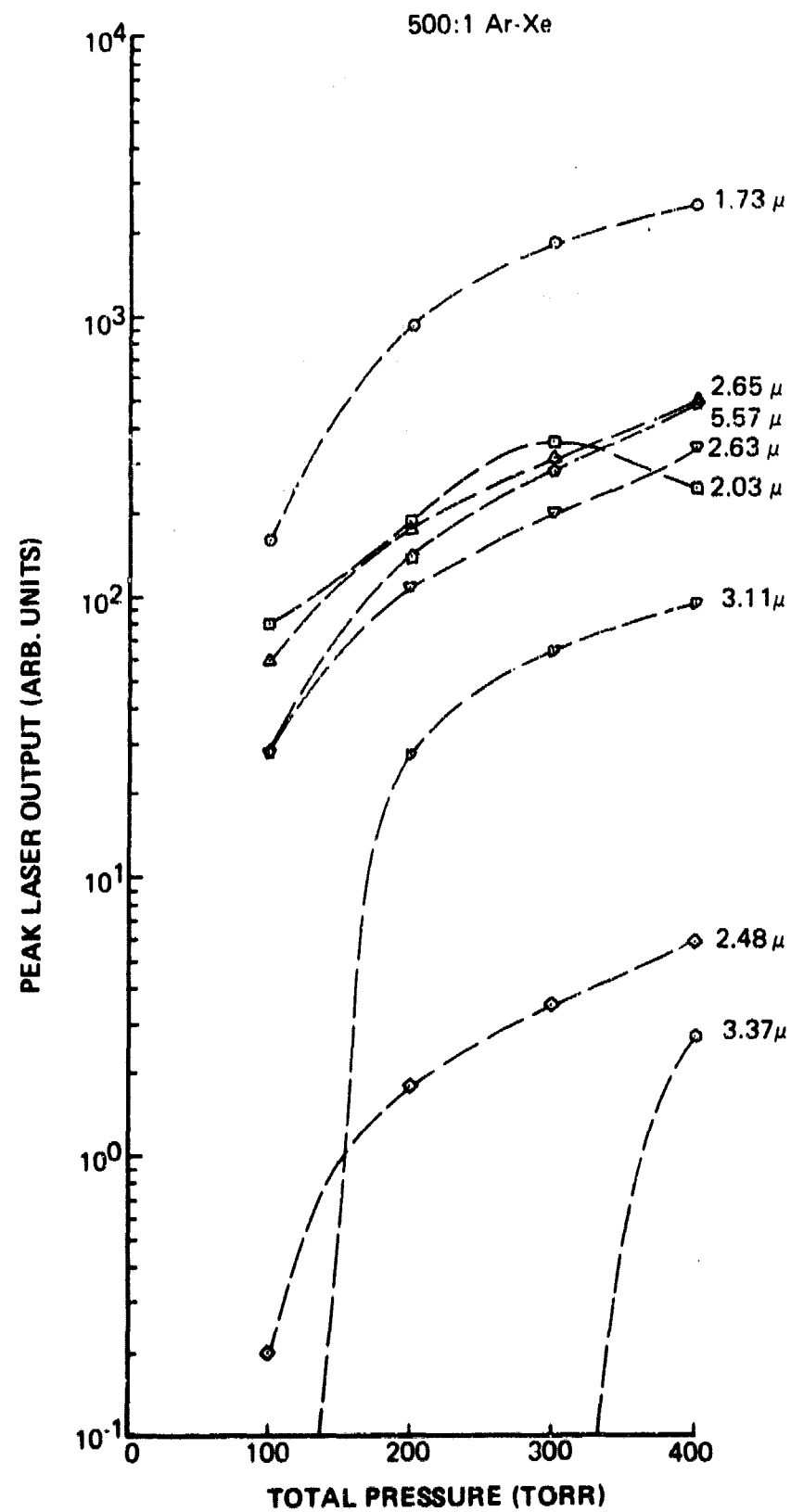


Figure 65. Pressure Dependence of Peak Output of Laser Pulses from Ar-Xe (500:1) in 25-cm-Gain-Length Laser

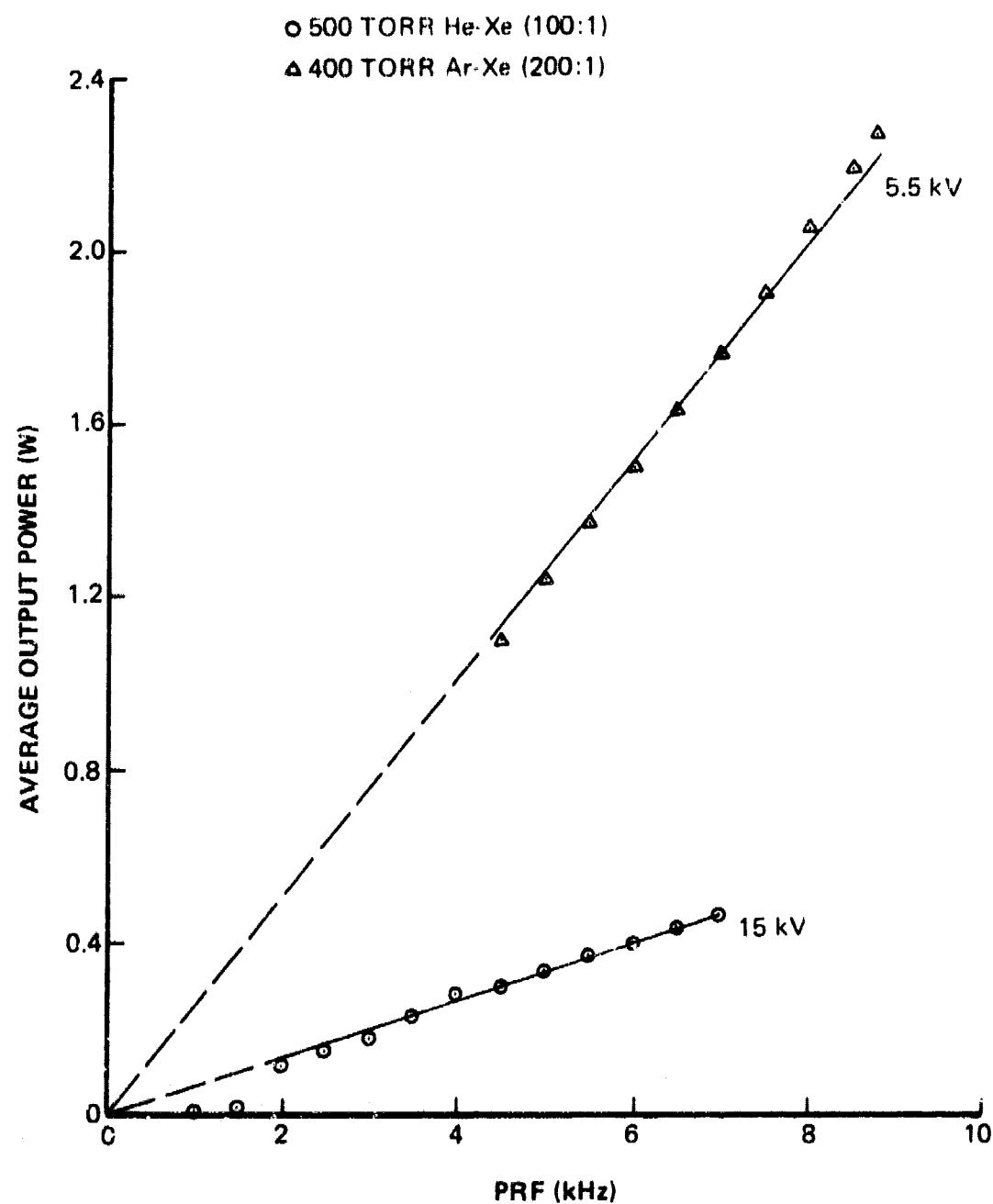


Figure 66. Dependence of Average Laser Output Power upon PRF for He-Xe and Ar-Xe Mixtures in 25-cm-Gain-Length Laser

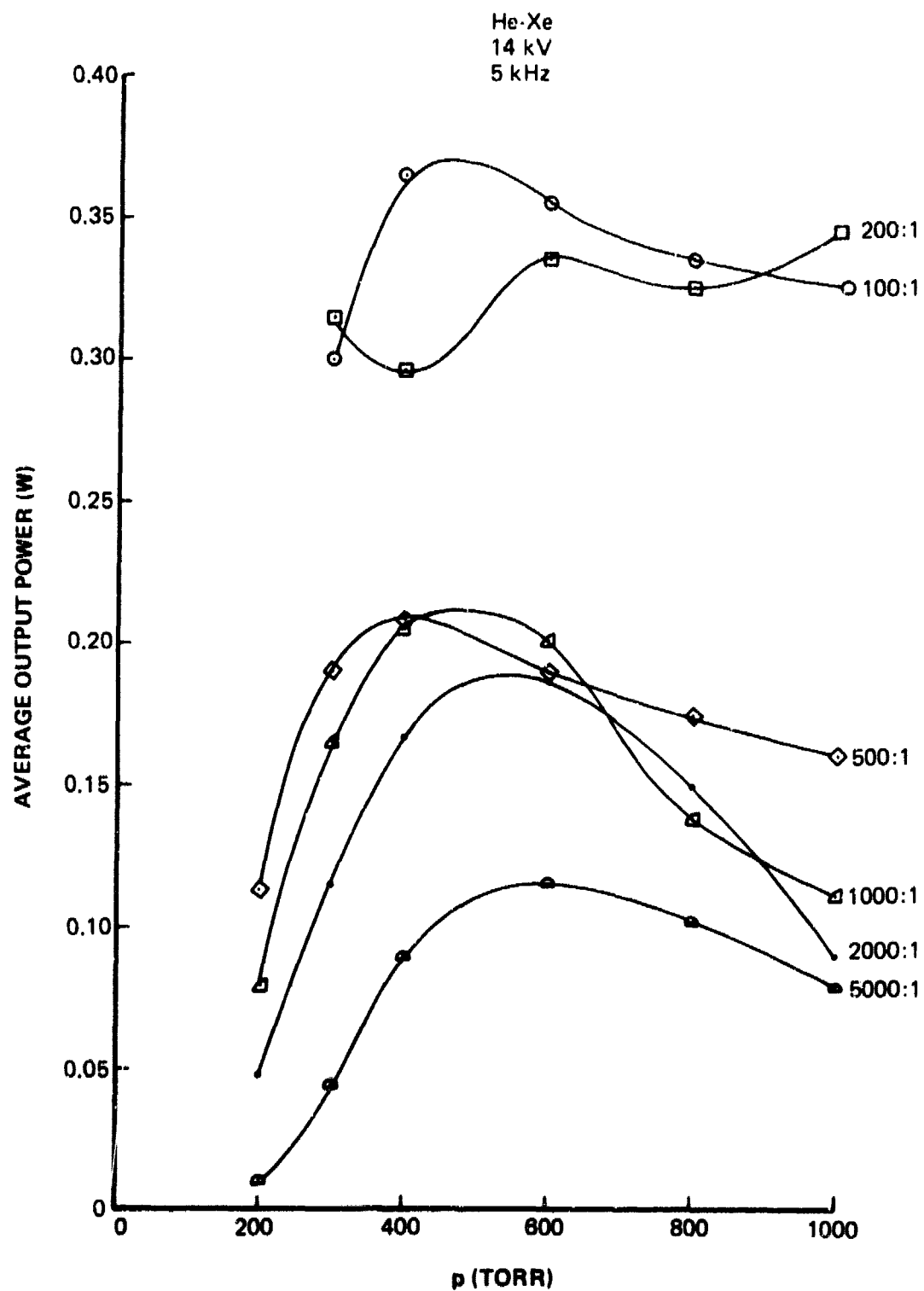


Figure 67. Pressure Dependence of Average Laser Output Power for He-Xe Mixtures in 25-cm-Gain-Length Laser

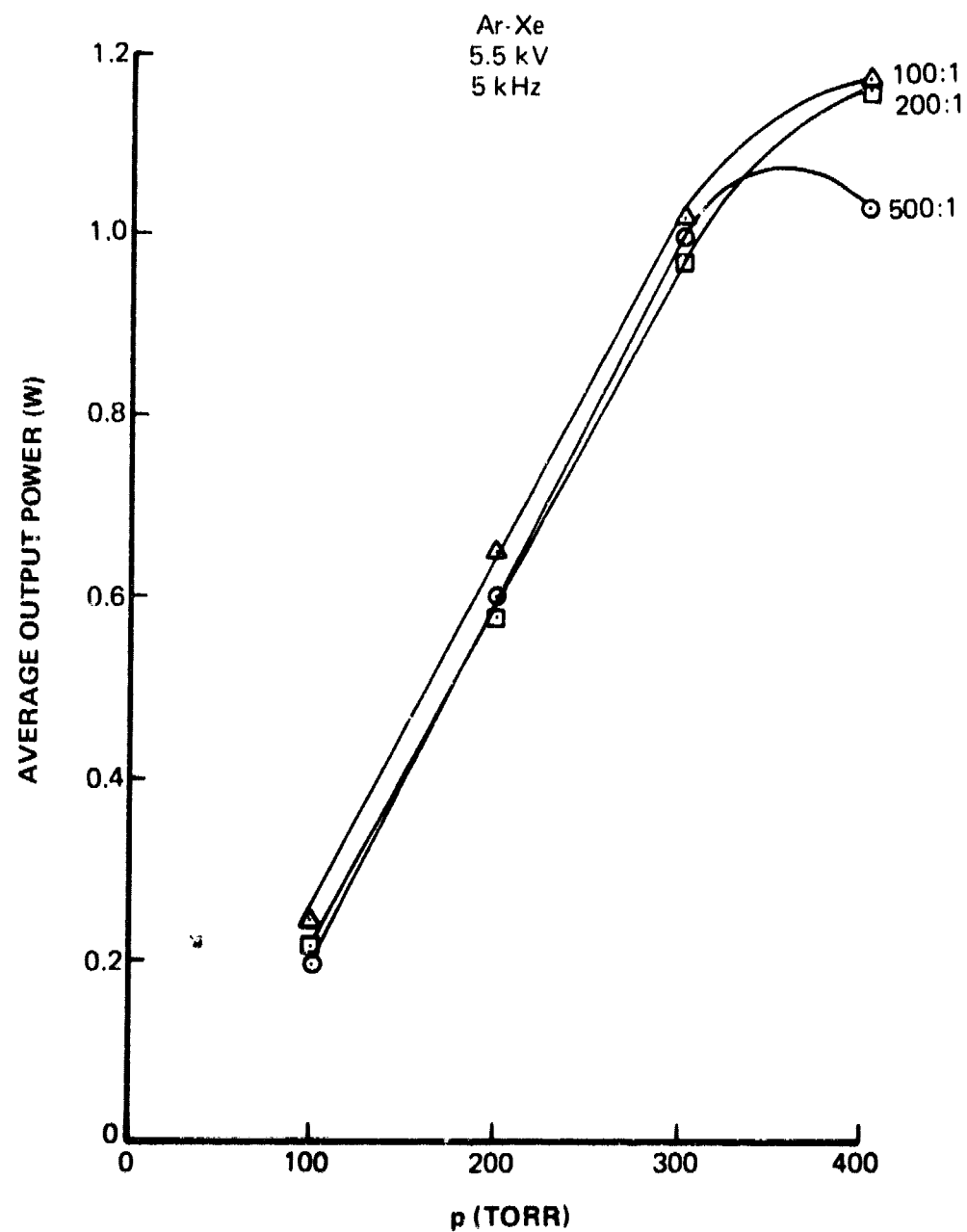


Figure 68. Pressure Dependence of Average Laser Output Power for Ar-Xe Mixtures in 25-cm-Gain-Length Laser

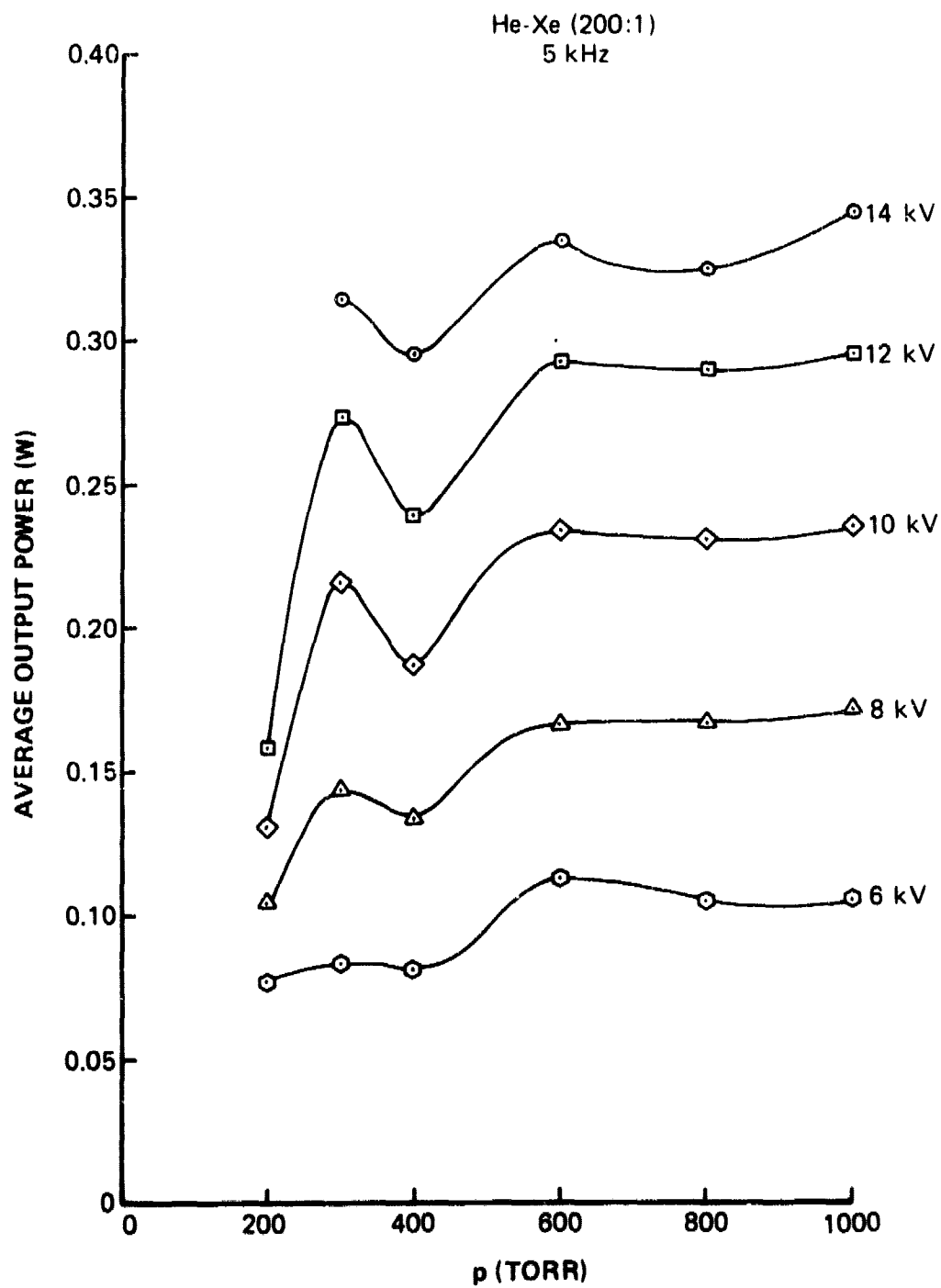


Figure 69. Pressure Dependence of Average Laser Output Power for He-Xe (200:1) at Various Charging Voltages in 25-cm-Gain-Length Laser



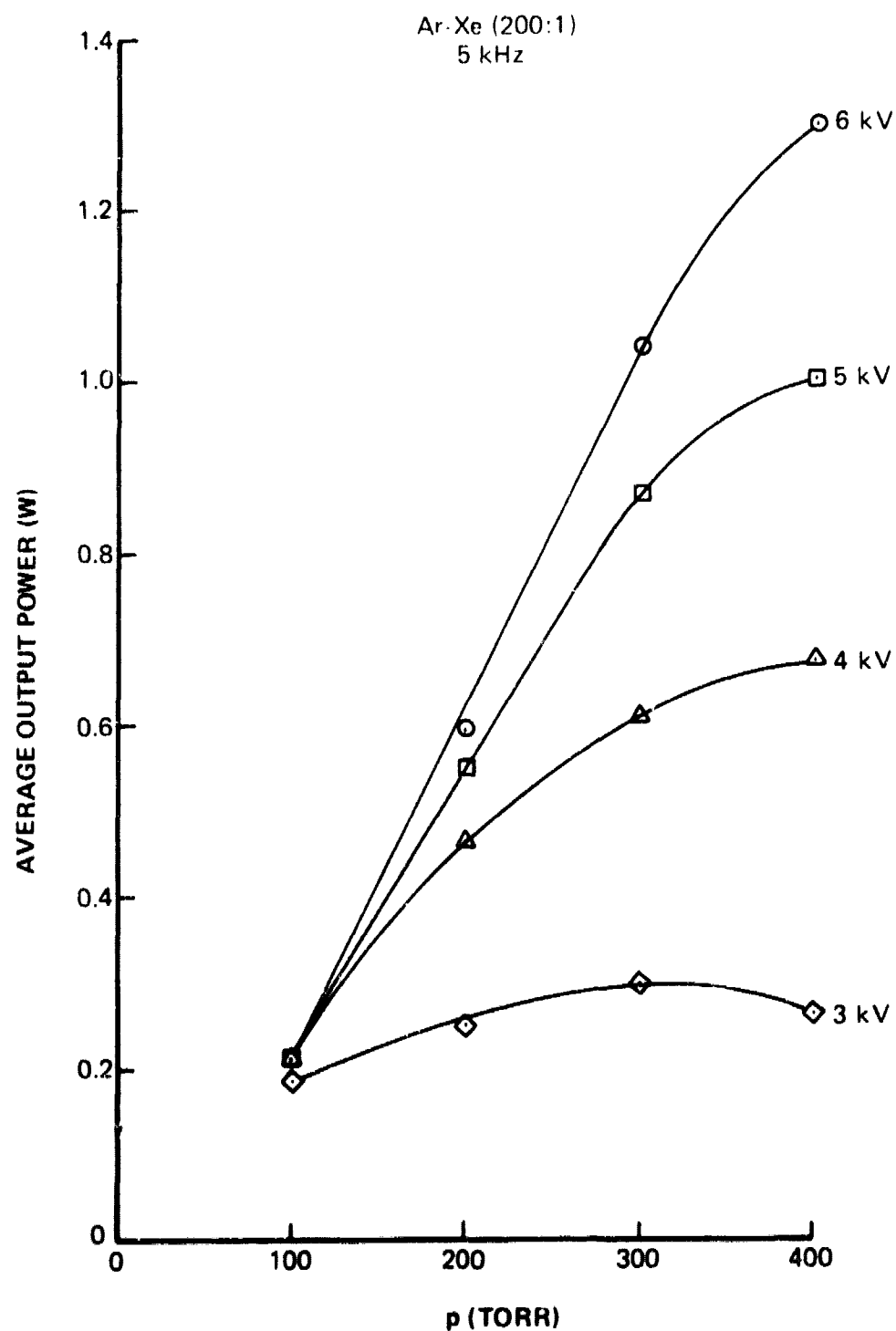


Figure 70. Pressure Dependence of Average Laser Output Power for Ar-Xe (200:1) at Various Charging Voltages in 25-cm-Gain-Length Laser

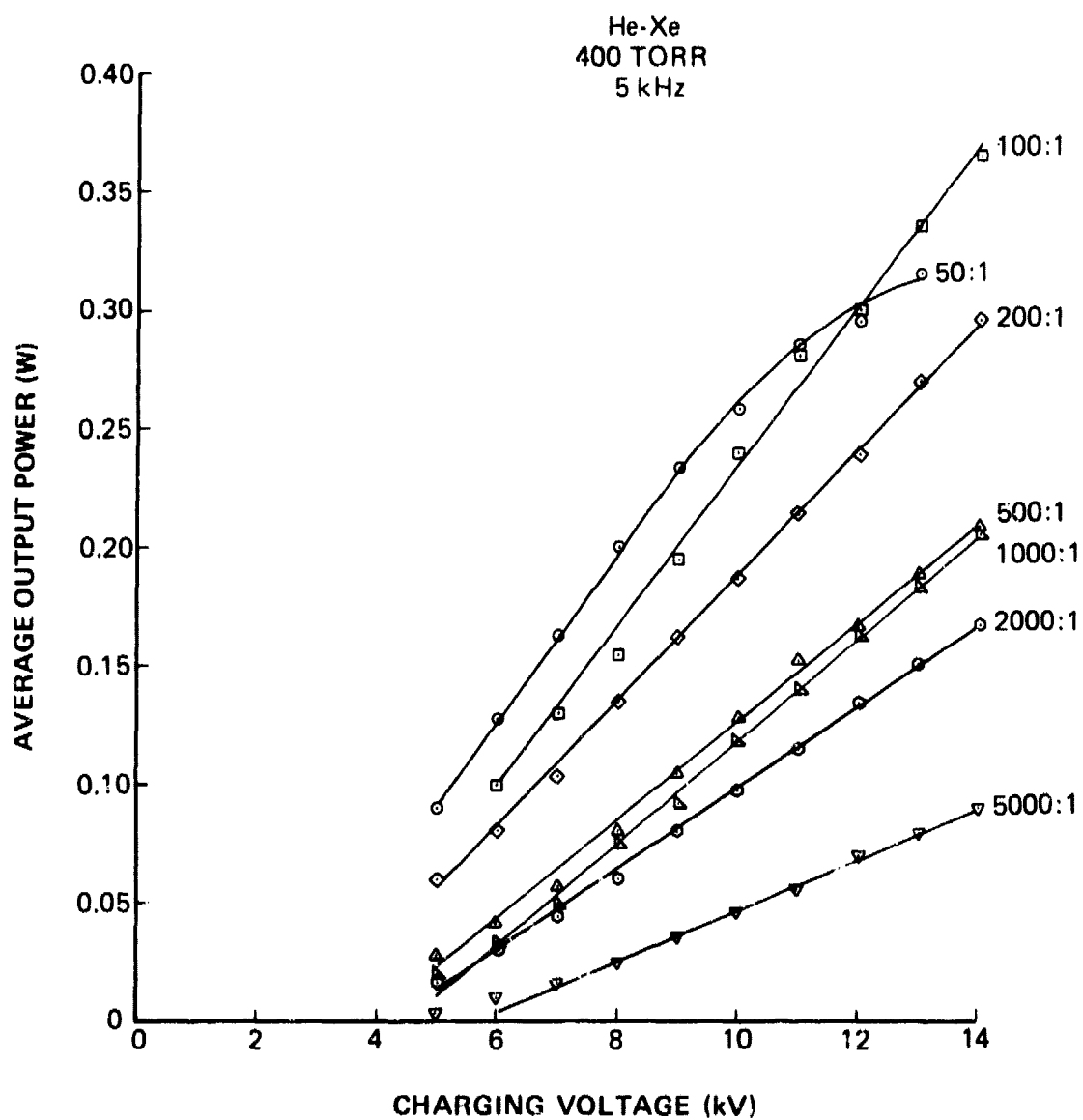


Figure 71. Dependence of Average Laser Output Power upon Charging Voltage for He-Xe Mixtures in 25-cm-Gain-Length Laser

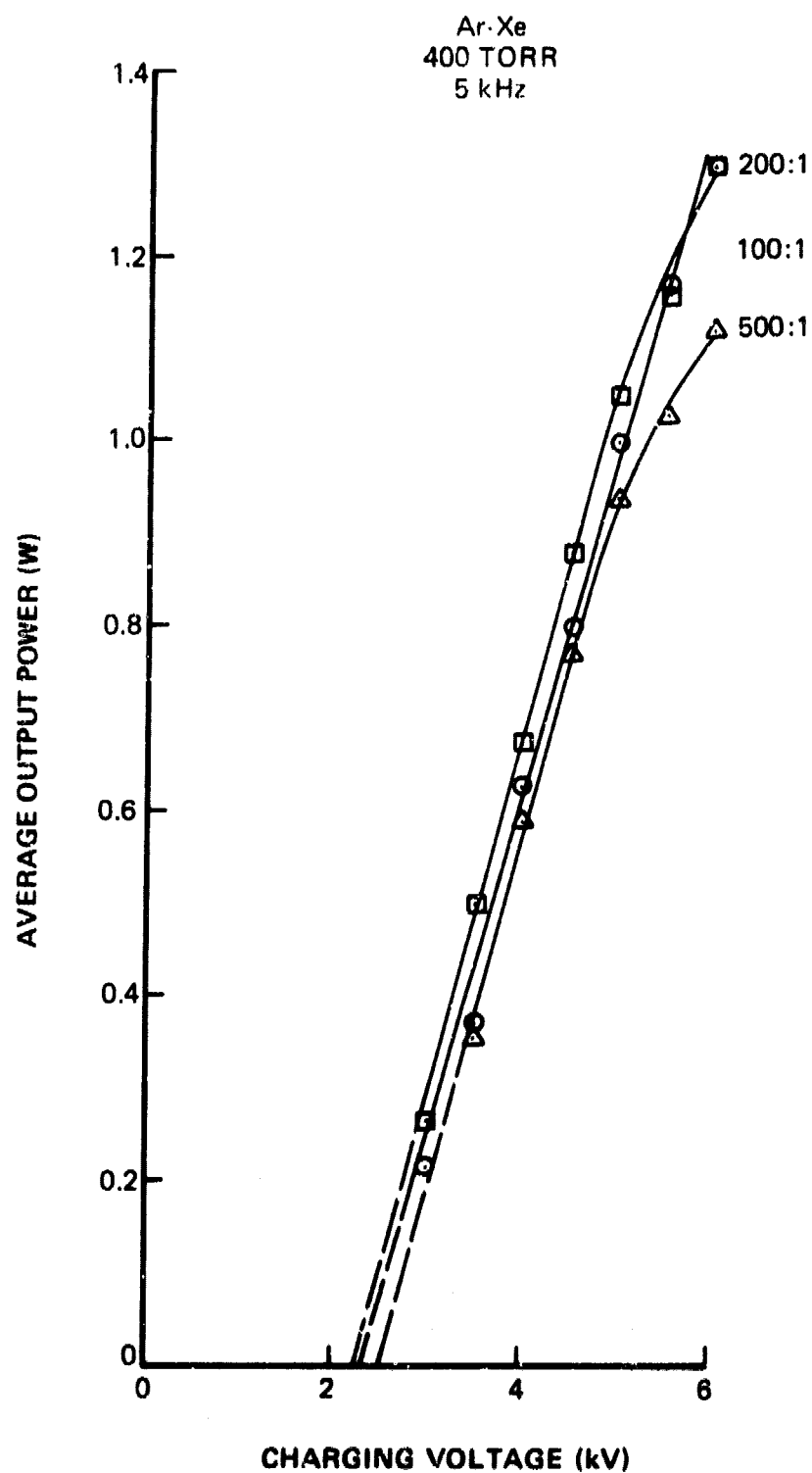


Figure 72. Dependence of Average Laser Output Power upon Charging Voltage for Ar-Xe Mixtures in 25-cm-Gain-Length Laser

output power at various pressures is shown in Figure 73 for He-Xe (200:1) and in Figure 74 for Ar-Xe (200:1). The data of Figures 67-74 demonstrate that maximum output power from He-Xe should occur at a pressure of 500 Torr, a mixture ratio of 100:1, and a charging voltage of  $> 14$  kV. The maximum output power from Ar-Xe should occur at a pressure of  $> 400$  Torr, a mixture ratio of  $\sim 100:1$ , and a charging voltage of  $> 6$  kV.

It should be pointed out that the output-mirror transmission was not optimized in the parametric study. The output mirrors were specified at 2% transmission in the 3.8-4.6  $\mu$  region. Transmission values taken from curves supplied by the mirror manufacturer are listed below for the laser wavelengths observed.

<u>Ge Mirror (He-Xe)</u>		<u>Si Mirror (Ar-Xe)</u>	
<u><math>\lambda</math> (<math>\mu</math>)</u>	<u>% Transmittance</u>	<u><math>\lambda</math> (<math>\mu</math>)</u>	<u>% Transmittance</u>
3.43	54	1.73	80
3.65	45	2.03	42
3.87	5	2.48	54
4.02	2.5	2.63	57
		2.65	55
		3.1	85
		3.37	63
		5.57	50

Most of the lines exhibit high gain by lasing with an output transmission of 40% or more. Optimization of mirror transmission should result in a substantial increase in laser-output power. Oscillation at 1.73  $\mu$  with 80% mirror transmission indicates extremely high gain for this line, which dominates the Ar-Xe laser output as shown in Figure 75.

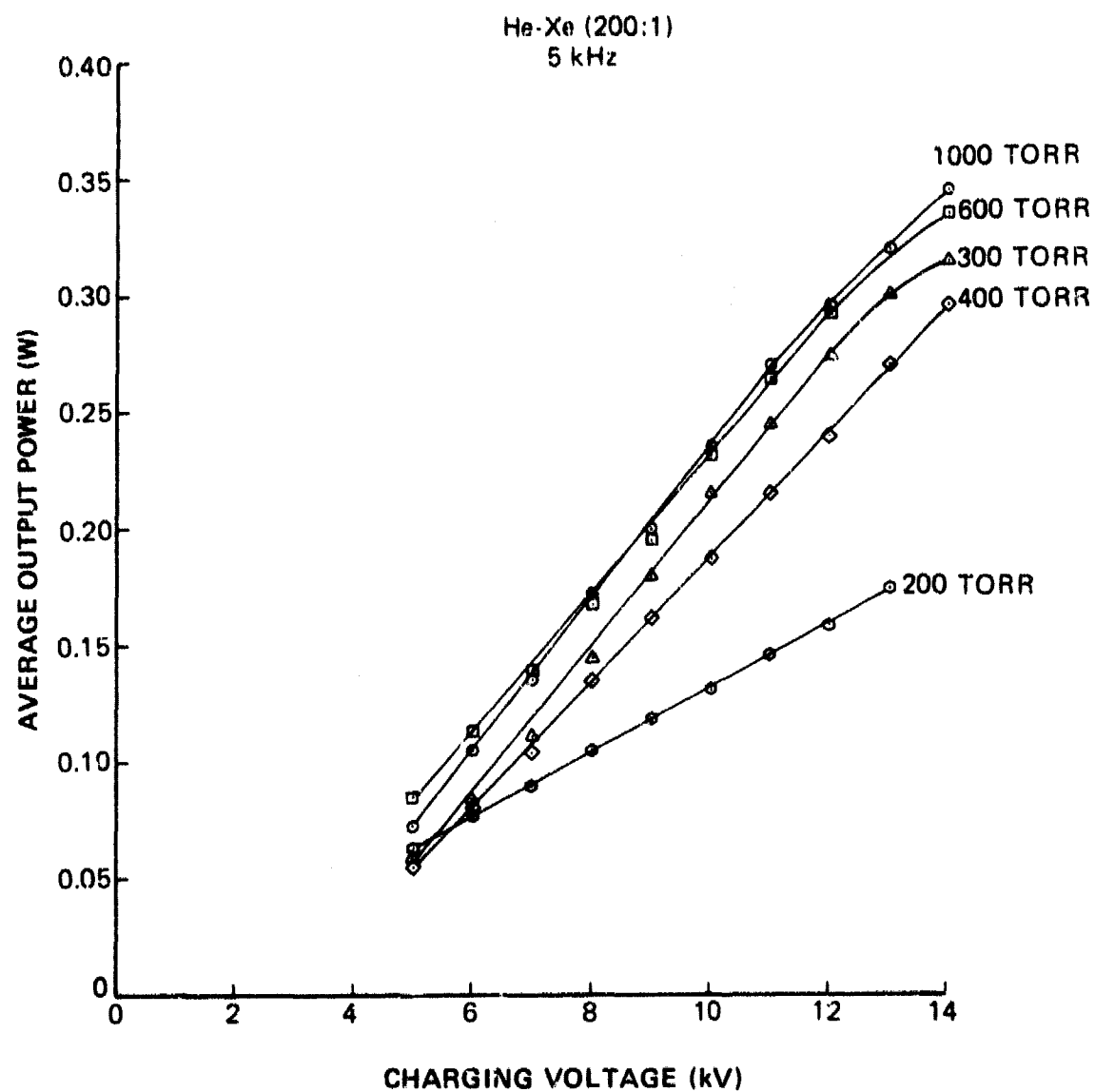


Figure 73. Dependence of Average Laser Output Power upon Charging Voltage for He-Xe (200:1) at Various Pressures in 25-cm-Gain-Length Laser

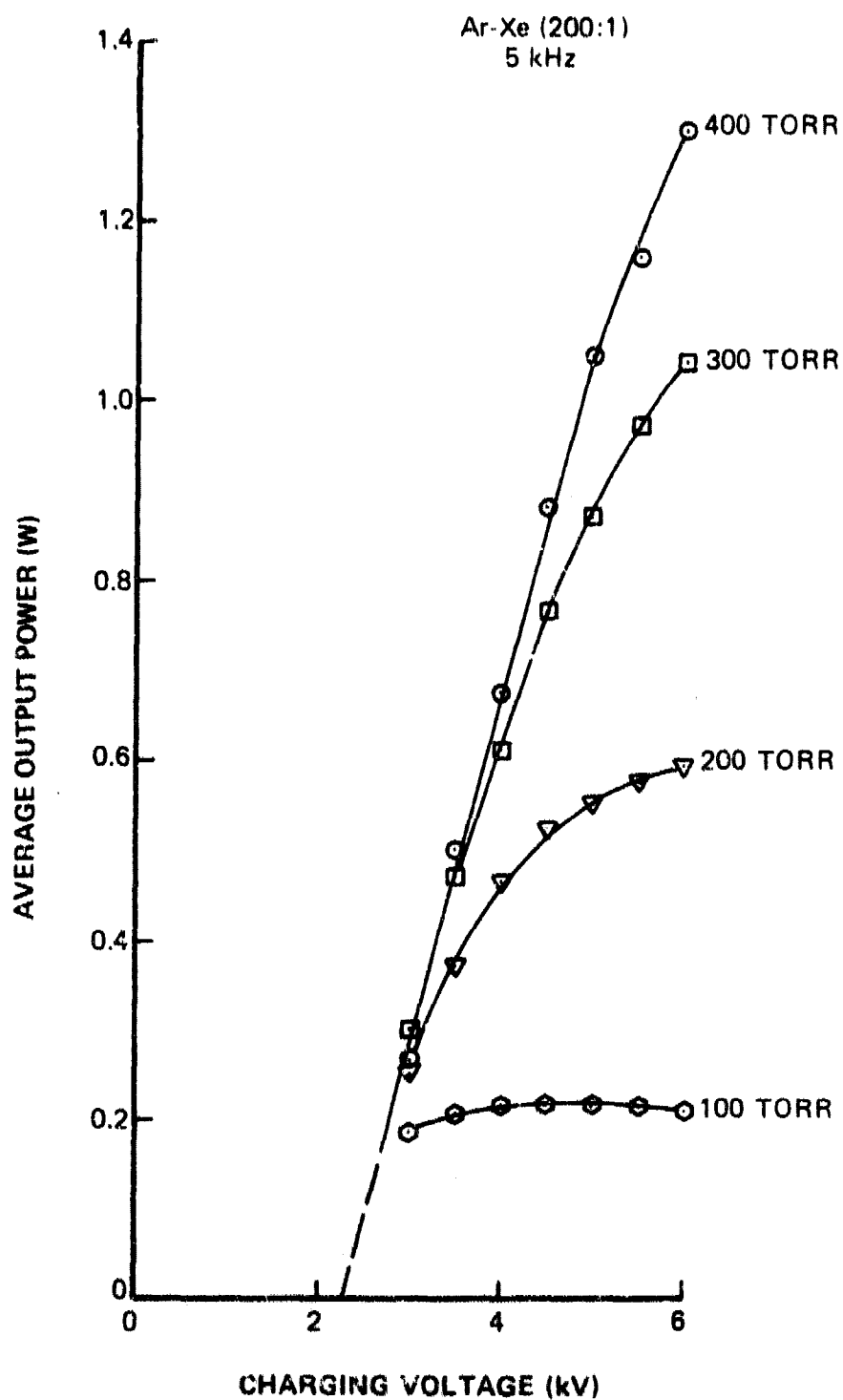


Figure 74. Dependence of Average Laser Output Power upon Charging Voltage for Ar-Xe (200:1) at Various Pressures in 25-cm-Gain-Length Laser

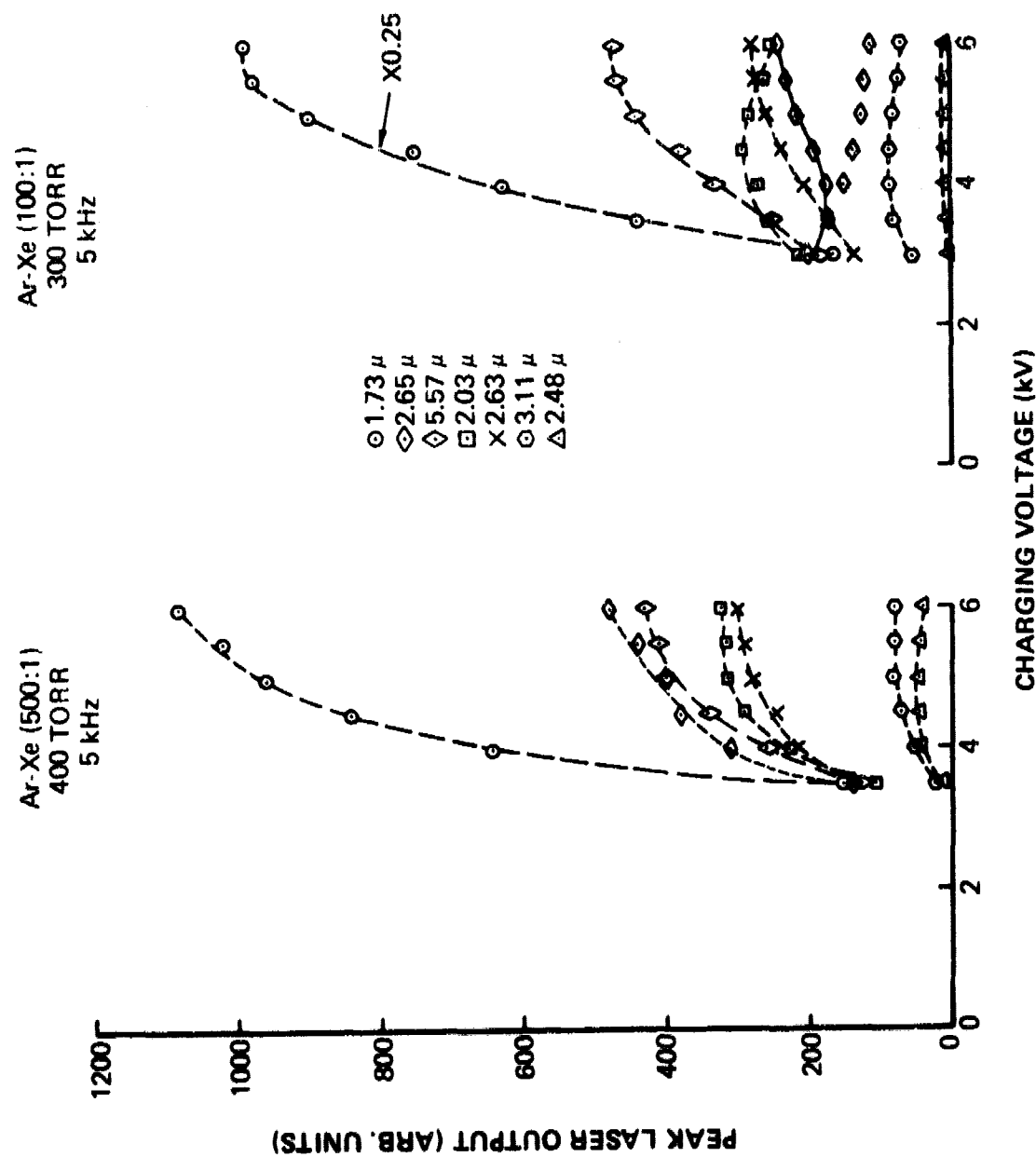


Figure 75. Dependence of Peak Laser Output at Various Wavelengths upon Charging Voltage for Ar-Xe Mixtures in 25-cm-Gain-Length Laser

#### 2.4 Discussion of Results

A compilation of performance data for the CCRGEDL, using He-Xe and Ar-Xe mixtures in the 12- and 25-cm-gain-length configurations, and for the recirculating-flow He-Xe laser investigated by Fahlen and Targ<sup>8</sup> is presented in Table 7. The absence of the 3.87 and 4.02  $\mu$  lines in the 25-cm-gain-length He-Xe results is due to the pressure and mixture ratio used. The data in Table 7 reveal that in comparison with the results of Fahlen and Targ, the CCRGEDL generated three additional lines--3.05, 3.87, and 4.02  $\mu$ --operated at approximately five-times-higher PRF with six-times-less laser-pulse energy/volume, and was about four times less efficient. The lower efficiency and laser-output energy/volume are due in part to the unoptimized output-mirror transmission. It is interesting to note that in Targ's results,<sup>8</sup> the efficiency increased strongly with PRF--from 0.04% at 100 Hz to 0.12% at 1 kHz. At high PRF a reduction in voltage was necessary to avoid arcing, and the assumption was made that the laser operated farther from its saturation power level with consequent greater efficiency. This effect was not observed for the CCRGEDL. It may be significant that Targ's results were obtained for a clearing ratio of  $> 1$ , whereas the CCRGEDL results were obtained at clearing ratios down to 0.25.

A listing of the Xe laser lines which have been generated by the CCRGEDL is given in Table 8, along with near-optimum gas mixtures and pressures and values of atmospheric transmission<sup>93</sup> (due to molecular absorption through a 10-km horizontal path) for each line. In addition to molecular absorption, attenuation due to molecular (or Rayleigh) scattering, aerosol scattering, and aerosol absorption must be considered. Since these attenuation mechanisms have a slowly varying dependence upon frequency, the highly frequency-dependent molecular absorption dominates in the determination of windows having good atmospheric transmittance. As can be seen in Figure 4 the 2.03-, 3.65-, and 4.02- $\mu$  lines generated by the He-Xe laser fall within the 2.0- to 2.4- $\mu$  and 3.4- to 4.2- $\mu$  windows. High-pressure lasing at 4.54 or 4.61  $\mu$  was sought to satisfy electro-optical countermeasure source requirements for the 4.5- to 5.0- $\mu$  window. Although these lines have not been observed in the CCRGEDL,



TABLE 7  
XENON GAS DISCHARGE LASERS WITH RECIRCULATING FLOW

Gas	Reference	$\lambda$ ( $\mu$ )	PRF (kHz)	Pulse Energy (mJ)	Average Output Power (W)	Efficiency (%)	Pressure (Torr)	Flow (m/sec) (CFM)	Discharge Dimensions (HWL) (cm)
He-Xe	Fahlen & Targ <sup>8</sup> (1973)	2.03	1.2 (2 kHz at reduced voltage)	9	11 [90 kW (peak)]	0.13	He:400 Xe:1	40 (6000 CFM)	5×3×76
		2.65							
		3.43							
		3.65							
He-Xe	Present Report	2.03	4 (10 kHz at reduced voltage)	0.031	0.125	0.03	He:1020 Xe:3.4	75 (250 CFM)	1×2×12
		2.65							
		3.43							
		3.65							
Ar-Xe	Present Report	4.02	7	0.24	1.68	0.48	Ar:497 Ne:10 Xe:3	75 (250 CFM)	1×2×12
		1.73							
		2.03							
		2.48							
		2.63							
		2.65							
He-Xe	Present Report	3.1	7	0.066	0.465	0.03	He:500 Xe:5	60 (450 CFM)	1×2×25
		3.37							
		5.57							
		2.03							
		2.65							
Ar-Xe	Present Report	3.05	8.75	0.26	2.27	0.86	Ar:400 Xe:2	60 (450 CFM)	1×2×25
		3.43							
		3.65							
		1.73							
		2.03							
		2.48							
He-Xe	Present Report	2.63	8.75	0.26	2.27	0.86	Ar:400 Xe:2	60 (450 CFM)	1×2×25
		2.65							
		3.1							
		3.37							
Ar-Xe	Present Report	5.57							
		5.57							

TABLE 8  
Xe-I LASER LINES OBTAINED FROM CCRGEDL

$\lambda_{\text{air}}$ ( $\mu$ ) (calc.)	$\nu_{\text{air}}$ ( $\text{cm}^{-1}$ ) (calc.)	Gas Mixture (Pressure in Torr)	Atm. Transmitt. due to Molec. Absorpt. Through 10 km Horiz. Path <sup>93</sup>	
			Sea Level	12 km
1.732578	5771.74	Ar-Xe (490:3)	0.83	1.00
2.026229	4935.27	He-Xe (800:8)	0.56	0.92
2.482462	4028.25	Ar-Xe (600:1.2)	0.08	1.00
2.626893	3806.77	Ar-Xe (600:1.2)	0	0.12
2.651093	3772.02	He-Xe (1000:3.3)	0	0.96
3.047981	3280.86	He-Xe (200:2)	0.02	1.00
3.106914	3218.62	Ar-Xe (600:1.2)	0	0.99
3.366652	2970.31	Ar-Xe (600:1.2)	0.21	0.99
3.433519	2912.46	He-Xe (200:2)	0.72	1.00
3.507040	2851.41	Ar-He-Xe (490:200:3)	0.91	1.00
3.650852	2739.08	He-Xe (1000:5)	0.59	1.00
3.678836	2718.25	Kr-Xe (20:10)	0.84	1.00
3.868932	2584.69	He-Xe (200:2)	0.66	0.74
3.893978	2568.06	He-Xe (215:35)	0.86	0.99
4.019615	2487.80	He-Xe (400:0.08)	0.69	0.97
5.573859	1794.08	Ar-Xe (600:1.2)	0	0.93

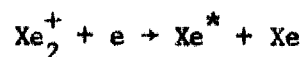
observation of the 3.87- $\mu$  line is encouraging in that the  $5d' [5/2]_3^0$  upper level of this transition is within  $300 \text{ cm}^{-1}$  of the  $5d' [3/2]_2^0$  upper level of the 4.61- $\mu$  line.

A partial energy-level diagram for Xe is shown in Figure 76 (based upon data from Ref. 94). Transitions for which laser oscillation has been attained in the CCRGEDL are shown. Only the 5d-6p transitions have been observed in Ar-Xe mixtures; in He-Xe mixtures 5d'-6p', 7p-7s, and 5d-6p transitions have been observed.

The nature of the population-inversion mechanism in He-Xe has not yet been adequately explained. The enhanced laser performance obtained when He is added to a Xe discharge can be attributed neither to atom-atom excitation transfer--since there are no energy-level coincidences between He metastables (atomic or molecular) and neutral Xe atoms--nor to increased electron temperature or density resulting from He-induced modification of discharge processes.<sup>95</sup>

The persistence of lasing well into the afterglow of high-pressure He-Xe and Ar-Xe discharges suggests energy-transfer pumping of the minority species. The following pumping mechanisms have been proposed:

1. Shuker, et al.,<sup>91</sup> propose for He-Xe mixtures that the upper laser levels are populated by radiative cascade from highly excited Xe atoms which are formed by the recombination of Xe ions generated by charge exchange and Penning ionization reactions.
2. Dissociative recombination of  $\text{Xe}_2^+$  could generate Xe atoms in excited levels below the potential minimum of  $\text{Xe}_2^+$  via the reaction<sup>96</sup>



According to Lorents,<sup>97</sup> this should populate the Xe 6p levels. Shuker<sup>91</sup> maintains that dissociative recombination is negligible in He-Xe mixtures due to the low rate of  $\text{Xe}_2^+$  production ( $8 \text{ sec}^{-1}$ ); however, it has been shown that  $\text{Xe}_2^+$  is a major ion in 20-Torr Kr containing 10-ppm Xe.<sup>98</sup>



3. The energy-level coincidence (within  $100 \text{ cm}^{-1}$ ) of the long-lived Ar [ $^1P_1$ ] and Xe 9d [ $3/2$ ] $_1^0$  results in a large ( $\sim 10^{-14} \text{ cm}^2$ ) energy-transfer cross section.<sup>99</sup> Lower Xe levels could then be populated by radiative cascade.
4. Electronic energy transfer from  $\text{Ar}_2^*$  to energy levels of Xe which overlap the  $\text{Ar}_2^*$  second molecular continuum could be an efficient pumping mechanism for the Xe 5d levels. This has been shown to be a resonant process for a wide range of excitation energies of the acceptor atom. The cross section for energy transfer from  $\text{Ar}_2^*$  [ $^1,^3\Sigma_u$ ] to Xe [ $^1P_1$ ] has been shown to be  $\sim 10^{-14}$  to  $10^{-13} \text{ cm}^2$ .

Figures 77 and 78 show the percentage of discharge energy into the formation of ionic and excited species in He-Xe and Ar-Xe mixtures as a function of E/N. These plots were generated by W. Bailey using the Boltzmann code of the Plasma Physics Group at Wright-Patterson Air Force Base. CCRGEDL operation at low E/N results in efficient production of  $\text{Xe}^+$  and  $\text{He}_m$  in He-Xe and  $\text{Xe}^*$  and  $\text{Ar}_m$  in Ar-Xe.

The differences in species formation, laser efficiency, and spectral and temporal properties of the laser pulses in He-Xe and Ar-Xe provide a basis for discrimination among the various pumping mechanisms shown in Figure 79. In Ar-Xe, the efficient production of Ar metastables, high laser efficiency, and lasing on the 5d-6p transitions favor the direct excitation of  $\text{Ar}_m$  followed by the formation of the Ar excimer  $\text{Ar}_2^*$  and the subsequent electronic energy transfer from  $\text{Ar}_2^*$  to the 5d manifold of Xe. The  $\text{Ar}_2^*$  potential well is situated just above the Xe 5d manifold (see Figure 76), and it has been shown by Gedanken, *et al.*,<sup>99</sup> that there is efficient molecule-atom energy transfer to Xe levels which overlap the  $\text{Ar}_2^*$  second molecular continuum. Since the formation of  $\text{Ar}_2^*$  is continuous during the current pulse, this pumping mechanism should be compatible with pulse stretching or possibly cw operation. In He-Xe, the efficient production of He metastables, low laser efficiency, enhancement of afterglow lasing, and lasing on the 7p-7s transitions suggest the following pumping sequence: Penning ionization of Xe by  $\text{He}^*$  or  $\text{He}_2^*$  followed by formation of the Xe dimer  $\text{Xe}_2^+$  with subsequent

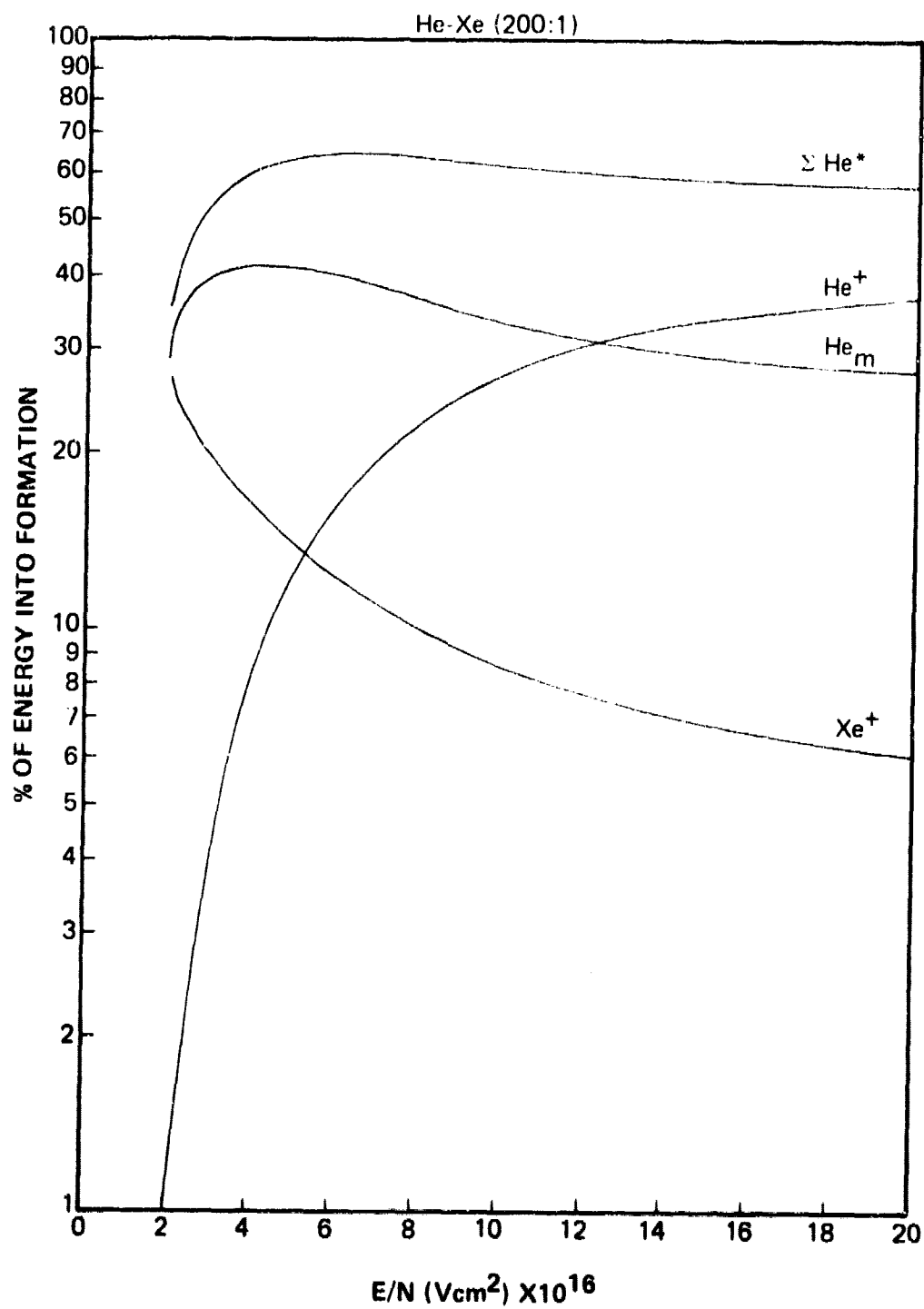


Figure 77. Percentage of Discharge Energy into Formation of Ionic and Excited Species in He-Xe (200:1) as a Function of  $E/N$

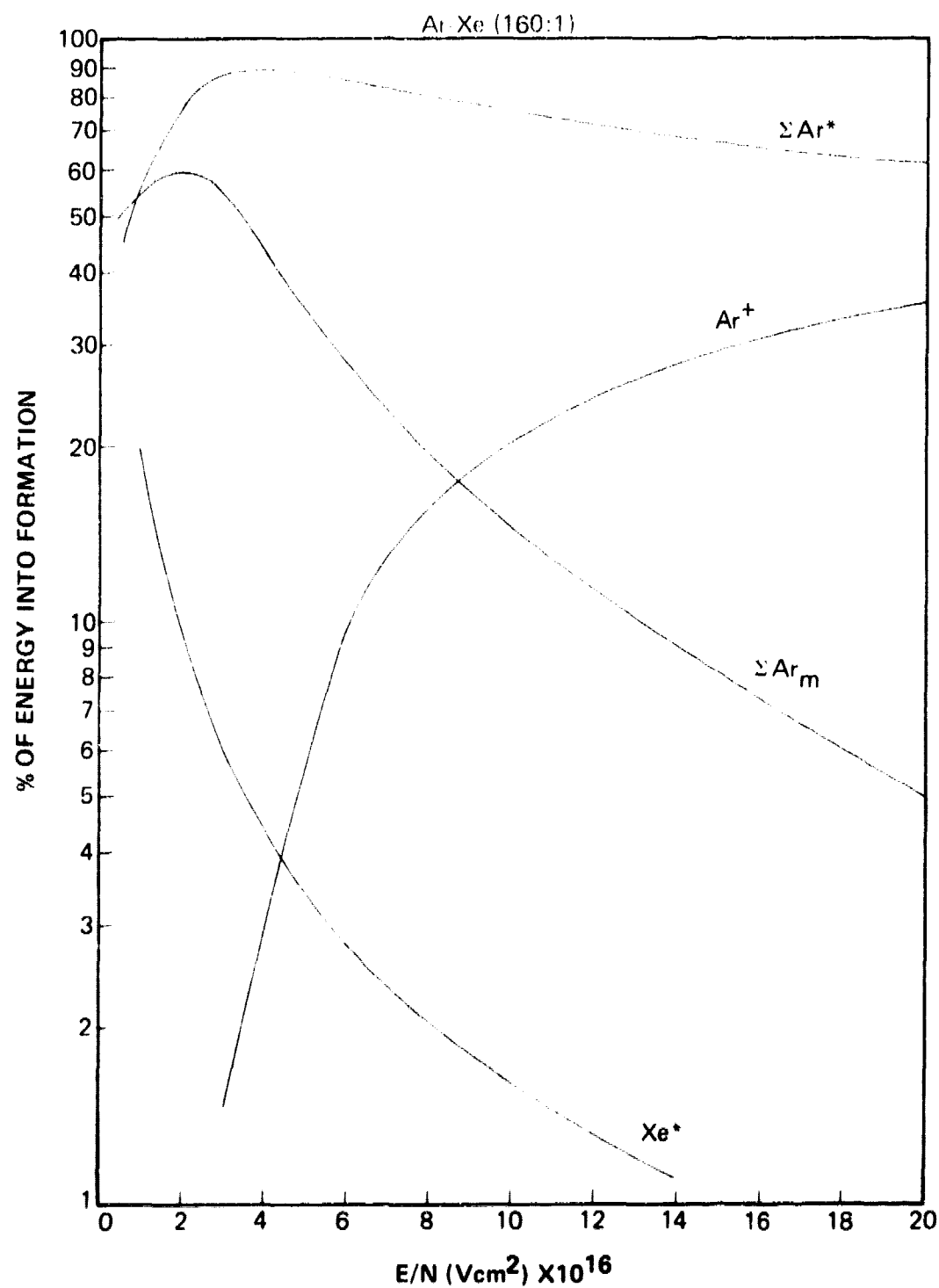
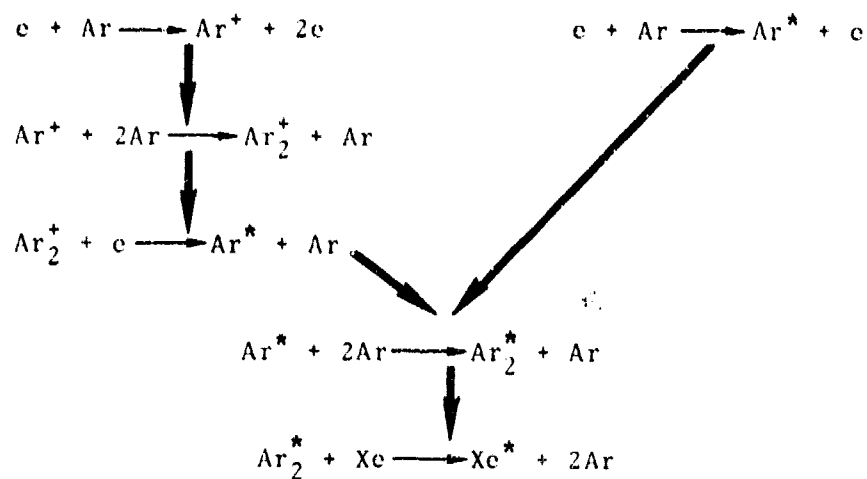


Figure 78. Percentage of Discharge Energy into Formation of Ionic and Excited Species in Ar-Xe (160:1) as a Function of  $E/N$

### Ar-Xe Reactions



### He-Xe Reactions

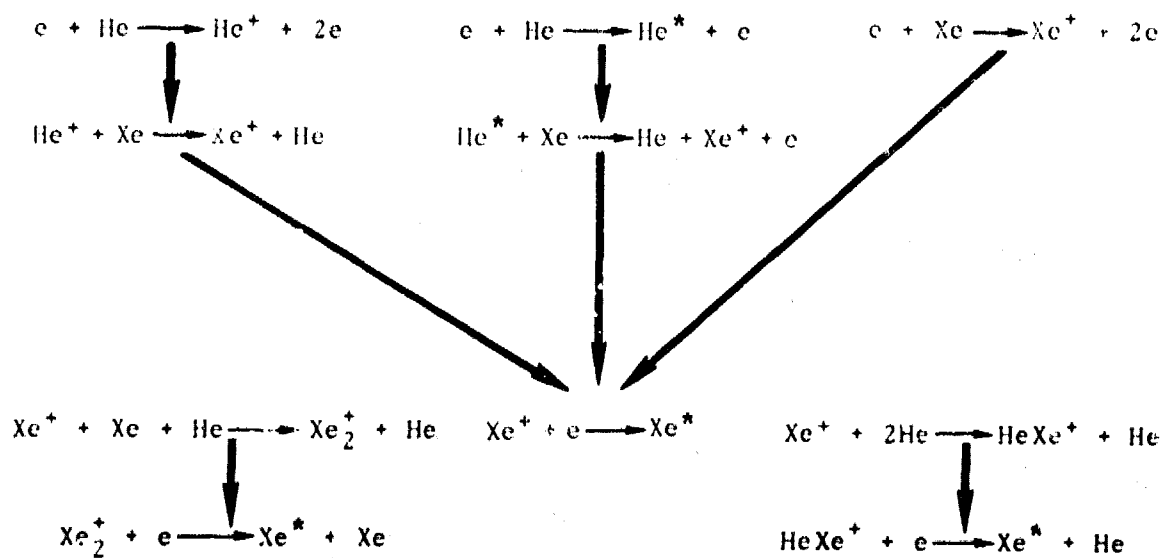


Figure 79. Pumping Mechanisms in Ar-Xe and He-Xe



dissociative recombination of  $\text{Xe}_2^+$  to populate the Xe 7p levels (note in Figure 76 that the bottom of the  $\text{Xe}_2^+$  potential well is just above the 7p levels). Because of the number of steps, this pumping mechanism is expected to result in lower laser efficiency and a delay in reaching population inversion.

In a recent study by Shiu, et al.,<sup>100</sup> the excited states of Xe produced by dissociative recombination of  $\text{Xe}_2^+$  were determined by comparing the decays of afterglow-radiation intensity and electron concentration. For room-temperature electrons, it was found that final states of  $\text{Xe}^*$  lying above the  $v = 0$  vibrational level of the  $\text{Xe}_2^+$  ground state were not produced. Microwave heating of the electrons to mean energies of  $\sim 1$  eV resulted in the observation of additional  $\text{Xe}^*$  states, lying as much as 0.6 eV above the  $\text{Xe}_2^+$  ground state. Population of the 7p [5/2]<sub>3</sub>, 7p [5/2]<sub>2</sub>, and 5d' [5/2]<sub>3</sub> upper levels of the 3.05-, 3.43-, and 3.87- $\mu$  transitions, respectively, was observed; however, population of the 7p [1/2]<sub>1</sub> upper level of the 4.02- and 3.65- $\mu$  transitions was not observed. Shiu's results, however, were obtained for pure Xe at pressures from 5 to 20 Torr, whereas the CCRGEDL operates at high pressures of dilute He-Xe mixtures.

## SECTION III

### UV PHOTOIONIZATION

#### 3.1 Introduction

Electron beams, heavy-particle beams, and UV radiation are currently being used for preionization (ionization prior to discharge initiation) in high-energy molecular lasers in order to achieve uniform large-volume glow discharges at high pressure. Although the e-beam technique has, to date, demonstrated the most success for CO and CO<sub>2</sub> lasers, the concept of using high-energy photons for ionization offers the potential advantages of decreased size, weight, and cost over the electron-beam system. More knowledge, however, is required in the areas of UV source characteristics, transmission properties of the source and laser gas, and absorption and ionization characteristics of the ionizing constituent. It has been demonstrated that the majority of the ions produced by UV radiation in CO and CO<sub>2</sub> lasers result from photoionization of impurities, rather than ionization of the main laser gases. This is due to the fact that photons with energies higher than ~ 12 eV are strongly attenuated by both CO and CO<sub>2</sub>, while the ionization thresholds of CO, CO<sub>2</sub>, N<sub>2</sub>, He, H<sub>2</sub>, and Ar are higher than 13 eV. Of particular interest, then, are the absorption and ionization characteristics of low-ionization potential-additives (seed compounds).

Although a number of excellent studies have been performed on the details of the photoionization process,<sup>101</sup> more quantitative data are required--particularly regarding the properties of seedants--to permit the application of modeling techniques which have been successfully utilized for other discharges, such as the electron-beam-ionized plasma. In this section measurements of laser-gas absorption, seed-compound absorption and ionization characteristics, and spark-source emission properties are described. Concentrating on single-step ionization, the wavelength region of interest extends from ~ 100 to ~ 170 nm. The lower boundary is determined by a sharp increase in absorption cross section of the two main gases of interest, i.e., CO and CO<sub>2</sub>. The upper limit is a result of the ionization potential of the seedants available (7.14-eV ionization onset for N,N-dimethylaniline,<sup>102</sup> equivalent to 173.6 nm).

Calibrated photoionization efficiencies and photoabsorption cross sections are limited to wavelengths above 116 nm because of the windowed calibration source.

### 3.2 Experimental Results

Both broadband and monochromatic illumination were utilized for absorption-coefficient measurements. Figure 80 shows the arrangement used for the broadband method. A microwave-excited continuum lamp (Ar, Kr, or Xe) was placed at one end of an absorption cell and a vacuum UV scanning monochromator at the other. Initially a background spectrum taken with the lamp on and chamber evacuated was stored in a minicomputer; the sample gas was then admitted to the cell and the spectral scan repeated. The ratio of incident intensity ( $I_0$ ) to transmitted intensity ( $I$ ) was then calculated. Since the number density ( $n$ ) and pathlength ( $\ell$ ) were known, the absorption coefficient ( $K$ ) was plotted as a function of wavelength ( $\lambda$ ), after normalizing to 1 cm at standard temperature and pressure. This coefficient is defined in Beer's Law

$$I = I_0 e^{-K\ell}$$

Figure 81 shows the measured photoabsorption coefficients of  $\text{CO}_2$  which are in general agreement with published data.<sup>103</sup> Photoabsorption data obtained for CO show a strong pressure dependence (see Figure 82) which is explained by the fact that the monochromator resolution was only  $\sim 2 \text{ \AA}$ , whereas the CO fourth-positive system is actually composed of many strong but narrow absorption lines. That is, measurements made with a low-resolution spectrometer result not only in the detection of a larger linewidth than is actually present but also in an integration over an area containing both high and low intensities. The end result is the erroneous recording of one wide, short line whereas, in reality, several strong, narrow lines are present. Nitrogen-photoabsorption-coefficient measurements from 125 to 160 nm indicated little absorption except for the weak Lyman-Birge-Hopfield bands.

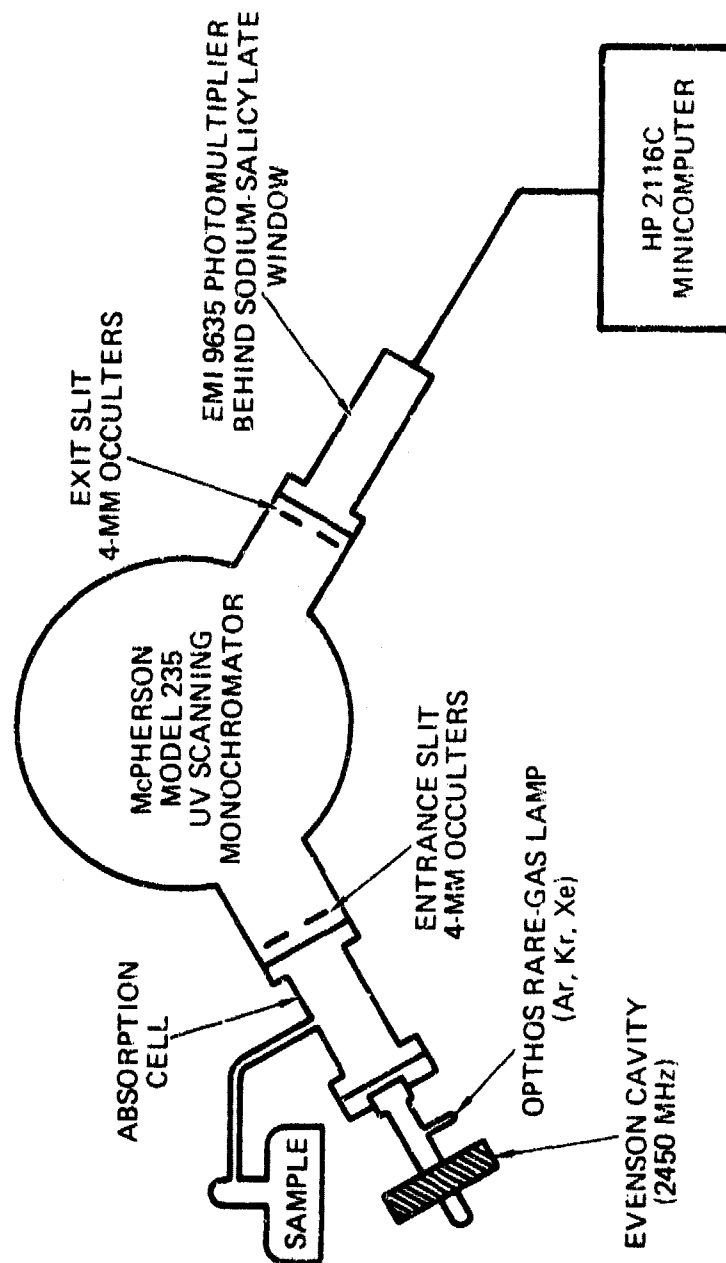


Figure 80. Experimental Apparatus for Absorption Measurements Using Continuum Illumination

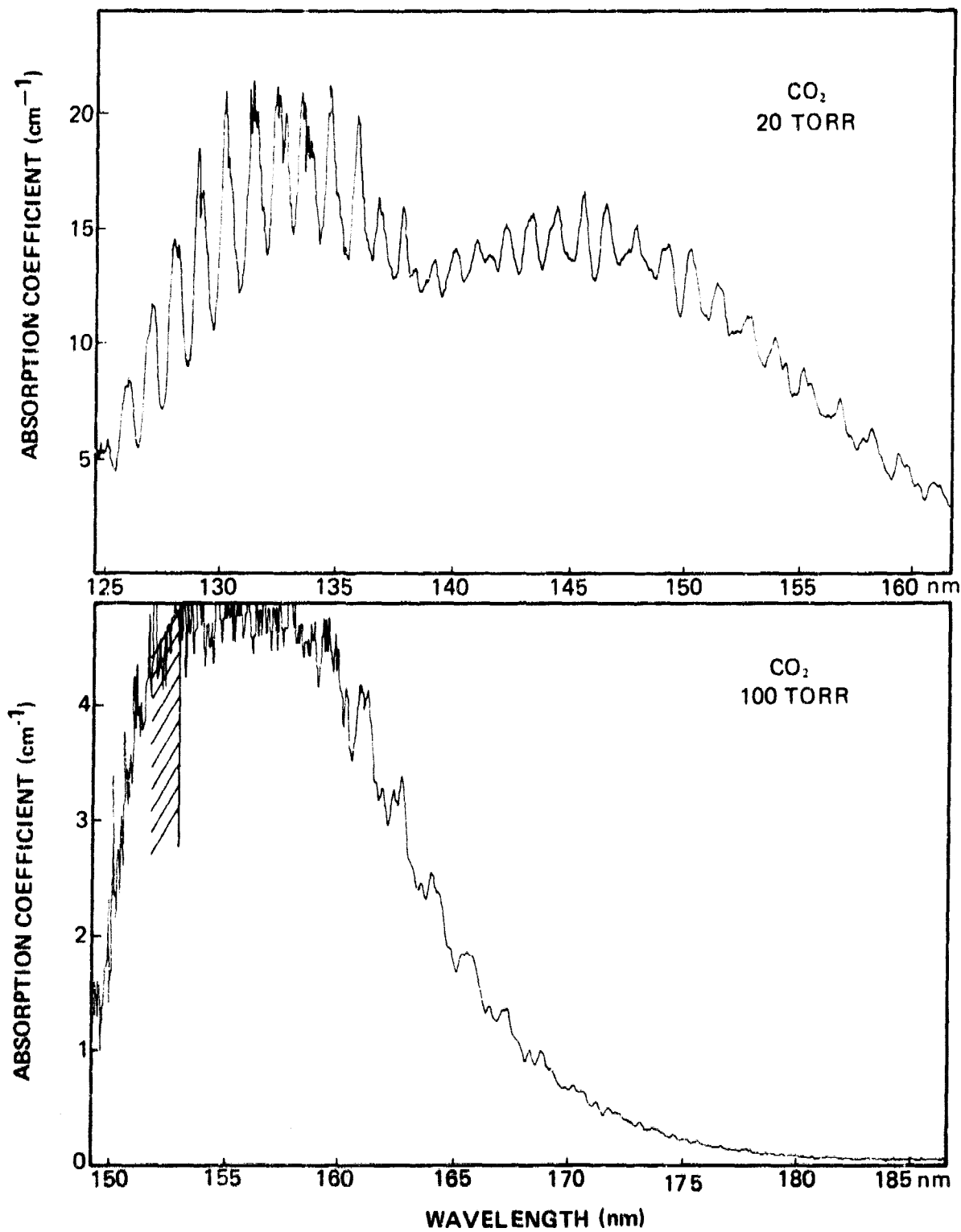


Figure 81. Absorption Coefficients of CO<sub>2</sub> for the Ranges  
(a) 125 to 160 nm and (b) 160 to 185 nm

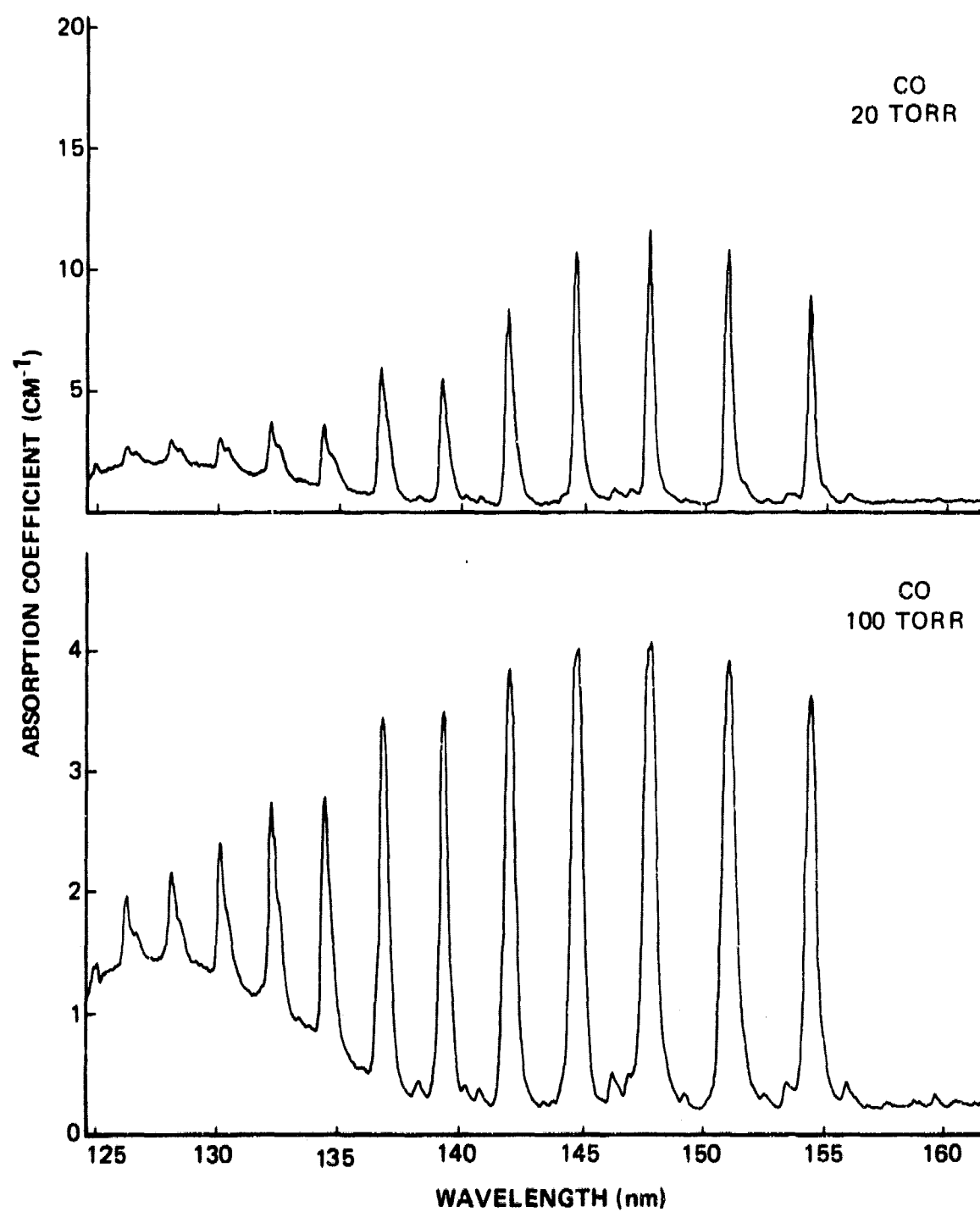


Figure 82. Measured Absorption Coefficient of CO Between 125 and 160 nm, Taken with Pressures of (a) 20 Torr and (b) 100 Torr

The absorption of several window materials was also measured. Figure 83 shows the transmission of a 5-mm sample of  $\text{CaF}_2$ . The transmission of a 2-mm-thick  $\text{MgF}_2$  window mounted on a Hinteregger lamp changed with use due to the formation of color centers. Figure 84 shows a transmission curve after use, including exposure to the discharge electrons. The transmission can be somewhat restored with overnight radiation from a mercury lamp. It is believed that the primary cause of the color centers is electron bombardment--not UV irradiation.

In the wavelength region below the ionization threshold, a double ionization chamber was used for measurement of the photoabsorption cross section as well as the photoionization yield. In this case a line-emission source rather than a continuum was utilized to permit more accurate measurement of the characteristics as a function of wavelength. Figure 85 shows the experimental arrangement. A 1-Torr  $\text{H}_2$  discharge in the Hinteregger capillary lamp illuminated the entrance slit of the 0.5-m vacuum UV scanning monochromator. The Samson-type double ionization chamber was mounted at the exit, with a calibrated photodiode mounted at the rear of the ion chamber. This diode, having quantum efficiency specified by NBS to  $\pm 6\%$  accuracy, provided the system calibration. The ion chamber and photodiode currents were monitored with stable varactor-type current-to-voltage (I-V) converters, with the data entering the on-line minicomputer through digital voltmeters. The measurement procedure was as follows:

1. The calibrated photodiode was installed on the rear of the ionization chamber, allowing an intensity calibration of the monochromator/ $\text{H}_2$  discharge combination as a function of wavelength (see Figure 86 for typical output spectrum). This procedure was performed with 50- $\mu$  entrance and exit slits, resulting in a spectral resolution of 1.75  $\text{\AA}$  (FWHM).
2. The photodiode was replaced with a blank flange, and the system was pumped out overnight in order to remove any residual vapor.
3. The test gas was introduced at a pressure sufficient to maintain an ion-current ratio of better than 3:1 (Chamber 1 to Chamber 2) over the wavelength-measurement interval. In order to prevent the ion-current ratio from becoming too large, data were collected in a series of 10-nm-wide intervals.

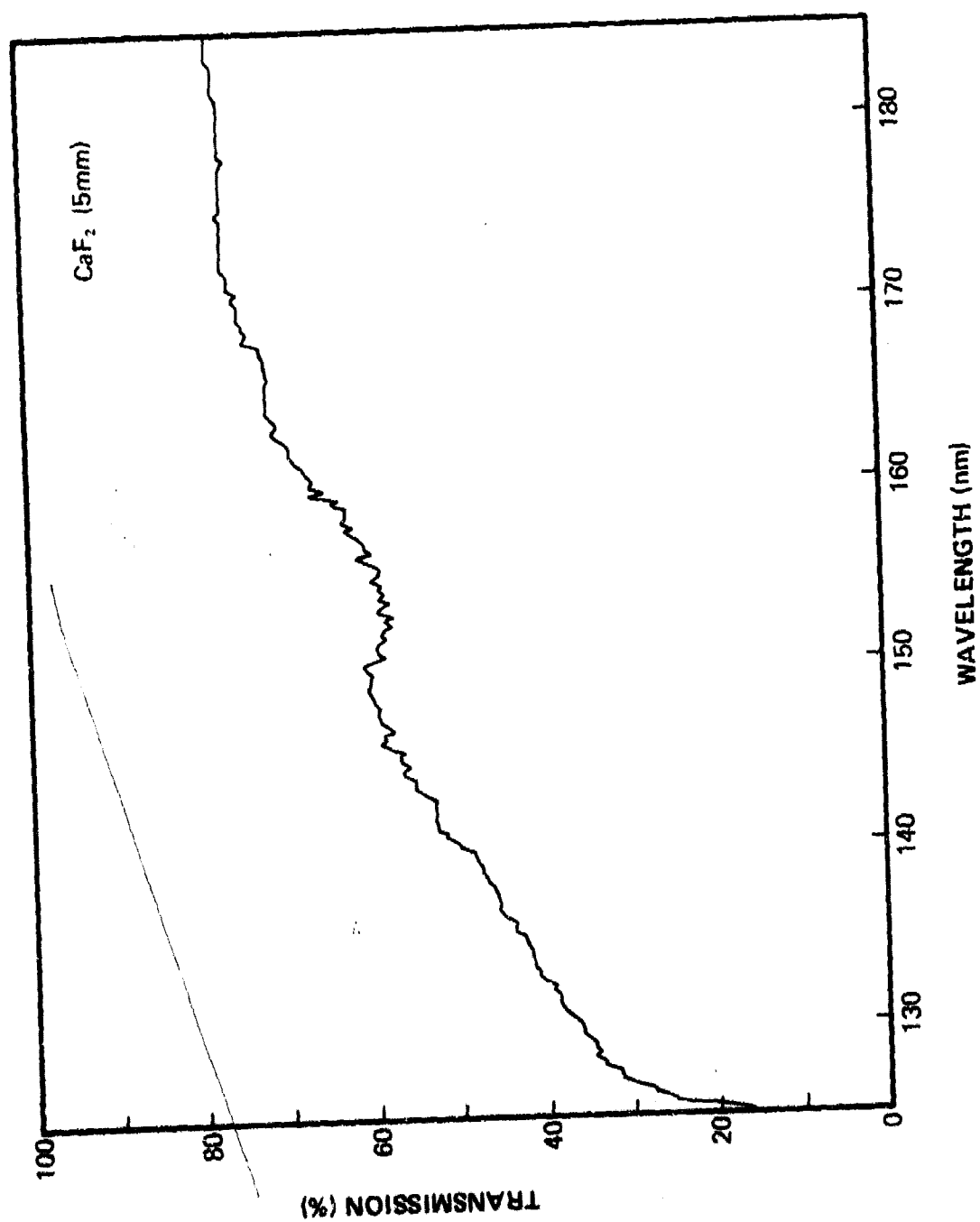


Figure 83. Measured Transmission of a 5-mm-thick Sample of Calcium Fluoride from 125 to 185 nm



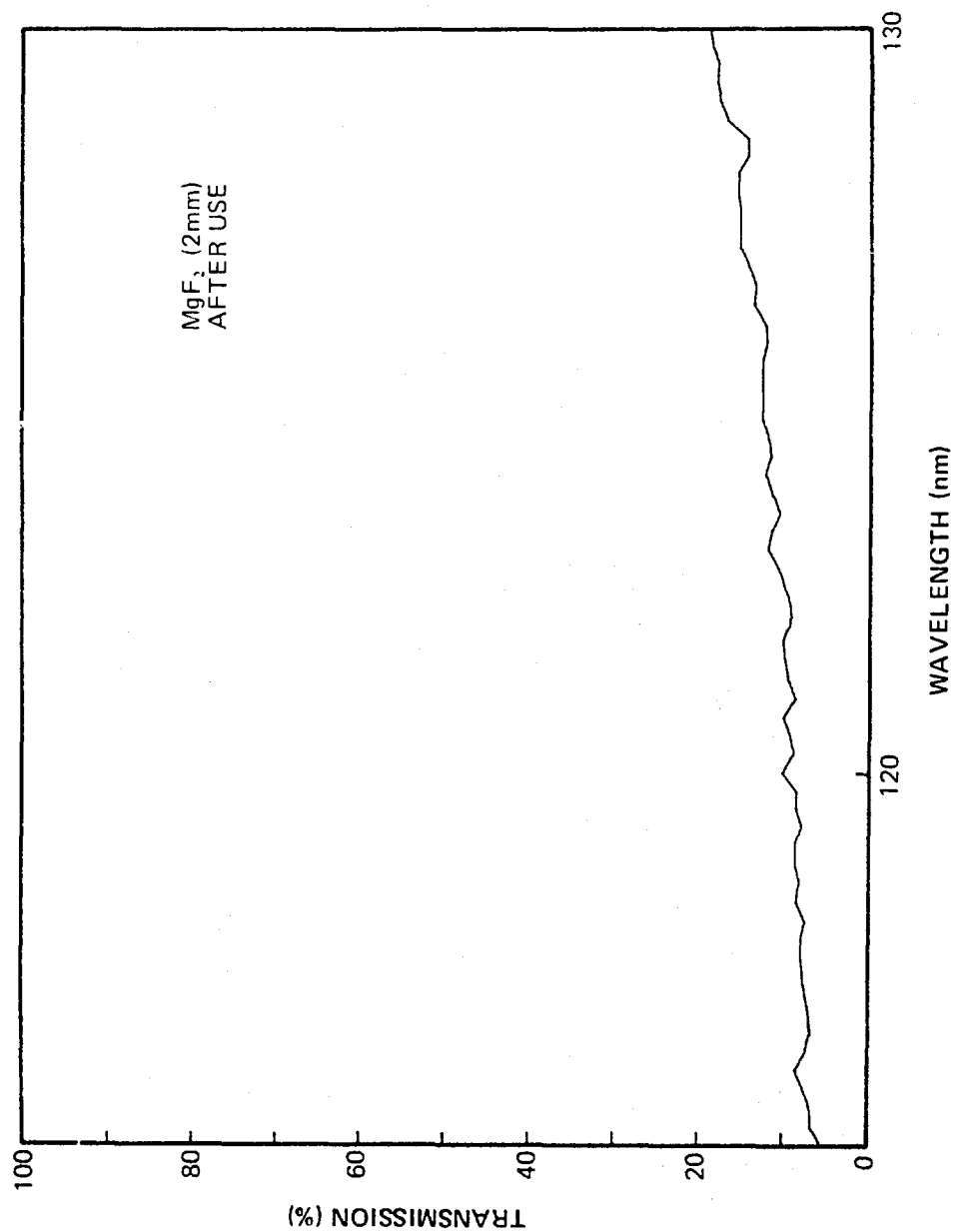


Figure 84. Measured Transmission of a 2-mm-thick Sample of Magnesium Fluoride from 115 to 130 nm After Use

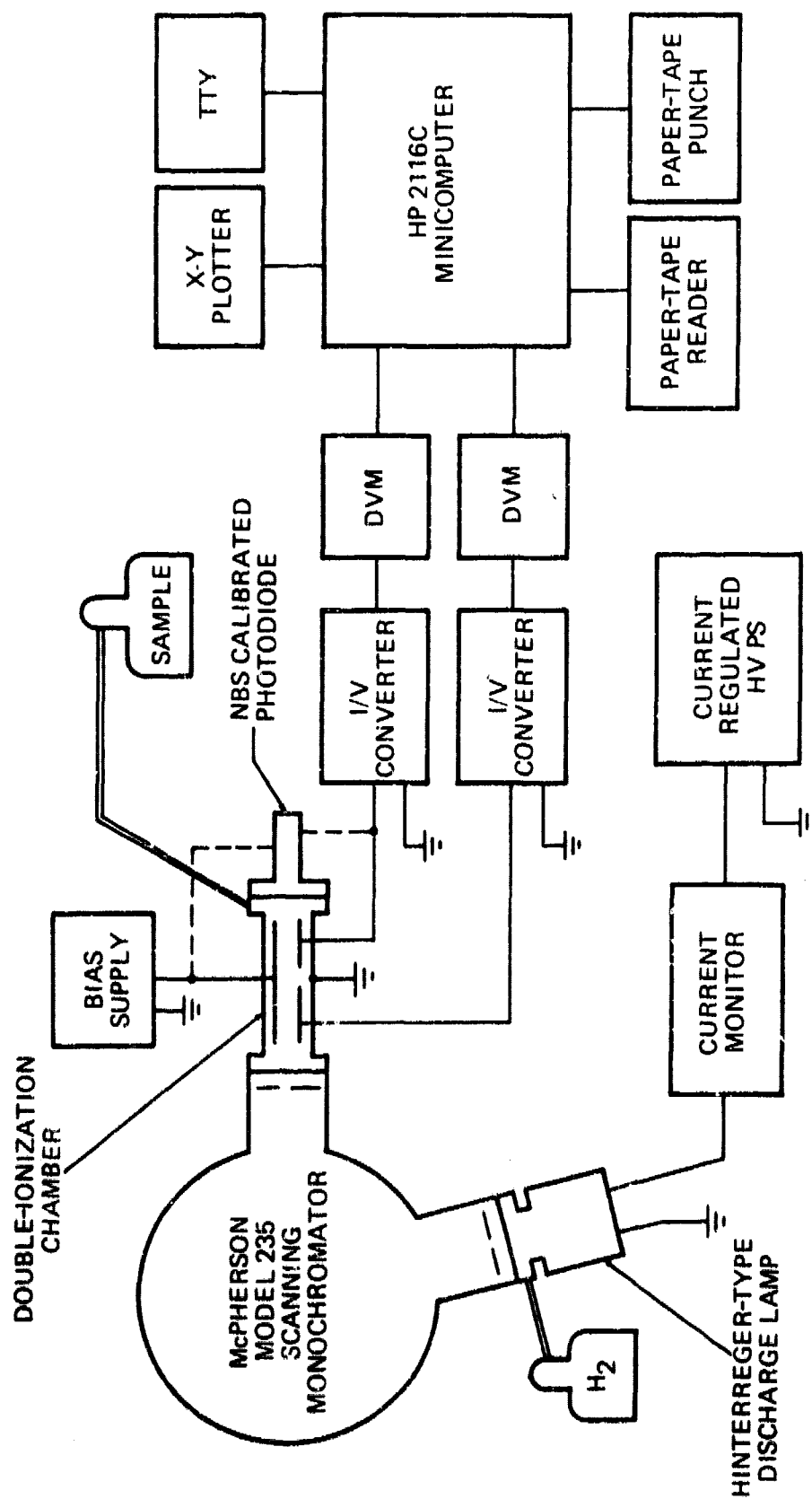


Figure 85. Schematic Diagram of Experimental Arrangement for Measurement of Photoionization Efficiencies and Photoabsorption Cross Sections

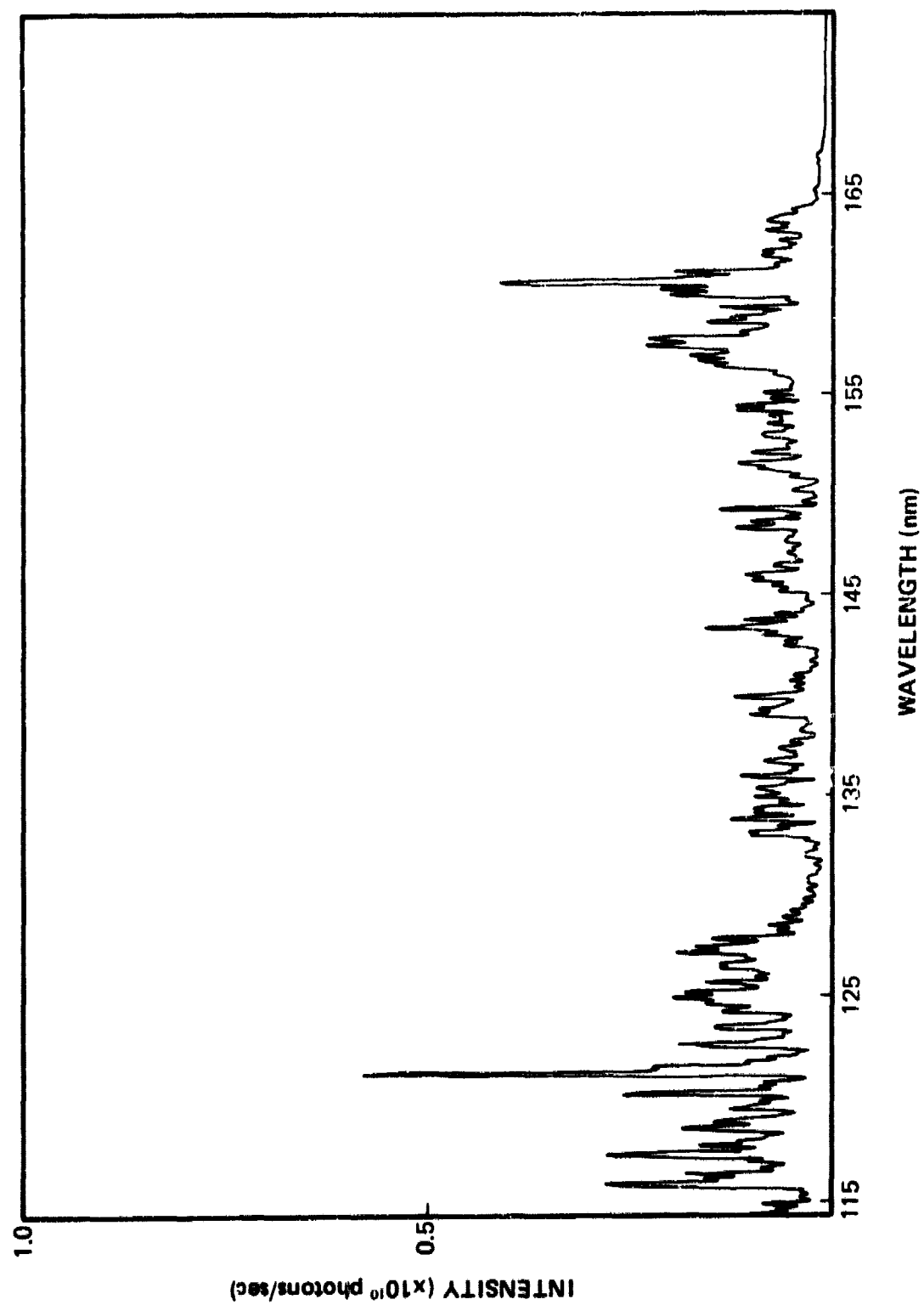


Figure 86. Typical Spectral Output of Monochromator for Photoionization Measurements

4. With the aid of the minicomputer, the ion-chamber data were correlated with the calibration spectra, resulting in ionization efficiency and cross-section values for the region from 116 nm to near the ionization threshold.

Figures 87 through 90 show the photoabsorption characteristics and ionization yields of N,N-dimethylaniline, triethylamine, trimethylamine, and tri-n-propylamine. The cross sections shown are the total photoabsorption cross sections, including the processes of photodissociation, photoexcitation, photoionization, and photon scattering. The absorption coefficient (K) in  $\text{cm}^{-1}$  is related to the ion-chamber data by

$$K = 0.187 \frac{T}{P} \log_e \left( \frac{i_1}{i_2} \right)$$

where P is the pressure in Torr, T is the temperature in °K, and  $i_1$  and  $i_2$  are the ion currents in the first and second chambers, respectively. The absorption cross section is simply the absorption coefficient divided by Loschmidt's number ( $2.69 \times 10^{19}/\text{cm}^3$ ). The photoionization yield ( $\eta$ ) is the percentage of the total absorption which results in ionization (either direct photoionization or photoexcitation which results in auto-ionization). That is,

$$\eta = \frac{\text{ions produced/sec}}{\text{photons absorbed/sec}}$$

$\eta$  is related to the ionization-chamber data by

$$\eta = \frac{i_1^2}{I_0 q (i_1 - i_2)} C$$

where  $I_0$  is the incident intensity as determined by the calibrated photodiode, q is the electronic charge, and C is a correction factor to account for the absorption between the monochromator exit slit and the entrance of the first ionization chamber.  $I_0$ ,  $i_1$ ,  $i_2$ , and, consequently, K and  $\eta$  are functions of wavelength. With a broadband absorption characteristic being assumed, the calculations were made at the peak of the H<sub>2</sub> emission lines only in order to

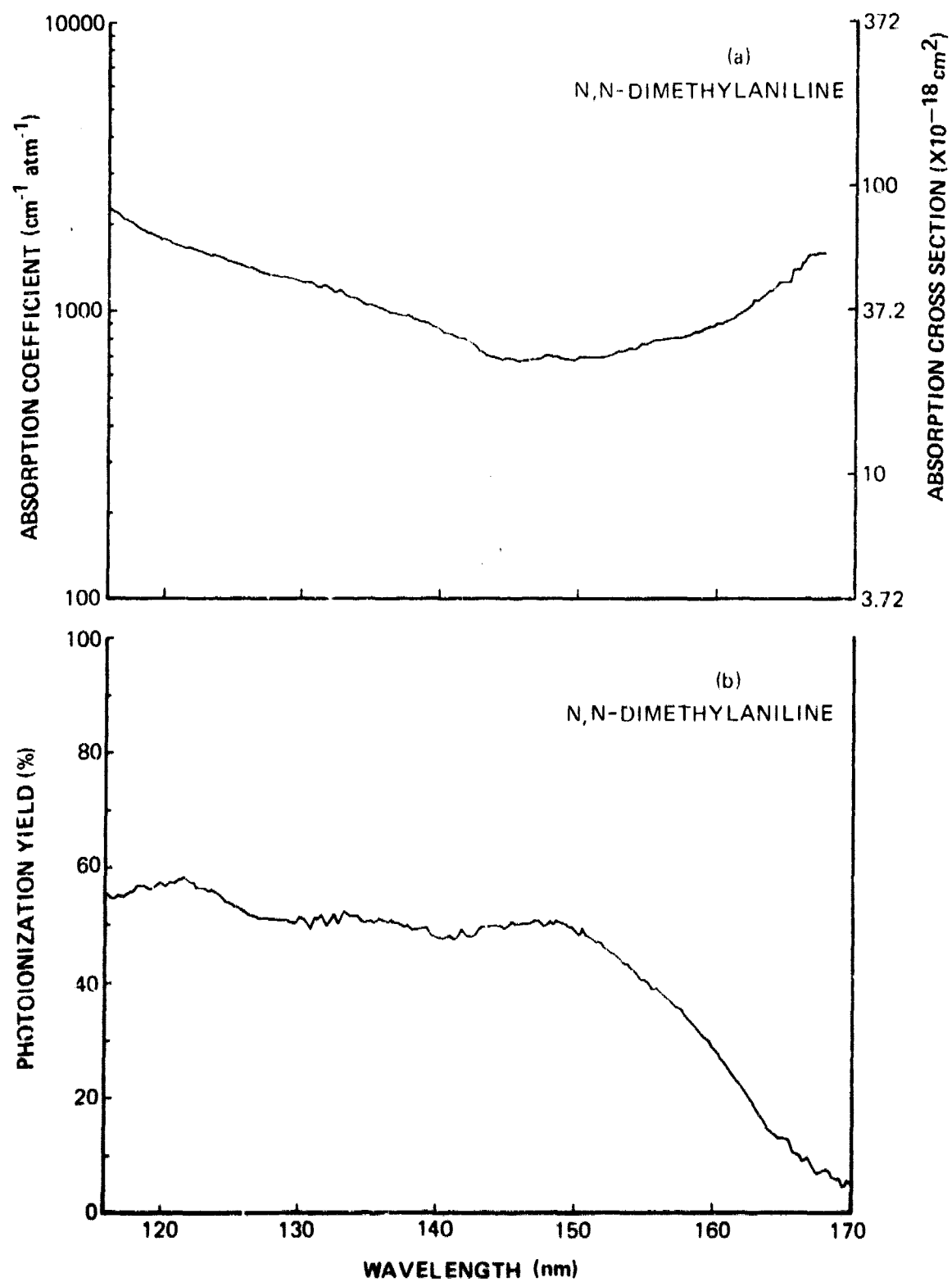


Figure 87. Photoabsorption Cross Sections (a) and Photoionization Yields (b) of N,N-dimethylaniline

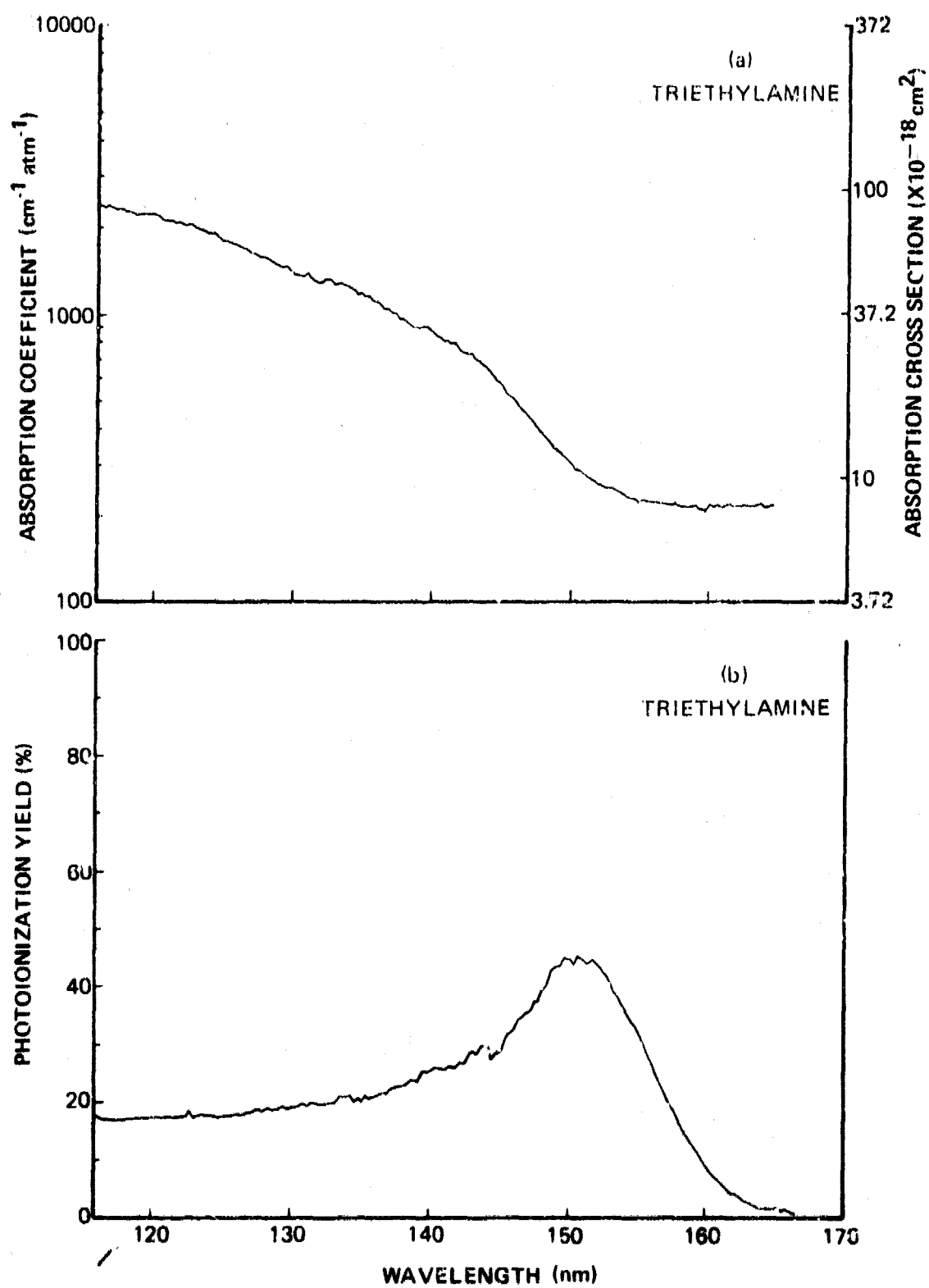


Figure 88. Photoabsorption Cross Sections (a) and Photoionization Yields (b) of Triethylamine

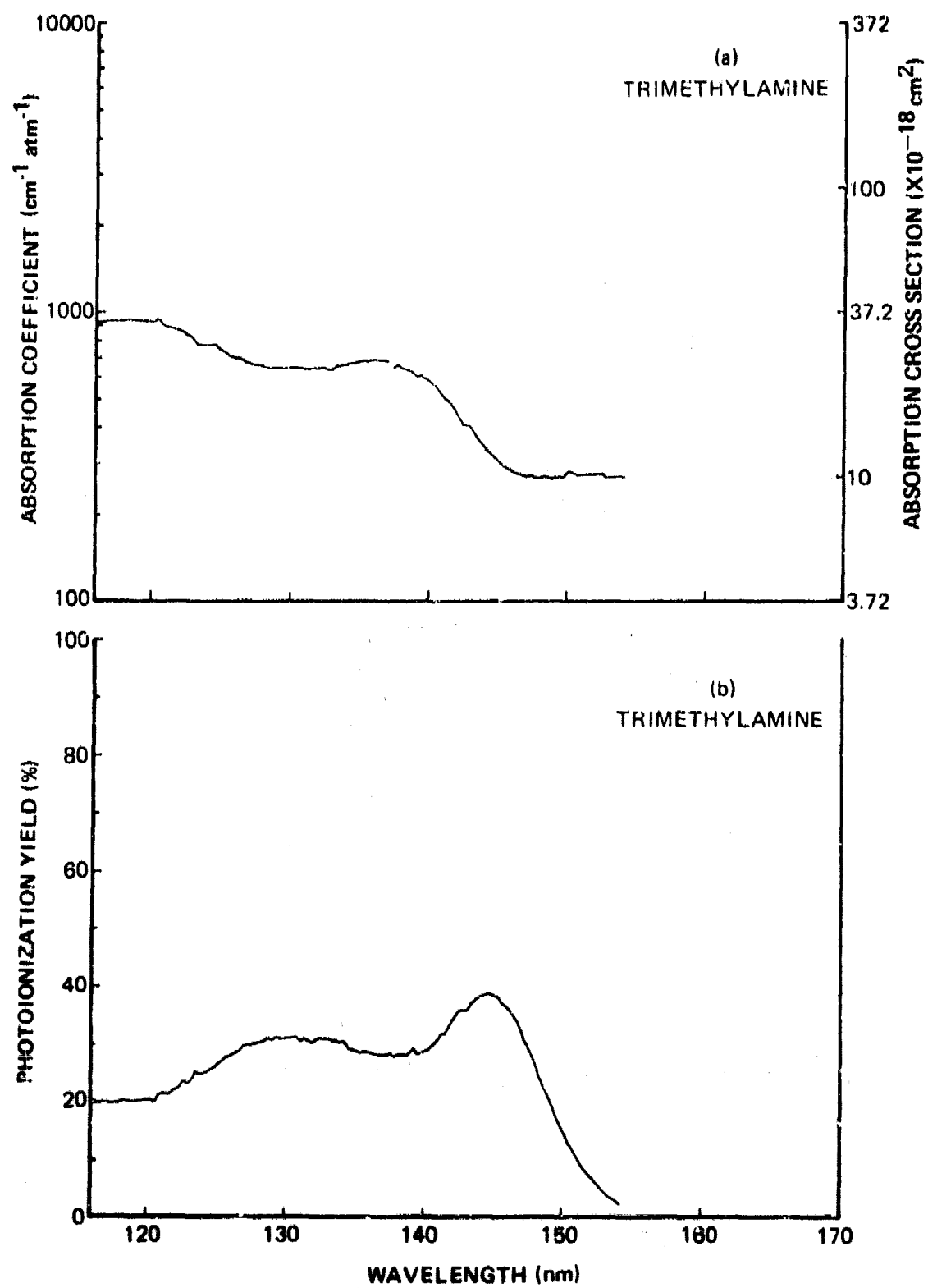


Figure 89. Photoabsorption Cross Sections (a) and Photoionization Yields (b) of Trimethylamine

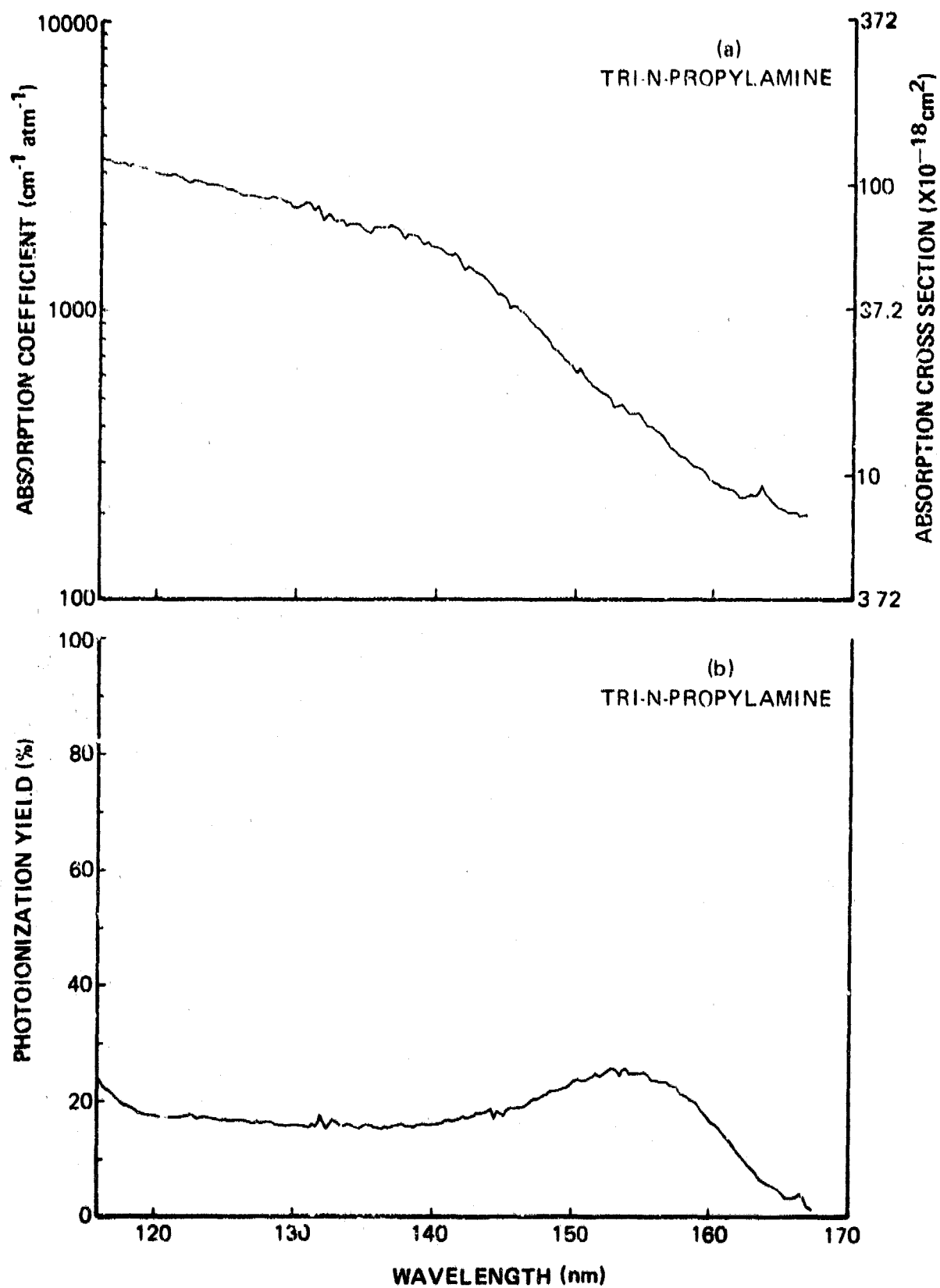


Figure 90. Photoabsorption Cross Sections (a) and Photoionization Yields (b) of Tri-n-Propylamine



eliminate errors caused by the slow response time of the I-V converters. The relatively smooth curves which resulted indicate the validity of this assumption.

Overall accuracy is estimated to be  $\pm 15\%$  for the yield measurements and  $\sim 19\%$  for the cross-section data. Data collection was terminated when the signal reached the I-V converter limit ( $\sim 10^{-12}$  A). For this reason, the trimethylamine curves extend only to 154 nm, while the dimethylaniline plots are valid out to  $\sim 170$  nm. Although a plateau for ion-chamber current as a function of retarding potential was not found with any of the four compounds, the data were collected with the retarding potential set in the center of the region of the least slope. A variation of  $\pm 15\%$  of the retarding field resulted in less than 1% change in the yield results. Reproducibility of the input intensity was ensured by monitoring the lamp-pressure, current, and coolant flow closely. Tests showed that, after a 15-min. warmup, the lamp spectra changed less than 2% from run to run. The most critical factor for the absorption calculations was the number-density determination. The pressure was monitored with a Baratron capacitance manometer having a specified accuracy of better than 1%. A potentially critical parameter was contamination level. The purity of the gas samples was the highest grade available from the manufacturers ("purified" tripropylamine, "superior" triethylamine and dimethylaniline, and minimum 99% pure trimethylamine). However, considering the generally large cross section (on the order of  $10^{-16}$  cm<sup>2</sup>) over the wavelength of interest, the data should not be particularly sensitive to impurities.

The photoionization yield of nitric oxide was measured and compared to the published data of Watanabe, *et al.*<sup>104</sup> Figure 91 shows the measured values, in general, to be  $\sim 10\%$  low, with the large dip at 117.6 nm indicating the existence of N<sub>2</sub>O in the sample. A mass-spectrometer analysis verified the presence of the nitrous oxide, as well as low levels of several other impurities. Considering the small absorption cross section of NO (on the order of  $10^{-18}$  cm<sup>2</sup>) for the wavelength region of interest, impurities exhibiting cross sections of  $10^{-16}$  cm<sup>2</sup> readily influence the data.

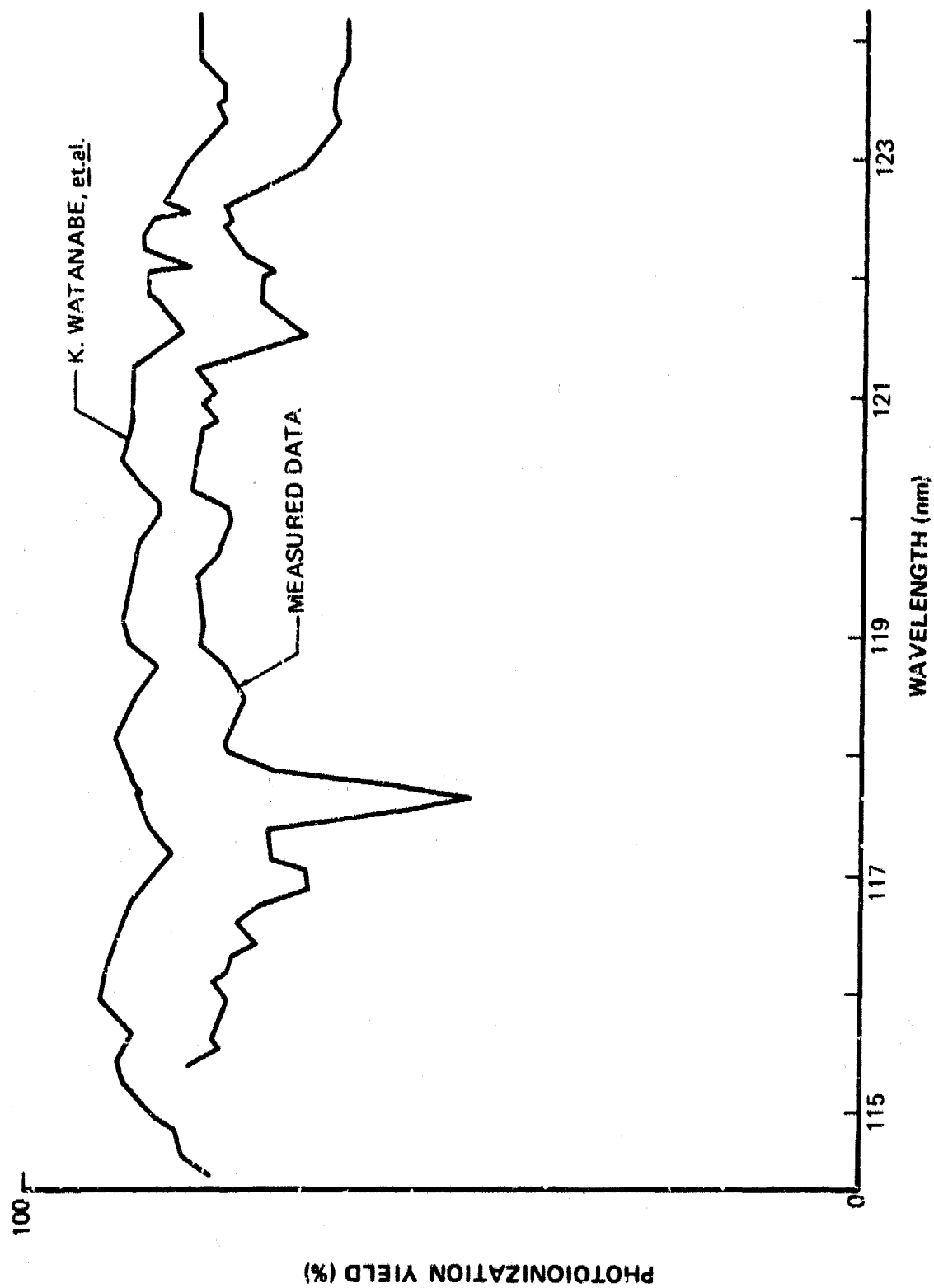


Figure 91. Comparison of Measured Photoionization Efficiency of NO with Published Data

In order to demonstrate the relative usefulness of each compound for independent ion production within a laser volume, a laser geometry of 1-cm path length from the UV source to the active volume and 5-cm path length through the active volume was assumed. The main point here is that the ionization of interest is produced within the main discharge volume by the radiation which penetrates more than 1 cm and is absorbed within the next 5 cm. The photoion production rate (R), therefore, is defined as

$$R = \frac{\text{active volume ions/sec}}{\text{source photons/sec}}$$

and is calculated from

$$R_{\lambda} = e^{-\mu_{\lambda} \ell_1} \eta_{\lambda} (1 - e^{-\mu_{\lambda} \ell_2})$$

where  $\mu_{\lambda}$  is the absorption coefficient at the number density of interest and  $\ell_1$  and  $\ell_2$  are the inactive and active path lengths, respectively. R is wavelength dependent, indicating that the choice of seed compound is highly influenced by the transmission characteristics of the laser mix.

The production rates of each compound [Figure 92 (a)-(d)] were calculated at two different pressures--one for optimum ion number at 121.6 nm wavelength and the other for maximum ions at 165 nm (154 nm for trimethylamine). The plots for tripropylamine show that for use in a CO<sub>2</sub> laser mix, efficient utilization of radiation occurs either at the window centered about 121 nm or above the CO<sub>2</sub> continuum absorption at about 165 nm--but not both at a given partial pressure. Dimethylaniline, however, is fairly efficient in both wavelength regions simultaneously. For a CO mixture, the UV source characteristics would be the determining factor in seed selection since CO is, for the most part, transparent within the region under study here. Again, dimethylaniline seems to be the best choice, although its low vapor pressure might create difficulties when used in a liquid-nitrogen-cooled environment.

Using the data of Watanabe, the ion production rate of NO was also calculated for the geometry described above. Figure 93 illustrates that for the NO seed pressure optimized at 121.6 nm (P = 3.85 Torr), the rate curve is much higher

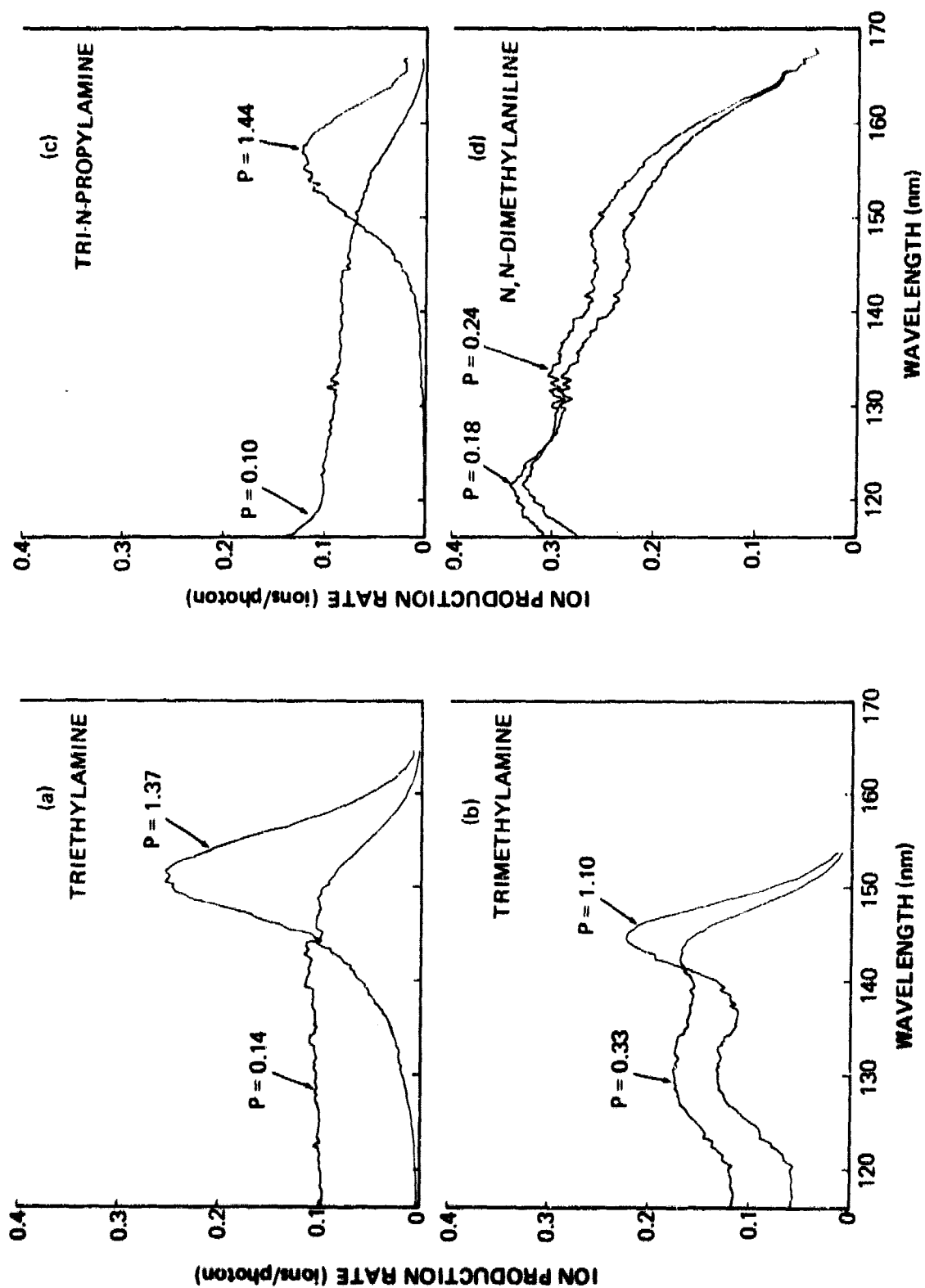


Figure 92. Ion-Production-Rate Curves with Pressure Optimized for Radiation at (a) 121.6 and 165 nm for Dimethylaniline, (b) 121.6 and 165 nm for Triethylamine, (c) 121.6 and 154 nm for Trimethylamine, and (d) 121.6 and 165 nm for Tripropylamine

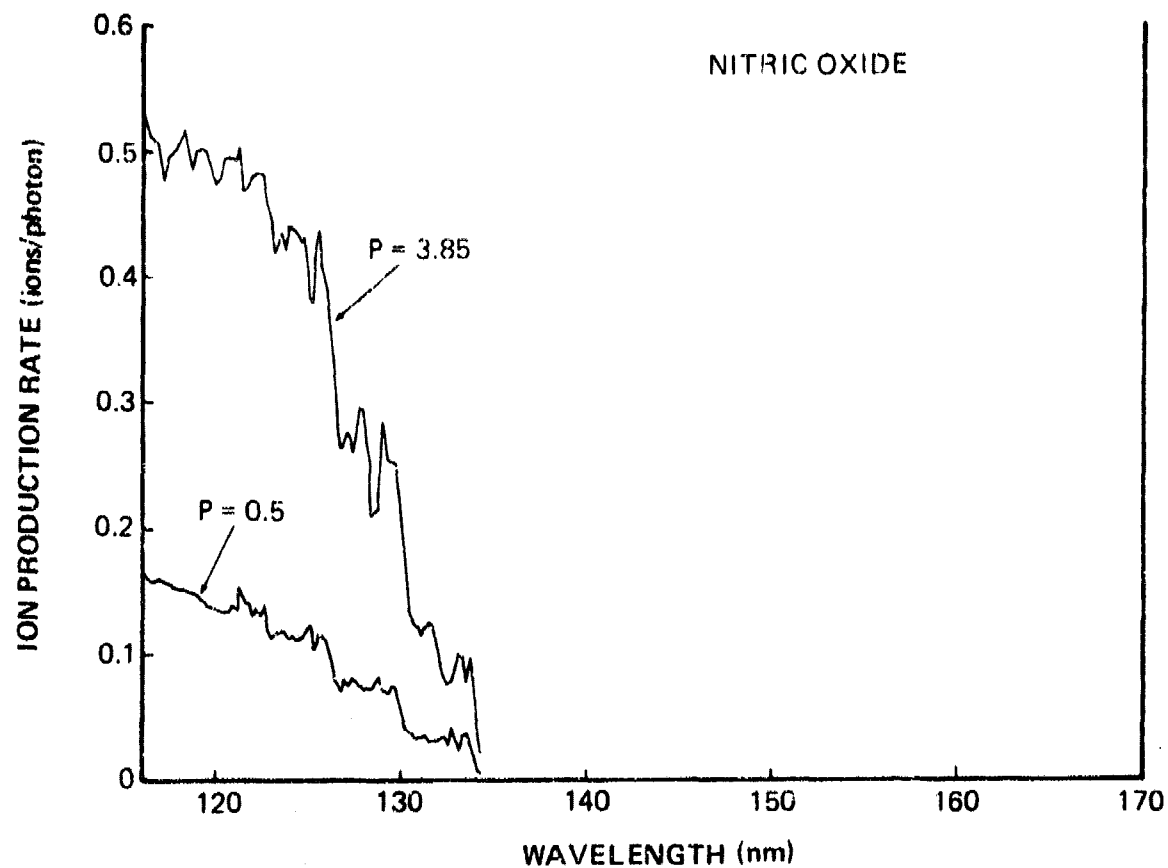


Figure 93. Ion-Production-Rate Curves for Nitric Oxide at Two Different Pressures, Calculated from Data of Watanabe, et al.<sup>104</sup>

for wavelengths shorter than  $\sim 126$  nm as compared to the measured organic seedants. However, after considering the high electron attachment rate of NO as well as the observed discharge degradation attributed to this compound above 1 Torr,<sup>105</sup> a second curve was computed at a more usable pressure (0.5 Torr). This curve indicates that NO would be competitive with the organic seedants only if the useful ionizing radiation was limited to wavelengths shorter than about 125 nm. Of course, other factors such as vapor pressure and transmission at the lasing wavelength must also be considered when choosing the optimum seed compound.

An investigation of the output characteristics of UV sources applicable to photoionization of CO and CO<sub>2</sub> lasers was made. The most commonly used source is a fast high-energy spark created by electrodes located behind the transparent cathode of the main discharge. The spark (actually a number of small arcs) occurs behind the cathode but within the laser-gas mixture. The emission characteristics of a representative source (a "sparker board") supplied by AFWL, with bare wire electrodes, was measured in CO and CO<sub>2</sub> mixes. Figure 94 gives some of the early results. It should be noted that a fast-rising pulse with medium current capability is required in order to obtain the multiple ionized states (note the C III and C IV lines of CO and CO<sub>2</sub>). The spectra resulting from the original pulse electronics, which yielded only  $\sim 1$  A with a rise time of several microseconds, showed much less structure. Figure 94 was initiated with a hydrogen thyratron pulser which yields a typical pulse of 400 A peak and a rate of rise of  $\sim 2 \times 10^9$  A/sec. Since the emission source was actually located a short distance from the monochromator, the top two traces (100-Torr CO<sub>2</sub> and 100-Torr CO) clearly show the large difference between the absorption characteristics. Due to the broadband absorption of CO<sub>2</sub>, only radiation within the low-wavelength "window" from  $\sim 118$  to 125 nm and radiation above  $\sim 160$  nm are present at any appreciable distance through the main gas volume. CO, however, appears relatively transparent, with the major attenuation being due to the very narrow absorption bands of the fourth positive system. The CO<sub>2</sub>-N<sub>2</sub>-He mixture (fourth trace) is a standard 1:1:8 laser mixture and the spectrum shows some structure within the broadband continuum only because of the relatively low CO<sub>2</sub> pressure. For atmospheric operation, however, very little

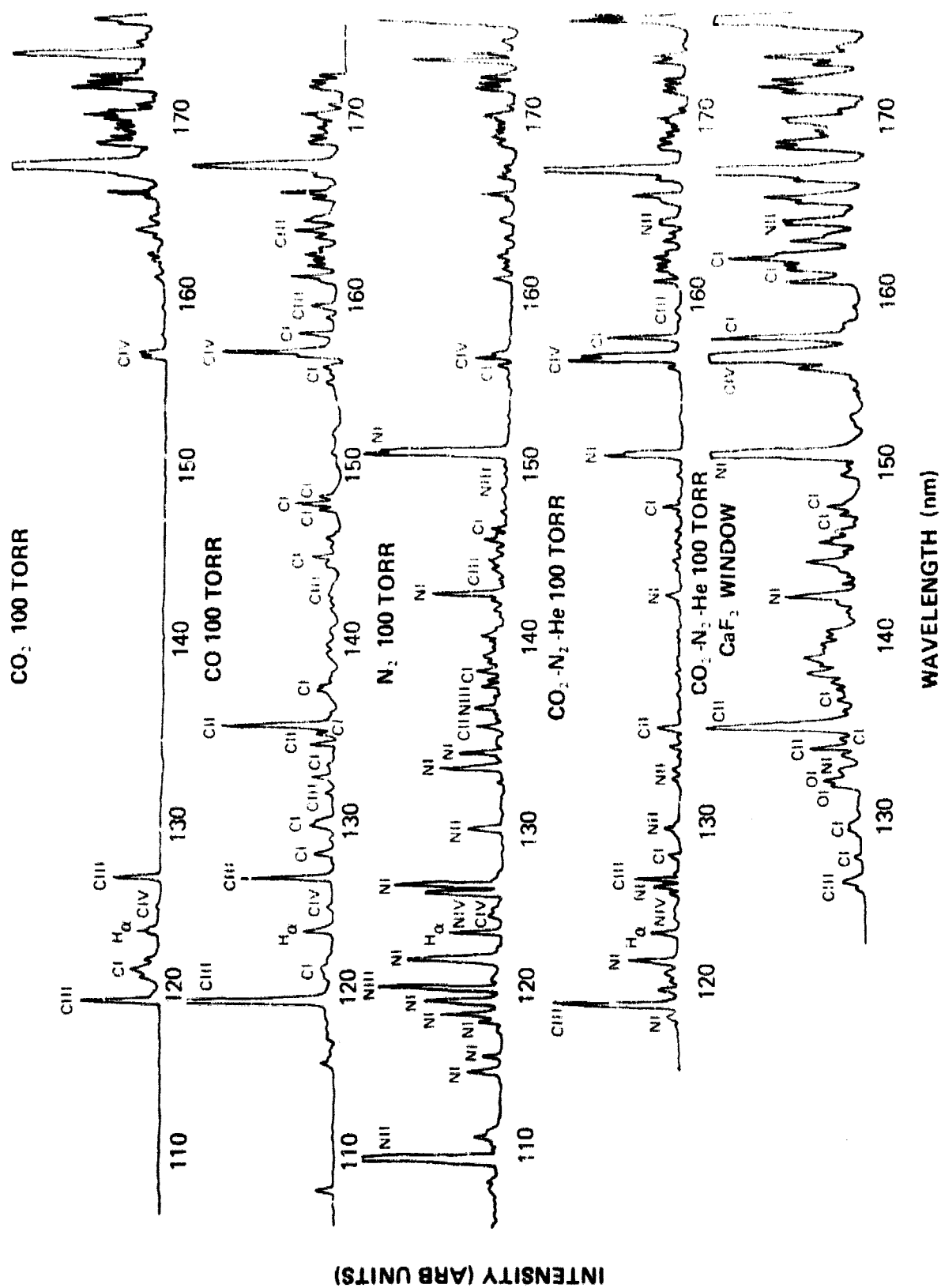


Figure 94. Comparative Spectral Emission (Qualitative) of Pin Spark in Several Molecular Gases

radiation would be present between 125 and 160 nm (similar to the top trace) since the  $\text{CO}_2$  partial pressure would be seven times higher. The bottom trace shows the effects of insertion of a 5-mm-thick  $\text{CaF}_2$  window between the spark and the monochromator. The discharge is the same as for the fourth trace, except that the  $\text{CaF}_2$  displaces some of the absorbing laser mixture. Even though the full-scale sensitivity of the bottom trace is only 20% of the other traces, significant radiation is present above  $\sim 130$  nm. The main drawback in using  $\text{CaF}_2$  is the high attenuation of radiation below  $\sim 125$  nm; that is, the lower-wavelength "window" of  $\text{CO}_2$  is not utilized. As the mixture pressure is increased toward atmospheric, the only radiation having useful penetration, then, is that above  $\sim 160$  nm.

Unfortunately, the spectra just discussed are not sufficiently quantitative to permit predictions of operational laser systems. The main problem is that the strong lines drive the detector into soft saturation and thus the weaker lines are accentuated. In order to rectify this situation, the detector electronics were improved, and the response of the monochromator/detector combination was calibrated at the Lyman- $\alpha$  wavelength (121.57 nm). Figure 95 shows the experimental arrangement. The calibration was accomplished by first recording the spectral content of a low-pressure  $\text{H}_2$  capillary discharge and then connecting this lamp to the input of a double ionization chamber, with a  $\text{MgF}_2$  window for gas isolation and for filtering out wavelengths below  $\sim 115$  nm. Nitric oxide was then used as the ionizable gas within the ion chamber along with  $\text{CO}_2$  which acted as an attenuator for all NO-ionizing wavelengths (those below 135 nm). However, the H- $\alpha$  line is attenuated to a lesser extent than other lines. With the aid of an on-line minicomputer, the ion-chamber output as a function of  $\text{CO}_2$  pressure (NO partial pressure held constant) was recorded, resulting in an intensity value for the strong  $\text{H}_\alpha$  radiation. This gave a system response in terms of photons  $\text{sec}^{-1} \text{sr}^{-1} \mu\text{A}^{-1}$  for a source at the entrance slit of the monochromator with several slit-width combinations at 121.57 nm. The calibration value is valid for other wavelengths only if the grating efficiency and detector quantum efficiency remain relatively constant over the wavelength region of interest ( $\sim 115$  to 180 nm). Although the grating efficiency has not been measured, large variations in response are not expected. The detector



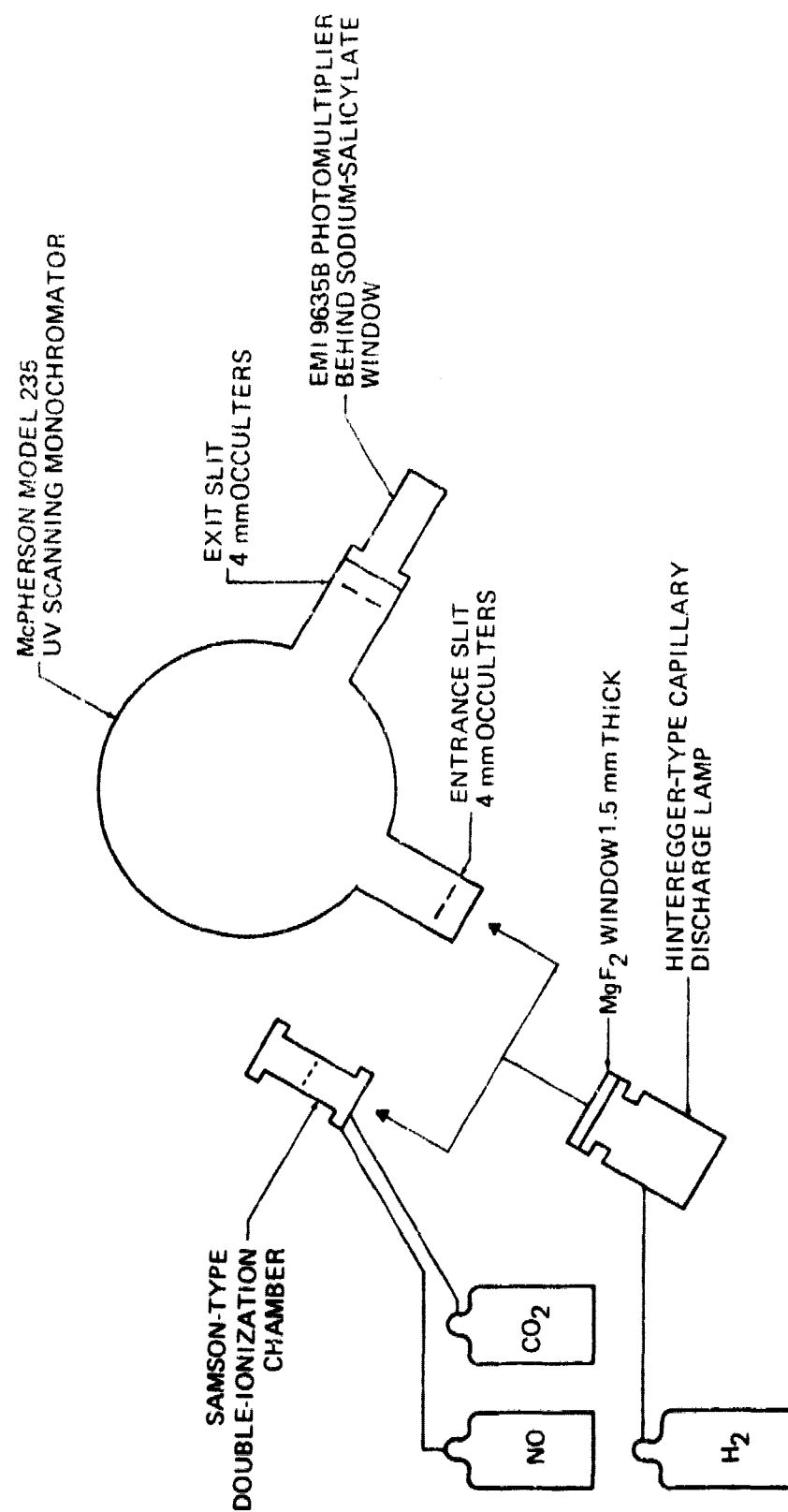


Figure 95. Schematic Diagram of the Experimental Arrangement for Calibration of UV Monochromator Response

efficiency, however, changes by a factor of two between 115 and 170 nm. Figure 96 shows the relative response of the sodium-salicylate/photomultiplier combination as a function of wavelength. The curve represents a comparison of photomultiplier output with data obtained from an NBS-calibrated photodiode, and the scale has been normalized to the response at  $H_{\gamma}$ . This plot yields the correction factor for the calibrated data of Figures 97 through 100.

Two other factors should be mentioned regarding the calibrated spectra. First, the lifetime of the optical pulses may vary considerably as a function of wavelength. Observed optical pulsewidths (FWHM) ranged from  $\sim 300$  nsec to better than 1 psec. The detector electronics were adjusted in such a way that only minor inaccuracies should result. The remaining calibration factor involves the inability to correct for the slit function of the monochromator. Since the system was properly focused, this function should be triangular; however, this correction was not applied to the data. Therefore, the strip-chart intensities of Figures 97 through 100 represent integrated values with an instrument resolution of  $0.8 \text{ \AA}$  (FWHM).

Figure 97 is a comparison of various quantitative CO spark spectra. The top two traces indicate that as CO pressure is increased, the self-absorption for radiation below  $\sim 157$  nm increases. That is, the radiation effective in ionization is decreased, although this decrease is large only at the C IV lines at 154.8 and 155.0. The attenuation can be attributed to the narrow fourth-positive system. However, the radiation above  $\sim 157$  nm, where photon energies are below that affected by the fourth-positive system, increases with CO pressure.

The third trace of Figure 97 shows that the use of He as a buffer gas results in decreased radiation at selective wavelengths. This is most apparent above 157 nm where ionized carbon lines (157.8-, 159.1-, 162.1- and 164.5-nm C III and 172.2-nm C II) almost disappear and the 164.0-nm He II line appears.

When Ar is used as the buffer gas, the overall radiation is greatly increased, as shown by the fourth trace of Figure 97. The amplitude of most of the lines in the mixture exceed that observed in CO alone (second trace) and Ar alone

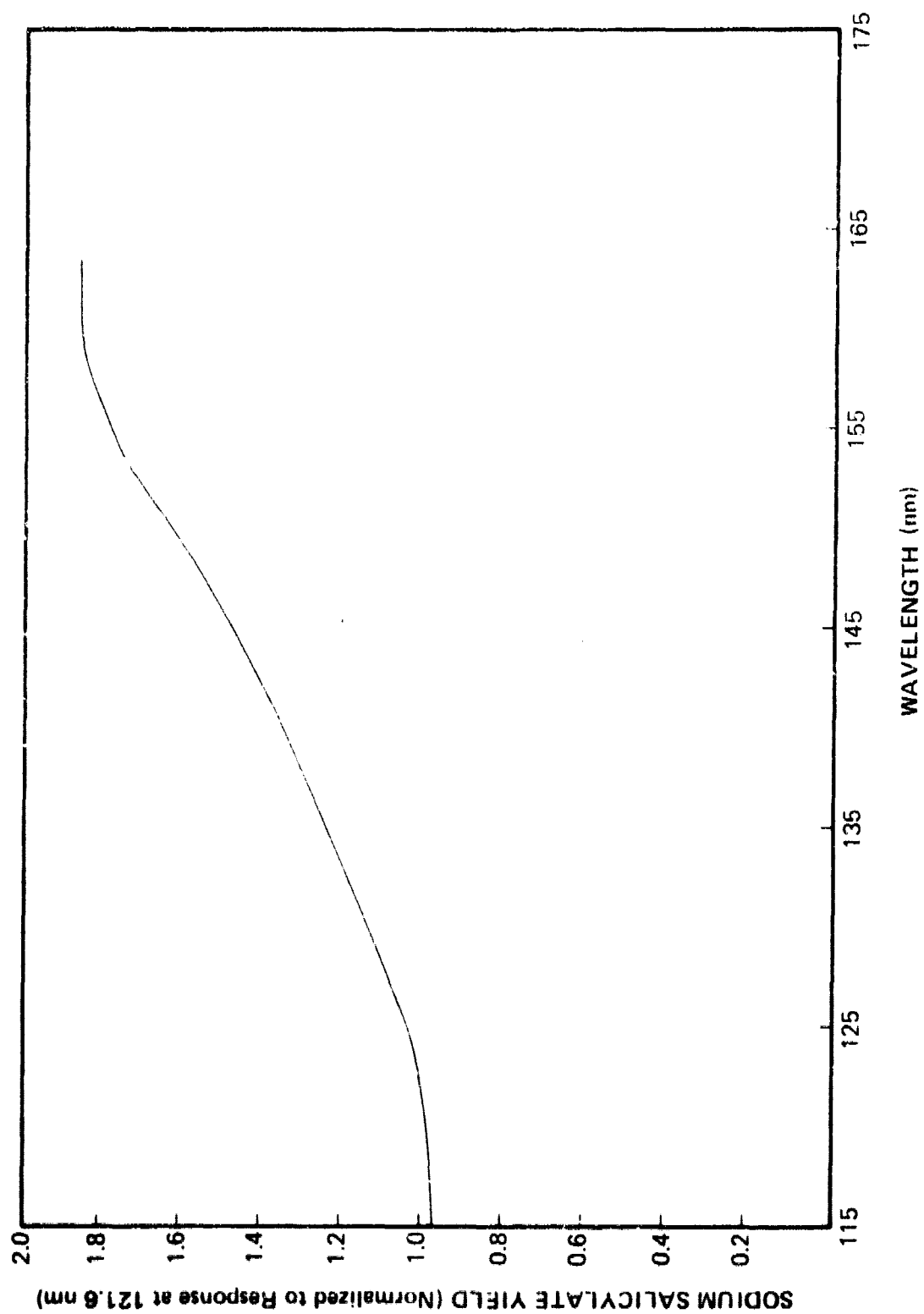


Figure 96. Normalized Quantum Yield of Sodium-Salicylate Detector

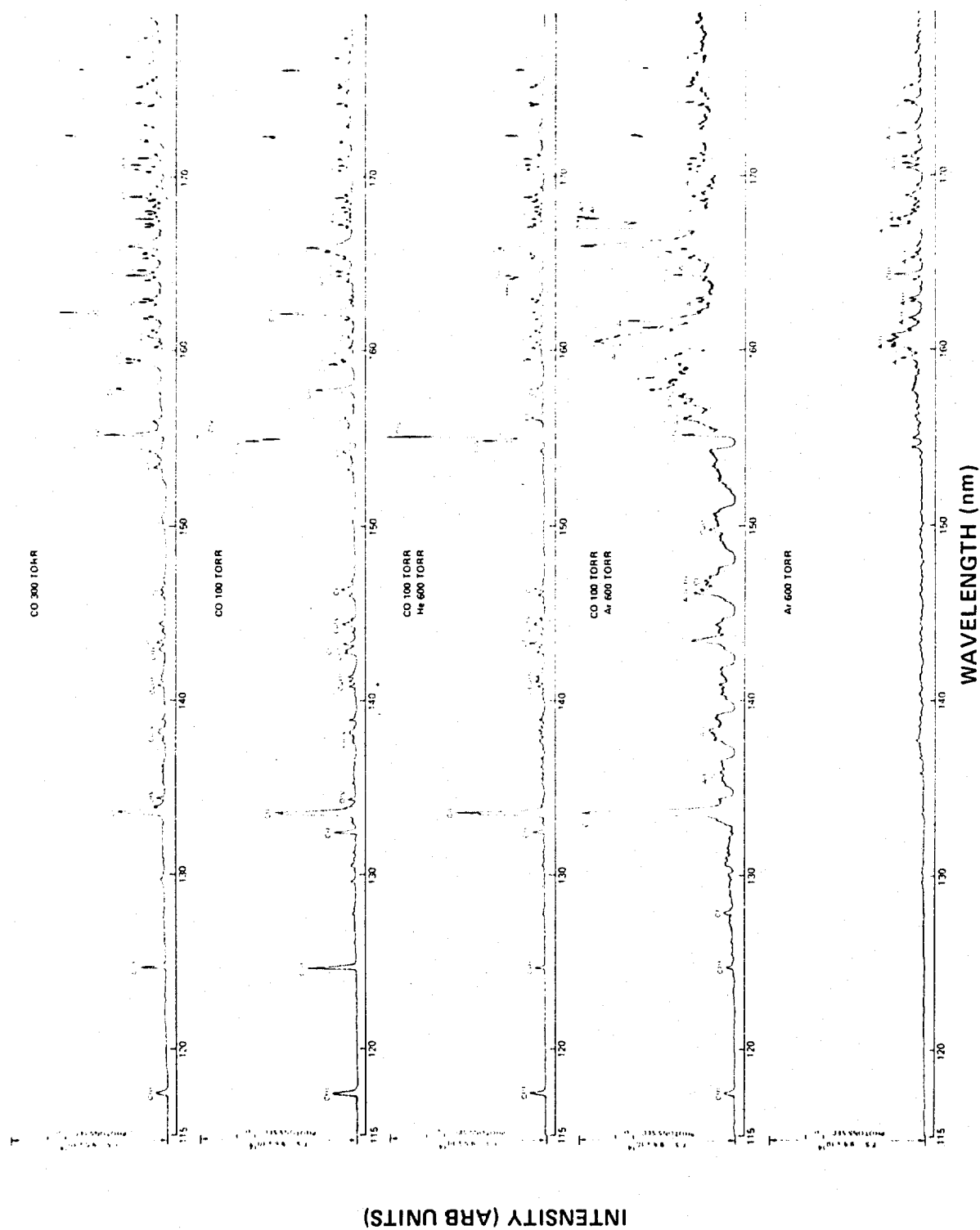


Figure 97. Comparative Spectral Emission of Pin Spark in CO Mixtures

(bottom trace). There is some decrease of radiation below  $\sim 133$  nm and a marked decrease of the C IV lines at 154.8 and 155.0 nm; however, many Ar II and Ar III lines appear above 140 nm and there is an indication of the Ar continuum (published continuum limits are 105 to 155 nm). It is interesting to note that the highly ionized carbon levels have decreased, while the number of C I lines appears to have increased (the proximity of many of the C I lines to Ar II and Ar III make this statement difficult to verify).

The spark spectra of Ar-Kr mixtures (100 Torr:  $\sim 1$  Torr) was also measured and is shown in Figure 98. Note that the vertical scale is double those of the previous figure. The overall output is much larger than the previously discussed mixtures. It is rich in singly and doubly ionized Kr and Ar lines, with an indication of both Kr and Ar continua (published Kr continuum is 125-180 nm). Of interest is the very strong C II impurity line at 133.6. This is attributed to small amounts of carbon deposited on the electrodes as a result of CO discharges. It should be noted here that when comparing with Figure 97 the absorption bands of CO are not indicated in the Ar-Kr spectra. In reality, the CO absorption will be present within the main laser-gas volume. However, even with this consideration being made, the overall radiation content of the Ar-Kr spark is superior to the CO mixtures, especially above 155 nm. Since neither the pressure nor the mixture ratio have been optimized, much better output should be possible. Correlation of the Ar-Kr spectrum with the transmission characteristics of  $\text{CaF}_2$  (see Figure 83) establishes the feasibility of using an independently optimized windowed source.

In addition to the spark spectra from two suspended pins, emission spectra of a surface spark were measured. This consisted of a spark occurring between two pads of an etched, copper-clad, glass-epoxy printed-circuit board. All other discharge conditions were the same as for the raised spark. Figure 99 shows the results. The different full-scale intensity value, as compared to Figure 97, reflects a small difference in monochromator positioning. In general, there is little difference in spark emission between the surface-spark and the raised-spark spectra. Comparing the 300-Torr CO scans of the surface-spark (top trace of Figure 99) with the

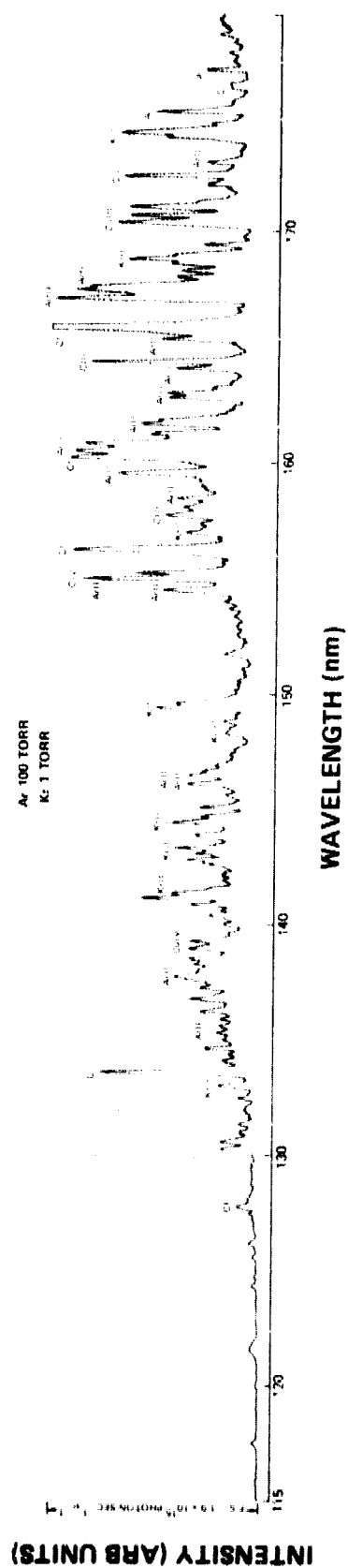


Figure 98. Spectral Emission of Pin Spark in 100-Torr Ar + 1-Torr Kr

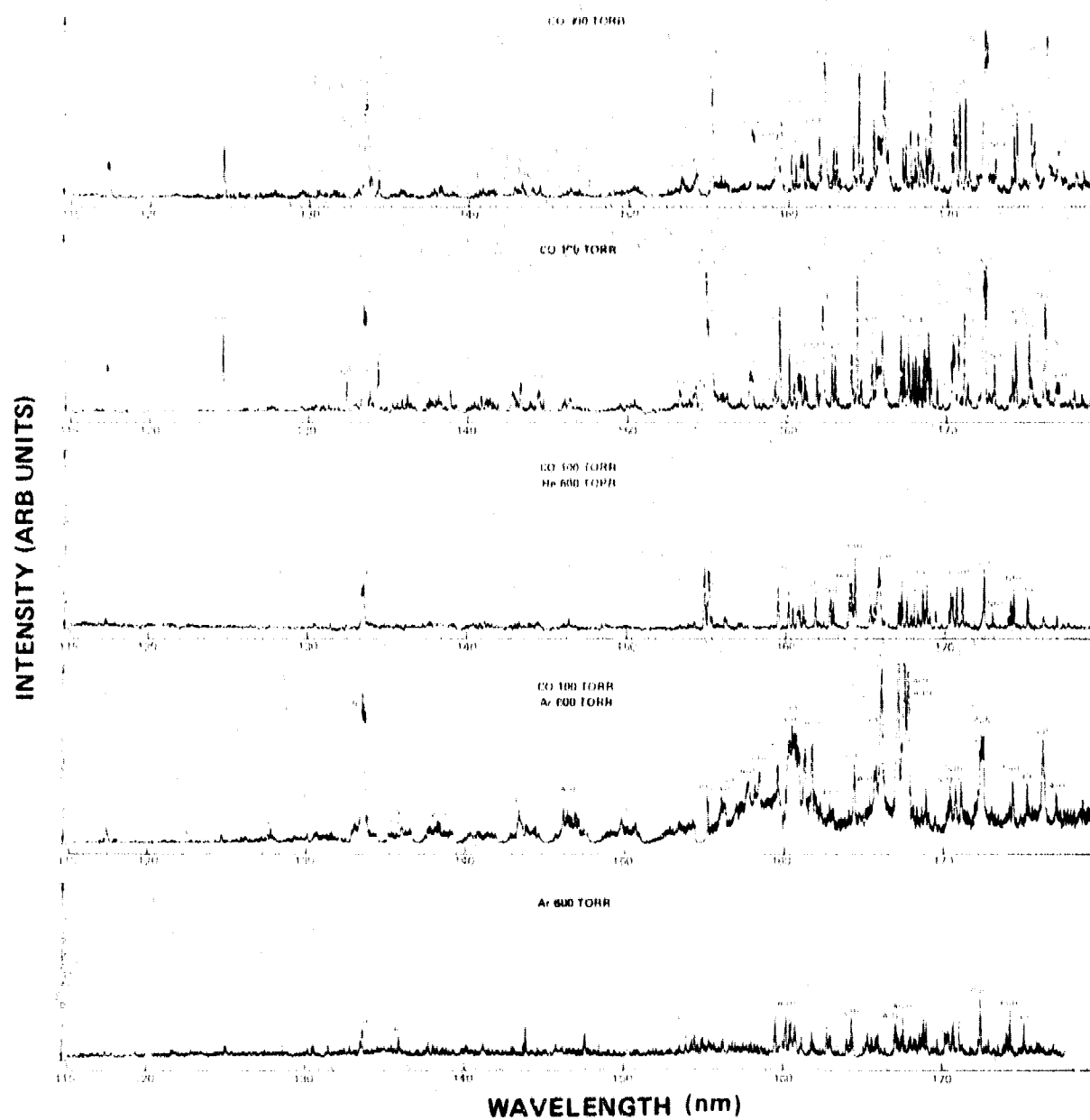


Figure 99. Comparative Spectral Emission of Surface Spark in CO Mixtures

corresponding raised-spark spectra (top trace of Figure 97), the surface method shows a slight increase in carbon lines, probably due to carbon deposition on the surface. There also is an increase in the number of unidentified lines which is attributed to impurities resulting from the local heating of the epoxy-glass board. The reproducibility of these lines is questionable.

One additional mixture was investigated with the surface spark. Figure 100 shows the measured spectrum of 100 Torr of CO with 600 Torr of N<sub>2</sub>. When comparing this to the pure CO spectrum of Figure 99, there is very little additional radiation below 172 nm as a result of the addition of N<sub>2</sub>. The only significant difference in this region is the appearance of the NI (149.3 and 149.5 nm) lines.



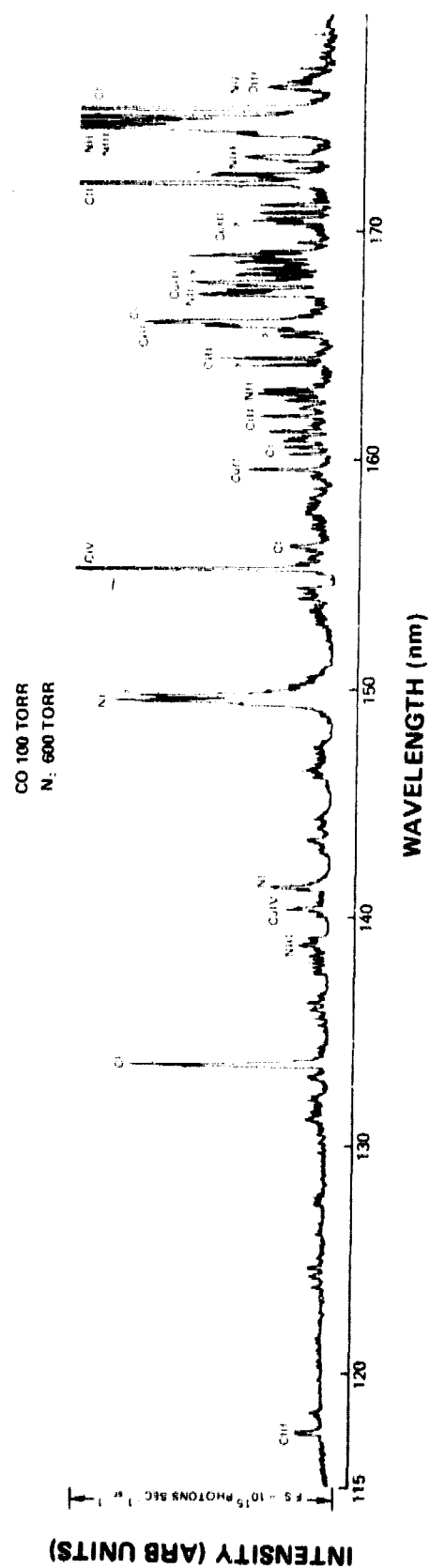


Figure 100. Spectral Emission of Surface Spark in a CO + N<sub>2</sub> Mixture

#### SECTION IV

#### CONCLUSIONS

The closed-cycle rare-gas electrical-discharge laser described in this report has been shown to be capable of high-repetition-rate, long-duration, closed-cycle operation with atomic gases. The experimental results obtained for He-Xe point up the most important features of CCRGEDL performance. Repetition rates of up to 10 kHz have been achieved, and there appears to be no fundamental limitation to increasing the PRF to 100 kHz where pulse overlap begins. The fact that lasing occurs primarily in the afterglow of the discharge indicates that increased average power is achieved by increasing the PRF rather than the current pulse length. The 4-hr continuous operation and month-long gas-fill lifetime indicate the potential for long-time operation. Economical operation has been demonstrated by the gas-fill lifetime of 30 days with no addition of gas to the system. System reliability has been demonstrated by the 180-hr operation with no major problems.

High-repetition-rate closed-cycle operation for long periods of time presents certain problems which do not appear--or are less serious--for single-pulse or low-repetition-rate operation. For example, in order to avoid the buildup of outgassing products, the system must be fabricated from UHV components (including the fan) and materials; this makes the system relatively expensive. Operation at high repetition rate requires a power source with high cw power capability; operation at high average power generates considerable heating of the pulser components which must be adequately cooled for sustained operation; waste heat from the laser discharge must be transferred from the system. Long-duration operation is possible only if system components are reliable. The high-speed fan and ferrofluidic seal must be precision made and well balanced for sustained operation at 11,500 rpm. The high-repetition-rate-pulser components must be capable of reliable operation at MW peak power levels for a large number of shots--for example, operation at 10 kHz for one year results in  $\sim 3 \times 10^{11}$  shots. This may exceed the state-of-the-art capabilities of some components, particularly thyratrons and energy-storage capacitors. Another problem which may be associated with long-duration operation is the coating of laser mirrors or windows by metal sputtered from the discharge electrodes. Gas cleanup may also be a problem, although at high pressure

It should be a very slow process. Operation at higher power will exacerbate the above problems as well as present new ones such as possible damage to electrode structures, mirrors, or windows at high intracavity power levels.

The photoabsorption and photoionization characteristics of gases applicable to the operation of photo-preionized gas discharges have been investigated with emphasis being placed on CO and CO<sub>2</sub> molecular-laser applications. Of the four seed compounds studied, N,N-dimethylaniline seems superior due to its relatively high ionization yield and its fairly uniform absorption cross section over the wavelength region of interest, although its low vapor pressure could cause some applications problems at temperatures below room temperature. Both trimethylamine and nitric oxide have much higher vapor pressures, but their useful wavelengths are limited. The seedant requirements of CO and CO<sub>2</sub> are quite different. The transmission characteristics of CO<sub>2</sub> demand a seedant with as low an ionization potential as possible for use above 160 nm or with a high production rate at the "window" region. CO, however, puts few spectral limits on the seedant, although low-vapor-pressure compounds make applications difficult and feasible possibly only in fast-flow systems.

Emission characteristics of some UV sources applicable to CO and CO<sub>2</sub> lasers have also been investigated. The radiation content of a fast high-energy spark in the laser gas mixture for the wavelength region of interest is primarily due to ionized carbon. Isolation of the spark source using a suitable window, however, is feasible for independent optimization of the UV source.

# REFERENCES

1. V. N. Karmiushin and R. I. Soloukhin, "Application of Gasdynamic Flows in Laser Technology," *Fiz. Goreniya Vzryva* 2, 162 (1972) (Lockheed Missiles and Space Co., N7311469, 1972).
2. H. Foster, "High Power CO<sub>2</sub> Lasers - A Review," *Opt. Laser Technol.* 4, 121 (June 1972).
3. A. J. Demaria, "Review of CW High-Power CO<sub>2</sub> Lasers," *Proc. IEEE* 61, 731 (June 1973).
4. O. R. Wood, II, "High-Pressure Pulsed Molecular Lasers," *Proc. IEEE* 62, 355 (March 1974).
5. S. E. Schwarz, T. A. De Temple, and R. Targ, "High-Pressure Pulsed Xenon Laser," *Appl. Phys. Lett.* 17, 305 (October 1970).
6. O. R. Wood, E. G. Burkhardt, M. A. Pollack, and T. J. Bridges, "High-Pressure Laser Action in 13 Gases with Transverse Excitation," *Appl. Phys. Lett.* 18, 112 (February 1971).
7. S. A. Ahmed and J. M. Schmidt, "Atomic Laser Action in High Pressure Gases," Presentation at the IEEE/OSA Conference on Laser Engineering and Applications, Washington, D. C., 2-4 June 1971 (unpublished).
8. R. Targ and M. W. Sasnett, "Xenon-Helium Laser at High Pressure and High Repetition Rate," *Appl. Phys. Lett.* 19, 537 (1971); R. Targ and M. W. Sasnett, "High-Repetition-Rate Xenon Laser with Transverse Excitation," *IEEE J. Quantum Electron.* QE-8, 166 (1972); T. S. Fahlen and R. Targ, "High-Average-Power Xenon Laser," *IEEE J. Quantum Electron.* QE-9, 609 (1973).
9. H. M. Lamberton and P. R. Pearson, "Improved Excitation Techniques for Atmospheric Pressure CO<sub>2</sub> Lasers," *Electron. Lett.* 7, 141 (March 1971).
10. A. Hertzberg and I. R. Hurle, "On the Possible Production of Population Inversions by Gas-Dynamic Techniques," *Bull. Am. Phys. Soc. (Series 2)* 9, 582 (1964); I. R. Hurle and A. Hertzberg, "Electronic Population Inversions by Fluid Mechanical Techniques," *Phys. Fluids* 8, 1601 (September 1965).
11. N. G. Basov and A. N. Oraevskii, "Attainment of Negative Temperatures by Heating and Cooling of a Gas System," *Sov. Phys. -JETP* 17, 1171 (November 1963).
12. W. B. Tiffany, R. Targ, and J. D. Foster, "Kilowatt CO<sub>2</sub> Gas-Transport Laser," *Appl. Phys. Lett.* 15, 91 (August 1969).

13. R. Targ and W. B. Tiffany, "Gain and Saturation in Transverse Flowing CO<sub>2</sub>-N<sub>2</sub>-He Mixtures," Appl. Phys. Lett. 15, 302 (November 1969).
14. J. A. Beaulieu, "High Peak Power Gas Lasers," Proc. IEEE 59, 667 (April 1971).
15. A. E. Hill, "Uniform Electrical Excitation of Large-Volume High-Pressure Near-Sonic CO<sub>2</sub>-N<sub>2</sub>-He Flowstream," Appl. Phys. Lett. 18, 194 (March 1971).
16. M. F. Turgeon, "High Repetition Rate TEA CO<sub>2</sub> Laser," IEEE J. Quantum Electron. QE-7, 495 (October 1971).
17. R. Dumanchin, M. Michon, J. C. Farcy, G. Boudinet, and J. Rocca-Serra, "Extension of TEA CO<sub>2</sub> Laser Capabilities," IEEE J. Quantum Electron. QE-8, 163 (February 1972).
18. H. J. Seguin and G. Sedgwick, "Low Voltage Gas Transport TE CO<sub>2</sub> Laser," Appl. Optics 11, 745 (April 1972).
19. C. O. Brown and J. W. Davis, "Closed-Cycle Performance of a High-Power Electric-Discharge Laser," Appl. Phys. Lett. 21, 480 (November 1972).
20. C. W. Glanford, M. F. Paris, P. R. Pearson, and D. C. Tyte, "High-Repetition-Rate Operation of a 'Double-Rogowski' TEA CO<sub>2</sub> Laser," IEEE J. Quantum Electron. QE-9, 683 (June 1973).
21. G. S. Dzakowic and S. A. Wutzke, "High-Pulse-Rate Glow-Discharge Stabilization by Gas Flow," J. Appl. Phys. 44, 5061 (November 1973).
22. J. Tulip, H. J. Seguin, and W. Faszer, "High-Repetition-Rate TEA-Laser Discharge Using Integrated Preionization and Switching," IEEE J. Quantum Electron. QE-12, 155 (February 1976).
23. R. Targ, "Pulse Nitrogen Laser at High Repetition Rate," IEEE J. Quantum Electron. QE-8, 726 (August 1972).
24. J. Wilson, "Nitrogen Laser Action in a Supersonic Flow," Appl. Phys. Lett. 8, 159 (April 1966).
25. D. C. Smith and J. M. McCoy, "Effects of Diffusion on the Saturation Intensity of a CO<sub>2</sub> Laser," Appl. Phys. Lett. 15, 282 (November 1969).
26. C. P. Christensen, C. Freed, and H. A. Haus, "Gain Saturation and Diffusion in CO<sub>2</sub> Lasers," IEEE J. Quantum Electron. QE-5, 276 (June 1969).
27. T. F. Deutsch, F. A. Horrigan, and R. I. Rudko, "CW Operation of High-Pressure Flowing CO<sub>2</sub> Lasers," Appl. Phys. Lett. 15, 88 (August 1969).
28. A. E. Hill, "Role of Thermal Effects and Fast Flow Power Scaling Techniques in CO<sub>2</sub>-N<sub>2</sub>-He Lasers," Appl. Phys. Lett. 16, 423 (June 1970).

29. T. Kan and W. Whitney, "Forced-Convective-Flow Carbon Monoxide Laser," Appl. Phys. Lett. 21, 213 (September 1972).
30. H. Shirahata and A. Fujisawa, "Aerodynamically Mixed Electric Discharge CO<sub>2</sub> Laser," Appl. Phys. Lett. 23, 80 (July 1973).
31. A. C. Eckbreth and J. W. Davis, "Cross-Beam Electric-Discharge Convection Laser," Appl. Phys. Lett. 19, 101 (August 1971).
32. J. P. Reilly, "Pulser/Sustainer Electric-Discharge Laser," J. Appl. Phys. 43, 3411 (August 1972).
33. R. J. Freiberg and P. O. Clark, "CO<sub>2</sub> Transverse-Discharge Lasers," IEEE J. Quantum Electron. QE-6, 105 (February 1970).
34. W. M. Brandenburg, M. P. Bailey, and P. D. Texeira, "Supersonic Transverse Electrical Discharge Laser," IEEE J. Quantum Electron. QE-8, 414 (April 1972).
35. D. B. Nichols and W. M. Brandenburg, "Radio-Frequency Preionization in a Supersonic Transverse Electrical Discharge Laser," IEEE J. Quantum Electron. QE-8, 718 (August 1972).
36. N. Ben-Yosef, E. Bin-Nun, F. Dothan-Deutsch, and S. Yatsiv, "Electrode Configuration and Power Output for a Transverse Flow CO<sub>2</sub> Laser," J. Phys. E - Scientific Instruments 4, 708 (September 1971).
37. C. J. Buczek, R. J. Wayne, P. Chenausky, and R. J. Freiberg, "Magnetically Stabilized Cross-Field CO<sub>2</sub> Laser," Appl. Phys. Lett. 16, 321 (April 1970).
38. C. J. Buczek, R. J. Freiberg, P. P. Chenausky, and R. J. Wayne, "Magnetic Stabilization of the Plasma Column in Flowing Molecular Lasers," Proc. IEEE 59, 659 (April 1971).
39. C. O. Brown, "High-Power CO<sub>2</sub> Electric Discharge Mixing Laser," Appl. Phys. Lett. 17, 388 (November 1970).
40. A. C. Eckbreth, J. W. Davis, and E. A. Pinsley, "Investigation of a CO<sub>2</sub> Laser Pulse Amplifier," Appl. Phys. Lett. 18, 73 (February 1971).
41. B. Lavarini, J. Bettini, J. Crancon, and M. Michon, "Laser a Excitation Electrique et Detente Adiabatique," Compt. Rend. (Series B) 272, 335 (February 1971).
42. P. R. Pearson and H. M. Lamberton, "Atmospheric Pressure CO<sub>2</sub> Lasers Giving High Output Energy Per Unit Volume," IEEE J. Quantum Electron. QE-8, 145 (February 1972).
43. M. C. Richardson, A. J. Alcock, K. Leopold, and P. Burtyn, "A 300-J Multigigawatt CO<sub>2</sub> Laser," IEEE J. Quantum Electron. QE-9, 236 (February 1973).

44. G. Girard, M. Huguet, and M. Michon, "High-Power Double-Discharge TEA Laser Medium Diagnostic," IEEE J. Quantum Electron. QE-9, 426 (March 1973).
45. J. Lachambre, J. Gilbert, F. Rheault, R. Fortin, and M. Blanchard, "Performance Characteristics of a TEA Double-Discharge Grid Amplifier," IEEE J. Quantum Electron. QE-9, 459 (April 1973).
46. H. Sequin and J. Tulip, "Photoinitiated and Photosustained Laser," Appl. Phys. Lett. 21, 414 (November 1972).
47. O. P. Judd, "An Efficient Electrical CO<sub>2</sub> Laser Using Preionization by Ultraviolet Radiation," Appl. Phys. Lett. 22, 95 (February 1973).
48. D. B. Cohn and E. R. Ault, "Photoinitiated Transversely Sustained CO<sub>2</sub> Laser," Appl. Phys. Lett. 22, 138 (February 1973).
49. R. K. Gainsworthy, L. E. S. Mathias, and C. H. H. Carmichael, "Atmospheric Pressure Pulsed CO<sub>2</sub> Laser Utilizing Preionization by High-Energy Electrons," Appl. Phys. Lett. 19, 506 (December 1971).
50. P. A. Belanger, R. Tremblay, J. Boivin, and G. Otis, "Atmospheric Pressure CO<sub>2</sub> Pulsed Laser with Semiconducting Plastic Electrodes," Can. J. Phys. 50, 2753 (November 1972).
51. T. W. Johns and J. A. Nation, "A Resistive Electrode, High Energy, Transverse Laser Discharge," Rev. Sci. Instrum. 44, 169 (February 1973).
52. W. R. Bennett, Jr., "Gaseous Optical Masers," Appl. Opt. Supplement on Optical Masers (December 1962).
53. W. R. Bennett, Jr., "Inversion Mechanisms in Gas Lasers," Appl. Opt. Supplement on Chemical Lasers (1965).
54. C. S. Willett, "Neutral Gas Lasers," in Handbook of Lasers (Chemical Rubber Company, Cleveland, Ohio, 1971), p. 183.
55. E. F. Labuda and E. I. Gordon, "Microwave Determination of Average Electron Energy and Density in He-Ne Discharges," J. Appl. Phys. 35, 1647 (May 1964).
56. A. D. White and E. I. Gordon, "Excitation Mechanisms and Current Dependence of Population Inversion in He-Ne Lasers," Appl. Phys. Lett. 3, 197 (December 1963).
57. P. O. Clark, "Investigation of the Operating Characteristics of the 3.5  $\mu$  Xenon Laser," IEEE J. Quantum Electron. QE-1, 109 (June 1965).
58. F. Horrigan, "Xenon Laser Research," AFAL-TR-65-221 (February 1966).

59. W. R. Bennett, Jr., P. J. Kindlmann, and G. N. Mercer, "Measurement of Excited State Relaxation Rates," Appl. Opt. Supplement on Chemical Lasers (1965).
60. O. Andrade, M. Gallardo, and K. Bockasten, "High-Gain Laser Lines in Noble Gases," Appl. Phys. Lett. 11, 99 (August 1967).
61. G. J. Linford, "High-Gain Neutral Laser Lines in Pulsed Noble-Gas Discharges," IEEE J. Quantum Electron. QE-8, 477 (June 1972); G. J. Linford, "New Pulsed Laser Lines in Krypton," IEEE J. Quantum Electron. QE-9, 610 (June 1973); G. J. Linford, "New Pulsed and CW Laser Lines in the Heavy Noble Gases," IEEE J. Quantum Electron. QE-9, 611 (June 1973).
62. C. T. Ryan, "Preliminary Investigation of a 'Superradiant' Neutral Argon Line in a TEA Laser," in MIT Quarterly Progress Report 108 (January 1973).
63. E. I. Shtyrkov and E. V. Subbes, "Characteristics of Pulsed Laser Action in Helium-Neon and Helium-Argon Mixtures," Optics and Spectroscopy 21, 143 (August 1966).
64. H. A. H. Boot, D. M. Clunie, and R. S. A. Thorn, "Pulsed Laser Operation in a High-Pressure Helium Neon Mixture," Nature 198, 773 (1963).
65. D. M. Clunie and N. H. Rock, "Optical Gain in Neon and Helium/Neon Pulsed Discharges," Phys. Lett. 13, 213 (1964).
66. E. H. Byerly, J. Goldsmith, and W. H. McMahan, "Observations of Increased Power Output from He-Ne Optical Maser by Means of Externally Applied High-Voltage Pulsing," Proc. IEEE 51, 360 (1963).
67. L. L. Antes, J. Goldsmith, and W. McMahan, "Pulsed Helium-Neon Gas Laser Applications," IEEE Trans. on Military Electronics MIL-8, 3 (1964).
68. N. Suzuki, "Decay Rates of Metastable Helium Atoms and Laser Enhancements in Afterglow Period," Jap. J. Appl. Phys. 3, 705 (1964).
69. S. Kobayashi, H. Okamoto, and M. Kamiyama, "Characteristics of a Pulsed High-Pressure He-Ne Laser," IEEE J. Quantum Electron. QE-1, 222 (1965).
70. K. Toyoda and C. Yamanaka, "Enhanced Lasing of the High Pressure He-Ne Laser," IEEE J. Quantum Electron. QE-1, 281 (1965).
71. P. Burlamacchi and R. Pratesi, "Comment on 'Enhanced Lasing of the High Pressure He-Ne Laser'," IEEE J. Quantum Electron. QE-2, 671 (1966).



72. P. Burlamacchi and R. Pratesi, "Study of Power Enhancements during the Initial and Afterglow-Transients of Pulsed He-Ne Gas Lasers," *Nuovo Cimento* 43B, 150 (1966).
73. M. Ohl, "Transient Behavior of He-Ne Lasers," *Jap. J. Appl. Phys.* 5, 1084 (1966).
74. G. G. Petrash, "Pulsed Gas-Discharge Lasers," *Soviet Physics Uspekhi* 14, 747 (May-June 1972).
75. D. M. Clunie, R. S. A. Thorne, and K. E. Trezise, "Asymmetric Visible Super-Radiant Emission from a Pulsed Neon Discharge," *Phys. Lett.* 14, 28 (January 1965).
76. D. A. Leonard, R. A. Neal, and E. T. Gerry, "Observation of a Super-Radiant Self-Terminating Green Laser Transition in Neon," *Appl. Phys. Lett.* 7, 175 (September 1965).
77. J. D. Shipman, Jr., "Traveling Wave Excitation of High Power Gas Lasers," *Appl. Phys. Lett.* 10, 3 (January 1967).
78. D. A. Leonard and W. R. Zinky, "Coherence Properties of the Super-Radiant 5401 Å Pulsed Neon Laser," *Appl. Phys. Lett.* 12, 113 (February 1968).
79. D. A. Leonard, "The 5401-Å Pulsed Neon Laser," *IEEE J. Quantum Electron.* QE-3, 133 (March 1967).
80. D. A. Leonard and R. F. Caristi, "Recent Developments in Superradiant 5401-Å Pulsed Neon Lasers," *IEEE J. Quantum Electron.* QE-4, 359 (May 1968).
81. A. A. Isaev and G. G. Petrash, "Mechanism of Pulsed Superradiance from 2p-1s Transitions in Neon," *Soviet Physics--JETP* 29, 607 (October 1969).
82. M. Corti, "Pulsed Neon Laser at 5401 Å with Subnanosecond Emission," *Optics Communications* 4, 373 (January 1972).
83. R. C. Bolden, R. S. Hemsworth, M. J. Shaw and N. D. Twiddy, "The Measurement of Penning Ionization Cross Sections for Helium 2 <sup>3</sup>S Metastables Using a Steady-State Flowing Afterglow Method," *J. Phys. B* 3, 61 (1970); "Measurement of Thermal Energy Ion-Neutral Reaction Rate Coefficients for Rare-Gas Ions," *J. Phys. B* 3, 45 (1970).
84. C. C. Leiby, Jr. and E. C. Dunton, "A Circulating Pump for Ultrapure or Toxic Gases," *Rev. Sci. Instrum.* 43, 1202 (August 1972).
85. S. S. Ballard, J. S. Browder, and J. F. Ebersole, "Transmission and Absorption of Special Crystals and Certain Glasses," in *AIP Handbook*, 3rd ed. (American Institute of Physics, New York, 1972), pp. 6-63, 6-66.

86. A. Yariv, Introduction to Optical Electronics (Holt, Rinehart and Winston, Inc., New York, 1971), p. 111.
87. P. W. Smith and P. J. Maloney, "A Self-Stabilized 3.5- $\mu$ m Waveguide He-Xe Laser," Appl. Phys. Lett. 22, 667 (June 1973).
88. J. Brochard and R. Vetter, "Etude du Deplacement des Raies Laser Infrarouges du Xenon sous l'Influence de la Pression," Phys. Lett. 33A, 398 (November 1970).
89. L. A. Newman and T. A. De Temple, "Electron Beam Initiated He-Xe Gas Discharge Laser," 28th Gaseous Electronics Conference, Rolla, Missouri, 21-24 October 1975; "High Pressure Infrared Ar-Xe Laser System: Ionizer-Sustainer Mode of Excitation," Appl. Phys. Lett. 27 (December 1975).
90. W. L. Faust and R. A. McFarlane, "Line Strengths for Noble-Gas Maser Transitions; Calculations of Gain/Inversion at Various Wavelengths," J. Appl. Phys. 35, 2010 (July 1964).
91. R. Shuker, A. Szoke, E. Zamir, and Y. Binur, "Energy Transfer in Noble-Gas Mixtures: Penning Ionization in He/Xe," Phys. Rev. A11, 1187 (April 1975).
92. W. B. Bridges and A. N. Chester, "Ionized Gas Lasers," in Handbook of Lasers (Chemical Rubber Company, Cleveland, Ohio, 1971), p. 242.
93. R. A. McClatchey and J. E. A. Selby, "Atmospheric Attenuation of Laser Radiation from 0.76 to 31.25  $\mu$ m," AFCKL-TR-74-0003 (Air Force Cambridge Research Laboratories, Bedford, Massachusetts, January 1974).
94. C. E. Moore, Atomic Energy Levels, Vol. III, NBS Circular 467 (National Bureau of Standards, Washington, D. C., 1958).
95. C. S. Willett, An Introduction to Gas Lasers: Population Inversion Mechanisms (Pergamon Press, New York, 1974), p. 166.
96. A. Barbet, N. Sadeghi, and J. C. Pebay-Peyroula, "Study of the Electron-Ion Recombination Processes in the Xenon Afterglow Plasma," J. Phys. B: Atom. Molec. Phys. 8, 1785 (1975).
97. D. C. Lorents, "The Physics of Electron Beam Excited Rare Gases at High Densities," Physica 82C, 19 (1976).
98. P. Kebarle, R. M. Haynes, and S. K. Searles, "Mass-Spectrometric Study of Ions in Xe, Kr, Ar, Ne at Pressures up to 40 Torr: Termolecular Formation of the Rare-Gas Molecular Ions. Bond Dissociation Energy of  $\text{Ar}_2^+$  and  $\text{Ne}_2^+$ ," J. Chem. Phys. 47, 1684 (September 1967).
99. A. Gedanken, J. Jortner, B. Raz, and A. Szoke, "Electronic Energy Transfer Phenomena in Rare Gases," J. Chem. Phys. 57, 3456 (October 1972).
100. Y. J. Shiu, M. A. Biondi, and D. P. Sipler, "Electron Temperature Dependence of Dissociative Recombination in Xenon," 29th Annual Gaseous Electronics Conference, Cleveland, Ohio, 19-22 October 1976.

101. H. J. J. Seguin, J. Tulip, and D. McKen, "UV Photoionization Density Measurements in TEA Lasers," Appl. Phys. Lett. 23, 344 (September 1973); F. Varsangi, O. P. Judd, and J. Y. Wada, "Impurity Effects and Ultraviolet Source Characteristics of a UV Preionized CO<sub>2</sub> Laser," IEEE J. Quantum Electron. QE-9, 682 (June 1973); H. J. Seguin, J. Tulip, and D. C. McKen, "Ultraviolet Photoionization in TEA Lasers," IEEE J. Quantum Electron. QE-10, 311 (March 1974); R. V. Babcock, I. Liberman, and W. D. Partlow, "Volume Ultraviolet Preionization from Bare Sparks," IEEE J. Quantum Electron. QE-12, 29 (January 1976); H. J. Seguin, D. McKen, and J. Tulip, "Photon Emission and Photoionization Measurements in the CO<sub>2</sub> Laser Environment," Appl. Phys. Lett. 28, 487 (May 1976); and D. C. McKen, H. J. Seguin, and J. Tulip, "Photoionization Parameters in the Carbon Dioxide Laser Gases," IEEE J. Quantum Electron. QE-12, 470 (August 1976).
102. E. P. Velikhov, E. A. Muratov, V. D. Pis'Mennyi, A. M. Prokhorov, and A. T. Rakhimov, "Atmospheric-Pressure CO<sub>2</sub> Laser with Nonautonomous Discharge Controlled by Ultraviolet Radiation," JETP Lett. 20, 47 (July 1974).
103. K. Watanabe, M. Zelikoff, and E. C. Y. Inn, AFCRC Technical Report No. 53-23, Geophys. Res. Paper No. 21 (1953), as reported by J. O. Sullivan and A. C. Holland, "A Congeries of Absorption Cross Sections for Wavelengths Less Than 3000 Å," NASA CR-371 (NASA, Washington, D. C., January 1966).
104. K. Watanabe, F. M. Matsunaga, and H. Sakai, "Absorption Coefficient and Photoionization Yield of NO in the Region 580-1350 Å," Appl. Opt. 6, 391 (March 1967).
105. A. L. S. Smith, T. H. Bett, and P. G. Browne, "The Effects of Gas Additives on TEA CO<sub>2</sub> Lasers," IEEE J. Quantum Electron. QE-11, 335 (July 1975); P. Bletzinger, D. A. LaBorde, W. F. Bailey, W. H. Long, P. D. Tannen, and A. Garscadden, "Influence of Contaminants on the CO<sub>2</sub> Electric-Discharge Laser," IEEE J. Quantum Electron. QE-11, 317 (July 1975).

**- Document -**  
**Reproduced From**  
**Best Available Copy**